Soft X-ray photoemission spectroscopy

Federica Venturini

To cite this version:

Federica Venturini. Soft X-ray photoemission spectroscopy. Physics [physics]. Université Joseph-Fourier - Grenoble I, 2005. English. NNT : . tel-00011953

HAL Id: tel-00011953
https://theses.hal.science/tel-00011953
Submitted on 15 Mar 2006

UNIVERSITE JOSEPH FOURIER – GRENOBLE I
SCIENCES, TECHNOLOGIE, MEDECINE

THESE

pour obtenir le titre de

DOCTEUR DE L' UNIVERSITE JOSEPH FOURIER

Spécialité : PHYSIQUE

Présentée par

Federica Venturini

Soft X-ray photoemission spectroscopy

Composition du jury :

Rapporteurs :	Dominique Chandesris Karol Hricovini
Examinateurs:	Marco Grioni Olivier Isnard
Directeur de thèse:	Nicholas B. Brookes

for Geo

The cover illustration is by Edith Schloss.

Acknowledgments.

In what follows I will attempt to thank the people who have made this experience a very special one. In trying to do so, my first and biggest thank you is for my supervisor, Nick Brookes. To him go my gratitude and friendship, for having motivated and guided me, for having never failed to show me the way beyond what I considered to be my limits. His honest enthusiasm and curiosity, his reliable presence and help, have made working together a rare privilege and a challenging experience. Despite the difficult moments, never once have I felt alone, very rarely have I worked without smiling. For this, especially, I thank Nick, knowing how complicated it is to appreciate each one of us in our own different ways. This thesis, as presented here, would not have been possible without his help.

I am grateful to Hubert Ebert and Jan Minar for the theoretical input that has motivated part of the investigations presented in this thesis, and to Paul Canfield for the high quality samples that have made challenging experiments possible. My thank you also goes to Oscar Tjenberg and Hao Tjeng for having shared ideas and experiments with me and to Anne-Marie Charvet who has helped in translating parts of this thesis into French.

I am not alone in missing Kenneth. Those who have experienced working with him know what a difference he made, and not only to our life at the synchrotron. He was interested and concerned, he would listen, always, and was adamant about me starting to write this thesis. Thank you for having shown me the way to where I am now.

My beamline colleagues and friends, who have never failed to help. For the time each one of them has spent listening to me and for the laughter we have shared, I am grateful to them. Céline, Gilles, Júlio, Peter and Stefan. Sharing an office with Céline and Júlio, from whom I have learnt a lot, has been reassuring and fun. To Júlio, who has participated in many of the experiments and has followed each step of writing this thesis, a very special thank you for his patience, precious advice and friendship.

Finally and most importantly, I thank Geo for having changed my life by teaching me what love is all about.

Contents

Chapter 1

Chapter 2

Chapter 3

Introduction générale.

Dans un processus de photoémission un photon donne son énergie, $h\nu$, à un électron qui l'utilise pour faire une transition de son état fondamental initial vers un état final excité. Exception faite de l'atome d'hydrogène et ses isotopes, les systèmes étudiés ont plusieurs électrons; l'état final possède, donc, un électron en moins ou un trou en plus et peut souvent être différent de l'état initial. La spectroscopie de photoémission est un technique expérimentale qui mesure un état final à plusieurs électrons et la théorie qui décrit le processus de photoémission est une théorie à plusieurs corps [1, 2]. Toutes les théories du phénomène ont en commun l'hypothèse de base que la réponse du système à la création d'un trou est immédiate et que l'interaction entre le photoélectron sortant et le système est négligeable. L'intensité spectrale est donnée par le carré de l'élément de matrice de particule simple multiplié par la fonction spectrale. Pour les systèmes qui ont des faibles interactions entre les électrons, la quantité obtenue expérimentalement en mesurant tous les électrons d'une énergie donné, sans se soucier de leur angle d'émission, est simplement la densité des états occupés, modulée par les éléments de matrice. Quand les interactions entre les électrons deviennent plus importantes la situation se complique: les corrélations modifient la fonction spectral et les états finals obtenus après l'émission d'un électron ne sont plus comparables avec les calculs des structures de bandes de l'état initial. La Figure 1 (page 7) montre les fonctions spectrales dans les deux cas d'un système avec et sans interactions entre les électrons [1]. La théorie de Landau [3, 4] est basée sur une correspondance linéaire entre les excitations de particule simple d'un système de référence qui n'a pas d'interactions entre les électrons et les excitations élémentaires d'un système qui en a, les quasi particules. En présence d'interactions, le delta représentant un électron qui n'a pas d'interaction avec le reste du système et qui possède une énergie et un vecteur d'onde bien précis, se déplace en énergie et s'élargit. Cette structure spectrale, souvent appelée le pic de quasi particule, est la partie cohérente du spectre de photoémission. En présence d'interactions le système qui reste après l'émission d'un électron peut se trouver dans un état final excité . Dans ce cas, la partie incohérente du spectre, qui se trouve à des énergies de liaison plus élevées, augmente d'intensité et des nouveaux satellites apparaissent.

La spectroscopie de photoémission mesure un état final à plusieurs électrons. Cependant, les calculs de structure de bandes sont des calculs à un électron et les spectres de photoémission résolus en angle peuvent être comparés aux résultats théoriques seulement si les corrélations entre les électrons sont négligeables. Un grand nombre de structures de bandes de systèmes tridimensionnels a été déterminé expérimentalement avec cette technique [5, 6], la conclusion la plus importante étant que dans le cas des métaux simples, pour lesquels les interactions entre les électrons sont faibles, il y a un bon accord entre les calculs et les résultas expérimentaux. Un tel accord signifie que pour ces systèmes un écrantage très efficace crée un état final qui est très semblable à l'état initial. Cependant, même quand l'accord avec la théorie est bon, les corrélations entre électrons ne sont pas tout à fait négligeables [7, 8, 9, 10, 11].

Le satellite observé à 6eV dans le spectre de photoémission de Nickel (Ni) a été bien étudié [12, 13, 14, 15]. En règle générale, le trou produit dans la bande de valence pendant le processus de photoémission agit comme un potentiel attractif pour les autres électrons et baisse l'énergie totale du système. Par conséquence, des états qui ne sont pas occupés dans l'état initial peuvent se déplacer en dessous du niveau de Fermi dans l'état final. Dans l'état initial de Ni les électrons $3d^9$ se trouvent superposés aux états $4s$ et dans le spectre de photoémission deux états finals sont observés. Le premier, qui possède une énergie de liaison plus basse et pour lequel l'écrantage se produit dans la bande des électrons d, a une configuration $3d^9 4s$. L'autre, le satellite, pour le quel l'écrantage est dans la bande $4s$, a une configuration $3d^8 4s^2$. Le satellite à

6eV de Ni représente, donc, un état final qui a une configuration différente de celle de l'état initial. Les effets d'état final sont particulièrement importants pour comprendre les spectres de photoémission des terres rares. Dans ce cas, on peut assumer que les électrons f sont assez localisés et se comportent essentiellement comme des électrons de coeur. Cela veut dire qu'une expérience de photoémission mesure un état final qui a effectivement un électron f en moins par rapport à l'état initial. Cependant, au début de la série de terres rares, les électrons f ont une distribution radiale qui est plus étendue que celle des terres rares lourdes. Pour le Cérium (Ce), par exemple, les électrons 4f peuvent être considérés comme assez itinérants. Comme dans le case de Ni, cela donne deux états finals. Le schéma en Figure 2 (page 9) décrit le spectre de photoémission de la bande de valence de Ni et Ce [2]. Dans le spectre de Ce le satellite qui a une énergie de liaison de 2eV représente un état final donné par un trou 4f ou l'écrantage se déroule dans la bande de conduction. Au contraire, le signal qui est plus près du niveau de Fermi représente un état final où l'écrantage est produit par les électrons 4f eux-mêmes.

Quand l'énergie des photons incidents est basse, la photoémission résolue en angle est une technique expérimentale assez utilisée pour analyser les états électroniques des solides [2, 16]. En particulier, les systèmes fortement corrélés ainsi que ceux à une ou deux dimensions ont été beaucoup étudiés en haute résolution (en énergie et en angle) [17, 18, 19]. Cependant, quand l'énergie des photons est basse, la spectroscopie de photoémission est une technique très sensible à la présence de la surface [20] qui donne, souvent, des spectres ne correspondant pas aux structures électroniques de volume [21, 22, 23]. Cela explique le désir d'utiliser la technique avec des énergies incidentes plus élevées, à fin d'obtenir des informations plus directement liées aux propriétés électroniques de volume. Néanmoins, en augmentant l'énergie incidente, des nouveaux problèmes expérimentaux apparaissent. En raison de la diminution de la section efficace de photoionisation [24], mettre en œuvre la technique de photoémission résolue en angle à haute résolution dans la gamme d'énergie des rayons-X mous est un travail assez délicat. Cela nécessite un flux de photons élevé, un faisceau monochromatisé avec une bonne résolution en énergie, un système optique stable, ainsi qu'un analyser d'électrons performant avec une bonne résolution en énergie et en angle. D'où la nécessité d'utiliser, en préférence, des synchrotrons de troisième génération et des lignes de lumière construites *ad hoc*. En plus, pour cette gamme d'énergies incidentes, les spectres résolus en angles peuvent aussi être modifiés par la participation des phonons au processus de photoémission [25, 26, 27]. La photoémission résolue en angle à haute énergie n'est pas une nouvelle technique [28, 29] mais, jusque récemment, des limites pratiques, telles qu'une résolution insuffisante, ont empêché l'observation des structures de bandes, ainsi que celle des excitations élémentaires caractéristiques des systèmes fortement corrélés. De nos jours, grâce à la disponibilité des lignes de lumière consacrées à cette technique, mesurer des spectres avec une résolution en énergie et en angle relativement élevée est devenue possible [21, 23, 30, 31, 32, 33, 34, 35].

Le but principal de cette thèse a été de déterminer le potentiel, mais aussi les limites, de la spectroscopie de photoémission résolue en angle pour des énergies incidentes appartenant à la gamme des rayons-X mous. Les conditions expérimentales nécessaires à l'implémentation de cette technique ont donc été déterminées et seront décrites dans la Conclusion.

En raison de sa structure électronique bien connue, l'Argent (Ag) a été choisi comme système type pour vérifier si, et si oui sous quelles conditions expérimentales, la détermination de la structure de bandes est possible en utilisant des rayons-X mous. Le choix d'un système si simple a aussi été motivé par une collaboration avec le group de théorie du Prof. H. Ebert et de notre intérêt commun à comparer les résultas expérimentaux avec des nouveaux calculs. Les spectres de la bande de valence de l'Ag, obtenus pour quatre directions de haute symétrie dans l'espace réciproque et différentes polarisations de la lumière incidente, sont présentés dans le Chapitre 2. En gardant à l'esprit ce qui a été brièvement mentionné au-dessus au sujet de la possibilité de comparer les spectres de photoémission des métaux simples aux calculs d'état fondamental d'un électron, la bonne concordance entre nos résultats expérimentaux et les calculs bien établis de Eckardt *et al*. [36] est ensuite discutée. Entre autre, pour bien déterminer les limites intrinsèques de cette technique quand la sonde utilisée sont des rayons X-mous, le rôle des phonons est également adressé. Pour ce faire, des mesures le long d'une direction d'haute symétrie ont été enregistrées pour différentes valeurs de l'énergie incidente et de la température. La possibilité d'obtenir la structure de bandes dans cette gamme d'énergie incidente est clairement démontrée, bien que la température de Debye-Waller [37] du système étudié joue un rôle important pour déterminer les combinaisons appropriées de température et d'énergie des photons auxquelles des expériences semblables peuvent être réalisées.

Afin d'obtenir une compréhension plus profonde de la structure électronique des systèmes fortement corrélés, une haute résolution en énergie et en angle est d'importance fondamentale. Comme sera discuté plus en détails dans le Chapitre 3, le Cérium et ses composés sont bien connus pour avoir des propriétés électroniques surfaciques essentiellement différentes des propriétés volumiques [38]. C'est pour cette raison que l'utilisation des photons d'énergie relativement élevée est d'intérêt particulier. Pour étudier la structure électronique de trois composés iso-structuraux du Ce, $CeCu_2Ge_2$, $CeNi_2Ge_2$ et $CeCo_2Ge_2$, on a utilisé différentes types de spectroscopie: la photoémission résolue en angle résonnante et non résonnante, la photoémission résonnante, la photoémission des niveaux de coeur et la spectroscopie d’absorption. Pour ces systèmes l'hybridation entre les électrons 4f du Ce et les électrons de conduction d joue un rôle important. En absence d’hybridation, la fonction spectrale des électrons 4f montrerait seulement le satellite qui est plus éloigné du niveau de Fermi. En présence d’hybridation, l'intensité spectrale près du niveau de Fermi augmente, mettant en évidence des excitations de quasi particules. Pour les systèmes Kondo l'hybridation entre les électrons 4f et les électrons de conduction provoque un état fondamental de singlet [39, 40]. La résonance de Kondo, qui a une dépendance en température caractéristique, reflète l'existence d'un tel état fondamental. Afin d’obtenir une meilleure compréhension de cette phénoménologie compliquée, des études en température ont été réalisées. Les résultats sont en accord qualitatif avec le modèle d'impureté simple d'Anderson [41]. Néanmoins, dû à la résolution en énergie et en vecteur d’onde relativement élevée avec la quelle les mesures résonnantes résolues en angle ont été réalisées, on observe des effets dépendants du vecteur d’onde près du niveau de Fermi. A notre avis, ces observations marquent les limitations du modèle. Le premier chapitre de cette thèse présente brièvement les propriétés de base du rayonnement de synchrotron et des sources de lumière de la troisième génération. La ligne de lumière des rayons-X mous, ID08, en opération à l’European Synchrotron Radiation Facility (ESRF) de Grenoble, ainsi que l'analyseur d'électrons Scienta SES 2002, central à la réalisation des expériences présentées dans cette thèse, seront également décrits.

General introduction.

The main aim of this thesis has been to investigate the potentialities, and therefore also the limits, of soft X-ray angle-resolved photoemission spectroscopy. In a photoemission process a photon imparts its energy, $h\nu$, to an electron that is lifted from its initial ground state to an excited final state. Except for the hydrogen atom and its isotopes, the investigated systems always have more than one electron and the final state must be viewed as a state where one electron has been removed or a positive charge, a hole, has been added. This can often make the final state substantially different from the initial one. Therefore, in as much as photoemission spectroscopy measures a many-electron final state, the theory describing a photoemission process is a complicated many-body theory [1, 2]. At the heart of all photoemission spectroscopy theories is the so-called sudden approximation, that assumes an instantaneous response of the system to the creation of the photohole and a negligeable interaction between the escaping photoelectron and the remaining system. Within this approach, the spectral intensity is given by the product of the squared single-particle matrix element with the spectral function. For non-interacting systems, or for systems where the many-body interactions can be neglected, the quantity that is experimentally obtained by collecting all the photoelectrons of a given energy, irrespective of their emission angles, is simply the density of occupied states obtained from band structure calculations modulated by the appropriate matrix elements. When the many-body interactions are turned on the situation is rather more complicated: the correlations modify the spectral function and the final states obtained after the removal of one electron can no longer be compared with initial state calculations. Figure 1 schematically shows the spectral functions in the two different cases [1], for non-interacting and interacting systems respectively.

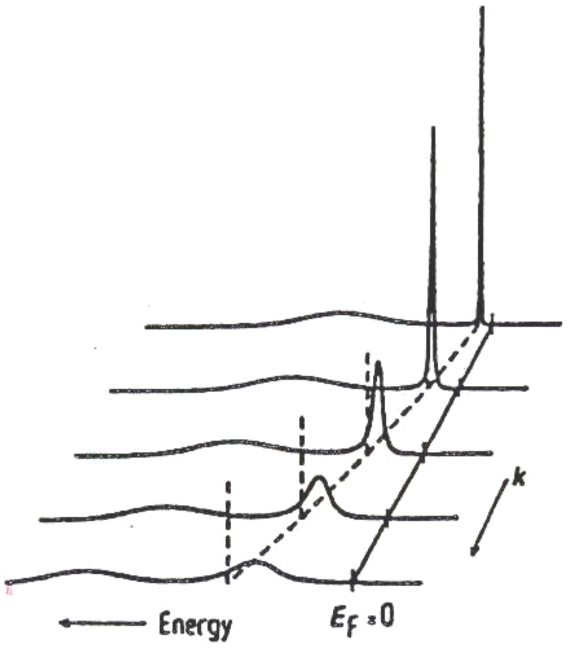

Figure 1: schematic representation of the spectral function for a non-interacting system (dotted line) and for a Fermi liquid (straight line) [1].

Landau's Fermi liquid theory [3, 4] is based on a one-to-one correpondance between the single-particle excitations of a non-interacting reference system and the elementary excitations of the correlated system, the quasi particles. In the presence of interactions, the delta peak of the non-interacting case, that represents a single electron with well defined energy and momentum, shifts in energy and broadens. This feature is normally referred to as the quasi particle peak or coherent part of the spectral function. Added to this, spectral weight is transferred to higher energy features, usually referred to as the incoherent part of the spectral function, giving rise to additional satellites in the photoemission spectrum. This incoherent contribution results from the fact that in the case of an interacting system the sudden removal of an electron can leave the remaining system in an excited final state.

Photoemission spectroscopy measures a many-electron final state. Band structure calculations are, however, one-electron calculations and only if the correlations are negligible can one compare photoemission spectra with the results of these calculations. A considerable number of three dimensional band structures have been experimentally explored with photoemission spectroscopy [5, 6]. The most important conclusion is that for free-electron-like metals, where the electron correlations are small, there is a general good agreement between the calculated band structures and the experimental energy distribution curves. Such a good agreement implies that in the case of simple metals the photoemission process involves a very effective screening which results in a final state that is quite similar to the initial ground state. Nevertheless, despite the fact that the overall picture is qualitatively similar to the calculated band structure, many-body interactions are always present, the main effect being a narrowing of the occupied bandwidth if compared to the independent particle calculations [7, 8, 9, 10, 11].

The 6 eV satellite observed in the photoemission spectrum of Ni metal [12, 13, 14, 15] is a reasonably well understood example of many-body final state effects. As a general rule, the hole produced by a photoemission process acts as an attractive potential for the other electrons lowering the energy of the system. Therefore, unoccupied states in the ground state can be pulled below the Fermi level in the final state. In the ground state of Ni, the $3d^9$ states lie within the 4s band and two final states are observed in the photoemission spectrum. The first, the main line, for which the screening takes place within the d band, has a $3d^9 4s$ configuration. The second final state, the satellite, for which the screening is produced within the 4s band, has a $3d^8 4s^2$ configuration. The well-known 6 eV satellite of Ni therefore represents a final state configuration that differs from the ground state one. Final state effects are especially important for understanding the valence band photoemission spectra of rare earth metallic systems, for which one can assume that the f electrons are rather localised and will therefore behave very much like core electrons. This implies that a photoemission experiment measures a final state that effectively differs by one f electron from the initial state. At the begining of the rare earth series, however, the f electrons have a radial distribution that is more extended than for the heavy rare earth elements and for Ce, for example, the 4f electrons can be regarded as fairly itinerant. As in the case of Ni, this gives rise to two final states. Figure 2 shows a schematic representation of the valence band photoemission spectrum of both Ni and Ce [2]. In the Ce spectrum, the satellite observed at approximately 2 eV binding energy represents a single 4f hole final state where the screening occurs in the conduction band. On the contrary, the signal closest to the Fermi level represents a final state where the screening comes from the 4f electrons themselves.

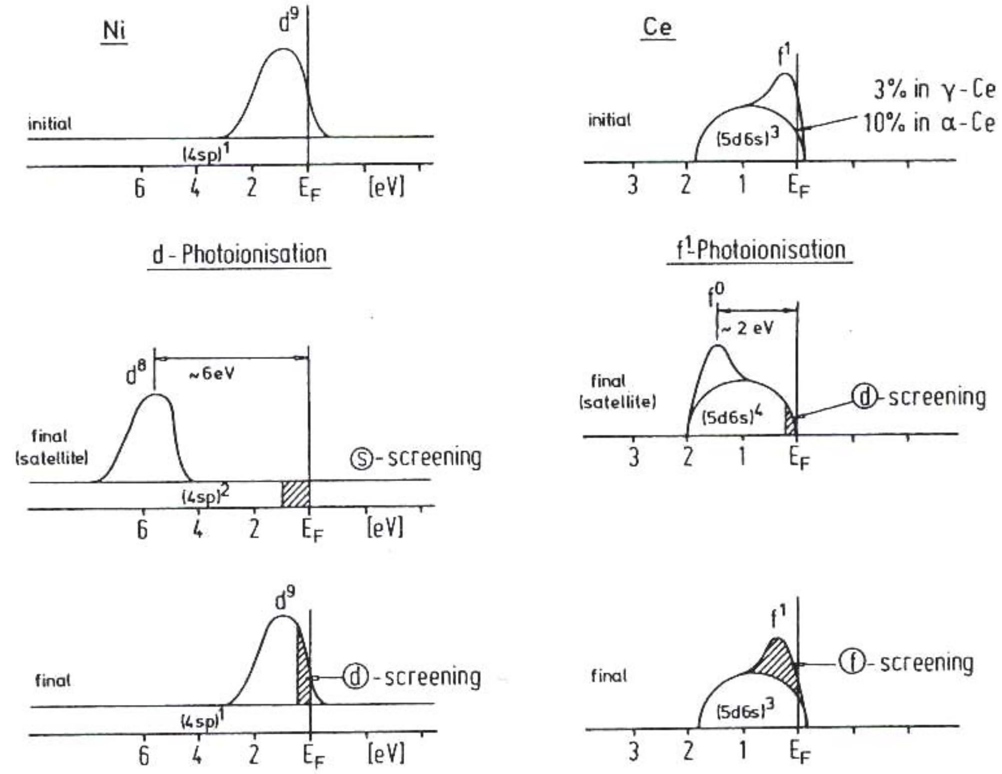

Figure 2: schematic representation of the mechanism that produces the two different final states in the valence band photoemission spectrum of Ni and Ce [2].

Ultraviolet angle-resolved photoemission spectroscopy [2, 16] is known as a useful and direct tool for probing the occupied electronic states in solids. In particular, strongly correlated systems and low dimensional ones have been extensively studied with high energy and momentum resolution experiments [17, 18, 19]. However, it is known that low energy photoemission spectroscopy is a very surface sensitive technique [20] that often provides spectral shapes that are not consistent with bulk electronic structures [21, 22, 23]. To overcome this difficulty, bulk sensitive angle-resolved photoemission spectroscopy performed in the soft X-ray energy range has been strongly demanded. Nevertheless, high energy angle-resolved photoemission spectroscopy presents several experimental difficulties. Due to the strong decrease of the photoionisation cross-section with increasing photon energy [24], high energy resolution soft X-ray angle-resolved photoemission spectroscopy is very demanding and the developement of the technique has represented a major scientific and technical challenge. High photon flux at the sample, high energy resolution of the monochromatised light, high stability of the optical system and high resolution performance of the electron analyser are essential ingredients, hence the necessity of dedicated beamlines on third generation light sources. Added to this, high angular resolution is also required since the momentum resolution not only depends on the angular resolution but also on the square root of the photoelectron kinetic energy. Finally, it is also believed that in the soft X-ray range angle-resolved measurements suffer from momentum averaging effects brought on by the participation of the phonons in the photoemission process [25, 26, 27]. High energy angle-resolved photoemission was performed for the first time many years ago [28, 29] but until recently experimental limits such as the unsatisfactory angular resolution, approximately $\pm 2^{\circ}$, and energy resolution, $\geq 300\,\mathrm{meV}$, have prevented both accurate band mapping experiments and the observation of low energy excitations in highly correlated systems. Nowadays, thanks to the availability of dedicated photoemission beamlines, measuring soft X-ray angle-resolved photoemission spectra with relatively high energy and angular resolution is possible [21, 23, 30, 31, 32, 33, 34, 35].

Silver (Ag) has been chosen as a well known system for investigating the band mapping potentialities of angle-resolved photoemission spectroscopy in the soft X-ray range. The choice of such a well characterised system is motivated by a collaboration with the group of Prof. H. Ebert and our common interest in comparing the obtained experimental results with new photoemission spectra calculations. The angle-resolved data of the valence band of Ag, obtained for four different high symmetry directions in $\underline{k}$-space and with different polarisations of the incoming light, are presented in Chapter 2. Keeping in mind what has been briefly mentioned above regarding the possibility of comparing photoemission spectra of simple metals with one-electron ground state calculations, the good agreement between our experimental results and the well established band structure calculations of Eckardt *et al.* [36], is discussed. In order to investigate the intrinsic limits of soft X-ray angle-resolved photoemission spectroscopy, the issue of phonon-assisted non-direct transitions is also addressed. To do so, measurements along one high symmetry direction have been recorded for different values of the both the incoming photon energy and the temperature. The possibility of performing accurate band mapping in the soft X-range is clearly evidenced, although the Debye-Waller temperature [37] of the investigated system plays an important role in determining the appropriate temperature and photon energy combinations at which similar experiments can be performed.

In order to obtain a deeper understanding of the electronic structure of highly correlated systems, high resolution angle-resolved spectra that exhibit clear signs of the correlation effects over all the relevant energy scales of the problem are of fundamental importance. As will be discussed in more detail in Chapter 3, Ce and its compounds are well known for having substantially different surface and bulk electronic properties [38] and the high energy application of angle-resolved photoemission spectroscopy is of particular interest in investigating the latter. Both resonant and non-resonant angle-resolved photoemission spectroscopy, resonant angle-integrated photoemission spectroscopy, core level X-ray photoemission spectroscopy and X-ray absorption spectroscopy have been used to investigated the electronic structure of three iso-structural Ce compounds, namely $CeCu_2Ge_2$, $CeNi_2Ge_2$ and $CeCo_2Ge_2$. For these systems the hybridisation between the Ce 4f electrons and the conduction d electrons plays an important role. In the abscence of hybridisation, the 4f spectral function would exhibit only the high energy satellite (see Figure 2) representing the single 4f hole final state. As the hybridisation is turned on, the spectral intensity close to the Fermi level increases, witnessing the quasi particle excitations. Within the Kondo scenario the hybridisation between the 4f and the conduction electrons gives rise to a singlet ground state [39, 40]. The Kondo resonance, that exhibits a characteristic temperature dependence, reflects the existence of such a state. In order to gain a better understanding of this complicated many-body phenomenology, temperature dependent investigations have been performed. The results are in qualitative agreement with the generally accepted single impurity Anderson model [41, 42, 43, 44, 45]. Nevertheless, owing to the relatively high energy and momentum resolution achieved for the resonant angle-resolved measurements, momentum-dependent effects are observed close to the Fermi level for both the Kondo resonance and its spin orbit partner, marking what we believe to be the limitations of the model, hence the necessity to take into account the presence of the lattice.

The necessary experimental requirements for bulk sensitive angle-resolved photoemission spectroscopy are determined as a natural consequence of the investigations presented in Chapters 2 and 3 and will be discussed in the Conclusions to this thesis. The following Chapter, Chapter 1, will briefly introduce the basic properties of synchrotron radiation and third generation light sources. The ID08 soft X-ray beamline at the European Synchrotron Radiation Facility, together with the Scienta SES 2002 electron analyser and the sample environment will also be described.

---

[1] M. Grioni, *A Photoemission Primer*, Lecture Notes in Physics **565**, Magnetism and Synchrotron Radiation, Springer (2001).

---

[2] S. Hüfner, *Photoelectron Spectroscopy*, 3rd edition, Springer (2003).

[3] L. D. Landau, Sov. Phys. JETP **3**, 920 (1957).

[4] E. K. U. Gross, E. Runge, O. Heinonen, *Many Particle Theory,* IOP Publishing (1991).

[5] T. C. Chiang, K. H. Frank, H. J. Freund, A. Goldmann, F. J. Himpsel, U. Karlsson, R. C. Leckey, W. D. Schneider, *Landolt-Börnstein*, New Series, Group III, Volume **23A**, ed. by O. Madelung, A. Goldmann, E. E. Koch, Springer (1989).

[6] A. Goldmann, Y. Ishii, R. Manzke, J. R. Naegele, M. Skibowski, *Landolt-Börnstein*, New Series, Group III, Volume **23B**, ed. by O. Madelung, A. Goldmann, E. E. Koch, Springer (1994).

[7] E. Jensen, R. A. Bartynski, T. Gustafsson, E. W. Plummer, M. Y. Chou, M. L. Cohen, G. B. Hoflund, Phys. Rev. B **30**, 5500 (1984).

[8] E. W. Plummer, Surf. Science **152/153**, 162 (1985).

[9] E. Jensen, E. W. Plummer, Phys. Rev. Lett. **55**, 1912 (1985).

[10] I. W. Lyo, E. W. Plummer, Phys. Rev. Lett. **60**, 1558 (1988).

[11] B. S. Itchkawitz, I. W. Lyo, E. W. Plummer, Phys. Rev. B **41**, 8075 (1990).

[12] S. Hüfner, G. K. Wertheim, Phys. Lett. A **51**, 299 (1975).

[13] S. Hüfner, G. K. Wertheim, Phys. Lett. A **51**, 301 (1975).

[14] C. Guillot, Y. Ballu, J. Paigne, J. Lecante, K. P. Jain, P. Thiry, R. Pinchaux, Y. Petroff, L. M. Falicov, Phys. Rev. Lett. **39**, 1632 (1977).

[15] D. K. G. de Boer, C. Haas, G. A. Sawatzky, Phys. Rev. B **29**, 4401 (1984).

[16] F. J. Himpsel, Adv. Phys. **32**, 1 (1983).

[17] A. Damascelli, Z. Hussain, Z.-X. Shen, Rev. Mod. Phys. **75**, 473 (2003).

[18] M. Grioni, I. Vobornik, F. Zwick, G. Margaritondo, J. Electron Spectrosc. Relat. Phenom. **100**, 313-329 (1999).

[19] M. Grioni, L. Perfetti, H. Berger, J. Electron Spectrosc. Relat. Phenom. **137-140**, 417-423 (2004).

[20] Y. Baer, M. G. Garnier, D. Purdie, P. Segovia, M. Hengsberger, J. Electron Spectrosc. Relat. Phenom. **114**-**116**, 257-268 (2001).

[21] S. Suga, A. Sekiyama, J. Electron Spectrosc. Relat. Phenom. **124**, 81-97 (2002).

[22] A. Sekiyama, T. Iwasaki, K. Matsuda, Y. Saitoh, Y. Onuki, S. Suga, Nature (London) **403**, 396 (2000).

[23] T. Claesson, M. Månsson, C. Dallera, F. Venturini, C. de Nadaï, N. B. Brookes, O. Tjenberg, Phys. Rev. Lett. **93** 136402 (2004).

[24] J. J. Yeh, I. Lindau, *At. Data Nucl. Data Tables* **32**, 1 (1985).

[25] N. J. Shevchik, J. Phys. C **10**, L555 (1977).

[26] N. J. Shevchik, Phys. Rev. B **16**, 3428 (1977).

[27] N. J. Shevchik, Phys. Rev. B **20**, 3020 (1979).

[28] Z. Hussain, E. Umbach, J. J. Barton, J. G. Tobin, D. A. Shirley, Phys. Rev. B **25**, 672 (1982).

[29] R. C. White, C. S. Fadley, M. Sagurton, Z. Hussain, Phys. Rev. B **34**, 5226 (1986).

[30] S. Suga, A. Shigemoto, A. Sekiyama, S. Imada, A. Yamasaki, A. Irizawa, S. Kasai, Y. Saitoh, T. Muro, N. Tomita, K. Nasu, H. Eisaki, Y. Ueda, Phys. Rev. B **70**, 155106 (2004).

[31] A. Sekiyama, S. Suga, J. Electron Spectrosc. Relat. Phenom. **137**-**140**, 681-685 (2004).

[32] A. Sekiyama, S. Kasai, M. Tsunekawa, Y. Ishida, M. Sing, A. Irizawa, A. Yamasaki, S. Imada, T. Muro, Y. Saitoh, Y. Onuki, T. Kimura, Y. Tokura, S. Suga, Phys. Rev. B **70**, 060506 (2004).

[33] Ch. Søndergaard, Ph. Hofmann, Ch. Schultz, M. S. Moreno, J. E. Gayone, M. A. Vicente Alvarez, G. Zampieri, S. Lizzit, A. Baraldi, Phys. Rev. B **63**, 233102 (2001).

[34] Ph. Hofmann, Ch. Søndergaard, S. Agergaard, S. V. Hoffmann, J. E. Gayone, G. Zampieri, S. Lizzit, A. Baraldi, Phys. Rev. B **66**, 245422 (2002).

[35] O. Tjenberg, T. Claesson, M. Månsson, C. Dallera, M. Finazzi, C. de Nadai, F. Venturini, N. B. Brookes, Phys. Rev. Lett., submitted (2005).

[36] H. Eckardt, L. Fritsche, J. Noffke, J. Phys. F: Met. Phys. **14**, 97 (1984).

[37] N. W. Aschroft, N. D. Mermin, *Solid State Physics*, Saunders College, Philadelphia (1976).

[38] L. Duò, Surf. Sci. Reports **32**, 233-289 (1998).

[39] J. W. Allen, S. J. Oh, O. Gunnarsson, K. Schönhammer, M. B. Maple, M. S. Torikachvili, I. Landau, Adv. Phys. **35**, 275 (1986).

[40] D. Malterre, M. Grioni, Y. Baer, Adv. Phys. **45**, 299 (1996).

[41] O. Gunnarsson, K. Schönhammer, Phys. Rev. Lett. **50**, 604 (1983).

[42] J. C. Fuggle, F. U. Hillebrecht, Z. Zolnierek, R. Lässer, Ch. Freiburg, O. Gunnarsson, K. Schönhammer, Phys. Rev. B **27**, 7330 (1983).

[43] O. Gunnarsson, K. Schönhammer, Phys. Rev. B **28**, 4315 (1983).

[44] O. Gunnarsson, K. Schönhammer, C. Fuggle, F. U. Hillebrecht, J. M. Esteva, R. C. Karnatak, B. Hillebrand, Phys. Rev. B **28**, 7330 (1983).

[45] J. C. Fuggle, F. U. Hillebrecht, J. M. Esteva, R. C. Karnatak, O. Gunnarsson, K. Schönhammer, Phys. Rev. B **27**, 4637 (1983).

Chapter 1

1.1 Synchrotron radiation.

A complete account of the properties of synchrotron radiation [1, 2, 3] would be beyond the aim of this thesis. Instead, we will give here a brief description of what it is and why we like using it.

Let us start with a very simple approach. Any charged particle that is accelerated or decelerated in a direction that is perpendicular to its motion emits electromagnetic radiation. If the imposed trajectory is a circular one, then the emitted radiation is called synchrotron radiation. As a general rule two different behaviours can be observed, depending on the speed of the electrons. When the electron velocity is low compared to the speed of light, the radiation is produced in a barely directional pattern and it's intensity is weak. On the contrary, as the electron velocity approaches relativistic values, the radiated intensity and the collimation of the beam increase enormously. In the relativistic case, from the experimentalist's point of view, the emitted radiation is seen as a cone whose axis is tangent to the electron's orbit. At the critical energy, the semi-angle of aperture of this cone, in the plane that is perpendicular to the orbit plane, is given by:

$$\frac{1}{\gamma} = \frac{m_0 c^2}{E} \tag{1.1}$$

The electrons stored at the European Synchrotron Radiation Facility (ESRF) circulate at an energy E = 6 GeV so that, given the electron's rest mass m_0c^2 = 0.511 MeV, the radiation is emitted in the vertical plane into a very small angle, with $1/\gamma$ = 80 μ rad. On the contrary, the horizontal emission angle is larger, implying that the majority of the radiation is collected in the plane of the orbit. Different parameters can be taken into consideration to define the quality of the beam, such as the flux and most important of all the brilliance. These quantities are defined as below:

F $(\text{photons}\cdot\text{sec}^{-1}\cdot\text{mrad}^{-1}[0.1\%\text{bandwidth}]^{-1})$ ≡ the flux is defined as the number of photons emitted per second and per unit angle in a relative bandwidth $\Delta\lambda/\lambda = 10^{-3}$.

$B = dF/d\Omega\, dS\, (\text{photons}\cdot\text{sec}^{-1}\cdot\text{mrad}^{-2}\cdot\text{mm}^{-2}[0.1\%\text{bandwidth}]^{-1})$ ≡ the brilliance is defined as the flux emitted per unit solid angle and unit area. The brilliance depends on the intensity and the collimation of the beam and on the dimensions of the source.

The brilliance of a synchrotron radiation beam is determined by the intrinsic divergence of the electron beam circulating in the storage ring. The emittance of the electron beam in the horizontal (vertical) direction is defined by $\varepsilon_x = \sigma_x \sigma_{x'}$ $(\varepsilon_y = \sigma_y \sigma_{y'})$, where σ_x and $\sigma_{x'}$ (σ_y and $\sigma_{y'}$) represent the spatial and angular extensions of the electron beam in the horizontal (vertical) direction. We can then say that the brilliance is given by:

$$B \approx \frac{\text{PhotonFlux}}{(2\pi)^2 \varepsilon_x \varepsilon_y} \tag{1.2}$$

This quantity can be taken as a measure of the possibility of concentrating all the photons emitted by the source into a very small spot. The energy that is lost by the radiating electrons is restored by the radio frequency cavities and synchrotron radiation can be produced for hours, even days. Synchrotron radiation is “organized”, meaning that the beam is highly polarised (most of the waves are oscillating in the same plane) and collimated (most of the waves are in the same direction). On the contrary, X-ray tubes produce radiation that is completely unpolarised and may be focused only with great difficulty. Last but not least, synchrotron radiation can be “shared”. A large synchrotron can have many beamlines and run hundreds of experiments in one year. Synchrotron facilities are expensive to build, but pay for themselves in sheer volume of research. Finally, synchrotron radiation has a number of unique properties if compared to the more conventional radiation sources such as vacuum ultraviolet lamps and X-ray tubes:

- wide and continuous energy spectrum, from the infrared to the X-ray region.
- high brilliance: synchrotron radiation is extremely intense and highly collimated.
- high linear or circular polarisation.
- small source size due to the small cross-section of the electron beam.
- pulsed time structure, with pulse lengths down to some 10’s of pico-seconds.
- an ultra high vacuum environment.

1.2 The European Synchrotron Radiation Facility (ESRF).

Although natural synchrotron radiation from charged particles spiraling around magnetic-field lines in space is as old as the stars, short wavelength synchrotron radiation generated by relativistic electrons in circular accelerators is only half a century old. The first observation, literally since it was visible light that was seen, came at the General Electric Research Laboratory in Schenectady, New York, on the 24th of April 1947. In the 60 years since, synchrotron radiation has become a research tool for the study of matter in all its varied manifestations, as facilities around the world constantly evolved to provide this light in ever more useful forms. High energy electron accelerators emerged as viable synchrotron radiation sources because, as electrons approach the speed of light, the synchrotron radiation is increasingly emitted in a narrow, forward-directed cone. Thus, the radiation is concentrated in a small solid angle and can be readily used by researchers. Early synchrotron light sources used photons that were created as the undesirable by-product of electron accelerators operated for high energy physics research. This parasitic use of synchrotron radiation showed such high promises that in the 1980's many dedicated synchrotron radiation sources were built and are generally referred to as second generation light sources. The ESRF (European Synchrotron Radiation Facility) [4], like Spring8 (Super Photon ring-8GeV) in Japan and APS (Advanced Photon Source) in the United States, and many other synchrotrons both operating and currently under construction, is one of the commonly called third generation sources. Thanks to the rapid developement of synchrotron radiation facilities, the brilliance of these X-ray sources is constantly increasing as shown in Figure 1.1.

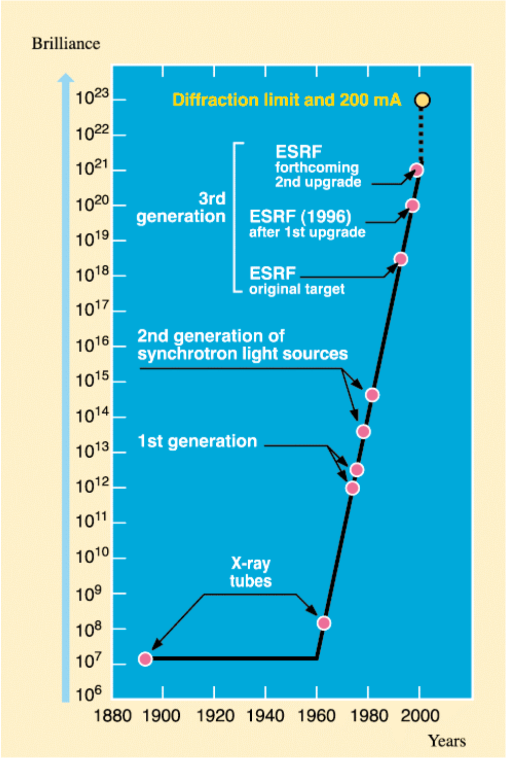

Figure 1.1: the graph shows the rapid increase in the brilliance of X-ray beams available for research [4].

Although different possibilities exist, we can generally say that a synchrotron radiation source is composed by a linear accelerator used as a pre-injector, a cyclic accelerator (booster) used as an injector, and a storage ring where the circulating particles are kept at the operating energy. This is also the configuration adopted at the ESRF. A LINear ACcelerator, or LINAC, is a particle accelerator that accelerates charged particles - electrons, protons or heavy ions – in a straight line. Alternating drift tubes and electromagnetic fields that change polarity compose the device. The drift tubes are necessary because without them the field would alternately accelerate and decelerate the particles. In practice, the drift tubes shield the electrons for the length of time during which the field is decelerating and their lengths are chosen so that when the electrons reach the end of a tube they get accelerated in the following one. A schematic drawing is shown in Figure 1.2. The ESRF LINAC is a 200 MeV accelerator that consists of a 100 KeV triode gun where the electron acceleration essentially starts, a buncher section where the electrons are packed into bunches, and finally two 6 meters long accelerating sections. The LINAC operates in two distinct modes. The first mode corresponds to the multibunch operation of the storage ring and in this mode a 1μs electron bunch is delivered to the booster, filling the whole booster circumference. In the second mode of operation a 2 ns beam pulse of the LINAC allows for the single bunch operation of the storage ring.

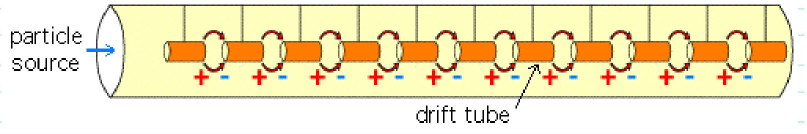

Figure 1.2: schematic drawing of a LINAC

The electrons extracted from the LINAC must be accelerated to even higher energies. The booster is a circular accelerator in which the electron beam circulates several times before being injected into the storage ring. Each time the electrons re-cycle through the same accelerating elements, the magnetic field is increased and this until the operating energy of 6 GeV is reached. The circumference of the booster measures 300 meters and the accelerator is provided with two radio frequency cavities in which electromagnetic fields oscillate in order to assure the required acceleration of the beam. A magnet lattice structure allows focalising the electron beam and consequently achieving a final emittance of $1.2 \cdot 10^{-7}$ mrad. A schematic drawing of a synchrotron radiation source is shown in Figure 1.3.

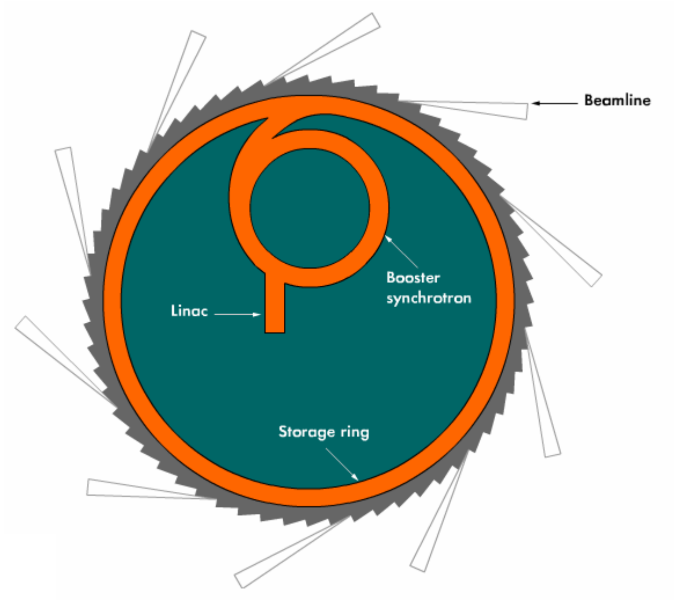

Figure 1.3: a synchrotron radiation source.

As shown below in Figure 1.4, a storage ring is essentially a succession of arcs (bending magnets, see Figure 1.5) and straight sections (insertion devices) that allow the current of electrons to circulate along a closed trajectory for a certain amount of time. The beam is stored in a vacuum chamber and the energy lost by the radiating electrons is restored by radio frequency cavities that are positioned around the ring.

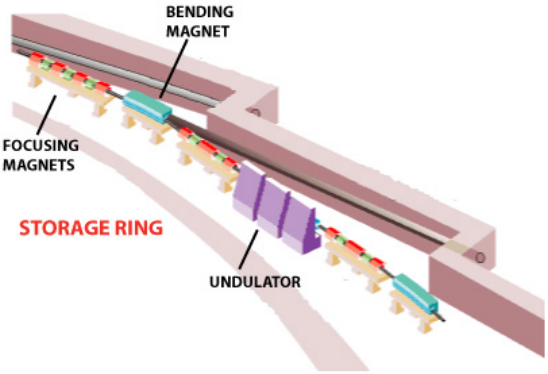

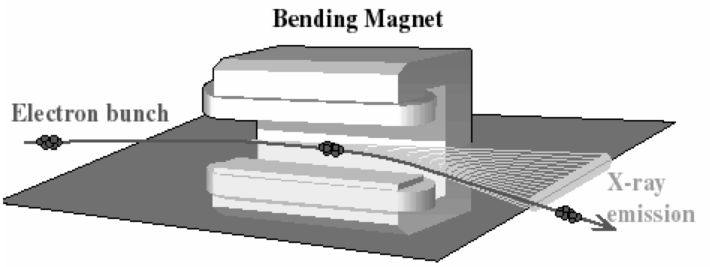

Figure 1.4: schematic view of a storage ring.

Figure 1.5: bending magnet.

The bending magnets, that give rise to a uniform dipolar magnetic field in the direction perpendicular to the motion of the electrons, form the curved sections of the storage ring. The effect of the applied magnetic field results in a centripetal acceleration of the particles, a curvature of their trajectory, hence the production of synchrotron radiation. From a spectral point of view the radiation emitted by an electron beam passing through a bending magnet is composed by a large number of harmonics of a fundamental frequency, which is the revolution frequency of the electrons in the storage ring. However, the distance between these harmonics is extremely small and the line width is finite so that the spectrum does not display this harmonic structure. On the contrary, the spectrum will show a smooth continuum, extended over a broad range of frequencies and characterized by a critical energy, ε_c. The critical energy ε_c divides the spectrum into two parts with equal power (half the power radiated above the critical wavelength and half below) and is given by:

$$\varepsilon_c(\mathrm{keV}) = 0.665 \cdot \mathrm{E}^2\left[\mathrm{GeV}^2\right] \cdot \mathrm{B}_0\left[\mathrm{T}\right] \tag{1.3}$$

where B_0 is the applied magnetic field inside the bending magnet and E is the particle energy. At the ESRF $\mathrm{B}_0 = 0.85\ \mathrm{T}$, $\varepsilon_c = 20\ \mathrm{KeV}$, and the brilliance of a bending magnet is of the order of $10^{14}\,\mathrm{ph}\cdot\mathrm{s}^{-1}\cdot\mathrm{mm}^{-2}\cdot\mathrm{mrad}^{-2}\cdot[0.1\%\mathrm{BW}]^{-1}$ at 10 KeV. A large number of quadrupole magnets provide the essential focusing that limits the dimensions of the beam in both the horizontal and the vertical planes. The magnetic quadrupole field cannot focus in both directions at the same time so a succession of focusing quadrupoles, appropriately designed, is used. A number of other multipole magnets provide higher order corrections, generating a periodic arrangement that is commonly referred to as a lattice. Around the 844.4 meters of the ESRF storage ring 64 bending magnets and 320 quadrupoles are installed and the photon beam is extracted tangentially from the ring throughout the beamlines.

While in second generation synchrotron light sources the radiation delivered to the beamlines is produced by the bending magnets, other magnetic devices are responsible for the birth of third generation facilities. These are called insertion devices and they form the straight sections of the storage ring, their purpose being to increase the flux or the brilliance of the emitted radiation. Such devices consist of a periodic array of magnets with alternating polarity of the magnetic field that is directed perpendicular to the electron beam path. This forces the electrons into a sinusoidal movement, giving rise to an emission of synchrotron radiation at each oscillation. The high flux and brilliance are obtained as an interference effect of the radiation due to the periodic motion of the electrons within the insertion devices themselves. The effect of the insertion devices is localized, i.e. they only affect the X-ray beam that leaves the storage ring throughout the port that is tangential to their position and consequently every beamline owns the insertion device that better satisfies its experimental needs. So whilst the bending magnets are needed to store the beam, and in addition the radiation they produce is used, the insertion devices can be designed to obtain light that is optimised for specific experiments. Insertion devices are of two different types, namely wigglers and undulators as shown in Figure 1.6.

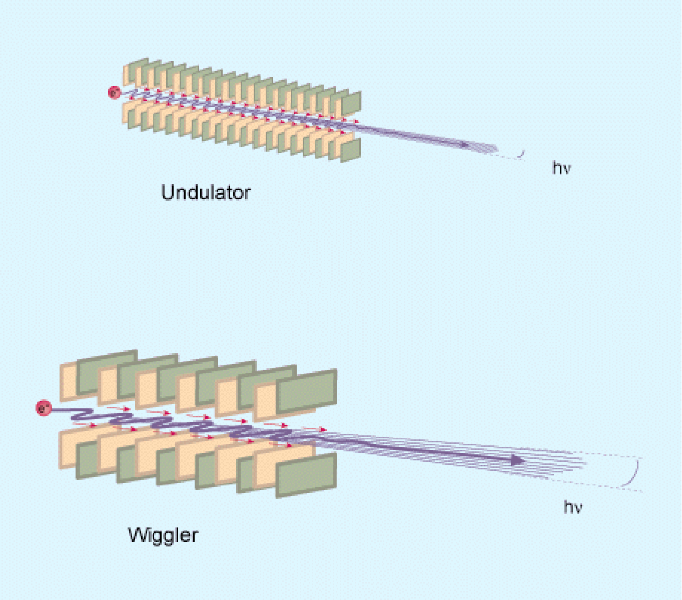

Figure 1.6: undulators and wigglers.

By defining the deflection parameter $K = \delta \cdot \gamma \approx 0.93 \cdot \lambda_0(\mathrm{cm}) \cdot B_0(\mathrm{T})$, where δ is the deflection angle of the electron with respect to its original trajectory, λ_0 is the period of the magnetic array and B_0 is the peak magnetic field, we can separate the two different cases, depending on the amplitude of the oscillations with respect to the axis of the straight section. In an N-pole wiggler each of the magnetic poles of the array bends the electron beam through a deflection angle δ that is large if compared to the natural opening angle $1/\gamma$. The advantage of using many magnet poles is to increase the photon flux, which results enhanced by a factor 2N. The radiation emitted from the various magnets interferes incoherently, giving rise to a spectrum that is for all practical purposes that of many bending magnets placed in series one after the other: the harmonic peaks are so closely spaced that they blur together. Because of the high value of δ, the brilliance cannot be greatly improved. Sometimes a wiggler with just a few poles is used, producing a magnetic field that is higher than the ring bending magnet field and whose aim is to shift the critical energy, ε_c, towards higher values.

An N-pole undulator causes the electrons to be only weakly deflected from their original trajectory (small δ) so that the angular divergence is essentially not increased. In this case, the radiation emitted at the various magnetic poles interferes coherently, resulting in a discrete spectrum with light emitted at a fundamental wavelength, λ, and at its higher harmonics λ_n:

$$\lambda = \frac{\lambda_0}{2\gamma^2}\left(1 + \frac{K^2}{2} + \gamma^2\theta^2\right) \qquad \text{and} \qquad \lambda_n = \frac{\lambda}{n} \tag{1.4}$$

where θ is the observation angle with respect to the undulator's axis and n is the harmonic order. The relative bandwidth for the n-th harmonic is determined by the number of undulator periods, N, and is given by:

$$\frac{\Delta\lambda_n}{\lambda_n} = \frac{1}{nN} \tag{1.5}$$

If the gap between the magnetic poles of the undulator is increased, the peak magnetic field B_0 decreases, hence the deflection parameter K also decreases. Therefore, the fundamental wavelength λ is shifted to shorter wavelengths. This is the basis of the tuning of an undulator and it depends on the undulator's geometry and on the flexibility in varying the gap. Due to the constructive interference of the emitted radiation, the beam is more collimated and the intensity per solid angle is increased if compared to the radiation produced by a wiggler. Hence the brilliance of the radiation is highly improved and at the ESRF it is of the order of $10^{20}\,\mathrm{ph}\cdot\mathrm{s}^{-1}\cdot\mathrm{mm}^{-2}\cdot\mathrm{mrad}^{-2}\cdot[0.1\%\mathrm{BW}]^{-1}$ at 10 KeV. The spectral distribution of the radiation emitted by undulators, wigglers and bending magnets is compared is compared in Figure 1.7.

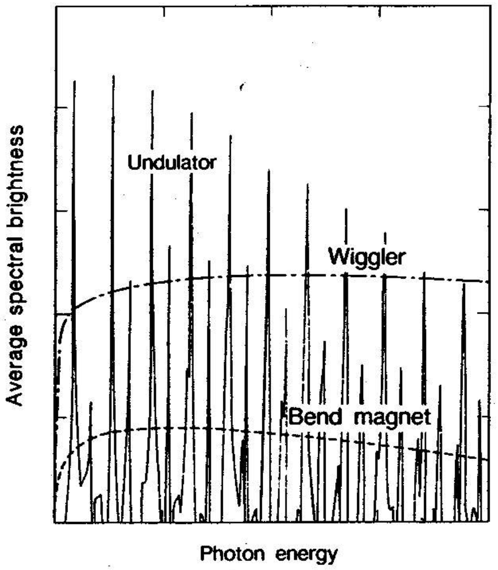

Figure 1.7: qualitative representation of typical radiation spectra from a bending magnet, a wiggler and an undulator.

The third generation synchrotron light sources can produce light with high spectral flux and brilliance in a wide range of energies. Typically, the low energies are covered by radiation coming from bending magnets and undulators, whereas the high energy range is covered by radiation coming from wigglers.

An electromagnetic wave is polarised when the direction of vibration of the electric field has a preferred orientation. For linear polarisation this direction is fixed, for circular or elliptic polarisation the direction rotates. The light produced by a bending magnet is always linearly polarised in the plane of the orbit and elliptically polarised if it is collected away from this plane. The "handedness" of the polarisation has opposite signs depending on wether one is above or below the plane. In the case of insertion devices the polarisation can be linear, elliptical or circular, depending on the magnetic geometry that is used. The radiation produced by symmetric wigglers and planar undulators is always linearly polarised. In particular, because of the combination of left-handed circular polarisation produced from one magnetic pole and right-handed circular polarisation produced by the following one, the out of plane elliptical polarisation expected from a bending magnet is absent. Thus, the off plane polarisation remains linear. The first experiments with circularly polarised light used bending magnet radiation collected off axis, with the disadvantage of a drastically reduced flux. Much effort was then devoted to the development of specific sources in order to provide intense circularly polarised photon beams. In planar undulators the magnetic field is set vertically, perpendicular to the plane of the orbit. If the magnetic array also includes horizontal magnetic fields, as in the case of a helical undulator, then the device produces elliptically polarised light that is perfectly circularly polarised if the horizontal and vertical fields have the same amplitude. In 1990 P. Elleaume proposed the construction of a linear/helical undulator by combining one magnet array that produces a vertical field, as in a normal undulator, with a second array that is especially designed to produce a horizontal field, hence introducing a vertical polarization component in the light. The polarization is controlled by longitudinally displacing one magnet array with respect to the other one (phasing). A variation of the phase results in a change of the polarisation of the light, from left-handed circular to linear to right handed circular. This concept resulted in the construction of Helios [5] that allows a full control of the polarisation with a switching time from one helicity to another of approximately 5 seconds. In 1993 Sasaki proposed a more advanced design [6], which generates a higher magnetic field. The price to pay is a variation of the energy of the fundamental harmonic with the polarisation and a significant mechanical complexity. Helical undulators based on the APPLE II (Advanced Planar Polarised Light Emitter) structure have been installed in a number of synchrotron radiation facilities around the world and three APPLE II undulators have been constructed and installed at the ESRF. Two identical devices are installed in the ID08 straight section covering the soft X-ray photon energy range (0.4 to 1.5 KeV), whereas the third device is installed in the ID12 straight section (5 to 9.1 KeV). Finally, without going into the details that can be found in [7, 8, 9, 10], it is important to know that elliptical multipole wigglers and asymmetric wigglers can replace the helical undulators in providing circularly polarised light in the high energy range. Further information regarding the insertion devices that are operational at the ESRF can be found in [11].

Because the stored beam is made of bunches, the emitted light has the periodicity of the bunches. However, since the time between bunches is very short most detectors see the light as a time continuum. On the other hand, for some applications the time structure of the light may be used for the study of fast phenomena. Added to this, the storage ring can be partially filled with electron bunches, giving an additional flexibility to such a time structure. This is the case at the ESRF where the number of bunches varies from 1 to 992, depending on the operation mode of the ring, and the time between the electron bunches varies from 2816 ns to 2.82 ns. On the contrary, the revolution frequency is fixed and equal to 355 kHz. Six filling modes are available at the ESRF: the four illustrated below plus the uniform mode, most commonly used for the investigations described in this thesis, that operates with 992 bunches that are equally distributed around the ring and the recent four bunch mode.

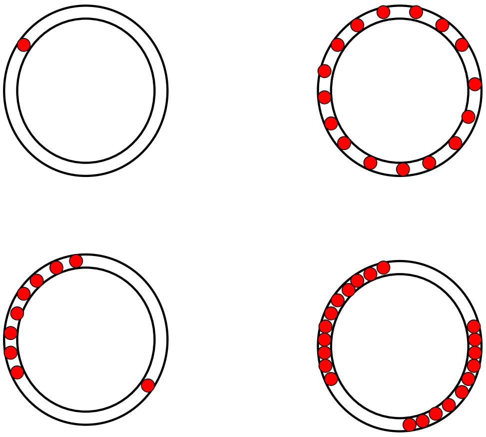

Figure 1.8: four of the six different operating modes used at the ESRF. Clockwise: single bunch, 16 bunch, hybrid mode, 2/3 fill mode.

1.3 The ID08 beamline.

The APPLE II helical undulator [6, 12, 13, 14] is a pure permanent magnetic structure composed of four arrays as shown in Figure 1.9. As a conventional undulator it has an upper jaw and a lower one, but unlike conventional undulators, each jaw is split into two halves creating a magnetic pattern with four quadrants. The arrangement of the magnetic array is such that for each quadrant there are four blocks per period. By moving two diagonal magnet arrays longitudinally with respect to the other two (a phase shift), the strengths of the vertical and horizontal magnetic fields can be varied and hence the polarisation of the radiation is controlled. The advantage of such a device is that the radiation can be polarised vertically, horizontally and circularly right and left by simply moving the magnetic arrays with respect to each other. Therefore, changing the vertical gap between the jaws controls the intensity of the magnetic field on the beam axis, i.e. the photon energy, whereas shifting the magnetic arrays varies the direction of the magnetic field, i.e. the polarisation of the photon beam.

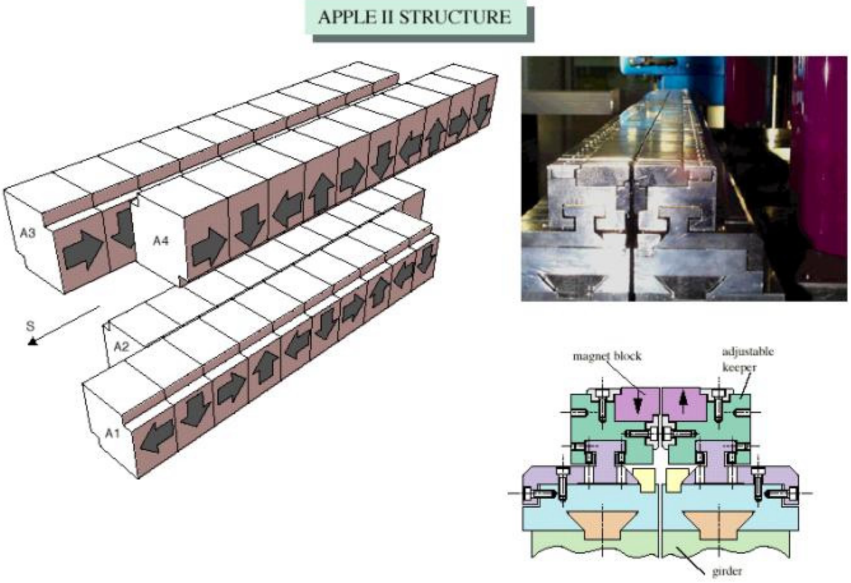

Figure 1.9: APPLE II undulator structure.

Two operation modes are foreseen. A first mode, where the two magnetic arrays (A_2 and A_4) are moved together and in the same direction with respect to the static arrays (A_1 and A_3), and a second mode where the two arrays are moved the same distance but in opposite directions to each other. In the first case, as the phase is shifted from zero to half a period the produced radiation goes from pure horizontal, through elliptical, to pure vertical. In the second case the radiation is always linear, going from horizontal to vertical over half a period phase shift. In particular, if φ is the phase shift, we can distinguish the three different regimes given below:

- $\varphi = 0$: the magnetic structure is equivalent to a standard linear undulator, with only $B_z \neq 0$ and the radiation is linearly polarised in the horizontal plane.
- $\varphi = \frac{\pi}{2}$: $B_z \neq 0$ and $B_x \neq 0$, the radiation is elliptically polarised. If then $B_z = B_x$ the radiation is circularly polarized.
- $\varphi = \pi$: only $B_x \neq 0$, the radiation is linearly polarised in the vertical plane.

The degree of polarisation given by the ID08 APPLE II undulator is equal to ≅ 100%, for all four polarisations and at all the used energies. In order to produce a very intense photon beam in the 400 eV to 1500 eV spectral range (soft X-ray range), the beamline is equipped with two APPLE II undulators installed in series. An electromagnetic phasing unit controls their synchronisation. Each undulator is 1.6 m long, with 18 periods of 88 mm each. The peak magnetic fields are $B_x = 0.55\,T$ and $B_z = 0.6\,T$ in the respective directions. After having passed through a $\approx 2.1 \cdot 2.5\,mm^2$ pinhole that can be adjusted by translating slits (primary slits), the beam is redirected and focused by a deflecting mirror, a horizontal focusing mirror (HFM) and a vertical focusing mirror (VFM), as shown in Figure 1.10.

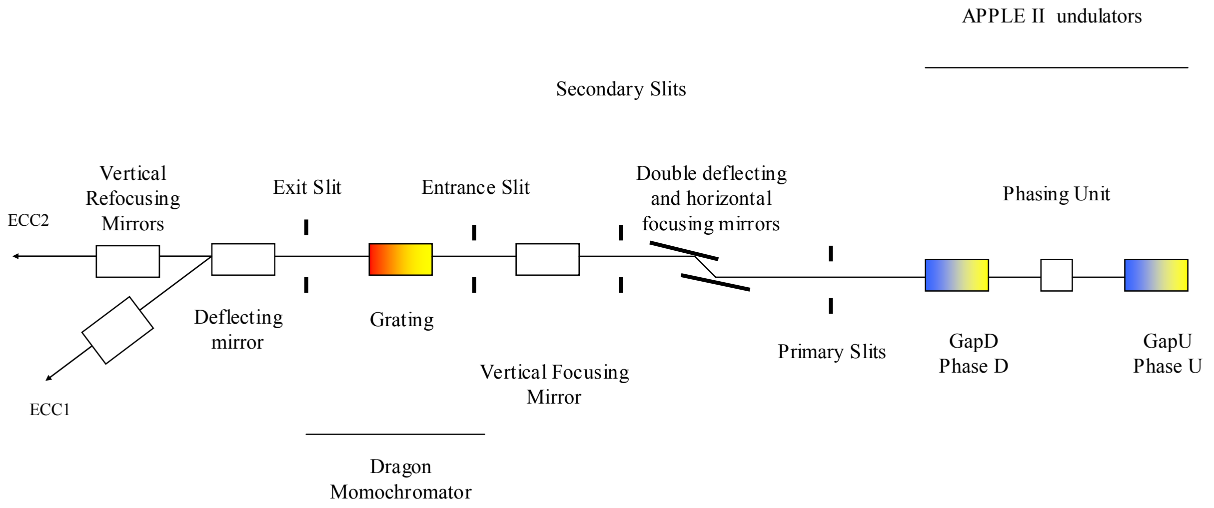

Figure 1.10: schematic top view of the ID08 beamline.

Because of their opposite angles of deflection, the first two mirrors don't vary the final direction of the beam but are mainly used to absorb all the high energy X-rays, most of the heat load and to horizontally focus the photon beam along the beamline. The offset of the beam caused by the double mirrors is approximately 20mm and helps to separate the Bremstralung radiation from the X-rays. Figure 1.11 shows the power spectrum of an APPLE II device as a function of the polarisation of the light and it can be easily seen that the minimum on axis heat load is obtained with circular polarisation.

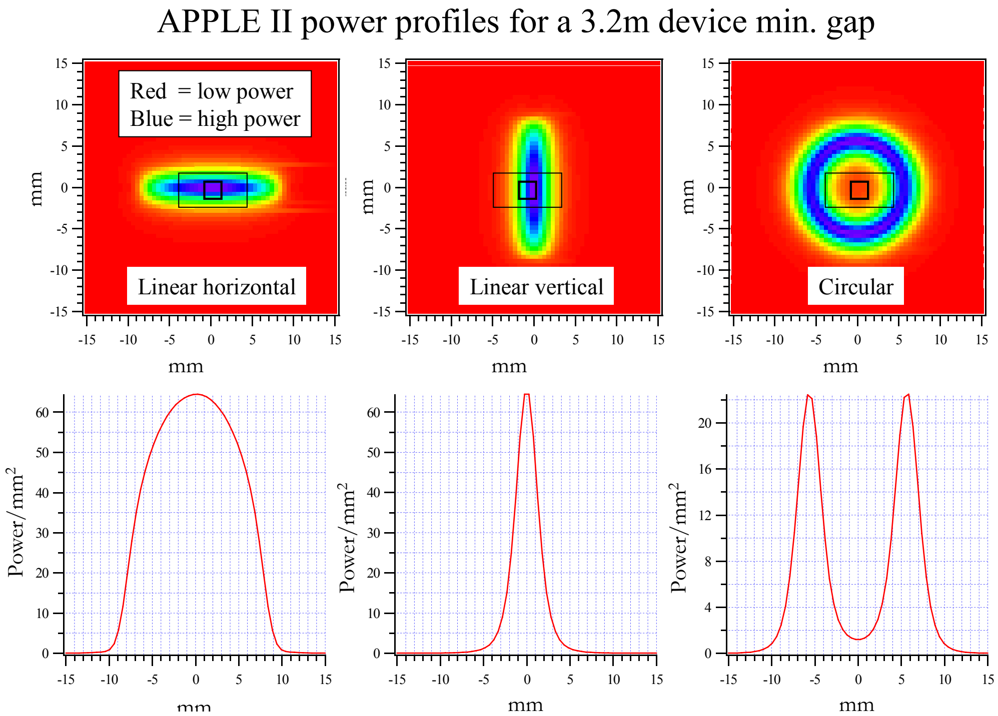

Figure 1.11: power spectrum of a 3.2 m long APPLE II device at minimum gap.

All the mirrors installed on the beamline are made of 50mm thick chemical vapor deposited (CVD) SiC substrates, an ideal material for applications where high thermal conductivity, low coefficient of thermal expansion and resistance to wear and abrasion are of primary value. The reflection efficiency of a mirror coating is a function of the coating material, its roughness, its thickness, the angle of incidence and the wavelength of the photons to be reflected. The coatings of the mirrors installed along the beamline can be varied (Au, Pt, SiC) and by doing so one varies the reflectivity according to the desired energy range. For almost all kinds of experiments using X-rays the light produced by the source has to be monochromatised. After adjusting the intensity of the undulator's magnetic field in order to obtain the right energy for the fundamental harmonic, the bandwidth has to be further reduced by a monochromator. The design and construction of a soft X-ray beamline is not a simple task. Crystal monochromators are inapplicable due to the strong soft X-ray absorption coefficient and inappropriate lattice spacings of the existing crystals. Grating monochromators are applicable [15]. However, they must work at very grazing angles (2° -4°) in order to have good reflectivity. At such small angles the aberrations and surface imperfections of the optical elements can cause appreciable image distortion and scattered light, therefore severely limiting the monochromator's energy resolution and transmission. To meet this challenge a cylindrical element monochromator (CEM) design was proposed by C. T. Chen at the end of the 1980's [16]. The ID08 beamline at the ESRF, also called the "Dragon" beamline, takes advantage of the spherical version (SEM) of the CEM design [17]. The concept of the Dragon monochromator is outstanding in its simplicity and a schematic layout is shown in Figure 1.12.

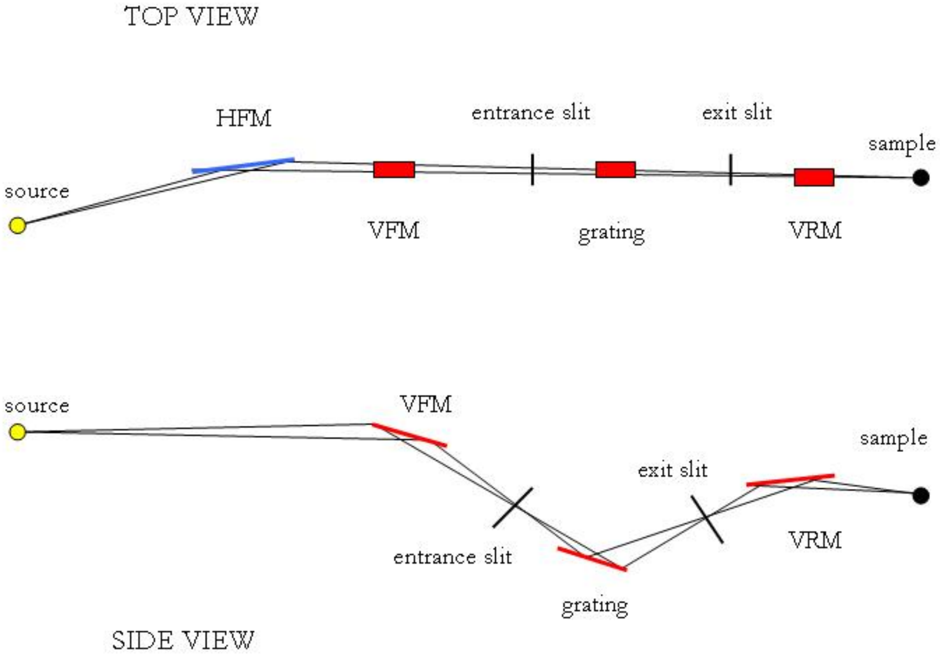

Figure 1.12: layout of a Dragon monochromator.

There are two mirrors close to each other at the left of the figure; the one closer to the source is the horizontal focusing mirror (HFM) whereas the other one is the vertical focusing mirror (VFM). The top view shows the HFM focusing the source inside the storage ring onto a chosen position, that is typically the sample position (as in the case of Figure 1.12), the entrance slit or the exit slit. The side view shows the VFM focusing the source onto the entrance slit. The VFM at the ID08 beamline has a $R = 450\ \mathrm{m}$ radius and gives a vertical beam size at the entrance slit of $\approx 20\,\mu\mathrm{m}$ (FWHM). The optical functions of the HFM and VFM mirrors are decoupled and one can envisage the possibility of adjusting these two elements separately, in order to compensate drifts in the position of the source inside the storage ring. After the entrance slit the grating diffracts and focuses the photon beam vertically into the exit slit. The ID08 beamline is equipped with three CVD SiC gratings with 1200, 1600 and 2100 lines/mm. The gratings are easily exchangeable by an in-vacuum translation. The exit slit is movable in order to optimise the performance at different wavelengths and this feature turns out to be essential in obtaining a high resolving power. The movable exit slit also allows eliminating the defocus aberration given by the spherical shape of the grating and thus exceeds the resolution limit of fixed slit monochromators. The resolving power of the monochromator installed at ID08, $E/\Delta E \approx 10^4$ at 400 eV, is obtained with comfortable slit openings. Because there is only one element, the grating, between the entrance slit and the exit slit the resolution limit is totally determined by the optical performance between these two slits. The rest of the monochromator transfers the radiation and focuses the source into the entrance slit and onto the sample and so determines the overall transmission. Photoemission processes have a cross-section that decreases as the energy of the incident photons increases [18]. This makes it necessary to have a high flux at the sample, i.e. a high transmission from the monochromator. The Dragon type monochromator uses only three optical elements and therefore has a high transmission rate that is determined by how well the VFM vertically focuses the photon beam into the entrance slit. A second deflecting mirror, positioned after the monochromator's exit slit, can change the beam trajectory by 4 degrees, in the direction of the first experimental control cabin (ECC1 in Figure 1.10). This mirror can also be translated aside in order to leave the beam trajectory unchanged and let it reach the second experimental control cabin (ECC2 in Figure 1.10). In both cases a spherical mirror, the so-called vertical refocusing mirror, refocuses the photon beam before entering the experimental hutches. Finally, the focused beam results in a spot with a vertical size of $40\,\mu\text{m}$ (FWHM) and a horizontal size in between $800\,\mu\text{m}$ and $1000\,\mu\text{m}$.

1.4 The Scienta SES 2002 electron analyser.

Over the past decade a great deal of effort has been invested in improving angle-resolved photoemission spectroscopy (ARPES). This has resulted in an order-of-magnitude improvement in both energy and momentum resolution, thus entering a new era in electron spectroscopy and allowing a detailed comparison between theory and experiment. The reasons for this progress are two fold: the availability of dedicated photoemission beamlines and the development of high resolution electron spectrometers. Synchrotron radiation offers important advantages if compared to gas-discharge lamps that can also be used as radiation sources in photoemission experiments, as previously discussed.

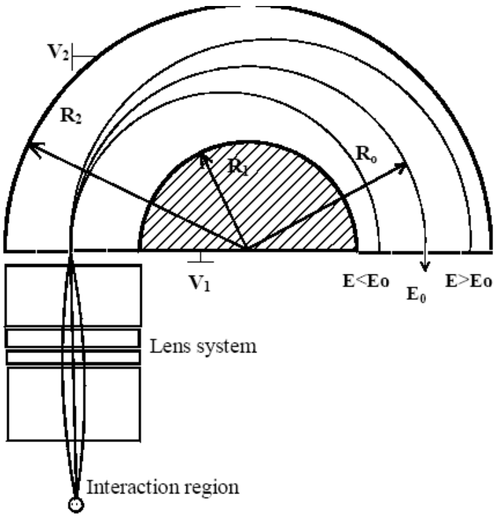

Figure 1.13: generic hemispherical analyser.

As shown in Figure 1.13, a conventional hemispherical analyser consists of a multi element electrostatic lens system and a hemispherical deflector with entrance and exit slits. The heart of the analyser is the deflector that consists of two concentric hemispheres of radius R_1 and R_2. These are kept at a potential difference, ΔV, so that only those electrons reaching the entrance slit with a kinetic energy that is found within a narrow range centred at the value $E_{pass} = e \cdot \Delta V / (R_1/R_2 - R_2/R_1)$ will pass through this hemispherical capacitor, thus reaching the exit slit and then the detector. In this way it is possible to measure the kinetic energy of the photoelectrons with an energy resolution given by $\Delta E = E_{pass}\left(w/R_0 + \alpha^2/4\right)$ where $R_0 = (R_1 + R_2)/2$ is the mean radius of the hemispheres, w is the width of the entrance slit and

α is the angular half aperture of the electron beam at the entrance slit. The potentials applied to the inner and outer hemispheres are defined by the pass energy and by the dimensions of the analyser:

$$V_1(R_1) = V_{pass}\ [2R_0/R_1 - 1]$$

$$V_2(R_2) = V_{pass}\ [2R_0/R_2 - 1]$$

where V_{pass} is the pass energy potential. All of these potentials are referred to a local ground. The role of the electrostatic lenses is to decelerate and focus the photoelectrons onto the entrance slit and by scanning the retarding potential one can effectively record the photoemission intensity versus the photoelectron kinetic energy.

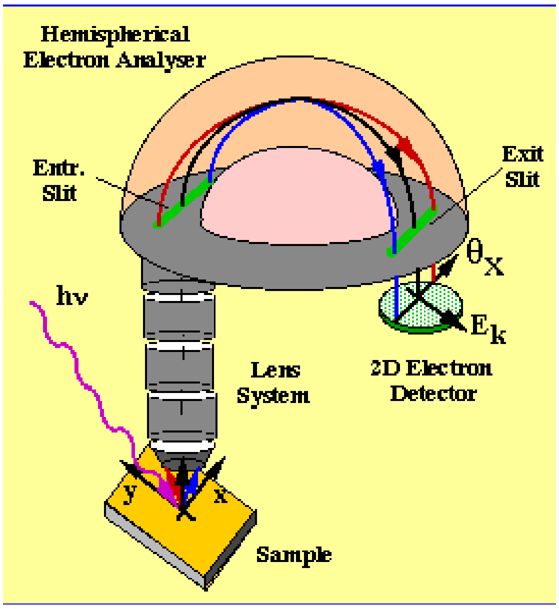

Figure 1.14: schematic drawing of a hemispherical electron analyser indicating the detected energy and angular directions.

The ID08 beamline is equipped with a Scienta SES 2002 electron analyser [19]. One of the innovative characteristics of the Scienta analyser is the two-dimensional position-sensitive detector consisting of two micro-channel plates and a phosphor plate in series, followed by a charge-coupled device (CCD) camera. In this case no exit slit is required: the electrons, which are spread along the energy dispersing axis of the detector (E_K) as a function of their kinetic energy, due to the travel through the hemispherical capacitor, are detected simultaneously. In other words, a range of electron energies is dispersed over one dimension of the detector and can be measured in parallel; scanning the lens voltage is in principle no longer necessary, at least not for a narrow energy window (a few percent of E_{pass}). Furthermore, in contrast to a conventional electron analyser in which the momentum information is averaged over all the photoelectrons within the acceptance angle, the Scienta system can operate in an angle-resolved mode which provides energy and momentum information along an extended cut in $\underline{k}$ -space. In particular, the photoelectrons within an angular window of approximately 14° along the direction defined by the analyser's entrance slit are focused onto different positions on the detector. Figure 1.14 illustrates the mapping of angles along the theta-line, θ_x, which is perpendicular to the energy dispersion direction E_k. The Scienta SES 2002 is a hemispherical analyser especially designed for high resolution spectroscopy. The electron lens system collects the electrons from the sample and transfers them to the entrance of the energy analyser. The lens has mainly two purposes. Firstly it matches the initial kinetic energy of the electrons to the pass energy of the analyser. A second purpose is to act as a focusing lens, producing a photoelectron image of the sample on the entrance plane of the analyser. The computer controls all lens voltages. The lens electrodes, like all other surfaces seen by the electrons, are coated with graphite in order to provide surfaces with an even potential distribution. The first element of the lens is at the sample (ground) potential and the last element is connected to the retardation/accelerating voltage. The functions of the initial kinetic energy and the pass energy that determine the three focusing voltages are defined by a set of tables in the computer software. Inside the third element of the lens a set of deflector plates has the purpose to correct eventual misalignments. A sketch of the lens system is shown below.

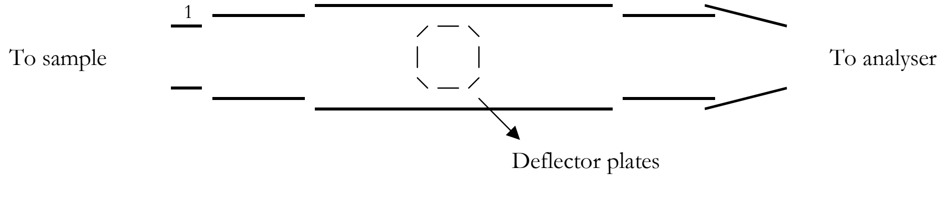

Figure 1.15: a schematic drawing of the Scienta SES 2002 electrostatic lens.

The hemispherical electron analyser is the part of the instrument that performs the actual energy dispersion. The Scienta SES 2002 electron analyser has a main radius $R_0 = 200$ mm and the separation between the hemispheres is 80 mm. With the standard 40mm diameter detector the energy range that can be simultaneously recorded is about $E_{pass}/10$. Again, the computer controls all the potentials and all the surfaces are graphite coated. The energy resolution of the spectrometer has been verified by measuring the $Xe\, 5p_{5/3}$ spectral line positioned at 12.13eV binding energy, using He Iα incident radiation and a 0.2mm curved entrance slit. The intrinsic analyser resolution is determined by correcting the measured line width for the VUV source contribution of 1.2meV and the Doppler broadening contribution of 3.25meV FWHM at T=293K. The results obtained for different values of E_{pass} are shown below and for $E_{pass} \geq 10$ eV the condition $E_{pass}/\Delta E \geq 1400$, where ΔE is the deconvoluted FWHM line width, holds.

$E_{pass} = 2$ eV ⇒ Absolute energy resolution = 2.9 meV
$E_{pass} = 5$ eV ⇒ Absolute energy resolution = 3.6 meV
$E_{pass} = 10$ eV ⇒ Absolute energy resolution = 6.18 meV
$E_{pass} = 20$ eV ⇒ Absolute energy resolution = 12.9 meV
$E_{pass} = 50$ eV ⇒ Absolute energy resolution = 28.6 meV

In addition to the angle integrated mode, the analyser features also an angle-resolved mode. The angular resolution has been tested at the ID12B beam line using a special wire and slit arrangement (see Figure 1.16) that consists of a 0.1mm Au wire and a plate with a series of narrow slits that are 0.1mm wide and 0.5mm apart. The excited Au wire acts as the sample and the emitted electrons pass through the plate slits and are guided through the multi element lens system. Here, the angular spread of the electrons is imaged along a direction, θ, that is perpendicular to the lens axis, z_L, and the energy dispersion takes place in a direction that is perpendicular to the plane defined by z_L and θ. The intensity profiles obtained with such a procedure give $FWHM \leq 0.3^{\circ}$ for all the peaks within an angle of $\pm 3.5^{\circ}$ from forward direction and $FWHM \leq 0.5^{\circ}$ for all peaks within an angle of interval of $\pm 5^{\circ}$ from forward direction.

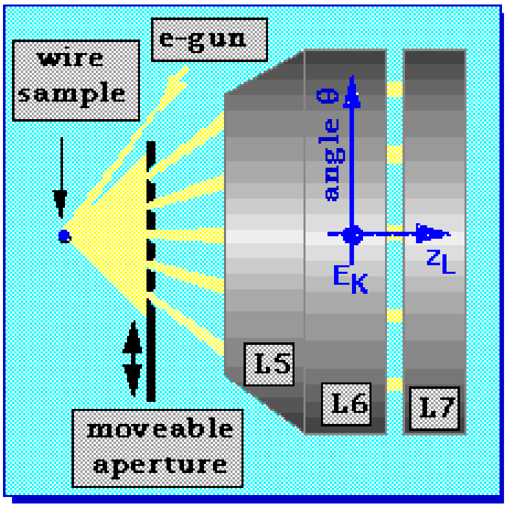

Figure 1.16: view of the setup used to study the angular imaging mode of the lens system.

Due to the imaging properties of the analyser, a narrow straight line of monochromatic electrons will be imaged as a narrow slightly bent line at the detector. The width of this line is defined mainly by the width of the entrance slit and by the angular divergence of the electrons in the energy dispersion direction. The pass energy and the analyser radius determine the energy dispersion and the resolution is then given by the ratio of the imaged line width to the energy dispersion. In order to facilitate the choice of a suitable compromise between resolution and sensitivity, the analyser is equipped with a slit carousel providing nine different apertures. Due to the spherical symmetry of the analyser a straight slit will be imaged onto a curved line at the detector. Since the detector in the non-imaging mode integrates the signals along one row of pixels for each energy channel, this curvature gives a contribution to the energy broadening. To eliminate this effect some of the entrance slits are curved with the appropriate radius in order to produce straight lines at the detector. A small drawback is that one then analyses electrons originating from a curved line on the sample.

The detector system is responsible for the detection of the photoelectrons and the determination of their exact two-dimensional position. This makes it possible to determine their energy and their angular position along the analyser's entrance slit. A field termination mesh is placed just in front of the detector. Its purpose is twofold: first it ensures a homogenous termination of the analyser's field and secondly it allows putting a bias voltage on the detector its self. A small negative bias is generally used to repel low energy secondary electrons, thus substantially reducing the noise. The detector assembly consists of two micro-channel plates and a phosphor screen. The micro-channel pair multiplies each incoming electron approximately 10^6 times and this electron pulse is visualised on the phosphor screen, where a light flash is produced at each pulse. The charge-coupled device (CCD) camera subsequently detects this signal. The position of the light flash along the θ_x direction (see Figure 1.14) of the detector corresponds exactly to the angular position of the incoming electron, whereas the radial position of the light flash (with respect to the analyser's centre) is a function of the kinetic energy with which the corresponding electron was emitted. The CCD camera viewing the detector is mounted in such a way that the camera lines are perpendicular to the energy axis. So for a given set of spectrometer voltages, the camera line where a light flash is detected is a unique function of the electron kinetic energy. The video signal from the camera is then transferred to the detector electronics system that contains a dedicated microprocessor that determines the kinetic energy of the electrons. A measurement is performed using one of two modes that are called "fixed" and "swept" mode respectively. In the fixed mode the instrument operates with a fixed retardation voltage, that is related to the midpoint of the scanned energy window, and the range of a measured spectrum is determined by the pass energy, E_{pass}, and by the physical dimension of the micro-channel plates. A swept mode measurement consists of several fixed mode measurements, where the retardation voltage is increased between measurements. In this way the different energy channels are "stepped" across the whole detector allowing the averaging out of the non-linearities. All communication between the instrument and the computer is performed through a 1Mb/s fibre optic cable.

1.5 The sample environment.

The inelastic mean free path (IMFP) of an electron is a measure of the average distance travelled by an electron through a solid before it is inelastically scattered; it is dependent upon the initial kinetic energy of the electron and the nature of the solid. As can be seen from the universal curve shown below in Figure 1.17, for electron kinetic energies ranging from 10 to 1400eV the inealstic mean free path is smaller than 20Å so that the photoemission signal is strongly influenced by the sample surface conditions. Therefore, if we wish to investigate the bulk properties of a system, it is necessary to work with atomically clean surfaces and/or relatively high incoming photon energies. For photoemission experiments performed in the soft X-ray range, ultra-high vacuum (UHV) conditions are needed: below a pressure of $10^{-10}\,\mathrm{mbar}$, if the sample is not too reactive, the residual gases do not usually alter the surface, at least not in the time needed for a standard measurement (5 to 24 hours).

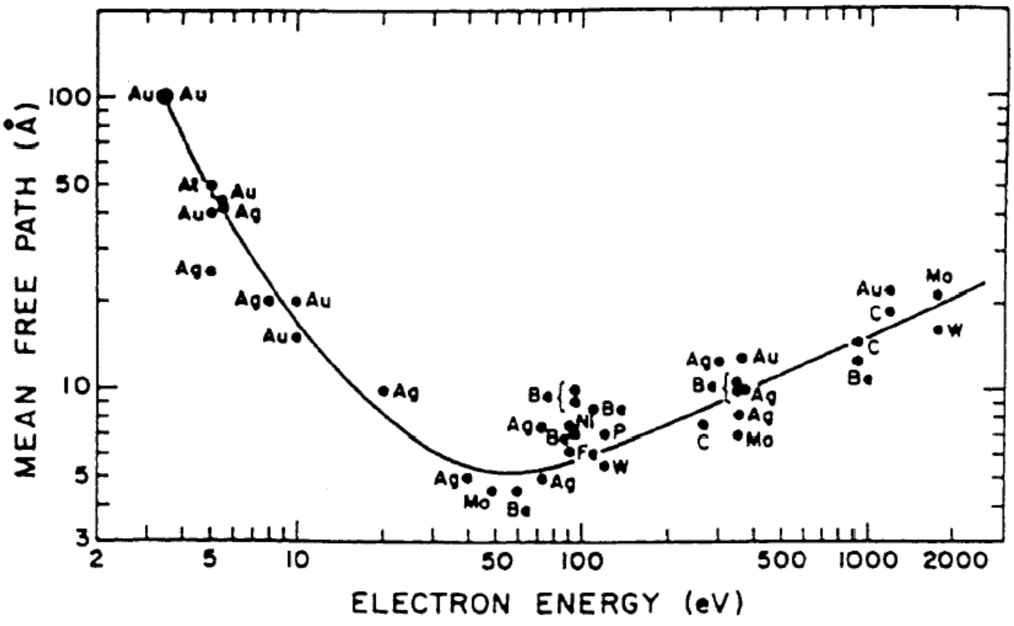

Figure 1.17: the universal curve for the variation of the inelastic mean free path with the electron kinetic energy.

Before entering the UHV system the samples are mounted onto a rectangular Al plate. They can be mounted either by gluing them with a two component silver epoxy conductive and UHV compatible glue (EPO-TEK H21D) or by fixing them with wires. The Al plate is then screwed onto a Cu sample holder. Once mounted the sample is ready to enter the UHV system. This is a three stage system that allows to gradually introduce the sample from air into the main chamber where the pressure is kept below $10^{-10}\,\mathrm{mbar}$ and where the sample is finally measured. A variety of methods exist for obtaining clean surfaces and the procedures that have been commonly used during this study are briefly described below.

1 Cleaving: single crystals are broken along lattice planes when they are in a UHV environment and the photoemission is measured from the freshly obtained surface.

2 *In situ* preparation: the surface of metallic samples is cleaned by means of ion bombardment within a UHV environment. To reverse the lattice crystallographic damage caused by the bombardment, the sample is heated to a typical temperature and subsequently cooled. This cleaning procedure is also applied to the substrate for metallic thin films and multi-layers that are grown within the UHV system by evaporation. As a general rule several cleaning cycles are necessary to produce a good surface.

The smaller chamber, shown to left of Figure 1.18, is the preparation chamber where the *in situ* procedure described above takes places before the sample is entered into the bigger main chamber.

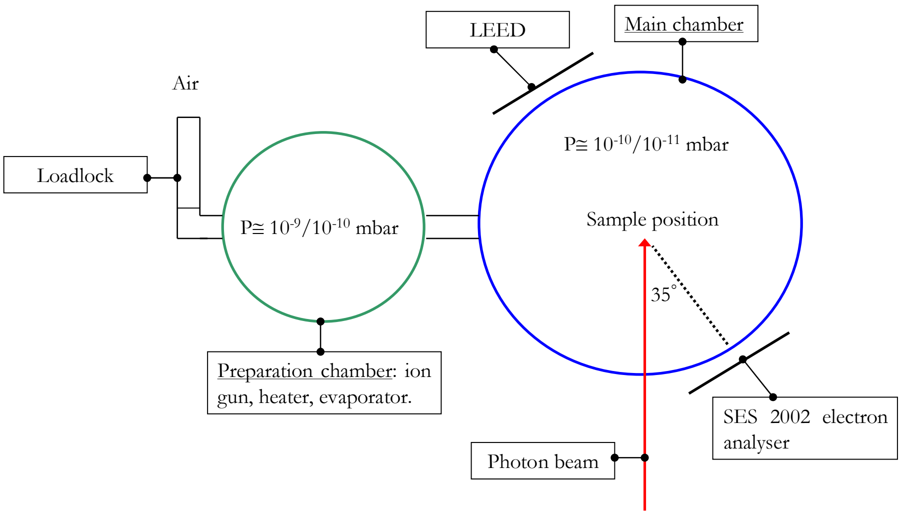

Figure 1.18: a schematic view of the ultra-high vacuum experimental set-up.

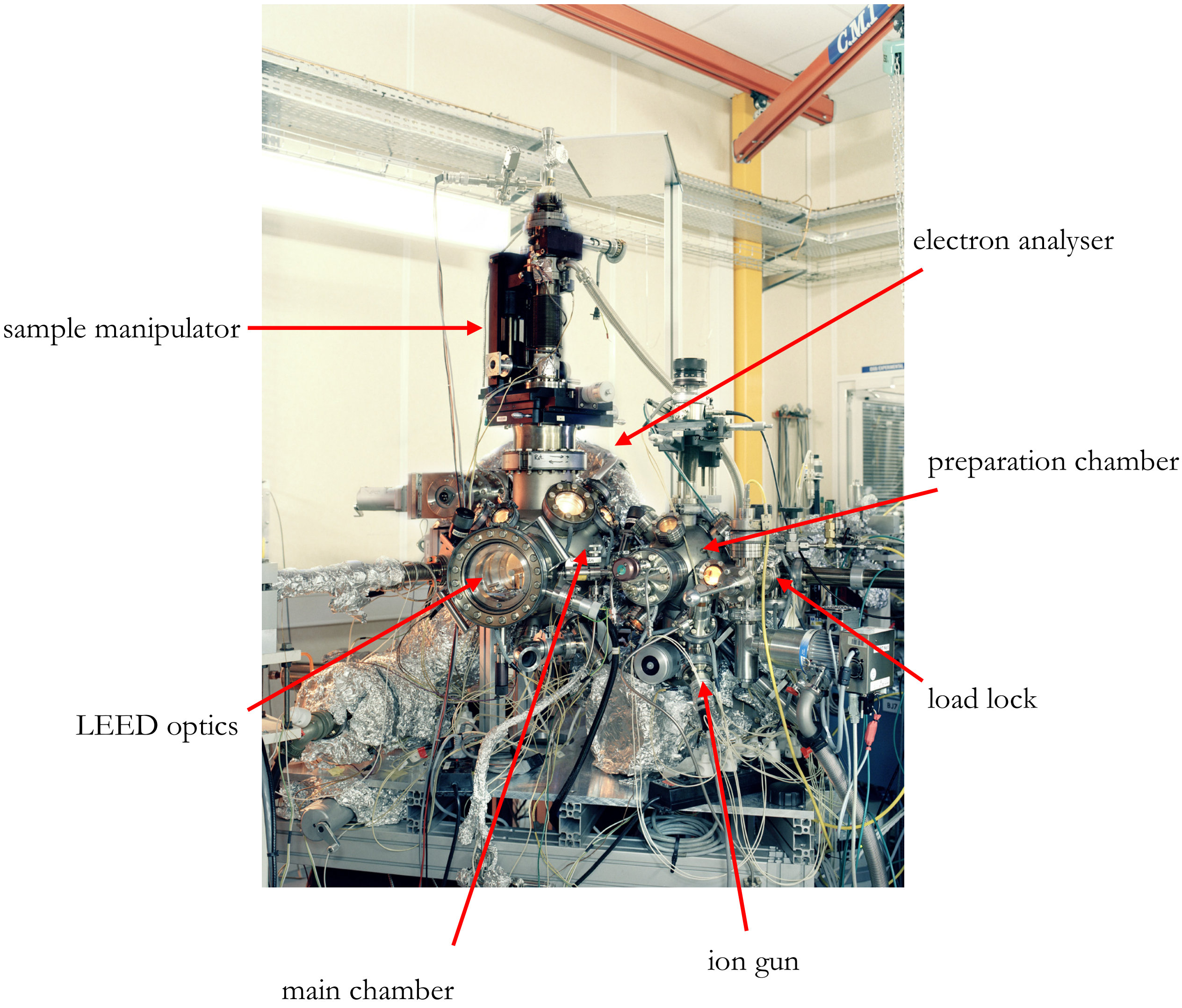

Figure 1.19: photo of the experimental set up. Both the preparation and the main chamber are clearly visible. The Scienta SES 2002 electron analyser is behind the main chamber and only its upper profile is visible [20].

The cleaving procedure generally takes place in the main chamber where a post, that has been glued in air onto the sample, is removed leaving a fresh surface. The crystallographic quality of the sample is then checked by means of Low Energy Electron Diffraction (LEED). This experimental technique is also used to orientate the clean sample when necessary. The LEED is positioned at an angle of approximately 180° with respect to the entrance of the electron analyser. By orienting a high symmetry axis of the sample's reciprocal lattice in a direction that is parallel to the analyser's entrance slit the desired orientation is ensured. It must also be said that, if compared to the illustration shown in Figure 1.14, the SES 2002 electron analyser installed at the ID08 beamline is rotated by 90°, giving the energy dispersion in the horizontal direction and the angular dispersion in the vertical one. The sample manipulator in the main chamber has six independent degrees of motion, three linear ones and three angular ones in order to ensure the desired orientation. A photograph of the entire experimental set up is shown [20] in Figure 1.19 and the geometry used for the photoemission experiments discussed in the following is shown below in Figure 1.20.

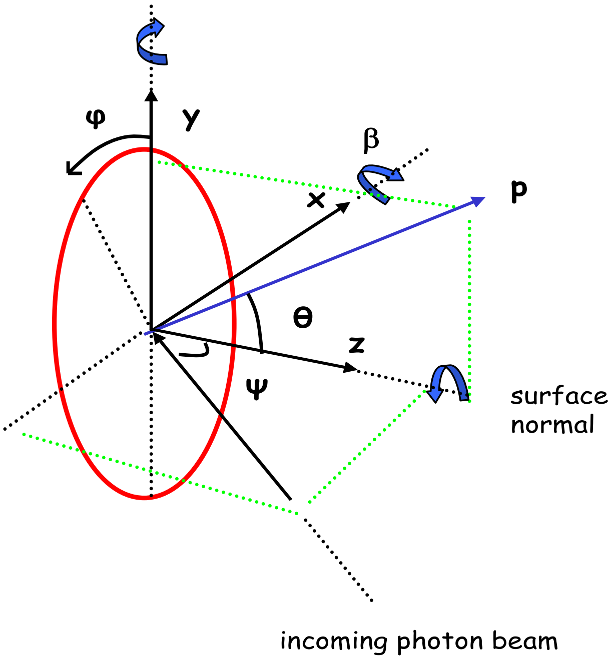

Figure 1.20: the crystallographic axes of the sample are labelled as $\underline{x}$, $\underline{y}$ and $\underline{z}$, where $\underline{z}$ is the direction normal to the surface. θ is the emission angle of the photoelectrons with respect to $\underline{z}$. The azimuthal angle, φ, is varied by rotating the sample around $\underline{z}$ in order to obtain the desired orientation. β is the angle that defines the tilt of the sample's x-y crystallographic plane with respect to the entrance plane of the analyser. In this particular example $\underline{x}$ and $\underline{y}$ coincide with the rotation axes that determine the tilt angle, β, and the normal emission condition.

The momentum of the emitted photoelectrons, $\underline{p}$, and the normal to the sample's surface, $\underline{z}$, define a plane that is perpendicular to both the sample's surface and the plane defined by $\underline{z}$ and the photon beam. The angle between the incoming light and the normal to the surface is fixed and $\psi = 35^\circ$. The magnitude of the θ angle, that is the emission angle of the photoelectrons measured with respect to the normal to the sample's surface, is determined by the angular acceptance of the electron analyser. The azimuthal angle, φ, can be varied in order to choose different high symmetry directions in the x-y crystallographic plane.

Finally, the main chamber described above is provided with a continuous flow cryostat that transfers liquid He through a high efficiency and vacuum insulated line to the copper sample mount inside the vacuum chamber. A needle valve is incorporated in the transfer line and is used to regulate the cryogen flow to the sample. A heater is also installed and experiments can be performed in a temperature range going from 20 K to 325 K. A diode is used to measure the temperature at the sample.

.

---

[1] G. Margaritondo, *Introduction to Synchrotron Radiation,* Oxford University Press, New York (1998).

[2] A. C. Thomson and D. Vaughan (eds), *X-ray data booklet*, Centre for X-ray Optics and Advanced Light Source, Lawrence Berkeley National Laboratory, University of California (2001).

[3] W. B. Peatman, "*Gratings, Mirrors and Slits*, *Beamline Design for Soft X-ray Synchrotron Radiation Sources"*, Gordon and Breach Science Publishers (1997).

[4] http://www.esrf.fr.

[5] P. Elleaume, J. Synchrotron Rad. **1**, 19-26 (1994).

[6] S. Sasaki, K. Kakuno, T. Takada, T. Shimada, K. Yanagida, Y. Miyahara, Nucl. Instrum. Meth. **A331**, 763-767 (1993).

[7] B. M. Kincaid, J. Appl. Phys. **48**, 2684-2691 (1977).

[8] J. Goulon, P. Elleaume, D. Raoux, Nucl. Instrum. Meth. **A 254**, 192-201 (1987).

[9] H. Kitamura, S. Yamamoto, Rev. Sci. Instrum. **63**, 1104-1109 (1992).

[10] X. M. Maréchal, T. Tanaka, H. Kitamura, Rev. Sci. Instrum. **66**, 1937-1939 (1995).

[11] http://www.esrf.fr/machine/groups/insertion_devices

[12] J. Chavanne, P. Van Vaerenbergh, P. Elleaume, T. Günzel, Proceeding EPAC2000, 2346-2348.

[13] J. Chavanne, P. Elleaume, P. Van Vaerenbergh, Proceeding PAC 99, 2662-2664.

[14] J. Chavanne, P. Elleaume, P. Van Vaerenbergh, Proceeding PAC 99, 2665-2667.

---

[15] H. A. Padmore, V. Martynov, K. Holis, Nucl. Instrum. Meth. **A 347**, 206-215 (1994).

[16] C. T. Chen, Nucl. Instrum. Meth. **A 256**, 595 (1987).

[17] C. T. Chen, F. Sette, Rev. Sci. Instrum. **60**, 1616 (1989).

[18] J. J. Yeh, I. Lindau, *At. Data Nucl. Data Tables* **32**, 1 (1985).

[19] http://www.gammadata.se/scienta

[20] With courtesy of Peter Ginter: http://www.peterginter.de

Chapter 2

2.1 The direct transition model.

Isolated atoms have discrete allowed energy levels similar to those that exist for a particle in a one-dimensional well, a linear harmonic oscillator or the hydrogen atom. When atoms come together to form a crystal, the distance between the atoms becomes comparable to, or less than, the spatial extension of the electronic wave functions associated with a particular atom. The consequence is that the electrons are no longer identifiable with specific atoms but belong to the crystal as a whole. The energy states of a crystal are therefore characterised by the single-electron energies, E, and their wave vectors, $\underline{k}$. The band structure of a crystal is the $E(\underline{k})$ representation of its electronic states. In a photoemission experiment a photon of known energy, $h\nu$, is used to impart energy to an electron that is lifted from its initial state, E_b, into an excited state above the vacuum level and travels to the detector with a kinetic energy, E_{Kin}. Conservation laws play a fundamental role in photoemission spectroscopy and the binding energy of the electron within the crystal, E_b, is given by the relation:

$$E_{Kin} = h\nu - E_b - \varphi \tag{2.1}$$

where the kinetic energy is measured with respect to the vacuum level, E_v, and E_b is given with respect to the Fermi level, E_F. The work function, φ, represents the energy that the photoelectrons use to overcome the attractive forces of the lattice and it is given by the difference in energy between the Fermi level of the crystal and the zero kinetic energy of the emitted photoelectron. A rigorous theoretical description of a photoemission event requires a quantum-mechanical treatement of the complete process during which an electron is removed from an occupied state within a solid and arrives at the detector. Theoretical approaches of this kind treat the photoemission process as a one-step event in which photon absorption, electron removal, and electron detection are considered simultaneously [1, 2]. However, due to the complexity of the one-step model, a more phenomenological but simpler approach, the three-step model [2, 3], has proven to be rather successful. A schematic representation of the three-step model is shown in Figure 2.1.

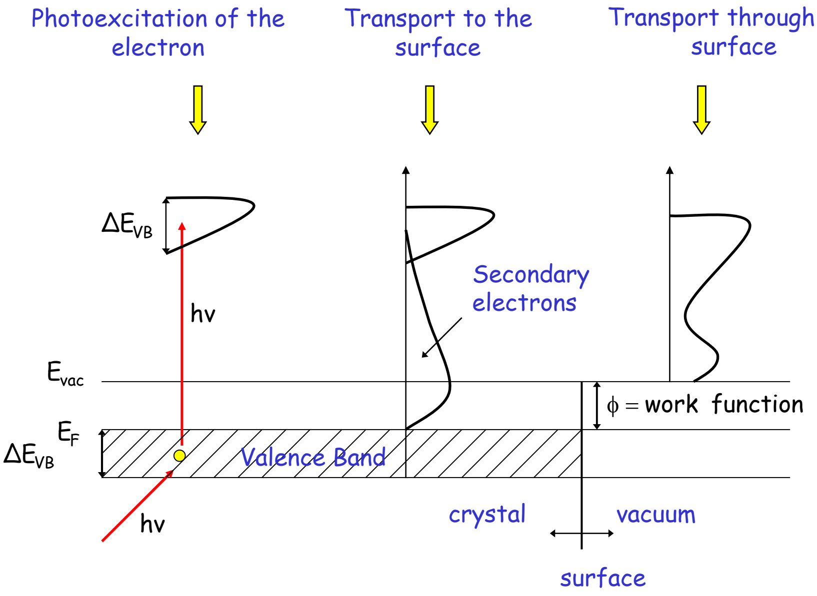

Figure 2.1: schematic representation of the three step model. From left to right: photoexcitation of a bound electron, transport to the surface and penetration through the surface barrier [5].

Within this model the photoemission process is divided into three independent and sequential steps:

(i) the optical excitation of the electrons within the crystal.
(ii) the propagation of the excited electrons to the surface.
(iii) the escape of the photoelectrons into the vacuum.

Band structures are usually plotted in the reduced zone scheme, which means that the bands outside the first Brillouin zone [4] are folded back into the first zone with the help of an appropriate reciprocal lattice vector, $\underline{G}$. In the reduced zone scheme an optical transition is a $\underline{k}$-conserving transition. Therefore, if $\underline{k}$ and $\underline{K} = \underline{k} + \underline{G}$ are the initial and final state wave vectors within the solid, the relation $\underline{k}_f = \underline{k}_i = \underline{k} = \underline{K} - \underline{G}$ holds in the reduced zone scheme. A schematic representation is shown in Figure 2.2.

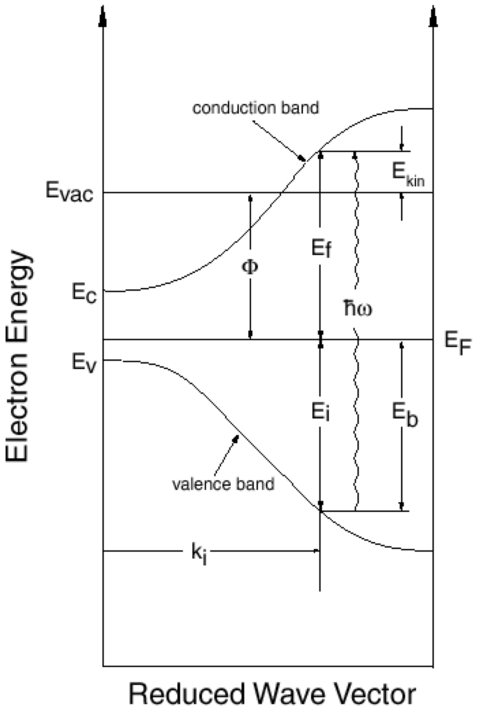

Figure 2.2: representation of the optical excitation process in the reduced zone scheme. E_V and E_C denote the top and the bottom of the valence and conduction bands, respectively. The energies of the initial state, E_i, and the final state, E_f, are referred to the Fermi level, E_F.

In the reduced zone, the energy distribution of the photoexcited electrons, $N(E_{Kin}, h\nu)$, is given by [5]:

$$N(E_{Kin}, h\nu) \propto \sum_{f,i} \left| \left\langle f, \underline{k}_f \middle| H^{int} \middle| i, \underline{k}_i \right\rangle \right|^2 \delta(E_f(\underline{k}_f) - E_i(\underline{k}_i) - h\nu) \times \delta(E_{Kin} - [E_f(\underline{k}_f) - \varphi]) \qquad (2.2)$$

where E_{Kin} is the measured kinetic energy, $E_f(\underline{k}_f)$ and $E_i(\underline{k}_i)$ denote the energies of the final and initial states $|f, \underline{k}_f\rangle$ and $|i, \underline{k}_i\rangle$ respectively, and $\left|\left\langle f, \underline{k}_f \middle| H^{int} \middle| i, \underline{k}_i \right\rangle\right|^2$ is the square of the transition matrix element. In (2.2) the energy conservation is imposed by the first delta function and the last delta function ensures that the kinetic energy measured outside the sample equals the final state energy minus the work function. In the second step of the model the photoexcited electrons travel to the surface. By doing so a large number of photoelectrons undergo inelastic scattering and therefore lose part of their energy. The dominant scattering mechanism that reduces the number of photoexcited electrons that reach the surface with a well defined energy is the electron-electron interaction. The scattered electrons that have lost information about their initial electronic levels give rise to a smooth background in the photoemission spectrum, the so-called secondary background. As already discussed in Chapter 1, the probability that an electron reaches the surface without being inelastically scattered is phenomenologically given by the inelastic mean free path.

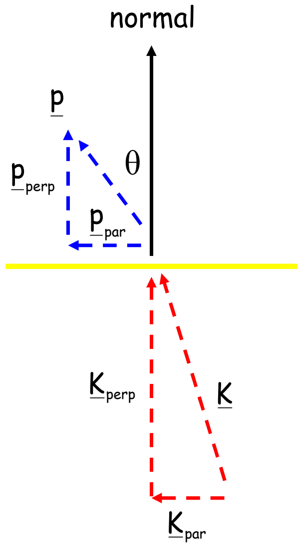

Figure 2.3: momentum relation at the solid-vacuum interface. It is assumed that the photoelectron has a wave vector $\underline{K}$ inside the solid and that $\underline{K}_{par}$ is conserved upon transmission through the interface.

Once the surface is reached, only the electrons that have a component of the kinetic energy normal to the surface that is sufficient to overcome the surface barrier are able to escape into the vacuum; the remaining electrons are reflected back into the bulk. As can be seen in Figure 2.3 the transmission of the photoelectron through the surface leaves the component of the wave vector that is parallel to the surface, $\underline{K}_{par}$, unchanged so that:

$$\frac{\underline{p}_{par}}{\hbar} = \underline{K}_{par} = \underline{k}_{par} + \underline{G}_{par} \tag{2.3}$$

where $\underline{p}$ is the momentum of the photoelectron in the vacuum. For an emitted photoelectron that travels in free space there is a simple relationship between its kinetic energy and momentum given by:

$$E_{Kin} = \frac{p^2}{2m} \tag{2.4}$$

Therefore, the measured momentum of the photoelectron provides information on the parallel component of the final state wave vector, K_{par}, through the relation:

$$K_{par} = \sqrt{\frac{2m}{\hbar^2} E_{Kin}} \cdot \sin\vartheta \tag{2.5}$$

where ϑ is the emission angle of the photoelectrons with respect to the surface normal. The initial state component parallel to the surface, $\underline{k}_{par}$, can then be obtained through equation (2.3). However, due to the lack of translational symmetry along the surface normal, the perpendicular component of the final state wave vector, $\underline{K}_{perp}$, is not conserved across the sample surface and the initial state component, $\underline{k}_{perp}$, remains unkown. This implies that a complete determination of the total crystal wave vector, $\underline{k}$, is in general not allowed unless some *a priori* assumption on the final state dispersion is made. To overcome this problem a free-electron-like final state is assumed, as shown in Figure 2.4.

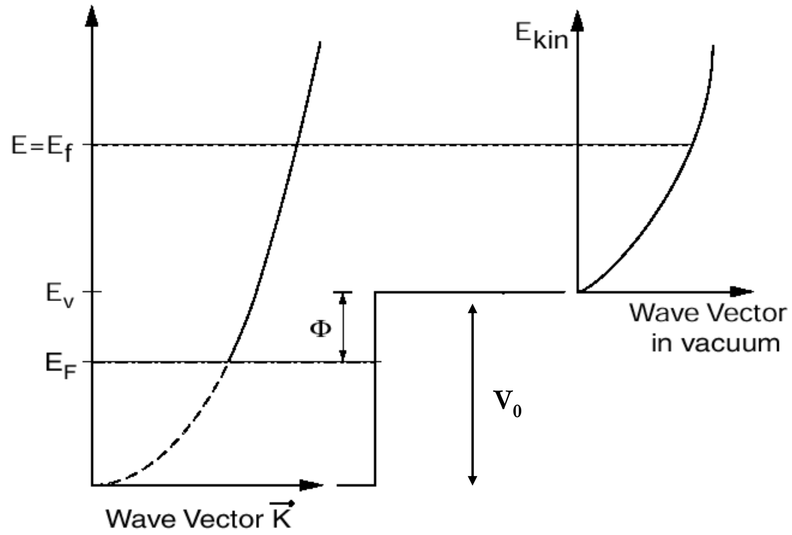

Figure 2.4: free-electron-like final state approximation. It is assumed that the final state wave vector within the solid is obtained by intersection of a free-electron parabola, with its zero at the bottom of the valence band, and the final state energy , E_f. The wave vector of the electron in vacuum is given by the intersection of a free-electron parabola, with its zero at the vacuum level, and the final state energy, E_f [5].

In this approximation the energy of the final state, E_f, is given by:

$$E_f = \frac{\hbar^2}{2m^*}K^2 - |V_0| = \frac{\hbar^2}{2m^*}\left(K_{par}^2 + K_{perp}^2\right) - |V_0| \tag{2.6}$$

where m^* is the effective mass and the energies are measured with respect to the vacuum level, E_V. The parameters that have to be determined are therefore the inner potential, V_0, and m^*. While for m^* the free-electron mass, m, is usually employed, for V_0 one generally uses a theoretical value such as the muffin-tin zero [4] that is given by the bottom of the extended states in the local density approximation calculations with respect to the vacuum level, E_V. Alternatively, the value of V_0 is determined by adjusting the data in such a way that the agreement between the experimental and the theoretical band structure for the occupied states is optimal. By substituting (2.5) in (2.6) the perpendicular component of the initial state wave vector is obtained:

$$K_{perp} = \sqrt{\frac{2m}{\hbar^2}\left(E_{Kin}\cos^2\vartheta + |V_0|\right)} \tag{2.7}$$

and by combining equations (2.5) and (2.7):

$$K_{perp} = \sqrt{\frac{2m}{\hbar^2}\left(E_{Kin} + |V_0| + \frac{\hbar^2}{2m}K_{par}^2\right)} \tag{2.8}$$

In normal emission conditions, when $K_{par} = 0\,\text{Å}^{-1}$, equation (2.8) simply becomes:

$$K_{perp} = \sqrt{\frac{2m}{\hbar^2}\left(E_{Kin} + |V_0|\right)} \tag{2.9}$$

The perpendicular component of the final state wave vector within the solid is therefore known and the initial state component can be determined through the relation:

$$\underline{K}_{perp} = \underline{k}_{perp} + \underline{G}_{perp} \tag{2.10}$$

As a general rule, depending on the angular acceptence of the electron energy analyser, photoemission spectroscopy (PES) can be separated into angle-integrated PES or angle-resolved PES (ARPES). In the angle-integrated measurements the solid angle of detection is large, which means that the $\underline{k}$-information is smeared out over the Brillouin zone and one essentially measures the density of the occupied electronic states. In an angle-resolved photoemission experiment the kinetic energies and the emission directions of the outgoing photoelectrons are measured and by assuming a free-electron-like final state the band structure of the investigated system can be determined. In this case the solid angle of detection must be small in order to define the emission direction of the photoelectrons, hence the initial state wave vector, $\underline{k}$. One of the basic requirements for angle-resolved photoemission spectroscopy is the momentum conservation during the optical excitation process. This requires the atoms within the crystal to be arranged in a periodic array. Added to this, surface irregularities induced by the mechanical polishing and the argon-ion bombardement of the surface and the presence of adsorbates and/or surface vacancies, can cause a breakdown of the conservation law as the photoelectron leaves the crystal. Therefore, the single-crystalline nature of the investigated sample is of fundamental importance and particular attention has to be devoted to the surface preparation. The majority of the angle-resolved photoemission experiments performed so far has been done at photon energies that are within the ultraviolet energy range where the photoionisation cross-sections are substantially higher and the high energy and momentum resolution requirement is more easily achieved than at higher photon energies. In particular, from equation (2.5) and neglecting the contribution due to the finite energy resolution, one obtains:

$$\Delta K_{\mathrm{par}} \cong \sqrt{\frac{2mE_{\mathrm{Kin}}}{\hbar^2}} \cdot \cos\vartheta \cdot \Delta\vartheta \tag{2.11}$$

where $\Delta\vartheta$ corresponds to the finite angular acceptance of the electron analyser. From equation (2.11) it is clear that the momentum resolution will be better at low photon energies, i.e. low E_{Kin}. Recently, great improvements have been made in the energy as well as the angular resolution that can be obtained with an ARPES experiment. This progress has been extensively applied to the investigation of low-dimensional systems where the $\underline{k}_{\mathrm{perp}}$ uncertainty discussed above is less important since a negligible dispersion is expected along the direction normal to the surface. In one and two-dimensional systems the electronic dispersion is almost entirely determined by $\underline{k}_{\mathrm{par}}$. On the other hand, for three-dimensional systems the dispersion in the perpendicular direction is as important as in any other direction and cannot be neglected. From equations (2.5) to (2.9) it appears that when performing an ARPES experiment at constant photon energy a spherical path in $\underline{k}$ -space rather than a straight line is covered. The radius of this circle is determined by the square root of the kinetic energy plus the inner potential. This is schematically displayed in Figure 2.5 where the spherical paths through the Brillouin zone of the body centred tetragonal lattice of $CeNi_2Ge_2$ [6] are shown for four different values of hν belonging to the ultraviolet energy range. It can be seen that, for a given photon energy, by increasing the value of K_{par} in order to probe the entire zone, one actually moves away from the desired high symmetry direction.

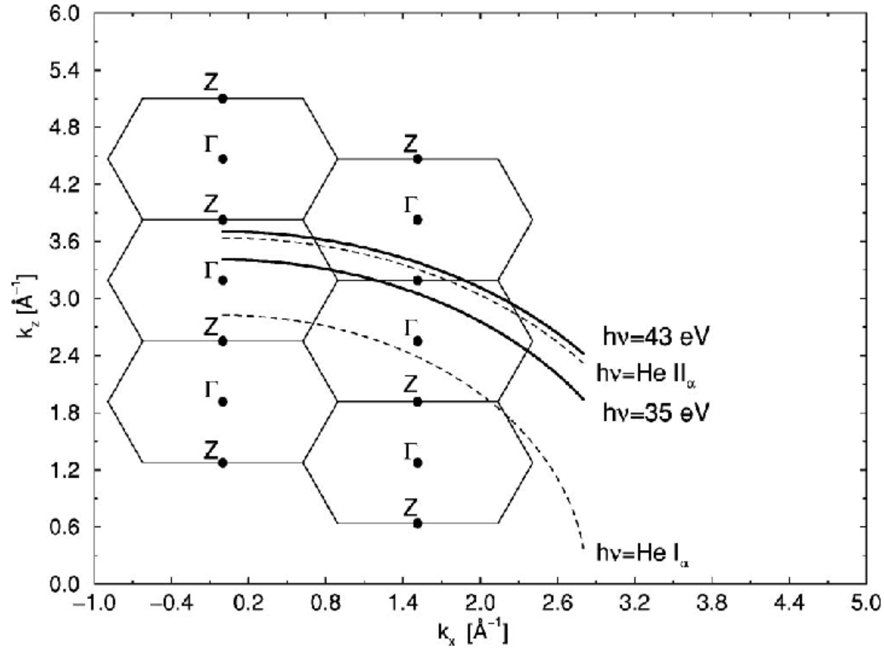

Figure 2.5: typical spherical paths through the Brillouin zone of $CeNi_2Ge_2$ for four different photon energies [6].

The classical way to deal with this problem has been to measure normal emission spectra as a function of the excitation energy. In this way, according to equation (2.9), the dispersion along a high symmetry direction that is perpendicular to the surface can be obtained in a straightforward way. However, the basic assumption of a free-electron-like final state is questionable in the case of highly correlated systems as well as in low energy ARPES experiments. Since the optical excitation takes place in the presence of a crystal potential, the free-electron final state can only be an approximation. The higher the excitation energy, the better the approximation because the effect of the crystal potential gets weaker with increasing kinetic energy of the photoelectron. From equation (2.5) it also appears that the higher the photon energy, i.e. the higher E_{Kin}, the smaller the ϑ angle that is necessary to cover a Brillouin zone. In other words, in the low energy regime the angle that covers a typical Brillouin zone is several tens of degrees and the corresponding $\underline{k}$ -space line is considerably curved as shown in Figure 2.6. On the contrary, if the photon energy is increased to the soft X-ray range, the angle needed to cover a Brillouin zone is several degrees and the corresponding $\underline{k}$ -space curvature is small if compared to the zone size.

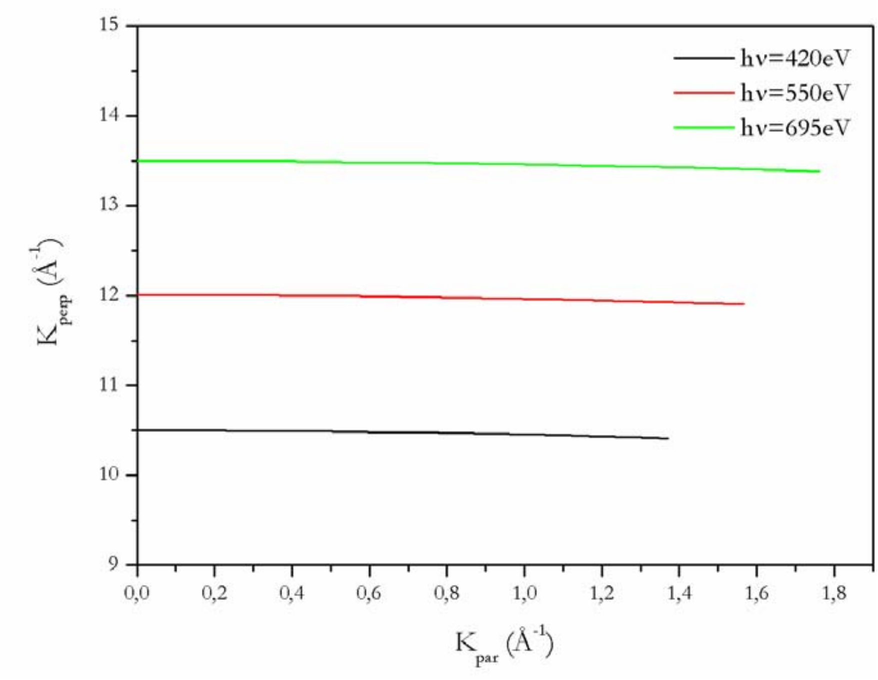

Figure 2.6: variation of the photoelectron wave vector as a function of the incoming photon energy, calculated for Ag (a=4.09Å). The maximum photoemission angle is $\vartheta = 7.5^{\circ}$ and hν varies from 420eV to 550eV to 695eV. Both the increase of the wave vector with increasing photon energy and the small $\underline{k}$ -space curvature are clearly visible.

Another important advantage of soft X-ray ARPES experiments is the increased bulk sensitivity of the technique if compared to the low energy measurements. In the low energy range, where most experiments are performed, the inelastic mean free path of the excited electrons is at its minimum (see Figure 1.17) and the measured intensity is dominated by the surface signal. For systems where the electronic structure differs markedly from bulk to surface [7], the use of high energy photons is therefore of capital importance in determining the more bulk-like properties. However, when working with high incoming photon energies particular attention must be devoted to the role of the photon momentum, $\underline{k}_{h\nu} = 2\pi/\lambda$. In the low energy regime neglecting the photon momentum in equations (2.2) – (2.9) is a totally justified approximation. In the particular case of Ag, whose lattice constant at room temperature and radius of the Brillouin zone are respectively $a = 4.09$ Å and $2\pi/a \cong 1.54$ Å^{-1}, at $h\nu = 21.2$ eV - HeIα line - the photon momentum is only 0.5% of zone radius ($\underline{k}_{h\nu} \cong 0.01\ \text{Å}^{-1}$), at $h\nu = 100\ \text{eV}$ it is 3.3% ($\underline{k}_{h\nu} \cong 0.05\ \text{Å}^{-1}$), whereas for $h\nu = 1487\ \text{eV}$ - Al K_α line – the photon momentum is nearly 50% of the zone radius ($\underline{k}_{h\nu} \cong 0.75\ \text{Å}^{-1}$). Therefore, as the incoming photon energy increases the photon momentum can no longer be automatically neglected and a possible deviation from the direct transition model discussed above must be taken into account.

2.2 The effect of phonon disorder.

From a historical point of view, photoemission spectroscopy rapidly appeared to be a powerful tool for determining the band structure of solids and the usefulness of the technique in metals was demonstrated early on by Berglund and Spicer [3] with their pioneering experiments on Cu and Ag. While the spectra unambigoulsy revealed the location of the metal d bands, the authours found that they could not reconcile their results with the conventional direct transtion theory. In a similar way, Heimann *et al.* investigated normal photoemission at $h\nu = 16.85\,\text{eV}$ and $h\nu = 21.22\,\text{eV}$ from the (110) faces of Cu, Ag and Au [8] and observed strong contributions that could not be accounted for by direct $\underline{k}$-conserving transitions. The results were instead interpreted in terms of the one-dimensional density of states of the bulk band structure. In contrast to these first investigations, numerous subsequent studies [9, 10, 11, 12, 13, 14, 15] have demonstrated that the simple direct transition model, which further assumes a strictly free-electron-like final state, can indeed predict most of the structures observed in photoemission spectra obtained in the low and intermediate energy range, with $h\nu \leq 200\,\text{eV}$, for both normal and non-normal emission. Since final-state band structure calculations at high energies were not available at the time, substantial approximations were in general required for the interpretation of angle-resolved X-ray photoemission spectra. In particular, two different models were proposed to interpret the changes observed in the spectra with emission direction in the high energy regime. In agreement with the low energy case, the early work [16] exploited the simple $\underline{k}$-conserving model to describe the transitions between initial electronic states with full bulk translational symmetry and final states with a free-electron-like dispersion. As already described in the introduction to this Chapter, the direct transition model requires a rigorous wave vector conservation according to:

$$\underline{K} = \underline{k} + \underline{k}_{h\nu} + \underline{G} \tag{2.12}$$

where $\underline{k}$ and $\underline{K}$ are the initial and final state wave vectors of the electrons within the solid, $\underline{k}_{h\nu}$ is the photon wave vector that can no longer be neglected at X-ray photoemission (XPS) energies and $\underline{G}$ is a reciprocal lattice vector. The matrix elements for all transitions are assumed to be constant and spectral changes as a function of the emission angle arise because different regions of the Brillouin zone are sampled for emission along different directions. Although calculations based upon this approach were initially found to predict qualitatively the spectral changes observed in the XPS regime for certain metals [16, 17], subsequent studies indicated that at these energies a rather complete averaging out over the reduced zone occurs [18, 19]. The second model [20, 21, 22], takes into account a completely different approach and assumes that complexities in the final state electronic wave functions as well as the finite angular acceptance of the electron analyser finally yield complete sampling of all the states in the Brillouin zone. The observation of strong direct transition effects in the low and intermediate energy range [9-15], with incoming photon energies ranging up to $h\nu = 200\,\text{eV}$, and the full zone averaging in the XPS region, for $h\nu \cong 10^3\,\text{eV}$, observed for several materials [18, 19], was explained by Shevchik [23, 24, 25] who was the first to consider the possible importance of phonon-assisted non-direct transitions. In his work an expression for the thermally averaged photocurrent was obtained: it appeared that thermal disorder destroys the $\underline{k}$-conservation in a photoemission process and that this phenomenon becomes extremely important for most materials at room temperature in the XPS regime. In particular, within Shevchik's model, two different contributions give rise to the photoemission spectrum: one from the $\underline{k}$-conserving direct transitions and one from the phonon-assisted non-direct transitions. The weaker selection rule imposed on $\underline{k}$ in the latter contribution allows transitions from different regions of the Brillouin zone giving rise to density-of-states-like spectra.

The temperature dependence of the intensity of a radiation that is elastically scattered by a crystal lattice is generally estimated in diffraction theory [26] from the Debye-Waller factor given by:

$$W(T) = \exp\left[-\frac{1}{3}\Delta k^2 U^2(T)\right] \tag{2.13}$$

where $\Delta \underline{k}$ is the wave vector change associated with the scattering and $U^2(T)$ is the temperature dependent mean squared atomic displacement given by :

$$U^2(T) = \frac{3h^2}{4\pi^2 M_a k_B \theta_D^2} \cdot T \tag{2.14}$$

where M_a is the atomic mass, k_B is Boltzmann's constant, θ_D is the Debye-Waller temperature and T is the temperature. In a simple one-electron picture, angle-resolved photoemission spectroscopy can be seen as a diffraction process in which the incident beam is represented by an initial state given by a photon of momentum $\underline{k}_{h\nu}$ and a bound valence electron state of momentum $\underline{k}$, whereas the scattered beam is given by the final state of momentum $\underline{K}$. Therefore the diffraction law describing elastic scattering by a crystal lattice also describes the direct transition requirement in photoemission spectroscopy through the identity:

$$\Delta \underline{k} = \underline{K} - (\underline{k} + \underline{k}_{h\nu}) = \underline{G} \tag{2.15}$$

Very simply, this implies that the intensity of a direct transition peak is expected to exhibit a temperature dependence that is consistent with equation (2.13) as well as a photon energy dependence given by the change in $\Delta \underline{k} = \underline{G}$ with changing $h\nu$. From a general point of view, the temperature dependence of a given photoemission process can therefore be described by the simple Debye theory assuming uncorrelated atomic motions within the crystal. In this approximation, the probability that an initial state of momentum $\underline{k}$ makes a transition to a final state with momentum $\underline{K}$ is proportional to [24]:

$$\sigma^{if}(\underline{K})\cdot\left([1-W(T)]+W(T)\sum_{\underline{G}}\delta(\Delta\underline{k}-\underline{G})\right) \qquad (2.16)$$

where $\sigma^{if}(\underline{K})$ is the photoionisation cross-section. The second term in equation (2.16) corresponds to the $\underline{k}$-conserving transitions multiplied by the Debye-Waller factor, whereas the first term has no restriction on momentum conservation and therefore corresponds to the non-direct transitions component. In terms of the photocurrent, the observed intensity at a finite temperature can be written as a sum of a temperature independent direct transition component, $I_{DT}(E)$, and a temperature independent non-direct transition component, $I_{NDT}(E)$, modulated by the temperature dependent Debye-Waller factor, $W(T)$, in the following way:

$$I(E,T)=W(T)I_{DT}(E)+[1-W(T)]I_{NDT}(E) \qquad (2.17)$$

It follows that the relative importance of the different contributions is determined by $W(T)$, so that the non-direct transitions become more significant at high temperatures and/or at high excitation energies. For room temperature photoemission studies direct transition processes should dominate in most metals at ultra-violet photoemission energies, whereas, due to the large value of $\underline{G}$ (i.e. the lower value of $W(T)$), the phonon-assisted processes are expected to take the lead at X-ray photoemission energies. It should be noticed that either of these limiting cases can be altered by varying the temperature, i.e. cooling in the XPS case to remove thermal disorder and emphasize direct transitions or heating in the UPS case to promote the phonon-induced contributions.

The temperature dependence of valence band spectra expected as a result of such phonon-induced transitions was experimentally observed for the first time in a low energy angle-resolved photoemission experiment performed on Cu [27]. The results agreed with a thermally induced breakdown of the direct transition model. However, an attempt to observe such effects in the XPS regime from Au and Pt [19] failed, leading the authors to conclude that complexities in the final electronic states were indeed responsible for the observed zone averaging. For high incoming photon energies, the temperature dependence of the photoemission spectra suggested in [23-25] was first observed for tungsten, W [28, 29]. It was shown that spectra obtained at different temperatures could be deconvoluted into two temperature independent components, namely a direct transition one and a non-direct transition one, in agreement with equation (2.17). In particular, the direct transition component was found to be consistent with a simple direct transition model based on constant matrix elements and a free electron-like final state, in agreement with [16, 17]. On the other hand, the non-direct transition component appeared to be similar to the density of states weighted by the appropriate matrix elements. This behaviour was then observed in many subsequent photoemission investigations [30, 31, 32, 33, 34, 35, 36], both in the high and low excitation energy range.

An obvious weakness of the studies cited so far comes from assuming that the atomic vibrations are uncorrelated so that the mean squared displacement is used to describe all atomic motions, although a larger value of $U^2(T)$ is allowed for in the vicinity to the surface [34, 35, 36]. The most important consequence of including to one degree or another the effects of correlated vibrations in the simple model is that a straightforward separation of the direct and non-direct contributions to the spectral intensity is no longer possible. In more recent investigations [37, 38] temperature and photon energy dependant angle-resolved photoemission spectra from Al have been analysed with a model that allows to calculate the contributions to the photoemitted intensity for transitions in which m phonons have been excited or absorbed, with $m = 0, 1, 2, ...$ [39]. The lattice vibrations are treated within the Debye model and larger vibrational amplitudes at the surface are taken into account. The results clearly show a decay of the direct transition peak with increasing temperature and photon energy that can be qualitatively understood in terms of Shevchik's simple model [23-25]. Nevertheless, it is shown that the direct transition peaks also contain contributions from electrons that have actually been scattered by one or more phonons. In agreement with [31, 33], this behaviour can be explained by the fact that the most likely scattering happens with phonons that have a wave vector, $\underline{q}$, close to zero such that the non-direct transitions are mostly localised close to the expected direct transitions and the wave vector of the outgoing photoelectron is changed only very little. Most importantly, the energy imparted by the phonon is also small.

2.3 A temperature and photon energy dependent investigation of Ag(001): does band mapping find its limits in the soft X-ray range?

Angle-resolved photoemission spectroscopy (ARPES) is the technique of choice for studying the valence band structures of solids. Because of their noble character and their accurately known theoretical band structure, Cu, Ag and Au have often served as models for understanding the underlying theory of the photoemission process. In order to investigate the possibility of performing accurate band mapping experiments with soft X-ray angle-resolved photoemission spectroscopy, silver (Ag) has been chosen as a well known metal who's electronic band structure has been extensively investigated from both a theoretical [40, 41, 42, 43, 44, 45, 46] and an experimental point of view [47, 48, 49, 50, 51, 52, 53, 54, 55]. A second motivation is to compare our experimental results with new, on-going, calculations. The (001) surface of a single crystal sample of Ag has been cleaned *in situ* by argon-ion bombardement and annealed at temperatures ranging between 450 and 550 C° in order to remove any surface damage given by the cleaning procedure. Several cleaning cycles are necessary to obtain an optimal surface. Throughout the measurements the base pressure in the main experimental chamber is kept below $1\cdot10^{-10}\,\mathrm{mbar}$. The cleanliness of the surface is checked by monitoring the C and O 1s peaks with core level X-ray photoemission spectroscopy and both types of contaminations are absent for the whole length of the data aquisition. Low energy electron diffraction (LEED) is used to verify the good surface order and to specify the orientation of the sample. A continuous flow of liquid He allows for the sample cooling and the heating system consists of a spirally-wound filament positioned on the sample holder. An ultra-high vacuum compatible fixing system unsures good thermal contact between the holder and the sample itself. The especially built sample holder allows for full polar (motorised) and azimuthal rotations, as well as for the adjustment of the β angle that defines the tilt of the sample's surface with respect to the entrance plane of the electron analyser. Polar rotations are performed about an axis that is perpendicular to the plane containing the directions of X-ray incidence and the surface normal, whereas azimuthal rotations are about the surface normal. The polar angle is measured with respect to the surface normal and the azimuthal angle, φ, is defined with respect to the [100] crystal direction. The angle, ψ, between the incident light and the surface normal is fixed and $\psi = 35^\circ$. Electron emission, defined by the ϑ angle of the emitted photoelectrons measured with respect to the [001] direction, takes place in a plane that is perpendicular to the one defined by the incoming radiation and the surface normal. The emission plane is shown in green in Figure 2.7 where the experimental geometry is sketched.

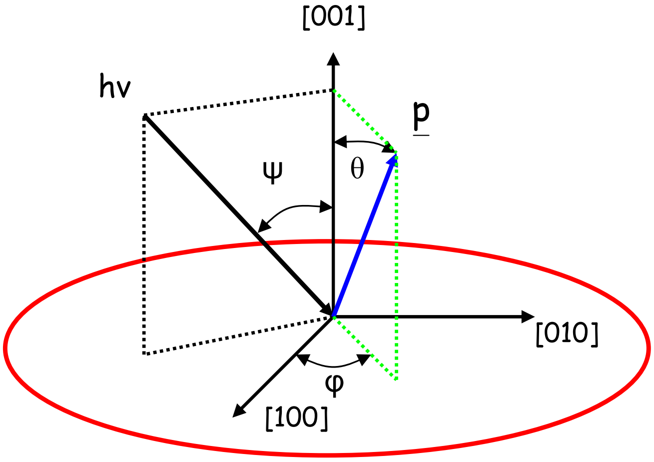

Figure 2.7: schematic representation of the experimental geometry. The incoming photon beam and the normal to the surface define the plane dotted in black. The angle of incidence of the light with respect to the [001] direction is fixed and $\psi = 35^\circ$. The photoelectron emission plane, dotted in green, is normal to the plane of incidence of the light. Different emission planes can be probed by varying the azimuthal angle, φ.

For a given crystallographic orientation the normal emission angle, Θ, is determined with the use of the LEED system that is installed in the main experimental chamber and forms an angle of approximately 180° with respect to the entrance of the electron analyser. To a first approximation, this procedure gives a reliable value of the polar angle required for normal emission. However, the accuracy of such an alignment procedure is checked and confirmed by performing several angle-resolved measurements while scanning the polar angle about the value determined with LEED. Keeping in mind that the spectra must be symmetric about the polar angle that defines normal emission, Θ, the value of the latter can be determined by comparing the experimental images. An example of such a procedure is shown below in Figure 2.8 where the data are taken with $h\nu = 551\,\text{eV}$, $\varphi = 45^\circ$ and T=20K. Despite the intensity differences, there are strong similarities between the spectra displayed in the left and the right column of Figure 2.8. The most stricking similarity can be seen for the two bottom spectra taken for polar angles of $\Theta_1 = 383.35^\circ$ and $\Theta_2 = 393.25^\circ$ respectively, where the binding energy of the minimum of the band crossing the Fermi level and circled in red in the plots is used as a reference feature. It can therefore be said that the normal emission condition is obtained for a polar angle, Θ, with $\Theta = \frac{\Theta_2 - \Theta_1}{2}$. This gives $\Theta = 388.3^\circ$.

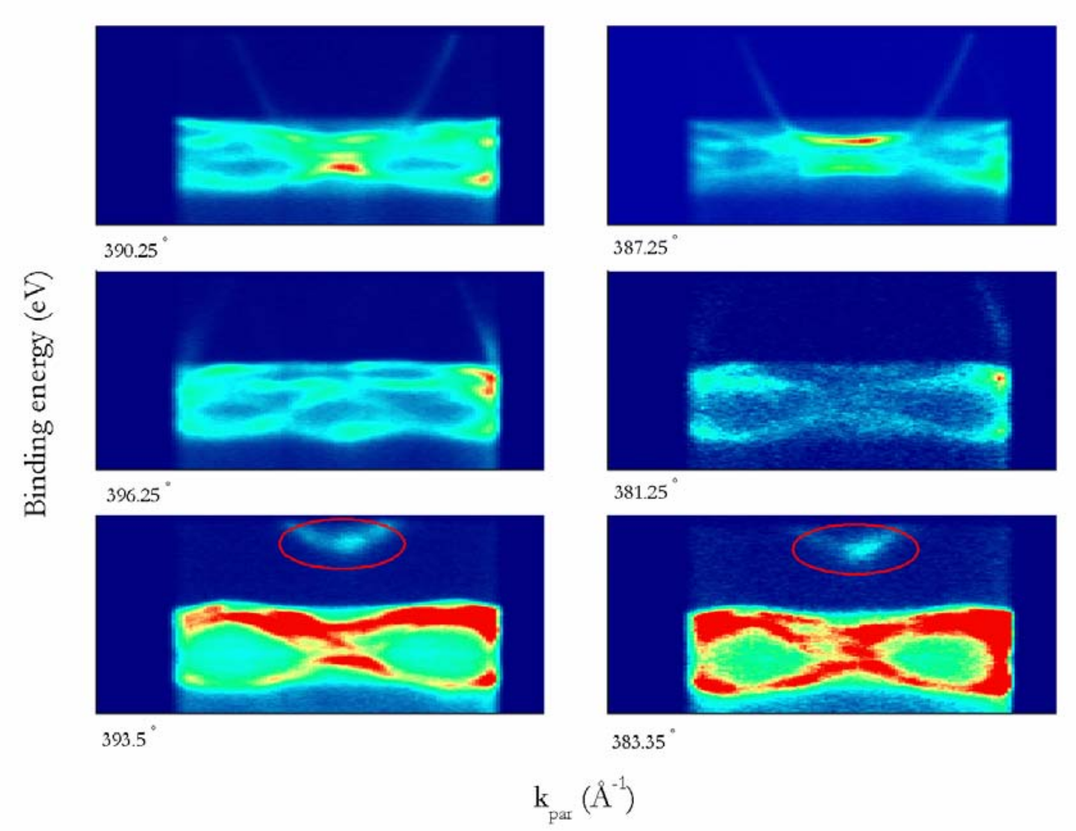

Figure 2.8: example of the procedure used to determine the normal emission condition (see text). Given the similarity of the features shown in the bottom panel (left and right), the normal emission angle, Θ, is chosen as the midpoint between 393.5° and 383.35°. The reference feature used for such an alignment is circled in red. The colour map shows the intensity: dark blue and red equal minimum and maximum intensity respectively.

The first Brillouin zone of Ag is shown below in Figure 2.9, where the different high symmetry points and directions are labelled with capital letters and red symbols respectively. The normal to the sample's surface is defined by the [001] direction. The value of the Ag lattice constant at T=20K is $a = 4.07\,\text{Å}$, giving a Brillouin zone size of $\frac{4\pi}{a} = 3.088\ \text{Å}^{-1}$. In the free-electron-like final state approximation, when considering only the electrons that are emitted in normal emission conditions, the $X - \Gamma - X$ high symmetry direction along the [001] direction can be probed by varying the energy of the incoming photons. If the momentum of the incoming photons is taken into account, equation (2.9) becomes:

$$\underline{K}_{\text{perp}} = \underline{k}_{\text{perp}} + \underline{G}_{\text{perp}} + \underline{k}_{h\nu\,\text{perp}} = 0.512 \cdot \sqrt{E_{\text{Kin}} + |V_0|} + \underline{k}_{h\nu} \cos 35^\circ \tag{2.18}$$

where 35° is the angle between the incoming light and the normal to the surface in the experimental set-up shown in Figure 2.7.

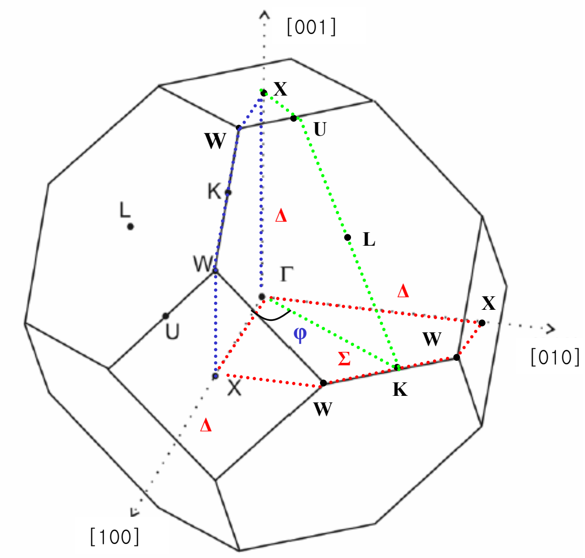

Figure 2.9: Brillouin zone of Ag with high symmetry points and directions. The planes dotted in blue and green show the investigated emission planes. The red plane denotes the (001) surface.

If $V_0 = 10.5\,\text{eV}$ [41] then, according to equation (2.18), a high symmetry X point is reached with $E_{\text{kin}} \cong 420\,\text{eV}$. In an identical way, the Γ point along the same direction is reached with $E_{\text{kin}} \cong 550\,\text{eV}$ and the following X point is reached with $E_{\text{kin}} \cong 695\,\text{eV}$. In order to experimentally determine the values of $h\nu$ that correspond to the different high symmetry points along the $X - \Gamma - X$ direction, measurements have been performed as a function of the photon energy with circularly polarised light. This is a standard procedure and for practical purposes both the resolution and the statistics are low. Added to this, the data are not normalised to the incoming flux. The sample orientation is defined by $\Theta = 0^\circ$ and $\varphi = 45^\circ$, therefore by varying the photon energy from 415 eV to 720 eV, the origin of the $\underline{K}$ wave vector travels along the [001] direction and the whole $\Gamma - K - L - U - X$ plane is probed, both above and below the plane defined by the [100] and [010] crystallographic directions. The measuring temperature is T=20K and the spectra relative to values of $h\nu$ varying between 520 eV and 590 eV are plotted below in Figure 2.10.

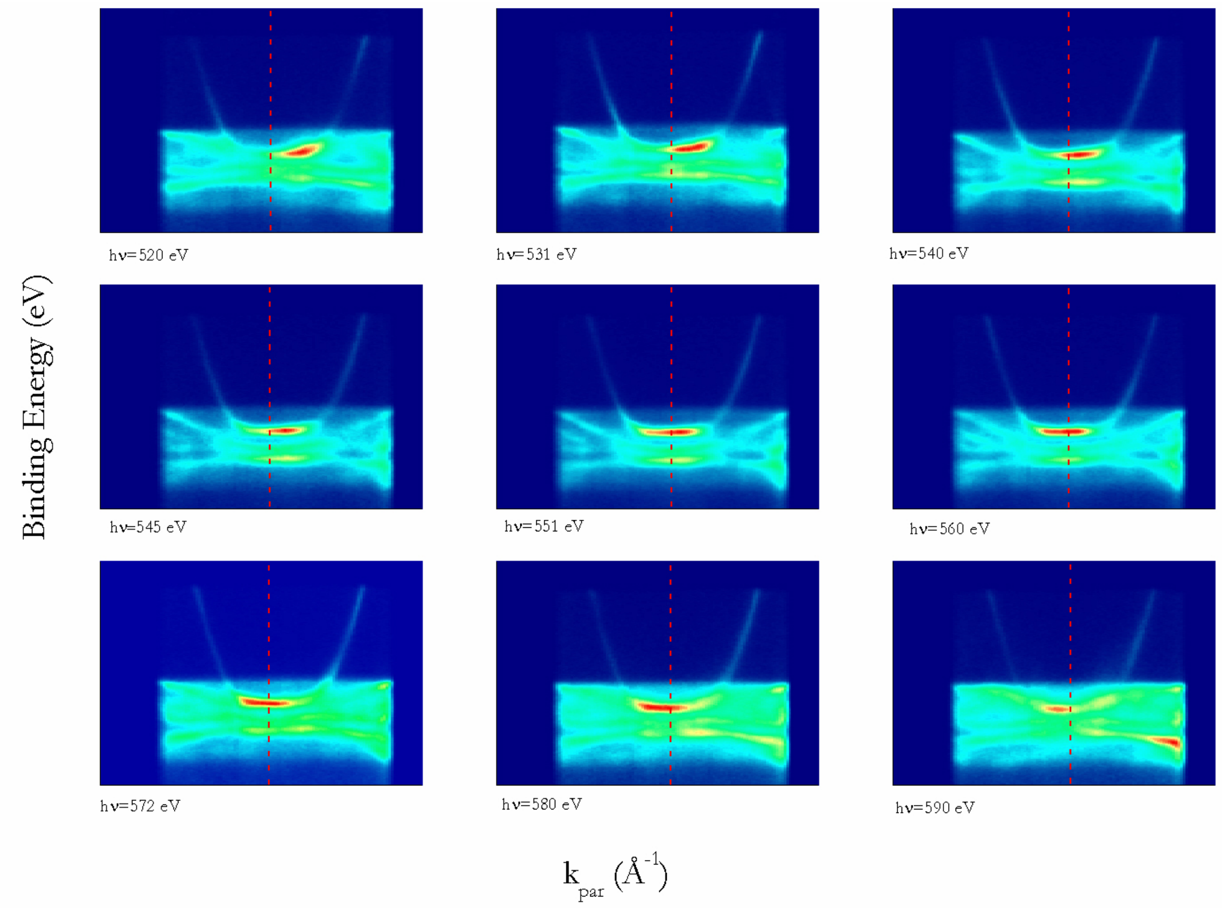

Figure 2.10: measurements taken by varying $h\nu$. The corresponding emission plane is dotted in green in Figure 2.9. $h\nu$ is varied from 520eV to 590eV, probing both above and below the Γ point along the [001] direction. The Γ point is reached with $h\nu = 551\text{eV}$. The red dotted line shows the $k_{par} = 0\text{Å}^{-1}$ position for each plot and the colour map represents the intensity: dark blue and red indicate minimum and maximum intensity respectively. T=20K

The nature of the various features that can be seen above will be discussed in the following. Here, it is important to observe that the entire data set is symmetric with respect to the image measured with $h\nu = 551\text{eV}$. Given the high photon energies, the variation of $\underline{K}_{perp}$ as a function of E_{Kin}, described by equation (2.18), is slow. Therefore, it is unnecessary to take into account the binding energies of the different valence band features and $h\nu = 551\text{eV}$ fixes the position of the Γ point along the [001] direction. From the remaining data sets not shown above it also appears that the low and high energy X points are reached with $h\nu = 424\,\text{eV}$ and $h\nu = 698\,\text{eV}$ respectively, although, because of the chosen photon energy range, fixing the position of the latter points it not as straightforward as in the case of the Γ point. For a more accurate determination, the photon energy should be varied about the expected values of $h\nu$ in order to observe a clear symmetry. However, these experimental findings are in good agreement with the values of $h\nu$ obtained with the use of equation (2.18).

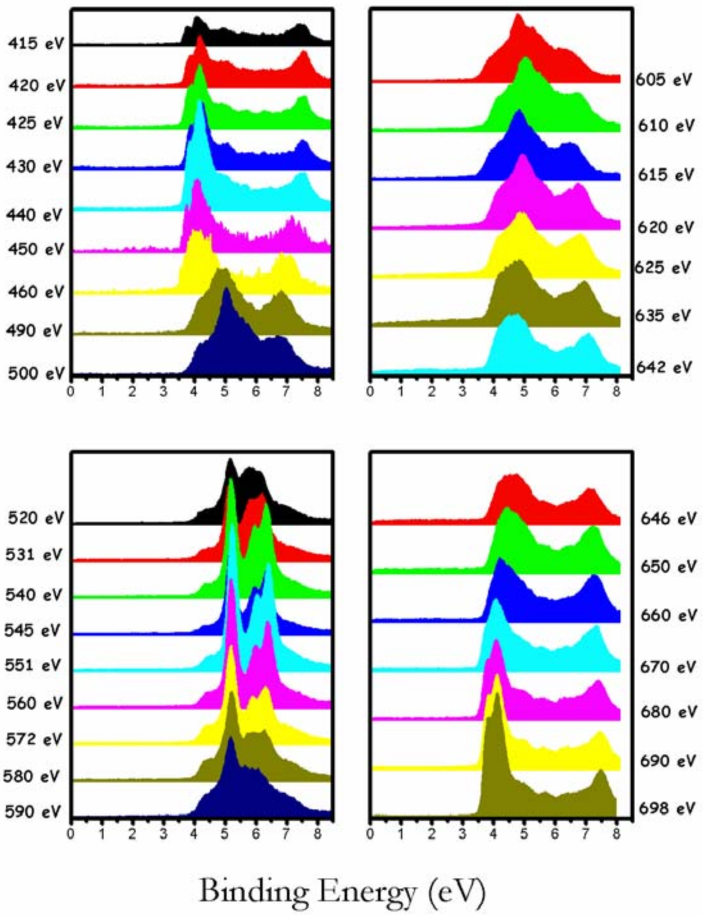

Figure 2.11: normal emission energy distribution curves plotted for $h\nu$ ranging from 415eV to 698eV. The normal emission location ($k_{par} = 0Å^{-1}$) is shown by the red dotted lines in Figure 2.10. The plots are symmetric with respect to $h\nu = 551eV$. The Fermi level, E_F, corresponds to 0eV binding energy and T=20K.

In Figure 2.11, for each photon energy, the normal emission spectra are plotted. These correspond to normal emission energy distribution curves taken at $k_{par} = 0\,Å^{-1}$. The data are normalised to the intensity of the background and shifted vertically for clarity. Again, a clear symmetry with respect to $h\nu = 551eV$ is observed, as the d bands disperse towards each other when approaching this value of $h\nu$ from both the high and low energy side.

Data from two different azimuthal orientations of the sample have been collected, namely $\varphi = 0^\circ$ and $\varphi = 45^\circ$. The final state wave vector, $\underline{K}$, therefore belongs to the $\Gamma - X - W - K - W - X$ plane for $\varphi = 0^\circ$, shown in blue in Figure 2.9, or to the $\Gamma - K - L - U - X$ plane for $\varphi = 45^\circ$, shown in green. It follows that the parallel component, $\underline{K}_{par}$, lies either along the [100] or the [110] crystallographic direction. For each sample orientation, measurements have been taken at T=20K for two different values of the incoming photon energy, $h\nu = 551\,eV$ and $h\nu = 698\,eV$, that correspond to the Γ and the X point along the direction that is perpendicular to the sample's surface. The four data sets are measured with right circularly polarised light. For each measurement the data are normalised both to the current measured at the sample and the acquisition time. The results obtained with $h\nu = 551\,\text{eV}$ are shown in Figure 2.12 and Figure 2.13 for $\varphi = 0^\circ$ and $\varphi = 45^\circ$ respectively. In Figure 2.12 the same data set is plotted in two different ways: in the bottom image the intensity contrast has been varied in order to highlight the s-p band crossing the Fermi level.

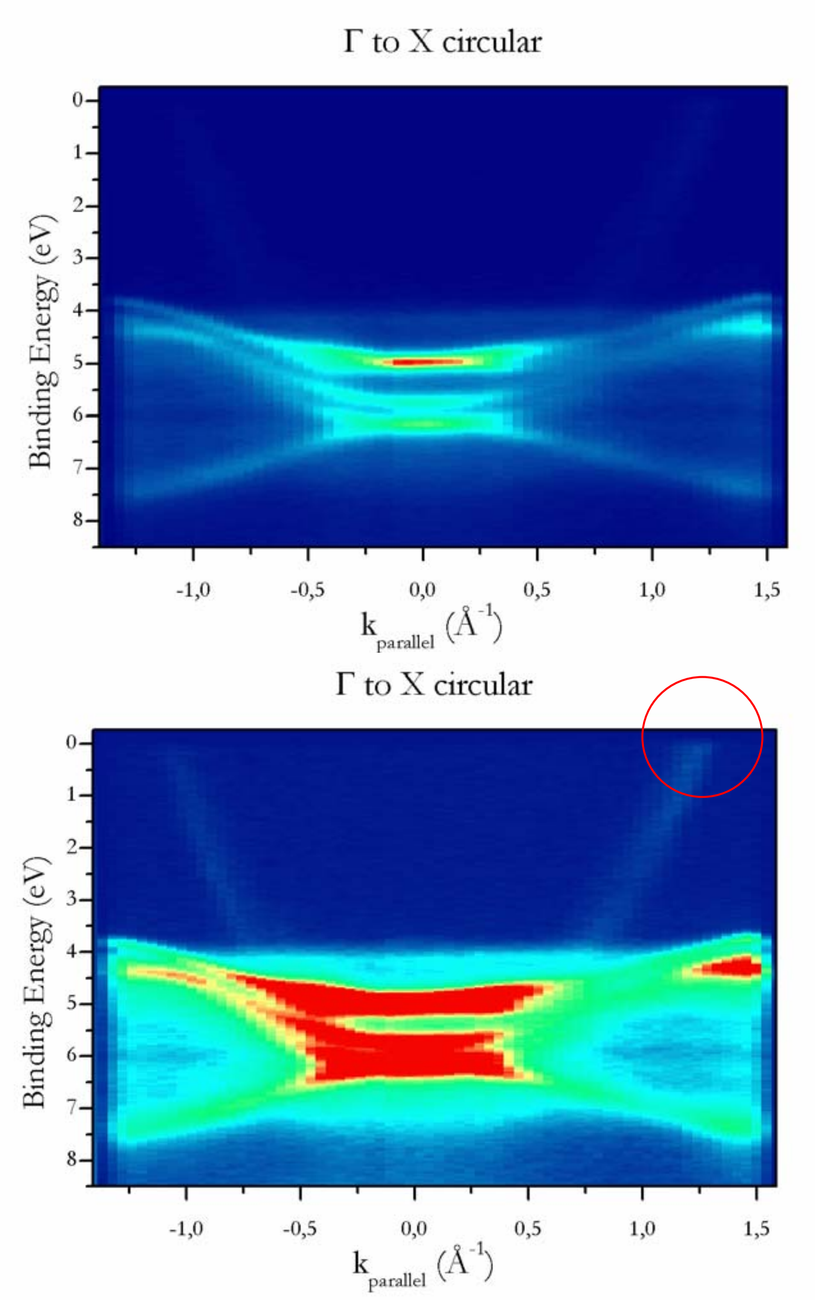

Figure 2.12: $\Gamma - X$ high symmetry direction (Δ) probed with circularly polarised light. $h\nu = 551\text{eV}$ and T=20K. The colour map represents the intensity and will be used for all the angle-resolved results presented in this chapter: dark blue and red indicate minimum and maximum intensity respectively. The Fermi level is found at $E_F = 0\text{eV}$. In the bottom plot the colour contrast is varied in order to enhance the sp band crossing the Fermi level (circled in red).

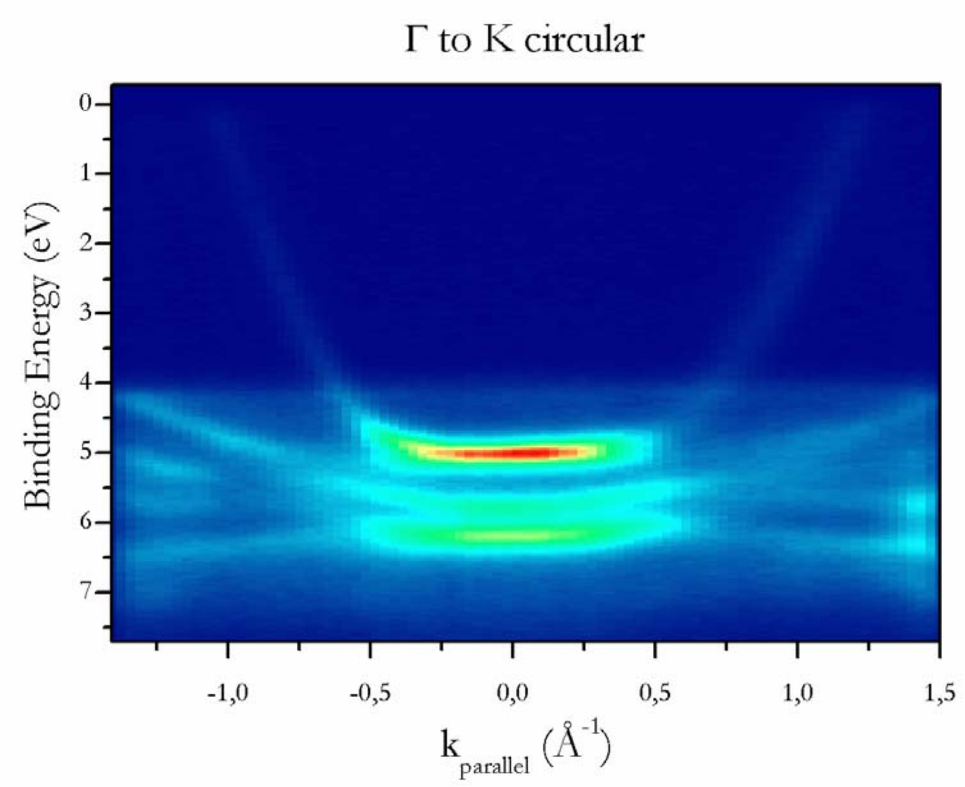

Figure 2.13: $\Gamma - K$ high symmetry direction (Σ) probed with circularly polarised light. $h\nu = 551\text{eV}$ and T=20K. For the colour map see Figure 2.12. $E_F = 0\text{eV}$.

Figure 2.12, for $\varphi = 0^\circ$, $\underline{K}_{par}$ varies along the Δ direction, whereas for $\varphi = 45^\circ$ the Σ direction is probed. The zone boundaries along theses two directions are found at $k_{par} = 1.54\,\text{Å}^{-1}$ and $k_{par} = 1.63\,\text{Å}^{-1}$ respectively. Therefore, according to equation (2.5), a photon beam of energy $h\nu = 551\,\text{eV}$ allows one to probe almost the entire Brillouin zone along these directions. In a similar way Figures 2.14 and 2.15 show the results obtained for $h\nu = 698\,\text{eV}$, with $\varphi = 0^\circ$ and $\varphi = 45^\circ$ respectively. In this case $\underline{K}_{par}$ varies along the Z and S high symmetry directions. The zone boundaries are found at $k_{par} = 0.73\,\text{Å}^{-1}$ and $k_{par} = 0.51\,\text{Å}^{-1}$ respectively. From equation (2.5) it follows that with an incoming energy of $h\nu = 698\,\text{eV}$ the zone boundary for both azimuthal orientations is not only reached but crossed. Along the Z direction, $\underline{K}_{par}$ moves from X to W and back to X again. Hence the obvious periodicity that appears in Figure 2.14. Instead, for $\varphi = 45^\circ$, $\underline{K}_{par}$ varies from X to U=K and then towards Γ. This is unambigously observed in Figure 2.15, where the s-p band is clearly seen crossing the Fermi level. This band is also observed in Figure 2.13 where, for a different value of $h\nu$, the energy dispersion from Γ to K along a similar Σ high symmetry direction is shown.

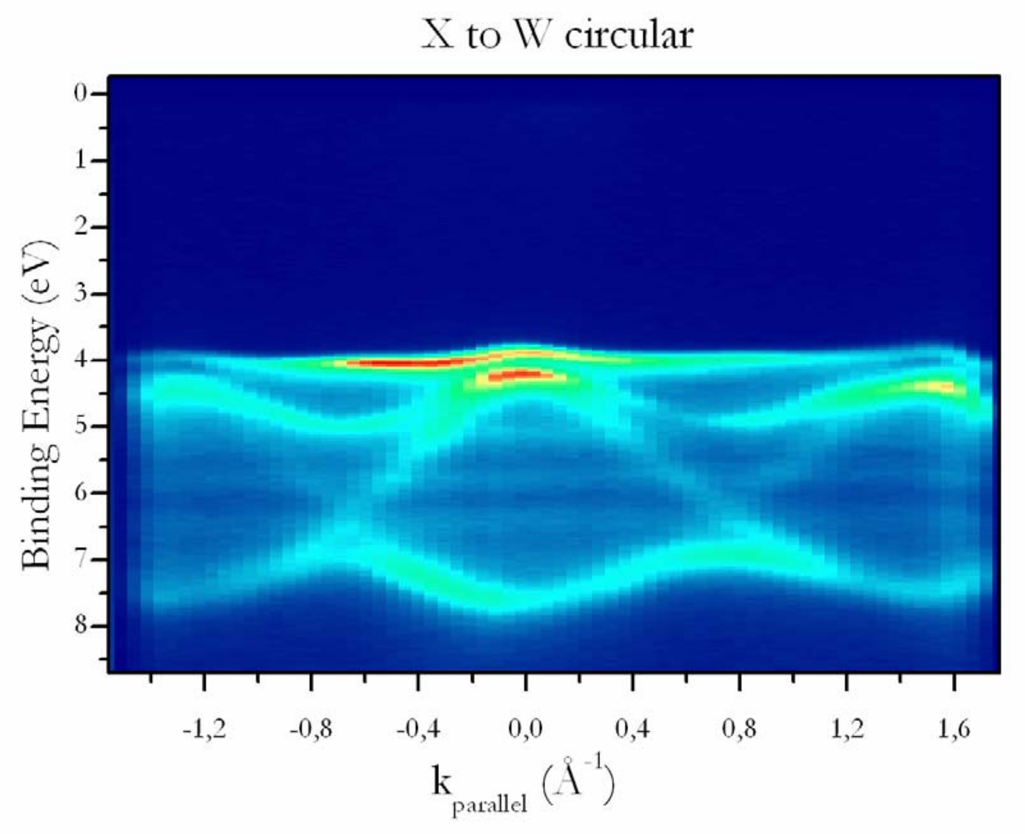

Figure 2.14: X - W high symmetry direction (Z) probed with circularly polarised light. $h\nu = 698\text{eV}$ and T=20K. For the colour map see Figure 2.12. $E_F = 0\text{eV}$.

The data are in good qualitative agreement with the calculations presented in [41, 42, 43, 45, 46] and the theoretical band structure [46] is shown in Figure 2.16 for each investigated high symmetry direction. Close to the zone centre along the Δ and Σ high symmetry directions (Figures 2.12 and 2.13 respectively), direct transitions originating from all the allowed initial states are visible, apart from transitions originating from the two deeper lying bands along both directions. For both the investigated orientations the $\Gamma'_{25} \rightarrow \Gamma_8^+ + \Gamma_7^+$ spin-orbit splitting is observed at Γ. On the contrary, the smaller $X_5 \rightarrow X_6^+ + X_7^+$ splitting at the zone boundary along the [100] direction is not obvious in Figure 2.12. This is also the case in Figures 2.14 and 2.15 where the data are measured with $h\nu = 698\,\text{eV}$ and the X point is found at $k_{par} = 0\,\text{Å}^{-1}$.

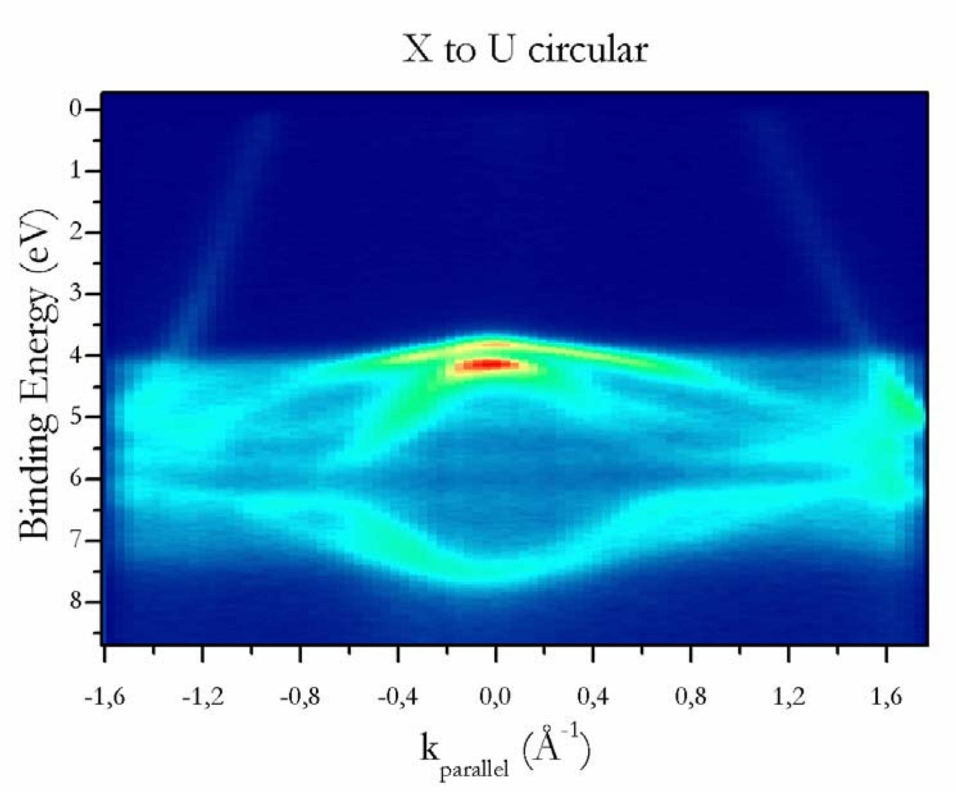

Figure 2.15: X - U high symmetry direction (S) probed with circularly polarised light. $h\nu = 698\text{eV}$ and T=20K. For the colour map see Figure 2.12. $E_F = 0\text{eV}$.

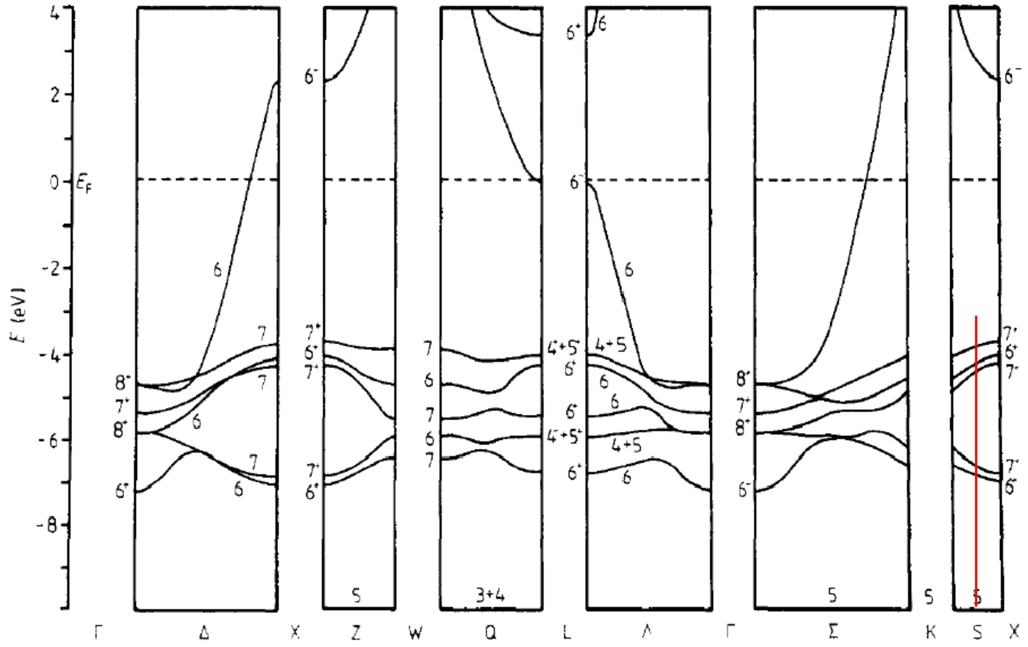

Figure 2.16: relativistic band structure of Ag along different high symmetry directions [46]. The red line has been added and indicates the position of $k_{par} = 0.25\text{Å}^{-1}$ along the S direction. This will be refered to later on in this chapter.

Symmetry	Experiment				Theory [46]
Γ_{6^+}					7.21
Γ_{8^+}	5.92 [49]	6.16 [50]	6.23 [53]	6.13	5.82
Γ_{7^+}	5.48 [49]	5.64 [50]	5.80 [53]	5.73	5.37
Γ_{8^+}	4.78 [49]	5.00 [50]	4.95 [53]	4.95	4.69
X_{6^+}		7.30 [50]		7.38	7.00
X_{7^+}					6.82
X_{7^+}		4.36 [50]		(4.31)	4.25
X_{6^+}		4.12 [50]		4.11	4.05
X_{7^+}		3.82 [50]		3.74	3.71

Table 1: energy values (eV) at selected high symmetry points of the Brillouin zone of Ag. The column shown in yellow lists our experimental results.

Table 1 shows a list of the energy levels at the two selected high symmetry points along the [001] direction, Γ and X respectively. The experimental values found in literature [49, 50, 53] are shown to the left of our results that are high lightened in yellow. The column to the far right lists the theoretical values [46]. The agreement between our results and the ones previously determined in [50, 53] is good, with a maximum deviation of 0.1 eV for the Γ_8^+ energy level. In this context it should be noticed that to the best of our knowledge, no experimental value for the most tightly bound Γ_{6^+} energy level is available. The spin-orbit split X_7^+ energy level is barely distinguishable at the zone boundary along the [100] direction and its binding energy is given in brackets in Table 1.

Keeping in mind what has been said in Section 2.2 regarding the possible difficulties in accurately determining the band structure of a material with soft X-ray angle-resolved photoemission spectroscopy, a futher aim of this study has been to investigate the limits of this technique both as a function of the incoming photon energy and as a function of the measuring temperature. Measurements have been taken for three different values of the incoming photon energy, namely $h\nu = 428\,\text{eV}$, $h\nu = 703\,\text{eV}$ and $h\nu = 1042\,\text{eV}$. These values of $h\nu$ correspond to three consecutive X points along the [001] direction. The azimuthal angle is kept constant and $\varphi = 45^\circ$. The Debye-Waller temperature of Ag is known to be $\vartheta_D = 215\,\mathrm{K}$ [4] and for each value of $h\nu$ measurements have been taken for three different temperatures, namely $T = 20\,\mathrm{K}$, $T = 100\,\mathrm{K}$ and $T = 215\,\mathrm{K}$. The mean squared atomic displacements, calculated according to equation (2.14), are shown below in Table 2a. The three equivalent high symmetry points are reached with $\underline{G} = \frac{4\pi}{a}(0,0,3.5)$, $\underline{G} = \frac{4\pi}{a}(0,0,4.5)$ and $\underline{G} = \frac{4\pi}{a}(0,0,5.5)$ respectively and, in agreement with equation (2.13), the Debye-Waller factors for each combination of $h\nu$ and T are listed in Table 2b. The data sets shown below are normalised to both the current at the sample and the acquisition time and the combined energy resolution of the beamline and the electron analyser are chosen to be similar for the different values of $h\nu$. Although in principle the chosen values of $h\nu$ probe three equivalent high symmetry points, when the photon energy increases the momentum resolution expressed by equation (2.11) worsens. Added to this, the mean free path of the outgoing photoelectrons increases. Hence the spectral features and the intensities of the data sets taken for different values of $h\nu$ at a given temperature cannot be directly compared. All the spectral variations observed with both temperature and photon energy are completely reversible and reproducible. Figure 2.17 shows the temperature dependence of the angle-resolved data for $h\nu = 428\,\mathrm{eV}$. In an identical way, Figures 2.18 and 2.19 show the T-dependence for $h\nu = 703\,\mathrm{eV}$ and $h\nu = 1042\,\mathrm{eV}$ respectively.

	$U^2(T)$ Å^2
T=20K	0.00058
T=100K	0.00298
T=215K	0.00621

	$h\nu = 428\,\mathrm{eV}$	$h\nu = 703\,\mathrm{eV}$	$h\nu = 1042\,\mathrm{eV}$
T=20K	0.977	0.963	0.945
T=100K	0.888	0.824	0.749
T=215K	0.782	0.667	0.548

Table 2. a (left): calculated mean square displacement for the investigated values of T. b (right): Debye-Waller factor calculated for nine different combinations of T and $h\nu$.

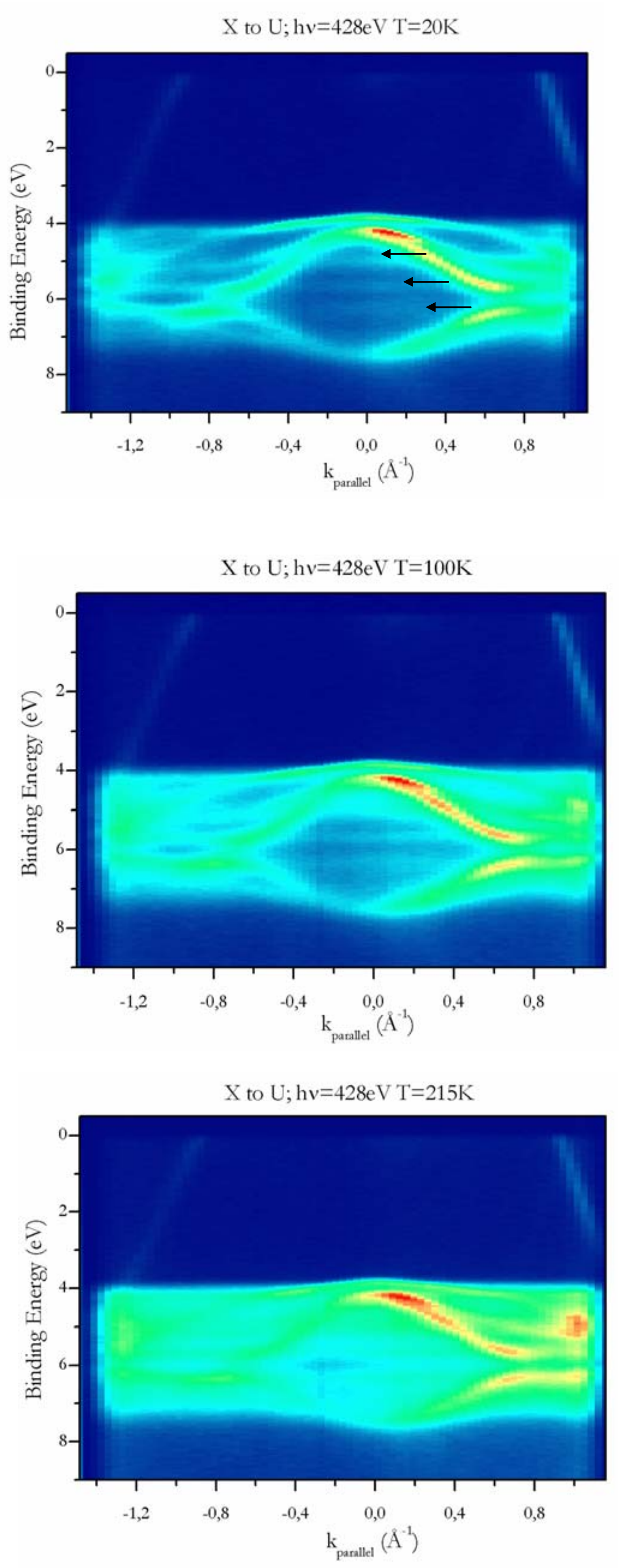

Figure 2.17: X - U high symmetry direction (S) probed with circularly polarised light. From top to bottom: hν = 428eV and T=20K, 100K and 215K, respectively. The arrows in the upper plot indicate the location of the non-direct transitons, labelled as d, e and f in the following. For the colour map see Figure 2.12. $E_F = 0$eV .

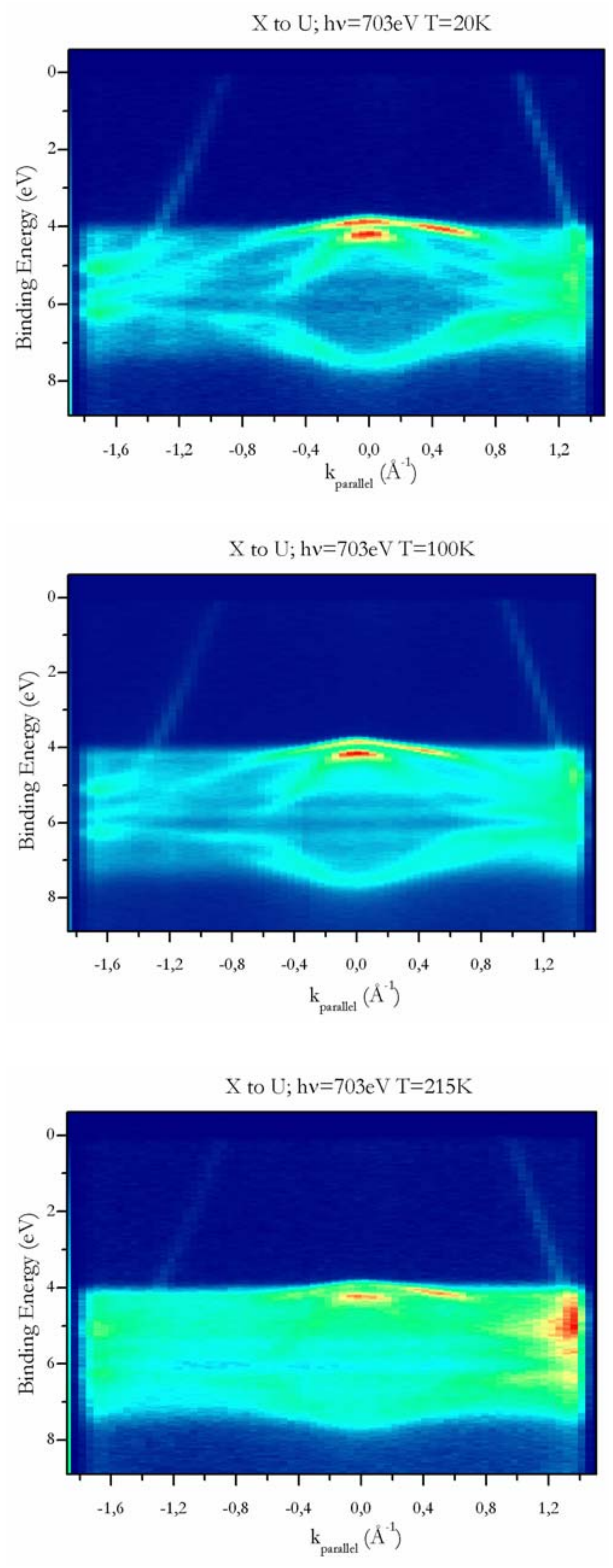

Figure 2.18. $X - U$ high symmetry direction (S) probed with circularly polarised light. From top to bottom: $h\nu = 703eV$ and T=20K, 100K and 215K, respectively. For the colour map see Figure 2.12. $E_F = 0eV$.

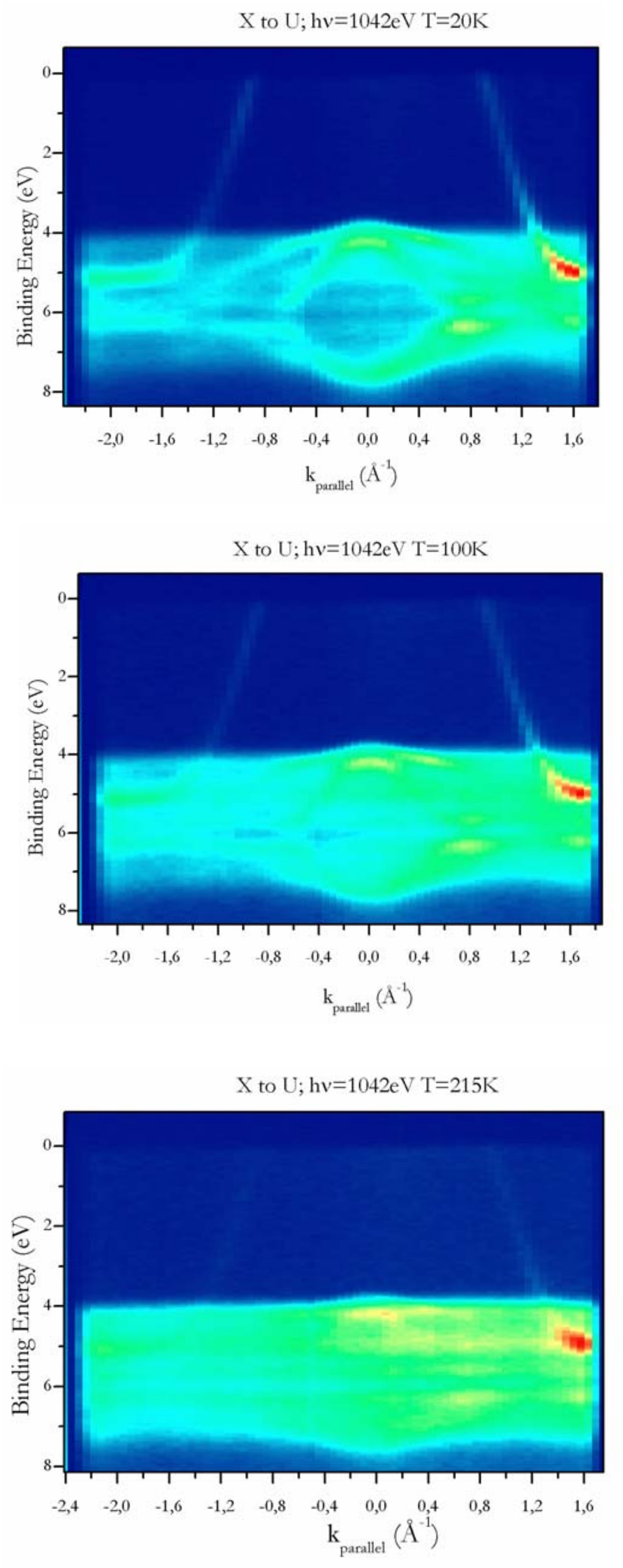

Figure 2.19: X - U high symmetry direction (S) probed with circularly polarised light. From top to bottom: $h\nu = 1042\text{eV}$ and T=20K, 100K and 215K, respectively. For the colour map see Figure 2.12. $E_F = 0\text{eV}$.

Clearly, the nine measurements shown above give results that are qualitatively in agreement with Shevchik's model [23, 24, 25], although the contribution of the non-direct transitions appears to be larger than expected. For example, according to Table 2b, at T=215K and $h\nu = 1042\,\mathrm{eV}$ over 50% of the transitions are expected to be direct. The situation in the lower plot in Figure 2.19 is different. Band like features are barely visible, the angle-resolved photoemission spectrum looses structure and is averaged out over $\underline{k}$-space. Consistently with the model, as the temperature and the photon energy are reduced, the phonon-assisted transitions decrease and the measured spectra can be compared with the band structure calculations shown in Figure 2.16. In particular, the results obtained for $h\nu = 428\,\mathrm{eV}$ and T=20K, plotted in the uppermost image in Figure 2.17, show a strong direct transition behaviour. Nevertheless, despite the low values of $h\nu$ and T, three features of constant binding energy are seen crossing the zone centre between approximately 4.7eV and 7eV. These features, that have also been observed in the ultra-violet photoemission results presented in [50], mark the existence of non-$\underline{k}$-conserving transitions originating from initial states in regions of $\underline{k}$-space that are not directly probed by our experimental geometry . In Figures 2.20a and b, for each value of $h\nu$ the energy distribution curves are plotted as a function of the temperature for $k_{\mathrm{par}} = 0\,\mathrm{Å}^{-1}$. The data are shifted vertically for a better comparison. As already mentioned, the structures that appear between approximately 4.7 eV and 7eV binding energy in all the spectra are ascribed to the non-direct transitions. It is clearly observed that for a given photon energy as the temperature is raised, the intensity of these features increases, suggesting an increase in the contributions originating from non-$\underline{k}$-conserving transitions. The same effect can be observed for a given temperature as a function of the photon energy. However, it has already been said that due to the increasing mean free path of the outgoing photoelectrons, the intensities of features measured with different values of $h\nu$ should not be directly compared. For both $h\nu = 428\,\mathrm{eV}$ and $h\nu = 703\,\mathrm{eV}$, three disctinct peaks that correspond to direct transitions originating from the X_7^+ and the two X_6^+ energy levels are observed. These peaks are labelled as a, b and c respectively. In a similar way the features arising from non-direct transitions are labelled as d, e, and f. The X_7^+ spin-orbit partner, labelled as g, is seen as a very weak shoulder that appears on the high energy side of the shallower X_6^+ level. For $h\nu = 428\,\mathrm{eV}$, despite a broadening of the features and an increase of the phonon-assisted transitions at T=215K, the direct transition peaks are visible for each value of T. For $h\nu = 703\,\mathrm{eV}$, as the temperature is increased to T=100K, peak b shifts towards lower binding energies by approximately 0.2eV. For $h\nu = 703\,\mathrm{eV}$ and T=215K the distinction between peaks a and b starts to fade and the deeper lying X_6^+ level, peak c, looses its structure giving rise to an apparent energy shift towards lower binding energies. The distinction between the X_7^+ and the shallow X_6^+ energy level dissapears altogether for $h\nu = 1042\,\text{eV}$, where only the X_6^+ peak remains visible and the X_7^+ feature, peak a, appears as a weak shoulder. In a similar way as for $h\nu = 703\,\text{eV}$, direct transitions originating from the deeper lying X_6^+ level are only visible for T=20K and T=100K but already at T=100K the broadening of the feature is significant. For $h\nu = 1042\,\text{eV}$ and T=215K most of the structure originating from the direct transitions is lost, the intensity between 4.7eV and 7eV increases and an accurate determination of peak c is no longer possible.

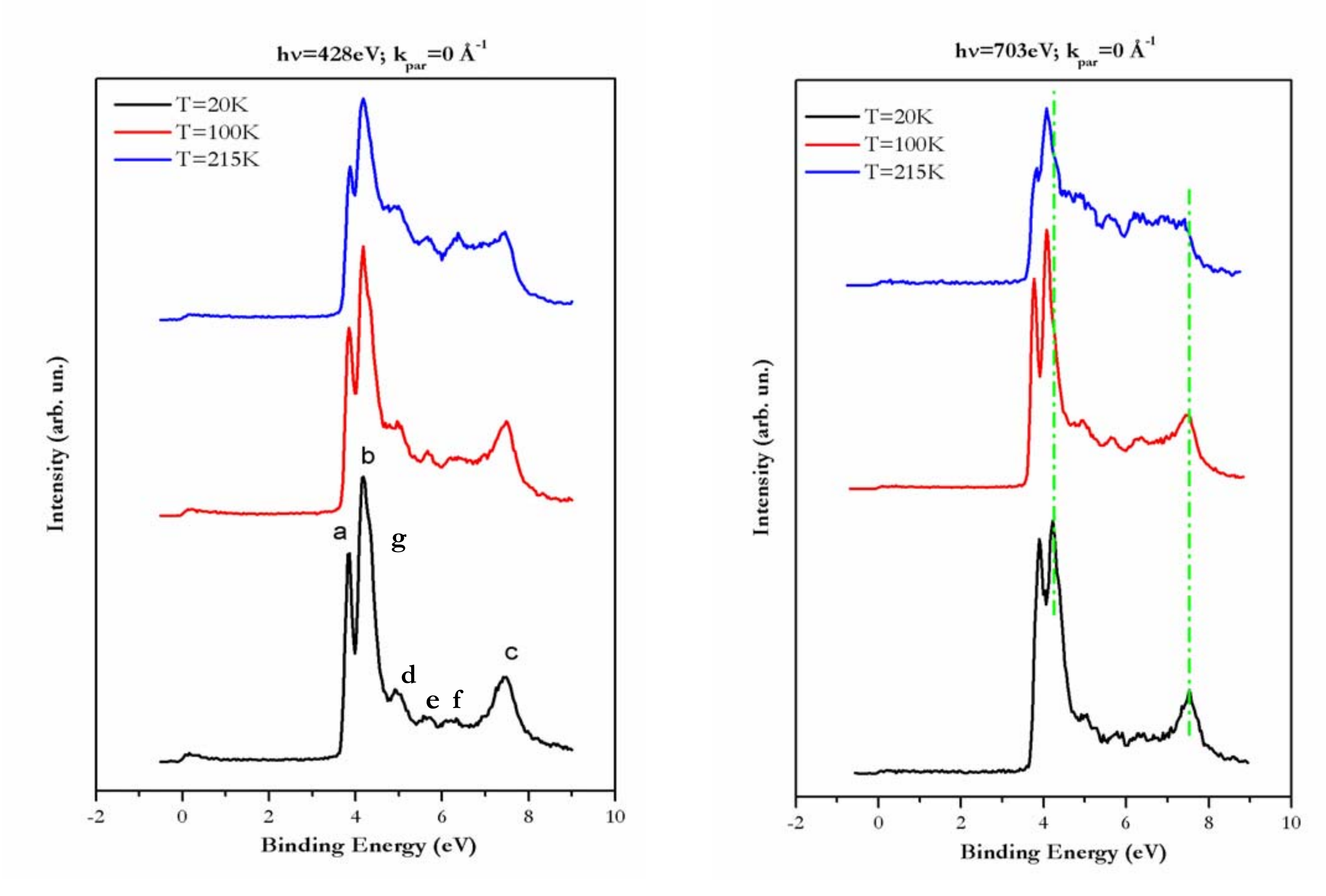

Figure 2.20a: normal emission ($k_{par} = 0\text{Å}^{-1}$) energy distribution curves. Left (from bottom to top): $h\nu = 428\text{eV}$, T=20K, 100K and 215K. Right (from bottom to top): $h\nu = 703\text{eV}$, T=20K, 100K and 215K. The direct transition peaks are labelled as a, b and c; the non-direct contributions as d, e and f. g indicates the spin–orbit partner. $E_F = 0\text{eV}$.

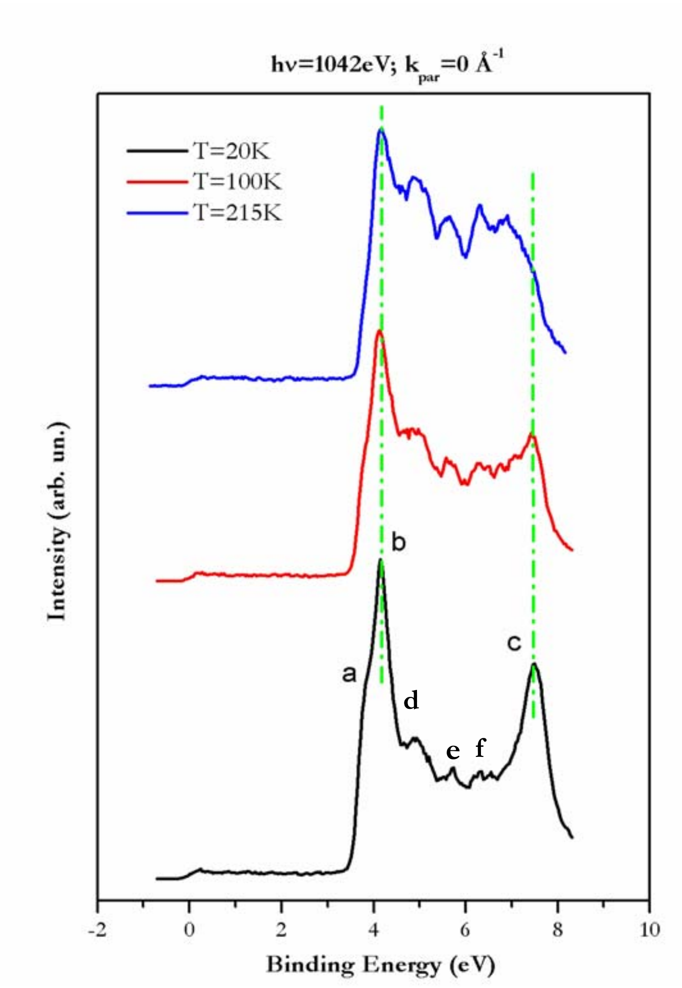

Figure 2.20b: normal emission ($k_{par} = 0Å^{-1}$) energy distribution curves. From bottom to top: $h\nu = 1042eV$, T=20K, 100K and 215K. $E_F = 0eV$. The green lines are guide to the eye that help following the T-dependent spectral changes.

In a similar way as above, for each value of $h\nu$ the temperature dependence of the energy distribution curves is shown in Figure 2.21 for $k_{par} = 0.25\,Å^{-1}$, whose location along the S direction is shown by the red line in Figure 2.16. Despite the different value of k_{par}, hence the modified features, the overall trend appears to be the same. In Figure 2.22 the ratio of the intensity of peak c to the intensity of peak f is plotted as a function of T, for the three different values of $h\nu$, for both $k_{par} = 0\,Å^{-1}$ (top) and $k_{par} = 0.25\,Å^{-1}$ (bottom). However, due to the strong spectral variations induced by the non-direct transitions, for the both measurements taken at $h\nu = 1042\,eV$ and T=215K an accurate determination of this quantity is somewhat difficult.

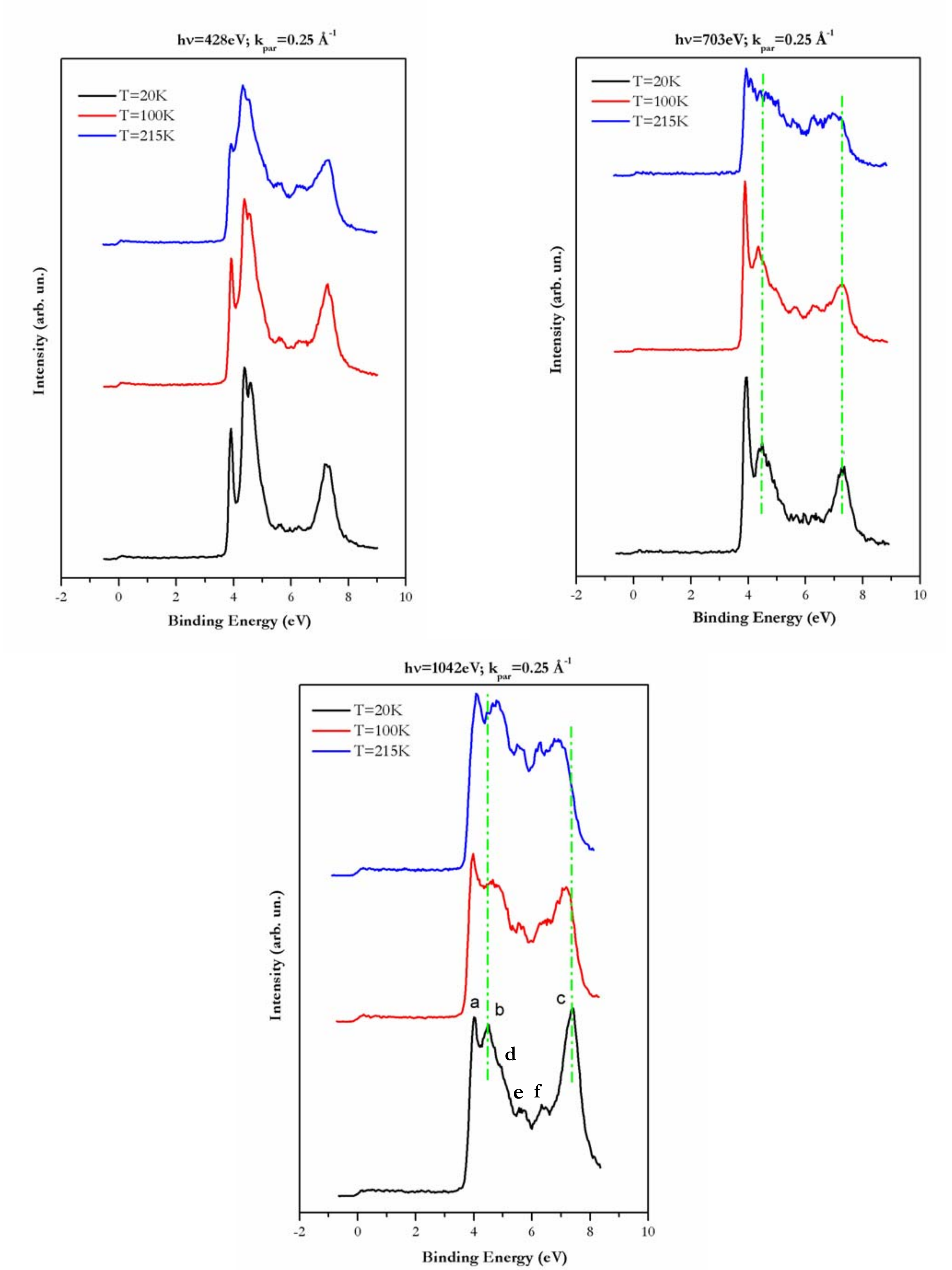

Figure 2.21: energy distribution curves measured for $k_{par} = 0.25Å^{-1}$. Top left: $h\nu = 428eV$. Top right: $h\nu = 703eV$. Bottom: $h\nu = 1042eV$. From bottom to top: T=20K, 100K and 215K. $E_F = 0eV$.

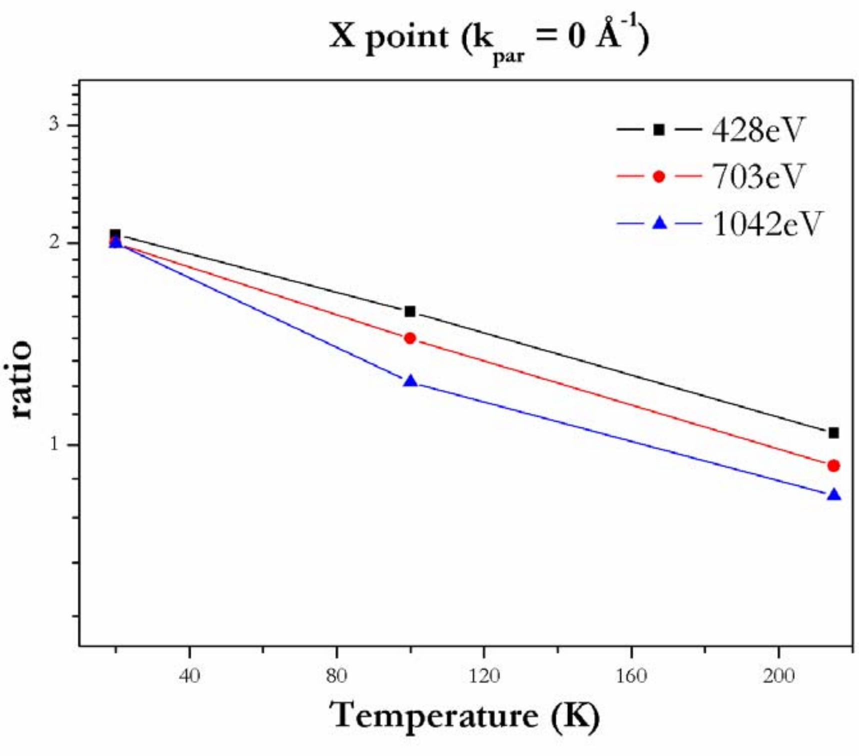

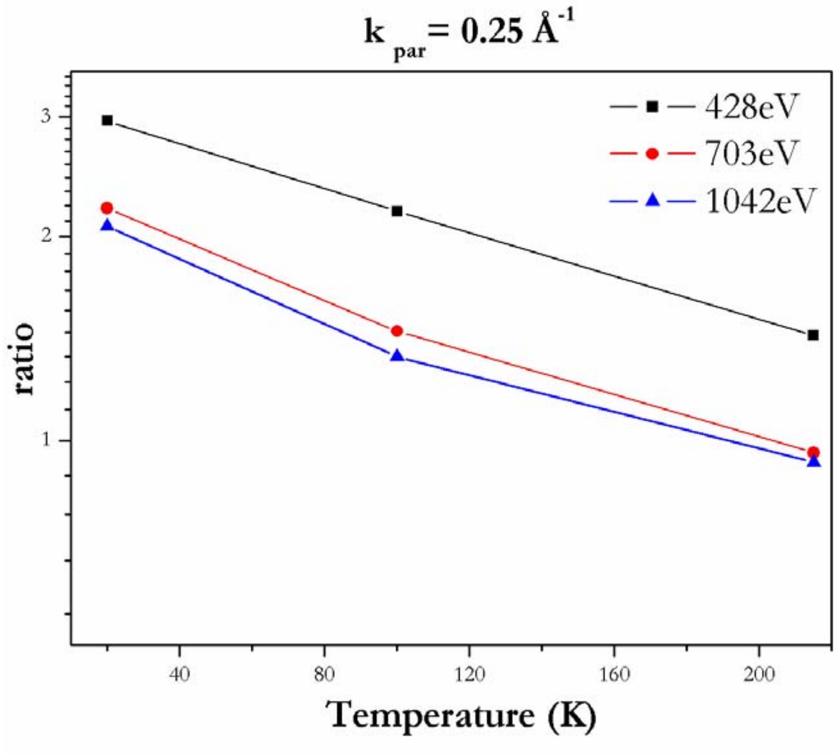

Figure 2.22: ratio of the direct transition intensity (peak c in Figures 2.20 and 2.21) to the non-direct transition intensity (peak f in Figures 2.20 and 2.21) as a function of T , for $h\nu = 428eV$ (black), $h\nu = 703eV$ (red) and $h\nu = 1042eV$ (blue). Top: $k_{par} = 0Å^{-1}$. Bottom: $k_{par} = 0.25Å^{-1}$.

As can be seen above, for each value of $h\nu$ and for both values of k_{par}, the ratio of the direct to the non-direct transitions decreases with increasing temperature. Added to this, for a given temperature and k_{par}, the contribution of the direct transitions is strongest at $h\nu = 428\,eV$ and decreases as the photon energy is raised to $h\nu = 1042\,eV$. By comparing the results obtained for $k_{par} = 0\,Å^{-1}$ and $k_{par} = 0.25\,Å^{-1}$ it can also be observed that the variation of the plotted ratio with temperature is slightly larger in the latter case. Therefore, the magnitude of the phonon-assisted contributions induced by the increase of both the temperature and the photon energy appears to be larger for $k_{par} = 0.25\,Å^{-1}$. This is in agreement with the idea that for a given combination of $h\nu$ and T, such non-direct transitions are more critical for values of k_{par} for which the band dispersion is more pronounced [31]. Finally, a different way of looking at the same effect is to consider the energy distribution curves at a given value of $h\nu$ and T, for different values of k_{par}. This is shown in Figures 2.23 and 2.24 for $h\nu = 428\,eV$ and $h\nu = 1042\,eV$ respectively. In doing so it should be remembered that the zone boundary along the probed high symmetry S direction is found at $k_{par} = 0.51\,Å^{-1}$, therefore the green plot shown in each of the images below belongs to the neighbouring zone. What appears to be clear is that for $h\nu = 428\,eV$ the spectra measured with T=20K, T=100K and T=215K can be directly compared with the band structure calculations [46], as the observed spectral features disperse in agreement with Figure 2.16. In particular, at the zone edge (blue plot) all of the five bands can be observed although the deeper lying one is seen only as a weak shoulder appearing on the high energy side of the spectrum. Nevetheless, at T=215K a direct comparison with the band structure is more difficult, as the underlying intensity of the non-direct contributions increases. For $h\nu = 1042\,eV$ the situation is different. At T=20K the direct transition features can still be distinguished but strong modifications of the line shape and of the relative intensities take place if compared to the equivalent spectra measured at $h\nu = 428\,eV$. On the other hand, the measurements taken with $h\nu = 1042\,eV$ and T=215K have lost most of their structure and are very similar for each value of k_{par}. If compared to the very recent results published in [56], where high energy angle-integrated photoemission measurements of the valence band of polycrystalline Ag are succesfully compared to the calculated bulk density of states, our results show that in the case of Ag ($\vartheta_D = 215\,K$), the transition from a band-like to a density-of states-like behaviour, called the XPS limit, is reached for $h\nu = 1042\,eV$ and T=215K.

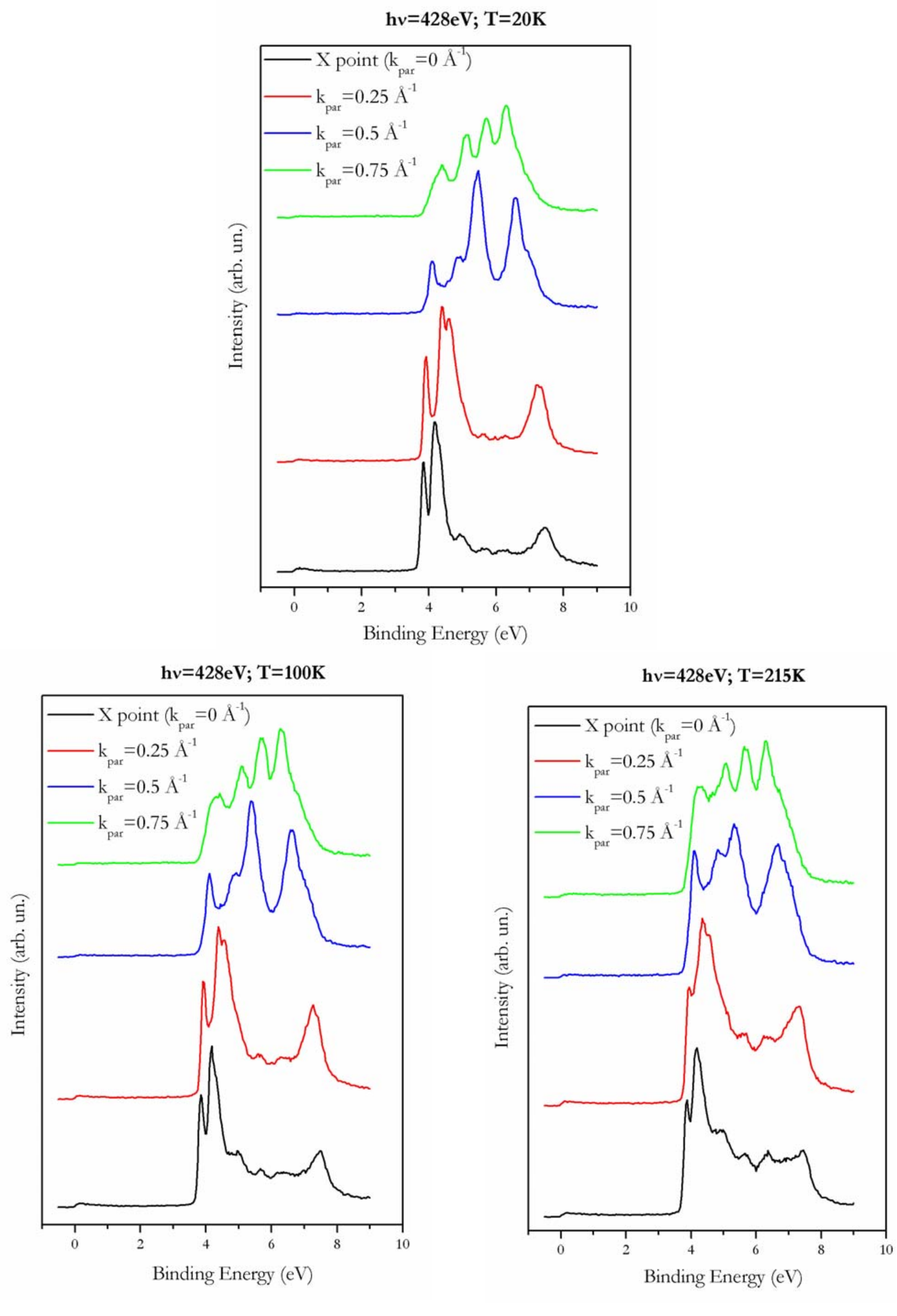

Figure 2.23: energy ditribution curves plotted as a function of k_{par}. Top: $h\nu = 428eV$ and T=20K. Bottom left: $h\nu = 428eV$ and T=100K. Bottom right: $h\nu = 428eV$ and T=215K. $E_F = 0eV$. The spectra are shifted vertically for clarity.

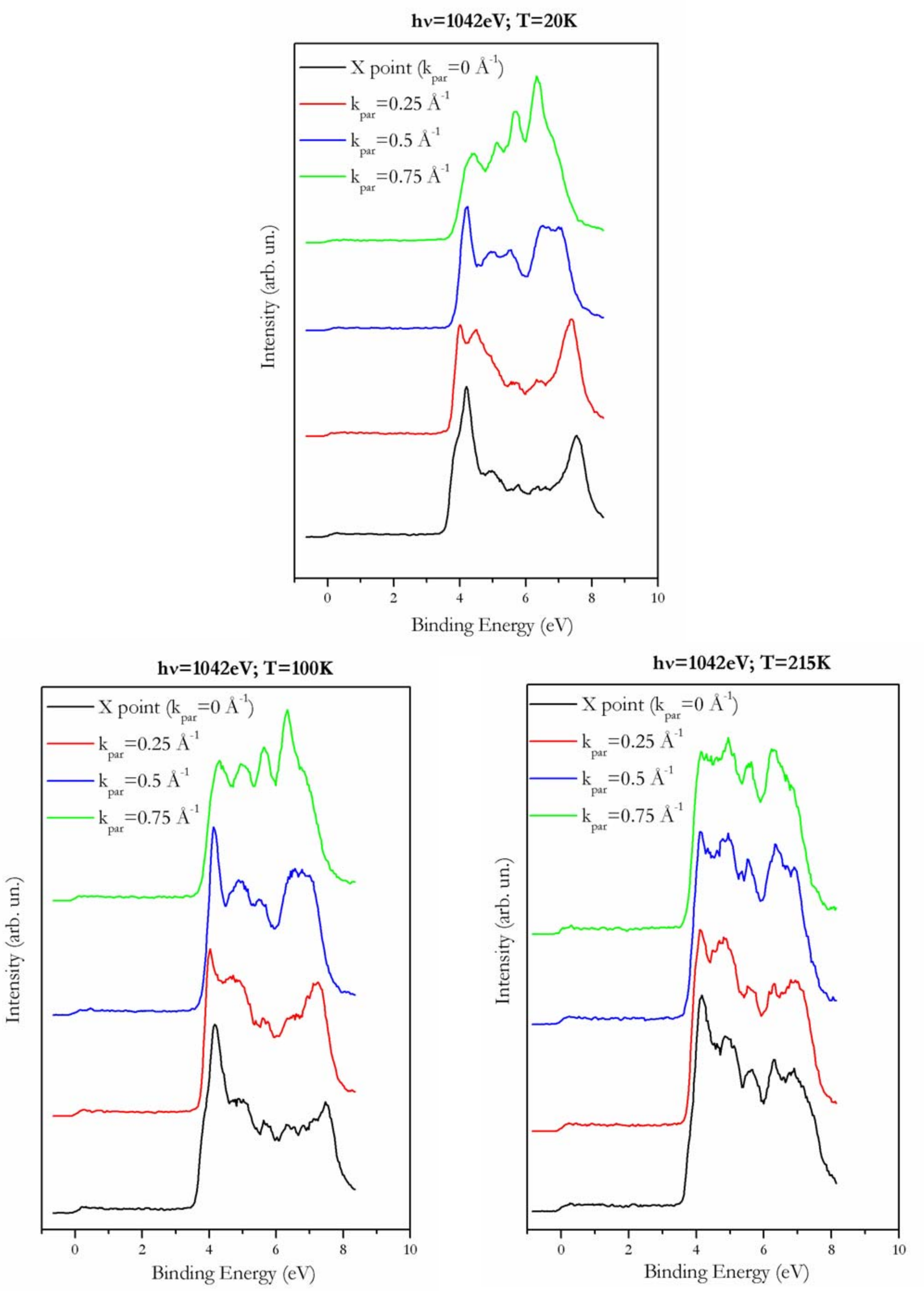

Figure 2.24: energy ditribution curves plotted as a function of k_{par}. Top: $h\nu = 1042eV$ and T=20K. Bottom left: $h\nu = 1042eV$ and T=100K. Bottom right: $h\nu = 1042eV$ and T=215K. $E_F = 0eV$.

The angle-resolved photoemission data presented so far show evidence of the fact that, for well-defined combinations of $h\nu$ and T, direct transitions in the soft X-ray regime can be observed. In particular, the simple direct transition model with a free-electron-like final state that takes into account the momentum of the incoming photon (see equation (2.18)) allows to accurately determine the values of $h\nu$ that correspond to the high symmetry points along the direction that is perpendicular to the sample's surface. The larger $\underline{k}$ -space sampling, if compared to the low energy application of the same technique, and the smaller $\underline{k}$ -space curvature as shown in Figure 2.6, together with the use of a two dimensional position sensitive detection system, allow measuring the band structure along specific high symmetry directions with a single measurement. This has been done for four different directions in $\underline{k}$ -space, namely the Δ, Σ, Z and S high symmetry directions belonging to the Brillouin zone of Ag. The results obtained at T=20K are in good agreement with both the relativistic band structure calculations presented in [46] and the low photon energy experimental results listed in Table 1.

The effects of phonon disorder have been investigated by measuring the same high symmetry direction, S, for three different values of $h\nu$ and T. For Ag, whose Debye-Waller temperature is $\vartheta_D = 215\,\mathrm{K}$, the XPS limit appears to be reached for $h\nu = 1042\,\mathrm{eV}$ and T=215K and accurate band mapping can only be performed in the low temperature and energy regime. For both $h\nu = 428\mathrm{eV}$ and $h\nu = 703\mathrm{eV}$ the direct transition peaks are visible up to $T = 100\mathrm{K}$ and a comparison with the theoretical band structure [46] is possible. At higher temperatures the contribution arising from the phonon-assited non-direct transitions increases and a general broadening of the spectral line shape, together with peak shifts of the order of 0.2eV, are observed in agreement with [31]. When probing the system with $h\nu = 1042\,\mathrm{eV}$ the phonon influence is dominant and even for T=20K an accurate determination of the direct transition peaks is difficult. Although our results suggest that equations (2.13) and (2.14) slightly underestimate the effect of phonon disorder, the simple model proposed in [23, 24, 25] gives a good qualitative description of its importance in interpretating angle-resolved photoemission spectra in the soft X-ray energy range. Therefore, relatively high energy and momentum resolution soft X-ray angle-resolved photoemission spectroscopy proves to be an accurate technique for sampling the electronic band structure of solids in the low temperature range, provided the value of the Debye-Waller temperature, that must not be too low, is taken into account. Nevertheless, even when the optimal experimental conditions are reached (in the study presented here $h\nu = 428\mathrm{eV}$ and T=20K) weak non $\underline{k}$ -conserving contributions are visible.

2.4 Exploiting the polarisation of the light.

In order to understand the role played by the polarisation of the incoming light in a photoemission measurement, it is necessary to consider the symmetry properties of the experiment. The symmetry operations for a given $\underline{k}$-point in the Brillouin zone form a point group, **G**. This point group is characterised by a set of so-called irreducible representations, which are used to classify the electronic states at $\underline{k}$. When neglecting the effect of spin-orbit coupling, these irreducible representations are also called single group representations, as they take into account only the spatial symmetries of the system and are used to distinguish the various electronic bands along a high symmetry direction. An arbitrary point in $\underline{k}$-space will have the lowest symmetry and the electronic states have no degeneracy other than the twofold spin degeneracy. The corresponding irreducible representations are one dimensional. At high symmetry points and directions, additional degeneracies may occur. These degenerate states are then characterised by representations of higher dimension. At the zone centre the symmetry and the degree of degeneracy are highest. The spatial symmetries (translation, reflection, rotation) of a crystal lattice enter the Hamiltonian of the system via the periodic potential, $V(\underline{r})$. The symmetry properties are therefore reflected in the electronic structure of the solid and the symmetry character of an electronic state can be used to treat the optical interband transitions by means of the dipole selection rules. Within the dipole approximation, the strength of a specific electronic transition is described by the matrix element:

$$\langle \psi_f | \underline{A} \cdot \underline{p} | \psi_i \rangle = \langle \psi_f | \underline{e} \cdot \underline{r} | \psi_i \rangle \tag{2.19}$$

where $\underline{A} \cdot \underline{p}$ is the electric dipole operator, $\underline{e}$ denotes the polarisation vector of the light and ψ_i and ψ_f represent the initial and final states respectively. In the non-relativisitc case, where the spin-orbit effects are neglected, the existence of this matrix element depends entirely on the spatial symmetry properties of the initial and final electron states in the solid and on the photon operator. This general principle can be translated into various sets of dipole selection rules for different lattice structures [57, 58]. In particular, for emission confined to a mirror plane containing the surface normal, the final state has even parity. This can be understood by considering the fact that at the detector the emitted electron is a plane wave with a momentum vector that lies in the mirror plane. Therefore, the final state has to be invariant under crystal symmetry operations that leave the surface component of the measured momentum unchanged. The determination of the initial state symmetry is based on the group theory result that the optical dipole matrix element (2.19) vanishes unless the integrand has an invariant component under the point group operations of the crystal. Therefore, if the symmetry of the final state is known, it is in principle straightforward to determine the corresponding symmetry of the initial state. In particular, if the final state has even parity, the initial state has to have the parity of the dipole operator with respect to the mirror plane. For a given experimental geometry the parity of the dipole operator is known and the symmetry of the initial states can therefore be determined. Furthermore, for normal emission along high symmetry directions the final state is totally symmetric under point group operations about the surface normal.

In reciprocal space the [001] direction is denoted as Δ and has C_{4V} symmetry. Its end points are given by the centre of the first Brillouin zone, Γ, and the zone edge at the high symmetry point X. The group C_{4V} has four irreducible representations, Δ^1, Δ^2, $\Delta^{2'}$ and Δ^5. These representations are one dimensional exception made for Δ^5 that is two dimensional. The non-relativistic selection rules for electrons emitted along the [001] direction are given in Table 3.

[001]	Δ^1	Δ^2	$\Delta^{2'}$	Δ^5
Δ^1	$\mathbf{e}_z$	-	-	$\mathbf{e}_x$, $\mathbf{e}_y$
Δ^2	-	$\mathbf{e}_z$	-	$\mathbf{e}_x$, $\mathbf{e}_y$
$\Delta^{2'}$	-	-	$\mathbf{e}_z$	$\mathbf{e}_x$, $\mathbf{e}_y$
Δ^5	$\mathbf{e}_x$, $\mathbf{e}_y$	$\mathbf{e}_x$, $\mathbf{e}_y$	$\mathbf{e}_x$, $\mathbf{e}_y$	$\mathbf{e}_z$

Table 3: dipole-allowed non-relativistic selection rules for emission along the [001] high symmetry direction in a cubic crystal. Left column (upper row) gives the symmetry of the initial (final) state. The polarisation vector is orientated normal ($\mathbf{e}_z$) or parallel ($\mathbf{e}_x$, $\mathbf{e}_y$) to the surface. The entry indicates the allowed transitions [64].

Outside the crystal, the electrons may be regarded as spherical waves, in order to be able to travel to the detector. The final state in the normal emission excitation process must therefore be of highest symmetry. Amongst the irreducible representations of the C_{4V} group, the Δ^1 representation is the most symmetric. According to Table 3, this practically limits the possible initial states for dipole excitation to Δ^1 or Δ^5, depending on whether the polarisation vector is normal or parallel to the surface. These selection rules essentially allow a distinction between states of Δ^1 and Δ^5 symmetry by simply varying the polarisation of the light. The inclusion of spin-orbit coupling reduces the symmetry of the electronic system, causing degenerate electronic states to split in energy. A different set of irreducible representations is therefore necessary to distinguish the electronic bands. These representations are taken from the relativistic double group, **DG**, that is formally obtained by multiplying the single point group, **G**, with the rotational group in spin space, i.e $\mathbf{DG} = \mathbf{G} \otimes \mathbf{SU}_2$. Whether or not the dipole selection rules have to be redifined has been a much debated matter [59, 60, 61]. In [59] an angle-resolved photoemission study has been performed on Ag(111); the authors conclude that relativistic dipole selection rules are essential for a consistent interpretation of the photoemission data, even for energy bands whose degeneracy is not affected by spin-orbit coupling and for elements with a low atomic number. The use of relativistic selection rules gives rise to a breakdown of the non-relativistic dipole selection rules [57, 58] derived with the single group formalism. As a consequence, transitions which are forbidden in the non-relativistic case may become allowed. Reference [59] is strongly criticised in [60] where it is shown that photoemission spectra from Cu(110), Cu(111), Ag(110) and Ag(111) can be understood with the use of non-relativistic selection rules, indicating that the symmetry behaviour is essentially determined by the spatial part of the wave functions. The validity of the non-relativistic selection rules has also been observed in [14, 62, 63], for Cu(110), Ni and Rh. In what follows we will see that in the case of Ag(001) the non-relativistic dipole selection rules appear to maintain their validity and only transitions between bands with an admixture of the allowed single group symmetries are possible. We will therefore keep the predominant single group representation and whenever the relativistic double group representation is necessary we will refer to it with a subscript. The connection between the non-relativistic and the relativistic representations is shown in Table 4 for the Δ and Σ high symmetry directions. The relativistic representations are shown in the right-hand columns. Figures 2.25 and 2.26 show normal emission spectra taken at $h\nu = 551\,\text{eV}$ and $h\nu = 698\,\text{eV}$ for horizontally, vertically and circularly polarised light. The plots represent direct transitions originating from different high symmetry points in $\underline{k}$-space along the [001] direction, namely at Γ and X.

[001]		[110]	
Δ^1	Δ_6^1	Σ^1	Σ_5^1
Δ^2	Δ_7^2	Σ^2	Σ_5^2
$\Delta^{2'}$	$\Delta_7^{2'}$	Σ^3	Σ_5^3
Δ^5	Δ_6^5	Σ^4	Σ_5^4
	Δ_7^5		

Table 4: connection between the single group and double group representations. For both the [001] and [110] high symmetry directions the non-relativistic single group representations are shown to the left [65].

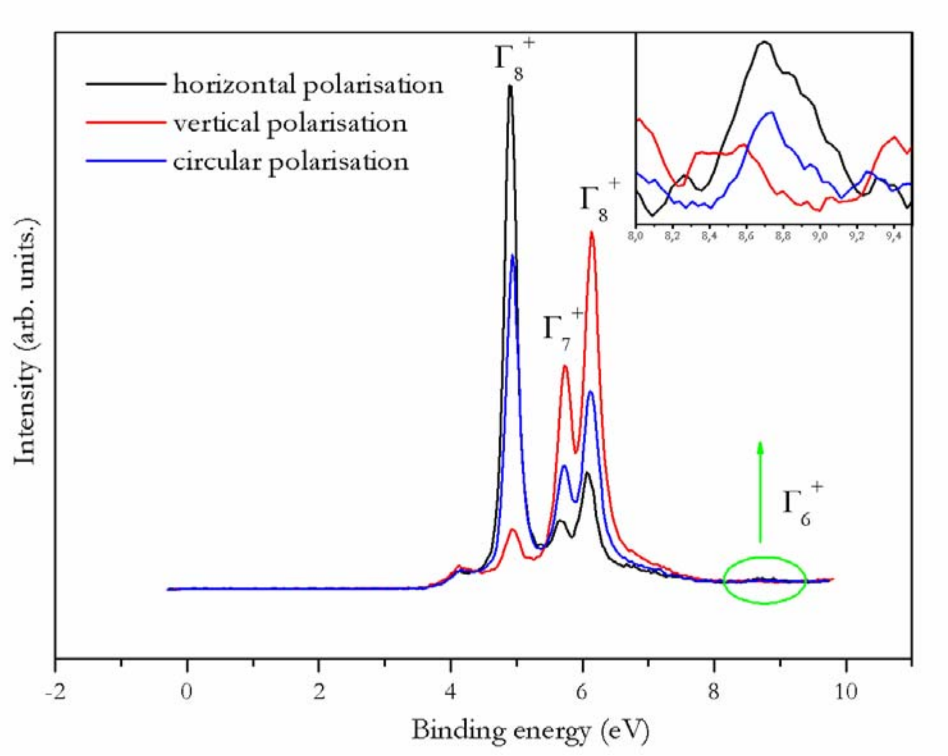

Figure 2.25: normal emission energy distribution curves measured at Γ for emission along the [001] high symmetry direction with $h\nu = 551\text{eV}$ and T=20K. The polarisation of the light is varied from vertical (red) to horizontal (black) to circular (blue). The inset shows a close up of the zone circled in green. $E_F = 0\text{eV}$.

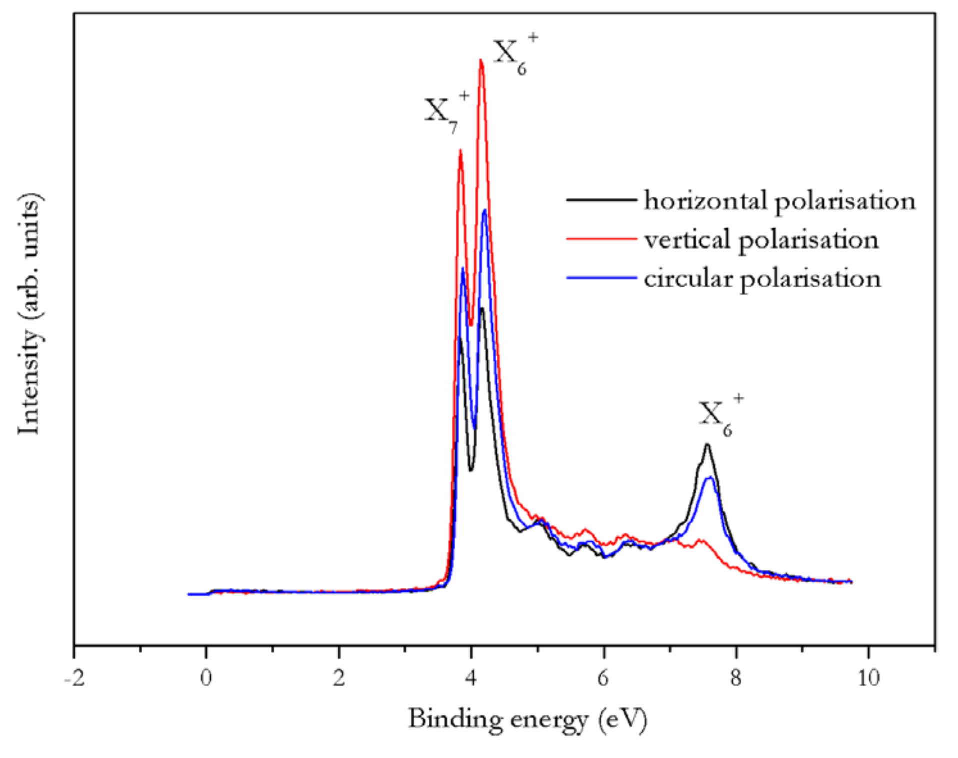

Figure 2.26: normal emission energy distribution curves measured at X for emission along the [001] high symmetry direction with $h\nu = 698\text{eV}$ and T=20K. The polarisation of the light is varied from vertical (red) to horizontal (black) to circular (blue). $E_F = 0\text{eV}$.

For $h\nu = 551\text{eV}$, the $\Gamma_{25}' \rightarrow \Gamma_8^+ + \Gamma_7^+$ spin-orbit splitting is clearly observed in Figure 2.25, regardless of the polarisation of the incoming light. From the experimental geometry sketched in Figure 2.7 it appears that only when the polarisation of the light is horizontal, does the polarisation vector have a component along the normal to the surface. In agreement with the non-relativistic selection rules listed in Table 3, the most intense features observed with vertically polarised light (red plot in Figure 2.25) have Δ^5 character and correspond to direct transitions originating from the Δ_6^5 and Δ_7^5 bands that disperse towards lower binding energies as the photon energy is varied from Γ to X. However, probably due to a relaxation of the selection rules caused by the finite angular acceptance of the electron analyser which allows off-normal emitted photoelectrons to contribute to the spectra, transitions arising from the Δ_6^1 states are also visible at a binding energy of 4.85 eV. Initial states with both Δ^1 and Δ^5 symmetry are probed when the polarisation of the light is horizontal (black plot) and the transition probabilites from the two initial states to the totally symmetric final state depend on the angle of incidence of the light with respect to the surface normal. Interestingly enough, in the horizontal polarisation measurement, a small contribution coming from the deep Γ_6^+ energy level is also observed at a binding energy of approximately 8.7 eV. Although this feature appears to be deeper than what is expected from the theoretical calculations in [46], we believe that this is the first time it is actually experimentally observed. Circularly polarised light can be regarded as a coherent superposition of two orthogonal linearly polarised plane waves with a phase shift of $\pi/4$. Therefore, when using circular polarisation, both the allowed initial states are probed as shown by the data plotted in blue. For $h\nu = 698\,\mathrm{eV}$ the energy resolution does not allow us to observe the smaller $X_5 \rightarrow X_6^+ + X_7^+$ spin-orbit splitting in Figure 2.26. In agreement with the non-relativistic selection rules, when probing with vertically polarised light, the intensity of the deeper lying X_6^+ level that has Δ_6^1 character is minimum, whereas the X_6^+ state found at approximately 4eV binding energy is enhanced due to its Δ_6^5 symmetry. As expected, when horizontally polarised light is used, initial states with Δ_6^1 symmetry are also probed, hence the intensity of the most strongly bound X_6^+ level increases at the expenses of the shallower one. The peak that is observed in Figure 2.26 at approximately 3.7eV binding energy originates from an initial state that has a Δ_7^2 symmetry in the double group representation. The apparent violation of the non-relativistic selection rules, that do not allow transitions originating from bands with Δ^2 or $\Delta^{2'}$ symmetry, can be explained by considering the changes in the band structure caused by the spin-orbit coupling [64, 65]. As can be seen in the non-relativistic band structure shown in Figure 2.27, along the Δ line two bands with Δ^2 and Δ^5 spatial symmetry are seen crossing (shown in red). These states originate from different spatial symmetries but belong to the same double group representation, namely Δ_7^2 and Δ_7^5. Under the influence of spin-orbit coupling bands of the same symmetry will avoid the crossing, leading to the formation of hybridisation gaps as shown in the bottom panel of Figure 2.27. As a consequence, throughout the hybridisation region the spatial symmetry of the band changes. The character of each of these two bands can therefore be seen as a mixture of Δ_7^2 and Δ_7^5 states, the ratio depending on the value of $\underline{k}$. This interpretation is confirmed by the calculations presented in [64, 65], where the fraction of a particular spatial symmetry contributing to a band along Δ is determined. In as much as one can imagine that only the Δ_7^5 states of the hybridised bands are excited, the observation of the intense low binding energy peak should not be considered as a weakening of the non-relativistic selection rules. The polarisation dependence of the structure that is visible between 4.7 and 7eV binding energy is very weak, further confirming the fact that these features originate from phonon-assisted transitions for whom the polarisation selection rules, that require $\underline{k}_{\text{par}}$ conservation, relax.

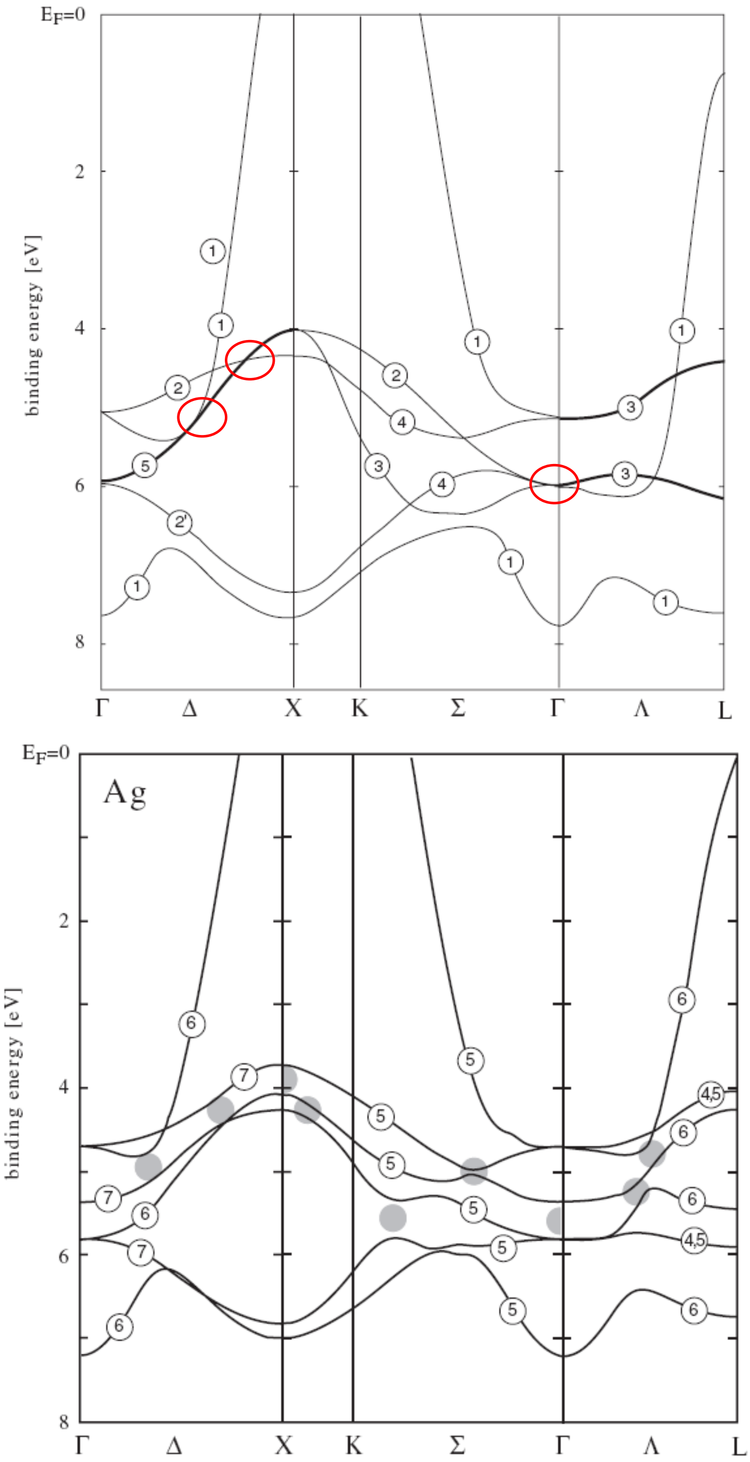

Figure 2.27. Top: non-relativistic band structure of Ag. The numbers indicate the single group labelling. The two-fold degenerate state Δ^5 is shown with a heavy line and the crossings of interest to us are circled in red. Bottom: relativistic band structure of Ag. The numbers indicate the double group labelling. The shaded circles indicate the location of the hybridisation gaps as mentioned in the text [65].

Figures 2.28 and 2.29 show angle-resolved data measured for emission belonging to the $\Gamma - X - W - K - W - X$ mirror plane and $h\nu = 551\,\text{eV}$, for vertically and horizontally polarised light respectively. The selection rules listed in Table 3 appear to maintain their validity even for small values of k_{par} centred around $k_{par} = 0\,\text{Å}^{-1}$. In particular, when probing with vertically polarised light, the two bands of Δ^5 symmetry, labelled Δ_7^5 and Δ_6^5 in the relativistic double group representation, are clearly visible and most intense. However, additional intensity corresponding to transitions arising from initial states of Δ_6^1 symmetry is also observed on both sides of the zone centre. This could either be due to the fact that when moving away from $k_{par} = 0\,\text{Å}^{-1}$ the normal emission selection rules relax and additional features appear, or to the hybridisation caused by the spin-orbit coupling between the Δ^1 and Δ^5 states (see crossing circled in red in Figure 2.27), in a similar way as to what has been briefly discussed above. In the case of horizontally polarised light, the majority of the photoemitted intensity is transfered to the initial states of Δ_6^1 symmetry and the Δ_7^5 and Δ_6^5 states, although much weaker, remain visible. In Figures 2.30 and 2.31 the results obtained with $h\nu = 551\,\text{eV}$ for emission in the $\Gamma - K - L - U - X$ plane are shown for both vertically and horizontally polarised light respectively. According to the relativistic selection rules, along the Σ high symmetry direction all the initial states may be observed without distinction [59]. On the contrary, the non-relativistic selection rules limit the allowed transitions [57, 58]. The results shown below indicate that the non-relativistic approach does, indeed, apply. In particular, for vertical polarisation, strong intensity originating from the Σ_5^3 and Σ_5^4 initial states is observed close to the zone centre, whereas for horizontally polarised light the intensity is transferred to the higher lying Σ_5^1 state. Nevertheless, forbidden transitions originating from initial states of Σ_5^2 symmetry are also observed and are circled in black in Figure 2.30 where they appear to be most intense. Again, this can be explained by considering the spin-orbit induced hybridisation gap at $k_{par} = 0\,\text{Å}^{-1}$. This initial state has previously been seen in [60], where the authors have related its observation to the non-zero width of the acceptance cone of the electron analyser. On the contrary, in [61] the observation of this peak is clearly considered as a result of the relaxation of the non-relativistic selection rules. However, it is important to emphasise that the strong intensity modulation observed as a function of the polarisation of the light in Figures 2.30 and 2.31 can only be explained within the non-relativistic approach.

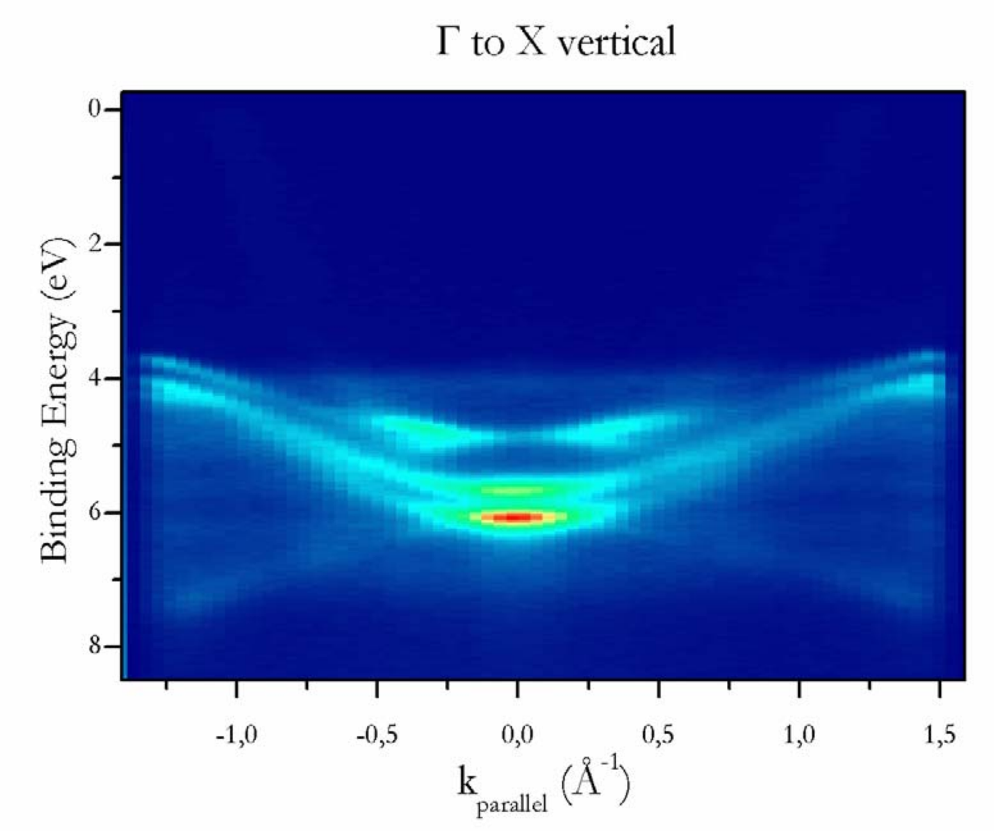

Figure 2.28: $\Gamma - X$ high symmetry direction (Δ) probed with vertically polarised light. $h\nu = 551\text{eV}$ and T=20K. For the colour map see Figure 2.12. $E_F = 0\text{eV}$.

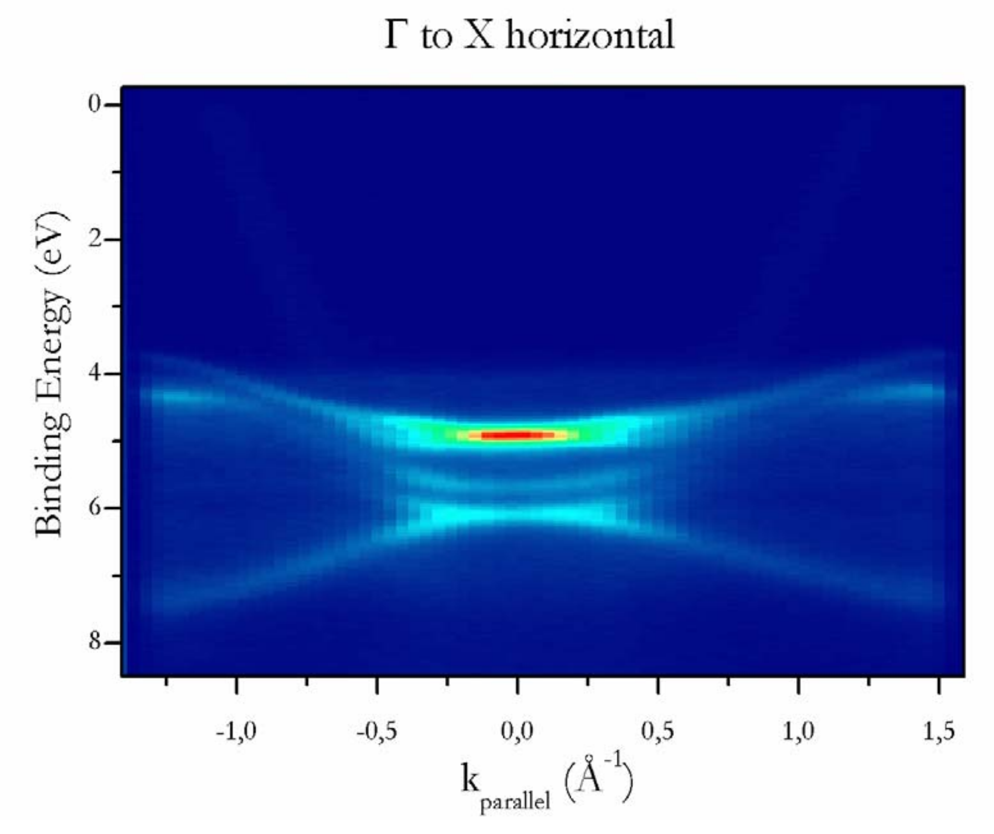

Figure 2.29: $\Gamma - X$ high symmetry direction (Δ) probed with horizontally polarised light. $h\nu = 551\text{eV}$ and T=20K. For the colour map see Figure 2.12. $E_F = 0\text{eV}$.

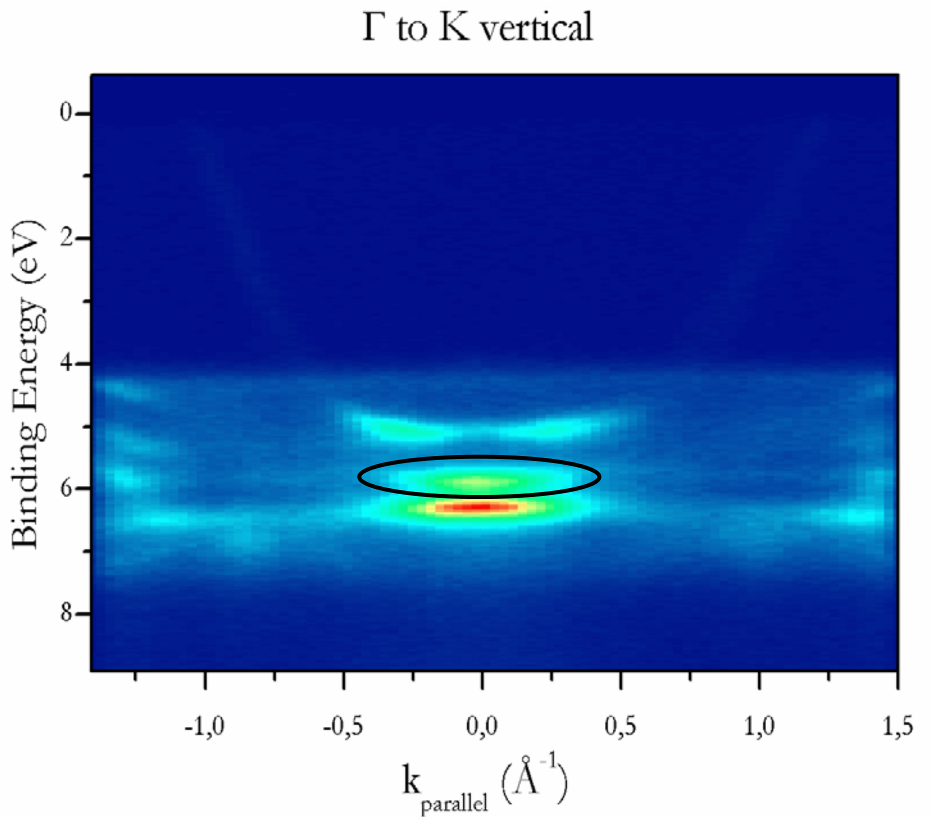

Figure 2.30: $\Gamma - K$ high symmetry direction (Σ) probed with vertically polarised light. $h\nu = 551\text{eV}$ and T=20K. For the colour map see Figure 2.12. $E_F = 0\text{eV}$. The black circle indicates the states of Σ_5^2 symmetry.

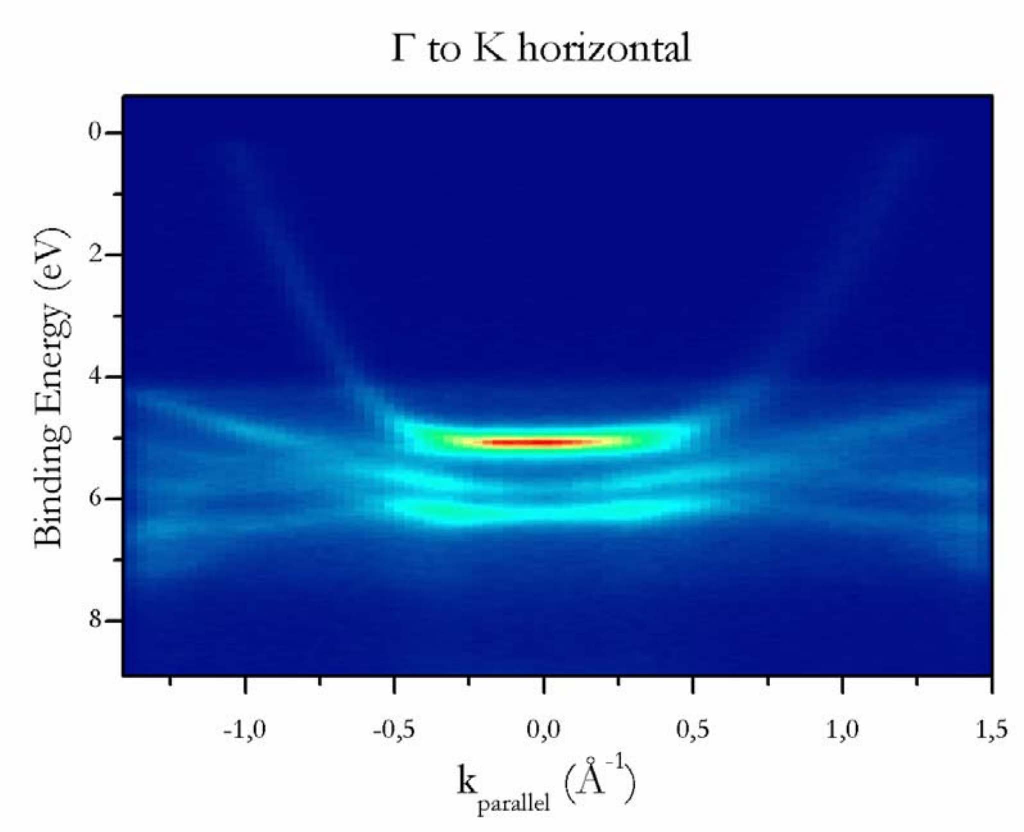

Figure 2.31: $\Gamma - K$ high symmetry direction (Σ) probed with horizontally polarised light. $h\nu = 551\text{eV}$ and T=20K. For the colour map see Figure 2.12. $E_F = 0\text{eV}$.

In agreement with [60], we therefore conclude that although the results presented in Section 2.3 can successfully be compared with band structure calculations that include the effect of spin-orbit coupling [46], the use of relativistic selection rules is not necessary. The non-relativistic selection rules do indeed show a certain degree of relaxation but, in our opinion, this can be explained by considering both the finite angular acceptance of the electron analyser and the spatial symmetry changes of the bands induced by the hybridisation. When the emission takes place in a mirror plane, as in the case of Figures 2.28, 2.29, 2.30 and 2.31, an additional relaxation of the normal emission selection rules should also be taken into account.

Finally, it is interesting to briefly introduce an example of circular dichroic effects in photoemission spectroscopy. In the broadest sense the term "dichroism" refers to the selective absorption of one of the two orthogonal polarisations of the light; circular dichroism (CD) then implies a differential absorption of right or left handed circular polarisation. Circular dichroism in photoemission or, more precisely, circular dichroism in the angular distribution of the photoelectrons (CDAD) from non-chiral species such as diatomic molecules, provided they are spatially oriented, was first predicted in [66]. Circular dichroism asymmetries are usually weak because they arise from the interference between the electric and the magnetic dipole transitions. If compared to common CD effects, a substantial difference is that CDAD occurs already in the pure electric dipole transition [67, 68]. Therefore the CDAD asymmetries are expected to exceed the normal CD asymmetries by orders of magnitude. In the low energy range, circular dichroism in the angular distribution of the photoelectrons has been observed for adsorbed molecules on transition metal surfaces [69, 70] and for clean graphite (0001), Pd(111) and Si(001) surfaces [71, 72]. As a general rule, circular dichroic effects appear when the system defined by the incoming light and the investigated sample exhibit a definite handedness that gives rise to an asymmetric response to photons of different helicity. In particular, the crucial handedness of the experimental set-up is defined via the non-coplanar spatial arrangement of the incoming photon beam, the momentum of the outgoing electron and the normal to the sample's surface. This is the case of our experimental geometry shown in Figure 2.7. In the reference frame of the crystal surface, the operator of circularly polarised light takes the form of:

$$O_{ph} = \underline{z}\sin 35^\circ + \underline{x}\cos 35^\circ \pm i\underline{y} \tag{2.20}$$

where $\psi = 35^\circ$ is the angle of incidence of the light with respect to the normal to the sample's surface. The incident photon beam will then exhibit a left or right circular polarisation depending on whether the last term in the expression (2.20) is added to or subtracted from the others. The matrix element that governs the interband transition induced by circularly polarised light therefore becomes:

$$\langle \psi_f | \underline{z}\sin 35^\circ + \underline{x}\cos 35^\circ \pm i\underline{y} | \psi_i \rangle \tag{2.21}$$

where ψ_i and ψ_f represent the initial and final states respectively. Without going into the details of the CDAD effect, let it be said that due to the $\pm$ sign in the dipole operator there are matrix elements that depend on the photon helicity. In particular, the matrix elements that are determined by the $\underline{y}$ -component of the photon operator will change sign when swithching from one helicity to the other causing the observed effect. An example is shown below in Figures 2.32 and 2.33. The data are taken at $h\nu = 698\,\text{eV}$ and $\varphi = 0^\circ$, with circular left and right polarised light respectively.

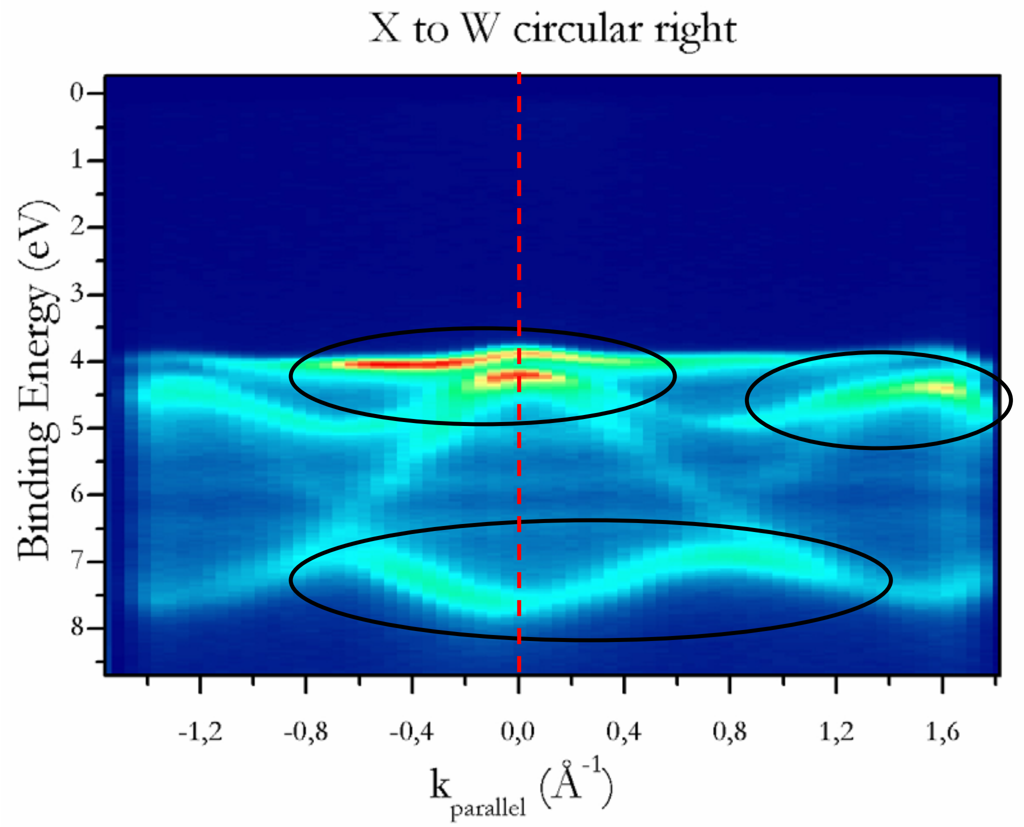

Figure 2.32: X - W high symmetry direction (Z) probed with circularly (right) polarised light. $h\nu = 698\text{eV}$ and T=20K. The areas of interest for the CDAD effect are circled in black. The red dashed line indicates the separation between positive and negative values of k_{par}. For the colour map see Figure 2.12. $E_F = 0\text{eV}$.

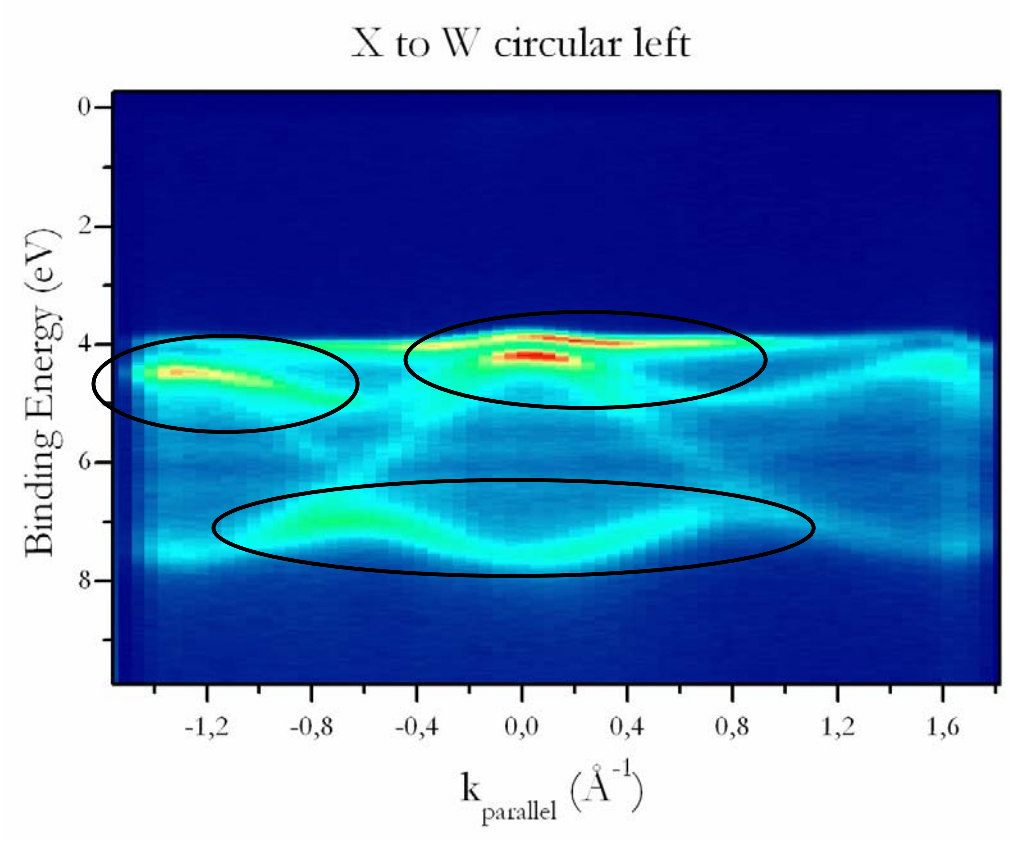

Figure 2.33: X - W high symmetry direction (Z) probed with circularly (left) polarised light. $h\nu = 698\text{eV}$ and T=20K. The areas of interest for the CDAD effect are circled in black. For the colour map see Figure 2.12. $E_F = 0\text{eV}$.

By comparing the two data sets a clear intensity modulation is shown upon switching the polarisation of the light, hence a dichroic effect is observed. The areas of interest are circled in black in the figures above. The distribution of the photoemitted intensity in the positive part of the emission plane in Figure 2.32 is equivalent to the intensity distribution obtained for negative values of k_{par} in Figure 2.33, showing that the dichroic effect is invariant upon application of the parity operator that changes both the photon helicity and the handedness of the vector arrangement. For the chiral experimental geometry shown in Figure 2.7 a reflection of the photoelectron momentum with respect to the normal to the sample's surface is equivalent to a change of photon helicity. Therefore, the dichroic effect can also be observed by comparing the results obtained, for a given polarisation, for both positive and negative values of k_{par} belonging to the same emission plane. To a much lesser extent an analogous effect has already been seen in Figure 2.10, where as the value of k_{perp} varies with the photon energy from above to below the Γ point along the [001] direction, the hot spot with maximum intensity close to the zone centre moves from one side to the other of the emission plane. If compared to the use of linearly polarised light circular dichroism in the angular distribution of the photoelectrons allows a more accurate determination of the initial state partial wave composition. The theoretical method described in [73] has very recently allowed J. Minár to obtain, to the best of our knowledge, the first calculations showing this effect. These results are shown in Figure 2.34, for the Z and S high symmetry directions respectively.

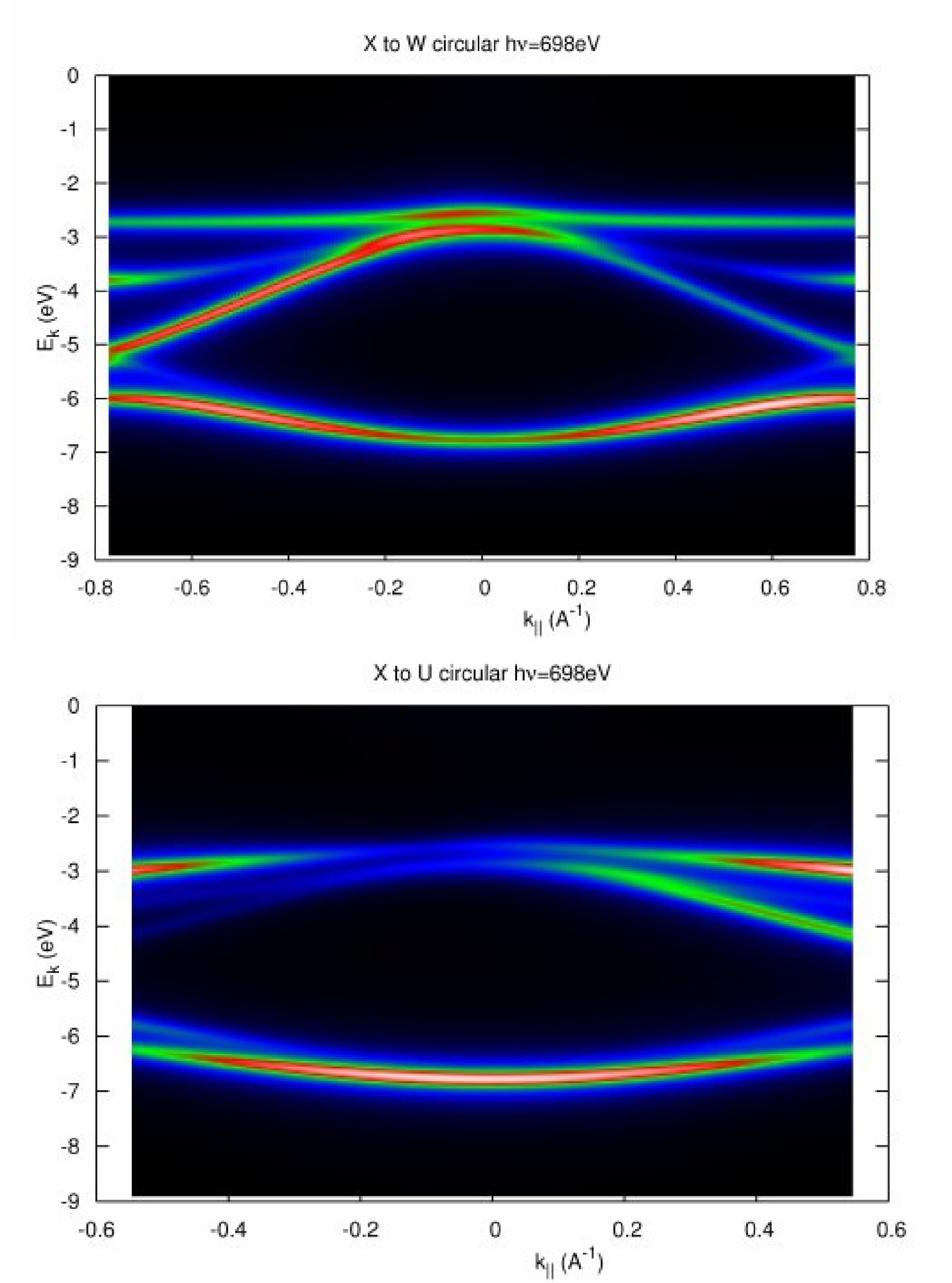

Figure 2.34. Top: calculated angle-resolved photoemission spectrum relative to the $X - W$ high symmetry direction (Z). $h\nu = 698\mathrm{eV}$. The colour map indicates the intensity: black and white are minimum and maximum intensity respectively. The intensity asymmetry typical of the CDAD effect is reproduced. $E_F = 0\mathrm{eV}$. Bottom: same as the upper panel but for the $X - U$ high symmetry direction (S).

The CDAD effect observed experimentally along the Z direction and shown in Figures 2.32 and 2.33, is reproduced in the top panel of Figure 2.34. The calculations relative to the S high symmetry direction show the same effect. From an experimental point of view, although an intensity asymmetry is difficult to see in Figure 2.15, it is clearly observed in Figures 2.17. The approximately 1eV binding energy shift that is observed with respect to the measurements is due to the fact that, although the code described in [73] allows for many-body correlation effects, such an implementation has not been used for these first theoretical results obtained for Ag, where the correlation effects are small but nevertheless present. A similar but larger discrepancy has recently been observed in [56] and is shown below in Figure 2.35.

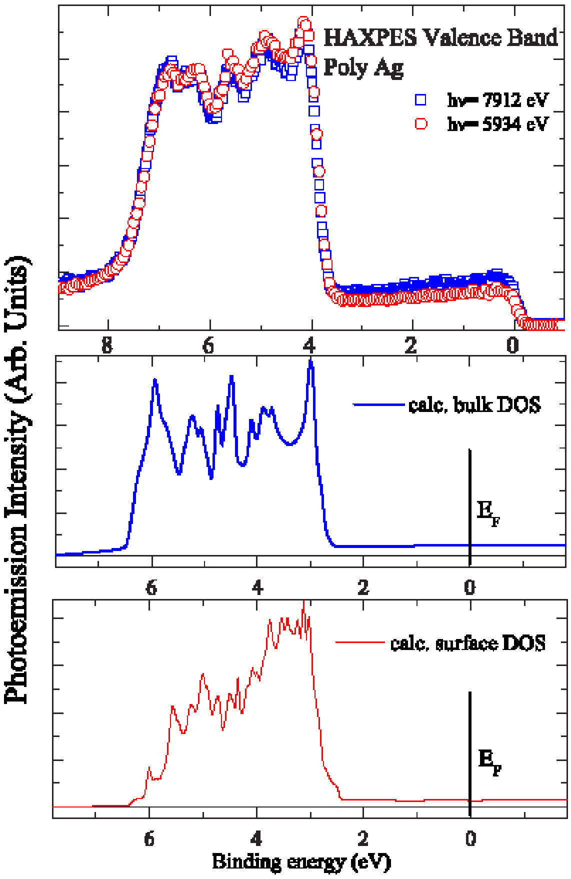

Figure 2.35. Top panel: angle-integrated valence band spectra of Ag measured at hν = 5934eV (red circles) and hν = 7912eV (blue circles). Middle panel: calculated bulk density of states. Bottom panel: calculated surface density of states [56]. The similarity between the top panel here and the bottom right panel of Figure 2.24 should also be noticed.

---

[1] G. D. Mahan, Phys. Rev. B **2**, 4334 (1970).

[2] P. J. Feibelman, D. E. Eastman, Phys. Rev. B **10**, 4932 (1974).

[3] C. N. Berglund, W. E. Spicer, Phys. Rev. **136**, A1030 and A1044 (1964).

[4] N. W. Aschroft, N. D. Mermin, *Solid State Physics*, Saunders College, Philadelphia (1976).

[5] S. Hüfner, *Photoelectron Spectroscopy*, 3rd edition, Springer (2003).

[6] D. Ehm, F. Reinert, G. Nicolay, S. Schmidt, S. Hüfner, R. Claessen, V. Eyert, C. Geibel, Phys. Rev B **64**, 235104 (2001).

[7] L. Duò, Surf. Sci. Reports **32**, 233-289 (1998).

[8] P. Heimann, H. Neddermeyer, H. F. Roloff, Phys. Rev. Lett. **37**, 775 (1976).

[9] N. V. Smith, Phys. Rev. Lett. **23**, 1452 (1969).

[10] N. V. Smith, Phys. Rev. B **3**, 1862 (1971).

[11] J. Stöhr, F. R. McFeely, G. Apai, P. S. Wehner, D. A. Shirley, Phys. Rev. B **14**, 4431 (1976).

[12] J. Stöhr, G. Apai, P. S. Wehner, F. R. McFeely, R. S. Williams, D. A. Shirley, Phys. Rev. B **14**, 5144 (1976).

[13] J. Stöhr, P. S. Wehner, R. S. Williams, G. Apai, D. A. Shirley, Phys. Rev. B **17**, 587 (1978).

[14] P. Thiry, D. Chandesris, J. Lecante, C. Guillot, R. Pinchaux, Y. Petroff, Phys. Rev. Lett. **43**, 82 (1979).

[15] Z. Hussain, S. Kono, L. G. Petersson, C. S. Fadley, L. F. Wagner, Phys. Rev. B **23**, 724 (1981).

[16] R. J. Baird, L. F. Wagner, C. S. Fadley, Phys. Rev. Lett. **37**, 111 (1976).

[17] L. F. Wagner, Z. Hussain, C. S. Fadley, R. J. Baird, Solid State Commun. **21**, 453 (1977).

[18] Z. Hussain, N. F. T. Hall, L. F. Wagner, S. P. Kowalczyk, C. S. Fadley, K. A. Thomson, R. L. Dodd, Solid State Commun. **25**, 907 (1978).

[19] O. B. Dabbousi, P. S. Wehner, D. A. Shirley, Solid Sate Commun. **28**, 227 (1978).

[20] F. R. McFeely, J. Stöhr, G. Apai, P. S. Wehner, D. A. Shirley, Phys. Rev. B **14**, 3273 (1976).

[21] G. Apai, J. Stöhr, R. S. Williams, P. S. Wehner, S. P. Kowalczyk, D. A. Shirley, Phys. Rev. B **15**, 584 (1977).

[22] P. S. Wehner, J. Stöhr, G. Apai, F. R. McFeely, D. A. Shirley, Phys. Rev. Lett. **38**, 169 (1977).

[23] N. J. Shevchik, J. Phys. C **10**, L555 (1977).

[24] N. J. Shevchik, Phys. Rev. B **16**, 3428 (1977).

[25] N. J. Shevchik, Phys. Rev. B **20**, 3020 (1979).

[26] R. W. James, *The optical principles of the diffraction of x-rays*, Ox Bow Press, Woodbridge (1982).

[27] R. S. Williams, P. S. Wehner, J. Stöhr, D. A. Shirley, Phys. Rev. Lett. **39**, 302 (1977).

[28] Z. Hussain, S. Kono, R. E. Connelly, C. S. Fadley, Phys. Rev. Lett. **44**, 895 (1980).

[29] Z. Hussain, C. S. Fadley, S. Kono, L. F. Wagner, Phys. Rev. B **22**, 3750 (1980).

[30] Z. Hussain, E. Umbach, J. J. Barton, J. G. Tobin, D. A. Shirley, Phys. Rev. B **25**, 672 (1982).

[31] R. C. White, C. S. Fadley, M. Sagurton, P. Roubin, D. Chandesris, J. Lecante, C. Guillot, Z. Hussain, Phys. Rev. B **35**, 1147 (1987).

[32] P. O. Nilsson, L. Ilver, H. I. Starnberg, D. S. L. Law, J Phys.: Condens. Matter **1**, 6159 (1989).

[33] R. C. White, C. S. Fadley, M. Sagurton, Z. Hussain, Phys. Rev. B **34**, 5226 (1986).

[34] H. Mårtensson, C. G. Larsson, P. O. Nilsson, Surf. Sci. **126**, 214 (1983).

[35] H. Mårtensson, P. O. Nilsson, Surf. Sci. **152/153**, 189 (1985).

[36] G. Jezequel, A. Barski, P. Steiner, F. Solal, P. Roubin, R. Pinchaux, Y. Petroff, Phys. Rev. B **30**, 4833 (1984).

[37] Ch. Søndergaard, Ph. Hofmann, Ch. Schultz, M. S. Moreno, J. E. Gayone, M. A. Vicente Alvarez, G. Zampieri, S. Lizzit, A. Baraldi, Phys. Rev. B **63**, 233102 (2001).

[38] Ph. Hofmann, Ch. Søndergaard, S. Agergaard, S. V. Hoffmann, J. E. Gayone, G. Zampieri, S. Lizzit, A. Baraldi, Phys. Rev. B **66**, 245422 (2002).

[39] M. A. Vicente Alvarez, H. Ascolani, G. Zampieri, Phys. Rev. B **54**, 14703 (1996).

[40] E. C. Snow, Phys. Rev. **172**, 708 (1968).

[41] N. E. Christensen, Phys. Stat. Sol. (b) **54**, 551 (1972).

[42] N. V. Smith, Phys. Rev. B **9**, 1365 (1974).

[43] O. Jepsen, D. Glötzel, A. R. Mackintosh, Phys. Rev. B **23**, 2684 (1981).

[44] A. H. MacDonald, J. M. Daams, S. H. Vosko, D. D. Koelling, Phys. Rev. B **25**, 713 (1982).

[45] R. L. Benbow, N. V. Smith, Phys. Rev. B **27**, 3144 (1983).

[46] H. Eckardt, L. Fritsche, J. Noffke, J. Phys. F: Met. Phys. **14**, 97 (1984).

[47] H. Becker, E. Dietz, U. Gerhardt, H. Angermüller, Phys. Rev. B **12**, 2084 (1975).

[48] G. V. Hansson, S. A. Flodström, Phys. Rev. B **17**, 473 (1978).

[49] P. S. Wehner, R. S. Williams, S. D. Kevan, D. Denley, D. A. Shirley, Phys. Rev. B **19**, 6164 (1979).

[50] R. Courths, V. Bachelier, S. Hüfner, Solid Sate Comm. **38**, 887 (1981).

[51] H. A. Padmore, C. Norris, G. C. Smith, C. G. Larsson, D. Norman, J. Phys. C: Solid State Phys. **15**, L155 (1982).

[52] R. Courths, H. Wern, U. Hau, B. Cord, V. Bachelier, S. Hüfner, J. Phys. F: Met. Phys. **14**, 1559 (1984).

[53] J. G. Nelson, S. Kim, W. J. Gignac, R. S. Williams, J. G. Tobin, S. W. Robey, D. A. Shirley, Phys. Rev. B **32**, 3465 (1985).

[54] S. C. Wu, C. K. C. Lok, J. Sokolov, J. Quinn, Y. S. Li, D. Tian, F. Jona, J. Phys.: Condens. Matter **1**, 4795 (1989).

[55] U. König, P. Weinberger, J. Redinger, H. Erschbaumer, A. J. Freeman, Phys. Rev. B **39**, 7492 (1989).

[56] G. Panaccione, G. Cautero, A. Fondacaro, M. Grioni, P. Lagovic, G. Monaco, F. Offi, G. Paolicelli, M. Sacchi, N. Stojić, G. Stefani, R. Tommasini, P. Torelli, J. Phys. : Condens. Matter **17**, 2671 (2005).

[57] J. Hermanson, Solid State Commun. **22**, 9 (1977).

[58] W. Eberhardt, F. J. Himpsel, Phys. Rev. B **21**, 5572 (1980).

[59] G. Borestel, M. Neumann, M. Wöhlecke, Phys. Rev. B **23**, 3121 (1981).

[60] A. Goldmann, D. Westphal, R. Courths, Phys. Rev. B **25**, 2000 (1982).

[61] G. Borestel, H. Przybylski, M. Neumann, M. Wöhlecke, Phys. Rev. B **25**, 2006 (1982).

[62] W. Eberhardt, E. W. Plummer, Phys. Rev. B **21**, 3245 (1980).

[63] G. Borestel, W. Braun, M. Neumann, G. Seitz, Phys. Status Solidi B **95**, 453 (1979).

[64] C. M. Schneider, J. Kirschner, Crit. Rev. Solid State Mater. Sci. **20**, 179 (1995).

[65] W. Kuch, C. M. Schneider, Rep. Prog. Phys. **64**, 147 (2001).

[66] B. Ritchie, Phys. Rev. A **12**, 567 (1975); **13**, 1411 (1976); **14**, 359 (1976); **14**, 1396 (1976).

[67] N. A. Cherepkov, Chem. Phys. Lett. **87**, 344 (1982).

[68] N. A. Cherepkov, V. V. Kuznetsov, Z. Phys. D **7**, 271 (1987).

[69] G. Schönhense, Physica Scripta **T31**, 255 (1990).

[70] G. H. Fecher, A. Oelsner, C. Ostertag, G. Schönhense, J. Electron Spectrosc. Relat. Phenom. **52**, 613 (1990).

[71] G. Schönhense, C. Westphal, J. Bansmann, M. Getzlaff, J. Noffke, L. Fritsche, Surface Science **251/252**, 132 (1991).

[72] K. Nakatsuji, H. Daimon, T. Furuhata, H. Takagi, M. Fujikawa, S. Suga, T. Miyahara, A. Yagishita, C. H. Solterbeck, W. Schattke, J. Electron Spectrosc. Relat. Phenom. **88-91**, 213 (1998).

[73] J. Minár, S. Chadov, H. Ebert, L. Chioncel, A. Lichtenstein, C. De Nadaï, N. B. Brookes, Nucl. Instrum. Meth. Phys. Res. A **547**, 151 (2005).

Chapter 3

3.1 Introduction

The unusual low temperature thermodynamic and transport properties of heavy Fermion Cerium (Ce) intermetallic systems [1, 2, 3, 4, 5], such as the enhancement of the resistivity, of the magnetic susceptibility and of the specific heat, are related to the intermediate character of the f states that, owing to the hybridisation with the conduction electrons, have both a localised and delocalised character. A description of the electronic properties of such heavy Fermion compounds is a complicated issue and, like in the case of single impurity systems or dilute magnetic ones, at temperatures that are higher than a characteristic temperature, T_K, they behave like ordinary magnetic systems while in the low temperature regime, when $T < T_K$, they usually exhibit a non-magnetic behaviour with large electronic masses. The partial delocalisation of the f electrons given by the hybridisation induces a reduction of the average ground state f occupation number, n_f, if compared to the unhybridised value of $n_f = 1$. As hybridisation takes place a decrease of the total energy of the system follows.

Resonant photoemission spectroscopy (RPES) at the Ce $4d \rightarrow 4f$ and $3d \rightarrow 4f$ edges, X-ray photoelectron spectroscopy (XPS) of the Ce 3d core levels, ultra-violet photoemission spectroscopy (UPS), inverse photoemission spectroscopy (IPES) and X-ray absorption spectroscopy (XAS) are powerful tools for probing the electronic structure of heavy Fermion Ce compounds and a deeper understanding of the spectroscopic results has been obtained as a result of numerical solutions of the single impurity Anderson Hamiltonian. In particular, the approach of Gunnarsson and Schönhammer (GS) [6, 7, 8, 9, 10] based on a T=0K perturbative expansion has been widely exploited. According to the single impurity Anderson model, the hybridisation of the highly correlated atomic-like 4f orbitals with the conduction electrons leads to a singlet non-magnetic ground state, which is separated by the Kondo energy, $k_B T_K$, from the magnetic $4f^1$ states. The presence of this singlet state is revealed in the excitation spectrum by a narrow resonance located close the Fermi level, E_F. This Kondo resonance influences the thermodynamic and transport properties and is responsible for the observed normalisation of the electronic mass, of the susceptibility and of the linear coefficient of the specific heat. Typical T_K values for these Ce-based materials go from a few Kelvin for poorly hybridised compounds with $n_f \approx 1$, to a few thousands of Kelvin for strongly hybridised systems with $n_f \approx 0.7 - 0.8$.

In the atomic-like limit the 4f states can be simply considered as weakly bound core levels. When the hybridisation between the 4f states and the band states is taken into account the total energy is lowered by a small energy, δ, that defines the Kondo temperature, $\delta = k_B T_K$. This mixing involves a decrease of the 4f count and the formation of band holes which must be concentrated within an energy range of δ above E_F in order to allow an energetically favourable hybridisation. In the sudden approximation the single impurity Anderson model allows to calculate the exact photoemission spectrum, both direct and inverse, in the limit of large degeneracy of the 4f level ($N_f \rightarrow \infty$) [6-10] and the modelling of the T=0K behaviour of the Ce 4f electrons with the single impurity Anderson model has provided numerical parameters that are much different than those previously expected [11, 12]. The values of the parameters, namely the ground state occupation number, n_f, the 4f level binding energy, ε_f, and the hybridisation strength, Δ, place all known metallic Ce materials in the Kondo regime so that the low energy and low temperature properties are controlled by spin fluctuations, with an energy scale set by the Kondo temperature, T_K. The distinction between the γ and α phase of Ce metal and of the many Ce materials whose properties mimic one or the other of the two phases can be understood by them having a low and high value of T_K respectively, and the Ce $\gamma - \alpha$ phase transition, with its large volume discontinuity, can be described as a Kondo volume collapse [13, 14]. However, as will be discussed in more detail below, whether or not a description of the 4f electrons in terms of the impurity model is appropriate has been a strongly debated issue.

3.2 The single impurity Anderson model.

Much of the theoretical discussion on Ce compounds has been based on the single impurity Anderson model where the 4f level of one atom and its interaction with the conduction states is taken into account. The single impurity model describes a N_f-fold degenerate local 4f orbital, with binding energy ε_f and f-f Coulomb repulsion U, that hybridises, via the hopping matrix V, with the band of conduction electrons. Within this model, the ground state is a singlet, where the magnetic moment of the 4f electrons is compensated by the spin of the conduction electrons. The single impurity Anderson Hamiltonian, that in principle is not adapted to account for coherence effects between the different 4f sites in a lattice, is explicitly given by [2]:

$$H = \sum_{k,\sigma} \varepsilon_{k,\sigma} a_k^+ a_k + \sum_{m,\sigma} \varepsilon_f a_{m,\sigma}^+ a_{m,\sigma} + \frac{U}{2} \sum_{m,\sigma,m',\sigma'} n_{m,\sigma}^+ n_{m',\sigma'} + \sum_{k,m,\sigma} \left(V_{k,m} a_{m,\sigma}^+ a_k + h.c \right) \qquad (3.1)$$

This Hamiltonian contains a conduction band with energy dispersion $\varepsilon_{k,\sigma}$ and an impurity level of degeneracy N_f characterised by the energy ε_f. U is the Coulomb correlation energy. $V_{k,m}$ is the hopping matrix element between the 4f orbital and the conduction state and a_k and $a_{m,\sigma}$ represent the destruction operators for the conduction and the 4f states respectively. The single impurity Anderson Hamiltonian (3.1) explicitly contains high energy scales (ε_f and U) corresponding to the $f^1 \to f^0$ and the $f^1 \to f^2$ charge fluctuations but it also exhibits a low energy Kondo scale, $\delta = k_B T_K$. In the infinite-U limit, when the interactions between 4f levels on different atoms are neglected, δ represents the energy gained by the hybridisation and is the energy separation between the hybrid singlet ground state and the pure magnetic $4f^1$ states. Figure 3.1 schematically shows the zero-temperature spectral function given by the single impurity Anderson Hamiltonian in the case of finite-U. The majority of the intensity of the spectral function displayed is concentrated in the two broad structures that reflect the high energy scale charge fluctuations: the first, at about ε_f in the photoemission spectrum, corresponds to the f^0 final states, the second structure, at about $\varepsilon_f + U$ in the inverse photoemission spectrum, corresponds to the f^2 final states. The bandwidth close to E_F is significantly renormalized giving rise to the narrow Kondo resonance and the spectral weight is very weak reflecting the nature of the heavy quasiparticles.

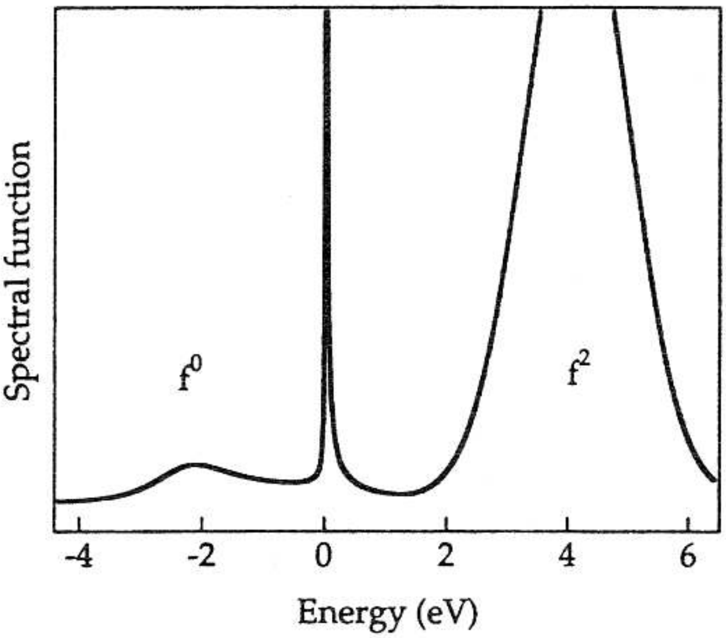

Figure 3.1: schematic form of the 4f spectral function of the finite-U Anderson impurity model [2].

An important refinement to the basic model comes from including the spin-orbit splitting of the ground state by defining two different values for the bare 4f energy, ε_f and $\varepsilon_f + \Delta_{S.O.}$, corresponding to the $j=5/2$ and $j=7/2$ levels. Due to the finite hybridisation with the conduction states the degeneracy of the $j=5/2$ spin-orbit multiplet is lifted and a singlet state, the Kondo ground state, is stabilized at an energy δ from the $f^1_{5/2}$ state. A singlet state is also formed from the $j=7/2$ multiplet, but its contribution to the ground state is small and neglected in the following. The ground state of the single impurity Anderson model can therefore be regarded as a linear combination of the f^0 and the $f^1_{5/2}$ states. When one electron is removed due to the photoemission process, several 4f final states need to be considered: the f^0 final state, which is the so-called poorly-screened state, and the well screened $f^1_{5/2}$ and $f^1_{7/2}$ final states which correspond to the tail of the Kondo resonance and its spin-orbit partner respectively. Such peaks can be observed in the Ce 4f photoemission spectra and a schematic diagram of the single impurity Anderson model is given in Figure 3.2. One can go a step further and include the splitting of the $f^1_{5/2}$ and $f^1_{7/2}$ states in the crystal field causing an even further reduction of N_f. Obviously, when model calculations including both types of interactions are fitted to the spectra, more realistic values of the low energy scale that characterises the ground state are obtained.

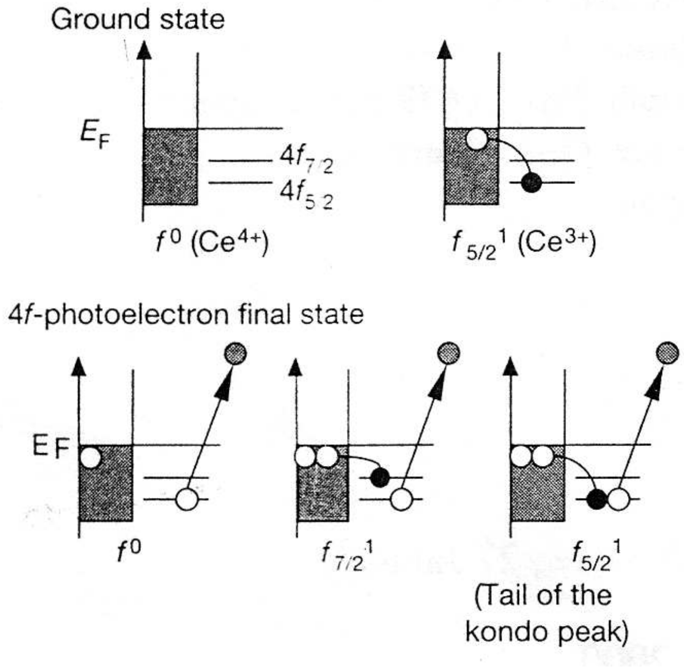

Figure 3.2: schematic representation of the single impurity Anderson model. Filled and open circles represent the electron and the hole respectively while shaded circles stand for the outgoing photoelectron [23].

Figure 3.3 shows the evolution of the spectral function when the spin-orbit and the crystal field interactions are successively activated in the model calculations. The striking feature in this figure is the weight transfer from the Kondo resonance to the higher component, $f^1_{7/2}$, when the spin-orbit interaction is included. The activation of the crystal field is not observed at the energy scale of curve (c).

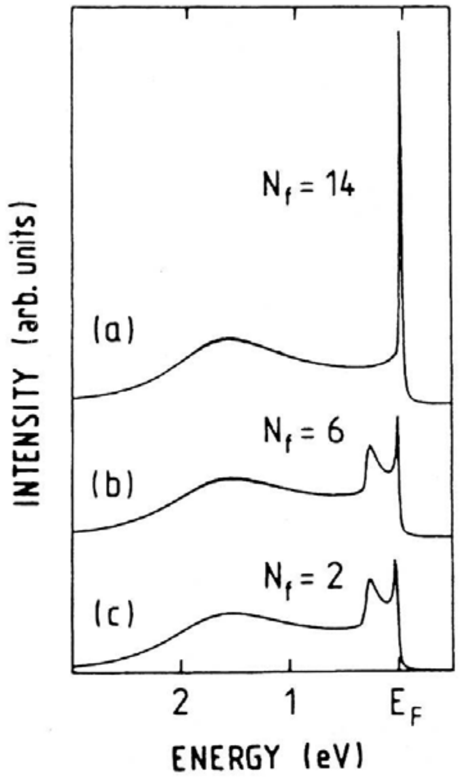

Figure 3.3: evolution of the 4f-spectral function calculated within the GS model. a) without spin-orbit interaction. b) with spin-orbit interaction. c) with spin-orbit and crystal field interaction [38].

In the calculations shown in Figures 3.1 and 3.3, T=0K has been implicitly assumed. However, the physical and spectral properties described by single impurity Anderson model exhibit a characteristic temperature dependence; most importantly, the model predicts the smearing out of the Kondo resonance for $T > T_K$. Therefore, if the measuring temperature is of the order of, or larger than, T_K the experimental data cannot be accurately compared to zero-temperature calculations. In order to make a valuable comparison between theory and experiments it is important to investigate the influence of finite temperature on the spectral function. As a general rule, the hybridised singlet ground state is destroyed by thermally activated spin fluctuations and T_K is a measure of the energy required to break up the singlet. When the temperature increases above T_K the magnetic $f^1_{5/2}$ states, located at an energy $\delta = k_B T_K$ above the singlet ground state, are populated, hence the 4f electrons gain in localisation and a local moment appears. The T=0K approach of Gunnarsson and Schönhammer (GS) is unable to describe the cross-over from the low temperature behaviour to the high temperature localised 4f regime. An alternative approach, the non-crossing approximation (NCA), gives the possibility to perform finite temperature calculations [15, 16]. Figure 3.4 shows the temperature dependence of the 4f spectral function calculated by the non-crossing approximation [16] in the infinite-U limit and with negligible crystal field splitting. The calculation takes into account the spin-orbit interaction of the 4f orbitals therefore, in addition to the Kondo resonance, two replicas associated with the $f^1_{7/2}$ final state appear away from the Fermi level. As already mentioned, with increasing temperature the $f^1_{5/2}$ magnetic states are progressively populated. Since these states are coupled in inverse photoemission spectroscopy (addition of an electron) only to the f^2 final states, the intensity of the Kondo resonance is reduced. A parallel evolution is observed for the spin-orbital side band. On the other hand, the spin-orbit satellite in the photoemission part of the spectrum has a smaller temperature dependence.

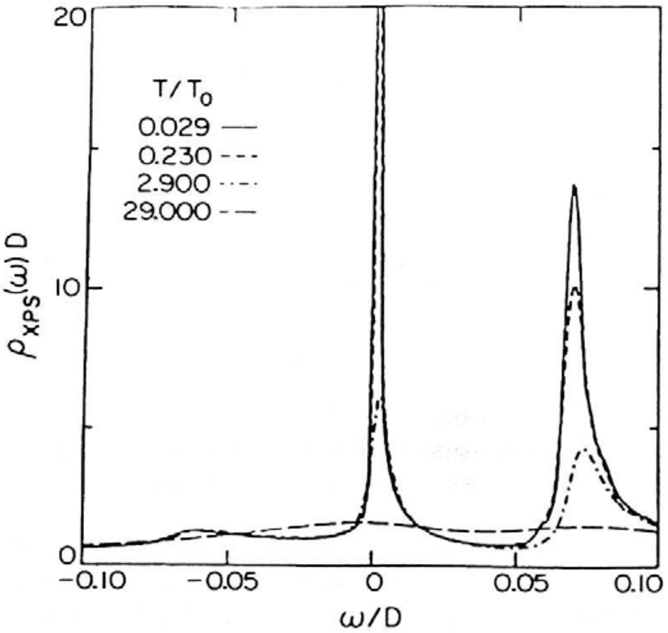

Figure 3.4: temperature dependence of the 4f spectral function in the NCA approximation for different values of T/T_0 where T_0 is the Kondo temperature [16].

The simple N+1 and N-1 electron energy diagrams shown in Figure 3.5 illustrate that in the low energy range two different final states exist [2], both of which correspond to the $4f^1$ structure that appears close to the Fermi level in the photoemission spectrum: the singlet hybridised $4f^0 - 4f^1$ states and the non-hybridised magnetic $4f^1$ states. The different couplings of these two final states with the initial state are responsable for the different temperature dependences observed for direct and inverse photoemission spectroscopy. Photoemission spectroscopy corresponds to the removal of one electron. At T=0K, where only the hybrid ground state $\psi = c_0 f^0 + c_1 f^1$ is occupied, only final states containing a $4f^0$ contribution can be reached and the structure that appears near the Fermi level has a spectral weight given by $(c_1 c_0)^2$. With increasing temperature the hybrid ground state is destroyed in favour of the pure magnetic states that are progressively populated. Since these states have a pure $4f^1$ character (i.e $c_1 = 1$), they too are coupled to the hybridised final states, but with a weight given by c_0^2.

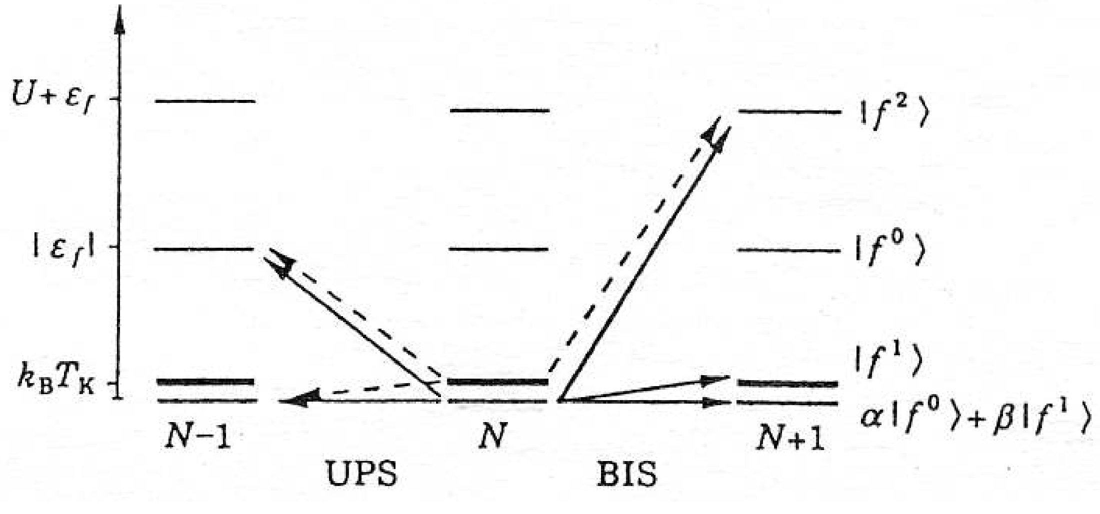

Figure 3.5: schematic energy diagrams of a Ce impurity in the initial (N) and the final states of photoemission (N-1) and inverse photoemission (N+1) [2].

In the Kondo limit ($n_f \approx 1$) c_1 is close to unity and c_0 is very small. Therefore, in this limit, only a weak temperature dependence is expected. In fact, since $c_0 > c_1 c_0$, the total integrated spectral weight of the $4f^1$ structure should very slightly increase with increasing temperature. This is associated with the diminishing of the resonance's height and the broadening of the spectrum as can be seen in Figure 3.4. In inverse photoemission spectroscopy the situation is different. Because of the addition of an electron, transitions are possible between the $4f^0$ part of the ground state and the $4f^1$ part of the final states. Therefore, the ground state is coupled to both the low energy final states, since they both have $4f^1$ character. On the contrary, because of its pure $4f^1$ character, the thermally populated ground state only contributes to the higher energy $4f^2$ final state. Therefore, with increasing temperature the hybridised ground state is depopulated in favour of the magnetic states and in the inverse photoemission spectrum the spectral weight is transferred from the $4f^1$ to the $4f^2$ final state structure.

3.3 Surface and hybridisation effects in Ce compounds.

It is a well known fact that the surface represents an important perturbation to the electronic structure of rare-earth materials. This is particularly the case for Ce and its compounds [17]. Despite the numerous studies and the generally acknowledged fact that the low energy properties of these systems are successfully described by the single impurity Anderson model, the interpretation of the experimental data in terms of the model is not universally accepted. In particular, the photoemission spectra of several Ce compounds measured at the $4d \rightarrow 4f$ edge show some discrepancies with the single impurity model calculations whose parameters are generally obtained from more bulk sensitive techniques such as X-ray photoelectron spectroscopy and inverse photoemission spectroscopy. Since the photon energy at the $4d \rightarrow 4f$ threshold is low, resonant photoemission at this edge is a rather surface sensitive technique and the discrepancy between an experimental resonant photoemission spectrum and a theoretical one can be understood in terms of surface effects. However, when the change of the electronic configuration at the surface is taken into account, consistency between theoretical and experimental results in regained. In this context, as the mean free path of the outgoing photoelectrons increases with increasing photon energy [18], resonant photoemission spectroscopy at the $3d \to 4f$ edge is a more appropriate tool for examining the bulk electronic structure of Ce compounds.

A typical manifestation of these surface-related changes in the electronic structure of rare-earth compounds is the lowering of the core level binding energies, the so-called surface core level shift (SCS), a general phenomenon that is directly related to the reduced cohesive energy at the surface with respect to the bulk. Surface effects have been observed in the 4f valence band spectra of Ce and its compounds [19, 20, 21]. However, unlike in heavy rare-earths, the surface changes of Ce and its compounds are not only driven by the usual surface core level shifts but also by a decrease at the surface of the 4f hybridisation with the delocalised conduction band. The existence of important surface effects was first demonstrated in [19] where an X-ray photoelectron spectroscopy investigation of three rather strongly hybridised ($\alpha-\text{like}$) compounds is shown. A significant modification of the Ce 3d core spectra is observed when the surface sensitivity is modified by varying the kinetic energy of the outgoing photoelectrons or their emission angles. A similar variation of the Ce 3d core spectra as a function of the incoming photon energy is observed in [20]. Finally, the comparison between resonant photoemission spectroscopy measurements of the valence band of metallic Ce taken at the $4d \to 4f$ and $3d \to 4f$ resonances [21], confirms the tendency of $\alpha-\text{like}$ materials to form weakly hybridised surfaces. In particular, in [21] it is observed that the spectral signature of the surface of $\alpha-\text{Ce}$ is similar to the signal given by $\gamma-\text{Ce}$. On the contrary, the bulk spectra of the two systems differ and the one relative to $\alpha-\text{Ce}$ is indicative of a highly hybridised material. These measurements directly reflect a $\gamma-\text{like}$ character of the surface of $\alpha-\text{Ce}$ and a far more hybridised bulk than previously assumed, when surface effects were not considered. These conclusions are further confirmed by the resonant photoemission results published in [22] for CeAl, a weakly hybridised compound, and $\gamma-\text{Ce}$, a more strongly hybridised system. Here, again, the two $d \to 4f$ thresholds are investigated and the larger surface sensitivity at the 4d edge results in a decrease of the coherent $4f^1$ intensity near the Fermi level. The more localised character of the surface 4f states is also shown in [23] where the $4d \to 4f$ resonant photoemission spectra of CeRu_2 ($T_K \approx 1000\text{K}$) and CeRu_2Si_2 ($T_K \approx 22\text{K}$) show a prominent $4f^0$ peak if compared to the respective $3d \to 4f$ spectra that reflect the more strongly hybridised character of the bulk. The detailed high resolution spectra of the near-E_F region confirm the fact that, despite the very different values of T_K, the two different compounds exhibit similar surface signals and very different bulk ones. This reflects the $\gamma-\text{like}$ character of the surface of $\alpha-\text{like}$ Ce compounds as already discussed above. Similar conclusions can also be found in [24] for CeNi_2 ($T_K \approx 500\text{K}$). The authors of [23] also conclude that the single impurity Anderson model finds its limit with increasing hybridisation. The bulk 4f spectral line shape of the strongly hybridised compound $\mathrm{CeRu_2}$ is in fact rather surprising as it is inconsistent with the predictions of the model. In contrast to such predictions, the spectrum seems to represent an itinerant 4f band character due to the very strong hybridisation that takes place with the conduction electrons, a situation that goes beyond the impurity model's framework. On the contrary, a subsequent investigation [48] shows that the bulk sensitive resonant photoemission spectra of extremely $\alpha-$like Ce compounds such as $\mathrm{CeRh_x}$ $(x = 2, 3)$ and $\mathrm{CeNi_x}$ $(x = 2, 5)$ are inconsistent with band structure calculations.

3.4 The Ce 4f electronic states in the iso-structural compounds $\mathrm{CeCu_2Ge_2}$, $\mathrm{CeNi_2Ge_2}$, and $\mathrm{CeCo_2Ge_2}$.

The aim of this study is to obtain a better understanding of the Kondo behaviour of three iso-structural heavy Fermion Ce compounds, namely $\mathrm{CeCu_2Ge_2}$, $\mathrm{CeNi_2Ge_2}$ and $\mathrm{CeCo_2Ge_2}$. The investigated systems are single crystalline samples that have been prepared by Prof. P. C. Canfield from Ames Laboratory, Iowa State University. These ternary systems belong to a wide class of Ce compounds that crystallize in the $\mathrm{ThCr_2Si_2}$ structure having a body centred tetragonal lattice as shown in Figure 3.6 for $\mathrm{CeNi_2Ge_2}$, the transition metal atoms being tetrahedrally coordinated to both the Ce and Ge atoms [25]. In passing from $\mathrm{CeCu_2Ge_2}$ to $\mathrm{CeNi_2Ge_2}$ to $\mathrm{CeCo_2Ge_2}$ only the transition metal is varied, favouring the analysis of the f-d mixing and the comparison of the experimental results with the theoretical predictions. The values of the lattice constants obtained by X-ray diffraction data are shown below in Table 1 [26]. Ce-based ternary compounds that crystallise in the $\mathrm{ThCr_2Si_2}$ structure include a variety of heavy Fermion systems with different ground states. For instance, $\mathrm{CeCu_2Si_2}$ was the first compound reported to exhibit heavy Fermion superconductivity [27]. Magnetic, calorimetric and transport measurements [28] characterise $\mathrm{CeCu_2Ge_2}$ as a system that undergoes a transition into a magnetically ordered ground state before a heavy Fermi liquid phase is completely built up. On the contrary, similar measurements carried out on $\mathrm{CeNi_2Ge_2}$ [29] show that this system exhibits a heavy Fermion ground state that is neither magnetic nor superconducting. So far, very little work has been done on $CeCo_2Ge_2$. From [30], this compound is believed to exhibit a Fermi liquid ground state below $T = 20\,K$. Therefore, for both $CeNi_2Ge_2$ and $CeCo_2Ge_2$ it is thought that the Kondo effect dominates the Ruderman-Kittel-Kasuya-Yoshida (RKKY) interactions, favouring a non-magnetic ground state. The values of T_K can be obtained from the temperature dependence of the quasielastic linewidth as observed in inelastic neutron scattering experiments and the measured values of T_K for $CeCu_2Ge_2$ and $CeNi_2Ge_2$ are reported below in Table 2 [29, 31]. To our knowledge, the value of T_K for $CeCo_2Ge_2$ has not been determined but from [30] we can assume it to be approximately 120 K.

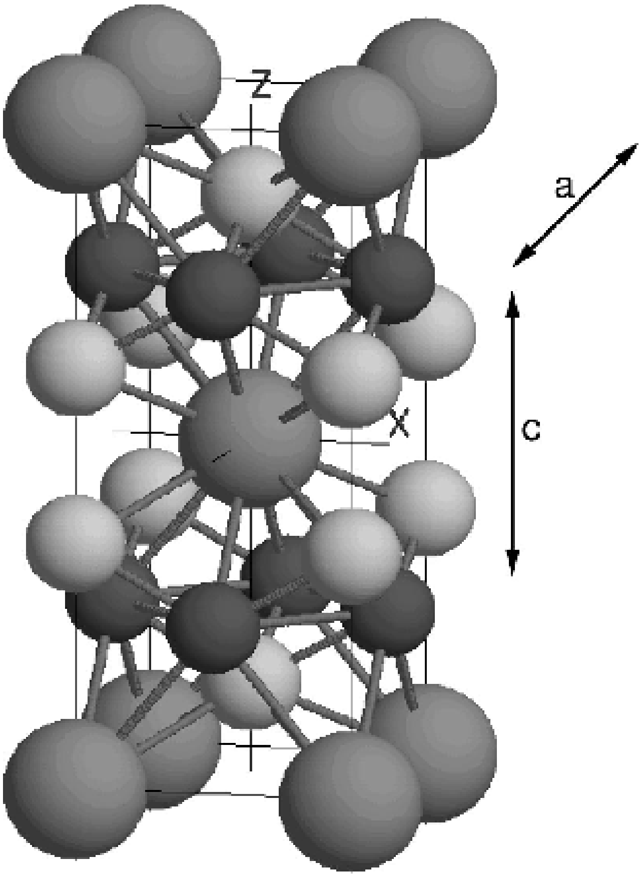

Figure 3.6: crystal structure of $CeNi_2Ge_2$. Ce, Ni and Ge atoms are shown in medium, dark and light grey respectively. x and z indicate the crystal axes and a and c are the lattice constants in the respective directions.

	a (Å)	c (Å)
$CeCu_2Ge_2$	4.16	10.23
$CeNi_2Ge_2$	4.15	9.85
$CeCo_2Ge_2$	4.07	10.17

Table 1: lattice constants, a and c, for the three investigated samples [26].

	$T_K (K)$
$CeCu_2Ge_2$	4
$CeNi_2Ge_2$	30
$CeCo_2Ge_2$	120

Table 2: measured [29, 31] and estimated [30] values of T_K.

As already described in Chapter 1, before entering the ultra-high vacuum system the samples are prepared in air. Each sample is mounted onto an Al plate with a conductive and vacuum compatible glue. Prior to the introduction into the experimental system, a small post is glued onto the sample surface in order to allow its cleavage along a known crystallographic axis. Added to this, a colloidal dispersion of fine graphite in acetone is painted around the sample itself, in order to minimize the possibility of measuring signals coming from other parts of the sample holder. The Fermi level of the measured sample is referred to a polycrystalline Au sample mounted on the Al plate. Figure 3.7 shows a photograph of a measured sample. The cleaved sample can be seen in the centre of the Al plate and the black area around it is the graphite solution. The Al plate is screwed onto a Cu sample holder and introduced into the main chamber via a three step process that takes the samples from air into the load-lock, from the load-lock into the preparation chamber and finally from the preparation chamber into the main chamber where the photon beam arrives and the Scienta SES 2002 electron analyser is mounted. The temperature is controlled by means of a liquid He cryostat connected to the sample manipulator and a heater. A diode positioned near the sample measures its temperature. Several additional screws on the sample manipulator itself ensure good thermal contact and the angular degrees of motion relative to the azimuthal angle φ and the tilt angle, β. The *in situ* cleaving of the single crystal is performed at low temperature ($T = 20\,K$) in order to minimize the diffusion of impurities from the bulk to the surface, although for these samples this does not seem to have been a problem. Because of the high reactivity of Ce, the experiments are performed under ultra-high vacuum conditions and the pressure is kept stable throughout the measurements, with $P < 1*10^{-10}\,\mathrm{mbar}$.

Figure 3.7: photograph of a measured sample. The Au foil that is used as a Fermi level reference is glued to the top part of the Al plate, whose dimensions are 18mm x 13mm. The post (bottom right) is attached to the sample holder, in order to avoid it falling into the UHV chamber once the cleave has taken place.

The presence of carbon and oxygen contamination is monitored with core level and Auger photoemission spectroscopy and the data are collected until noticeable contamination is visible. Figure 3.8 shows a "survey scan" taken twelve hours after a cleave. The incoming photon energy is $h\nu = 1000\,\mathrm{eV}$ and the O 1s contribution is just beginning to show at a kinetic energy of $KE = 469\,\mathrm{eV}$. On the contrary, the C 1s contribution is still not visible at $KE = 715\,\mathrm{eV}$. Given the low measuring temperatures and the ultra-high vacuum measuring conditions that reduce the contamination of fresh rare earth surfaces, data are typically collected for 12 hours at which time a fresh cleave is made.

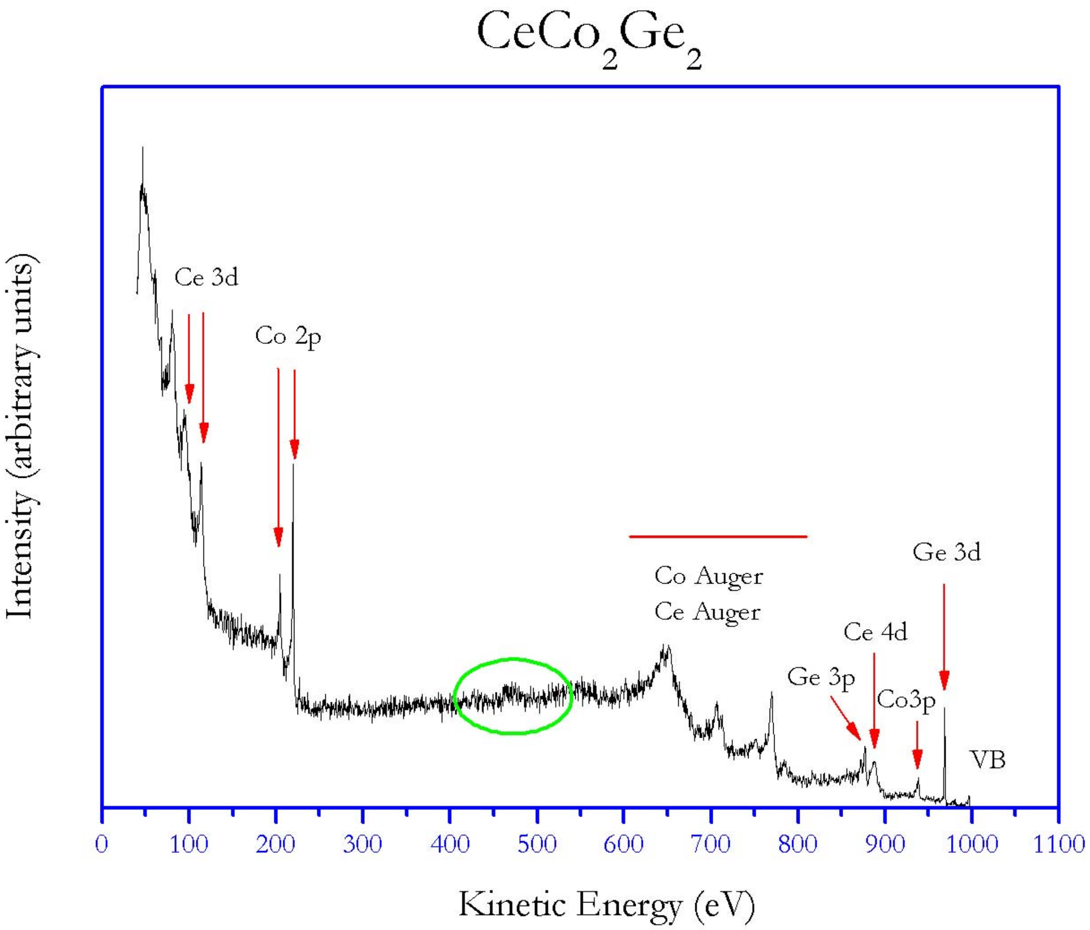

Figure 3.8: X-ray photoelectron spectroscopy measurement of $CeCo_2Ge_2$, taken approximately twelve hours after a cleave. The green circle shows the small O 1s contribution that is only just beginning to build up.

The single crystallinity of the sample and its orientation are checked with low energy electron diffraction (LEED). A typical LEED pattern from an aligned surface of $CeCo_2Ge_2$ is shown in Figure 3.9. As the other investigated compunds, $CeCo_2Ge_2$ has a body centred tetragonal lattice that is cleaved along the c axis, hence a fourfold symmetry and two equivalent high symmetry directions are clearly observed.

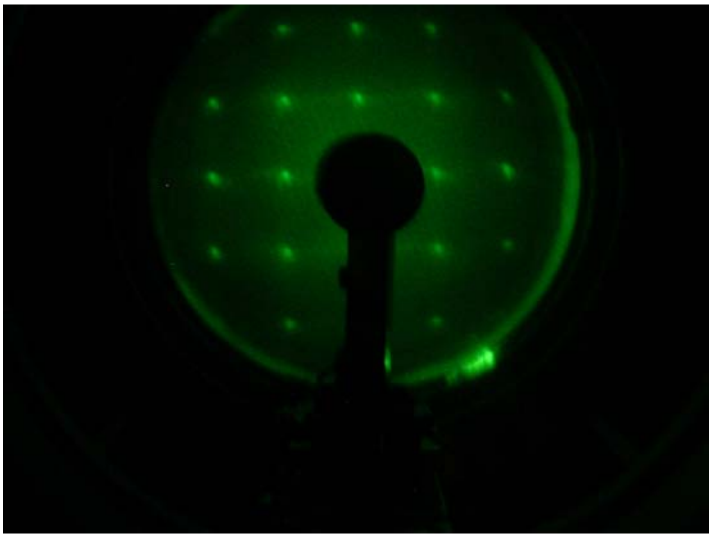

Figure 3.9: LEED pattern ($E_0 = 150\,eV$) of a freshly produced $CeCo_2Ge_2$ surface measured at T=20K.

3.4.1 How to obtain the 4f spectrum.

Before starting the discussion of the obtained results, it is important to determine how well the 4f spectral functions of the investigated Ce compounds can actually be known. Extracting the 4f part of the photoemission spectrum is not an easy task because the spectral weight of only one Ce 4f electron is comparable with, and often even smaller than, the weight of the other valence band electrons. Emission from the d electrons is always present in Ce (5d electrons) and for Ce compounds with transition metals this is especially so. In this latter case, the photoemission spectrum is dominated by the emission from the transition metal d bands. Therefore, some corrections must generally be made in order to isolate the 4f spectral function from the non-f valence contributions. To solve this problem, the chemical similarity of all rare-earth elements has often been used to model the non-f partial density of states of Ce-transition metal compounds. For example La has a completely empty 4f shell and its contribution to the photoemission spectrum is clearly absent. Therefore, by substituting La with Ce and by assuming that such a substitution does not alter the non-f partial density of states, the Ce 4f spectral function is the difference spectrum between the investigated system and the substitutional iso-structural rare-earth compound. Despite the qualitative validity of such an approach, differences in the non-f partial density of states upon substitution do actually exist, mainly because of the different spatial distribution of the rare-earth 5d wave functions and the different degrees of mixing with the transition metal's d valence states. A second approach is to exploit the photon energy dependence of the cross-sections in order to isolate the 4f contribution from the total measured photoemission spectrum. In order to do so a quantitative knowledge of the energy dependence of the cross-sections is necessary [18]: two spectra with weak and strong 4f contribution are scaled according to the known cross-section ratios and then subtracted or, if the 4f emission is known to be negligible for one of them, they are simply subtracted.

Resonant photoemission excitations to the Ce 4f states can be obtained by creating a d-hole via the allowed $d \rightarrow 4f$ absorption process. In particular, when exciting a system with a photon energy that is tuned to a threshold, two processes must be considered. The normal direct photoemission process given by:

$$d^{10}4f^{n} + h\nu \rightarrow d^{10}4f^{n-1} + e^{-} \tag{3.3}$$

and the threshold excitation ($d \rightarrow 4f$ absorption) that is followed by a super-Coster-Krönig Auger decay:

$$d^{10}4f^{n} + h\nu \rightarrow d^{9}4f^{n+1} \rightarrow d^{10}4f^{n-1} + e^{-} \tag{3.4}$$

as shown in Figure 3.10. These two processes have the same initial and final state, giving rise to photon energy dependent interference effects that have a minimum intensity (off-resonance condition) followed by a maximum intensity (on-resonance condition) for slightly larger values of $h\nu$ [32]. The resonant enhancement of the signal across both the thresholds, $4d \rightarrow 4f$ and $3d \rightarrow 4f$, strongly increases the 4f contribution to the experimental spectra.

However, many uncertainties in the proper normalisation of the on and off resonance spectra obtained at the $4d \rightarrow 4f$ edge have been found in the past and are well documented in [1], the basic problem being that, despite the use of the resonance, both Ce 4f and 5d cross-sections exhibit a resonance at this threshold and a quantitative separation of the two different contributions is not straightforward.

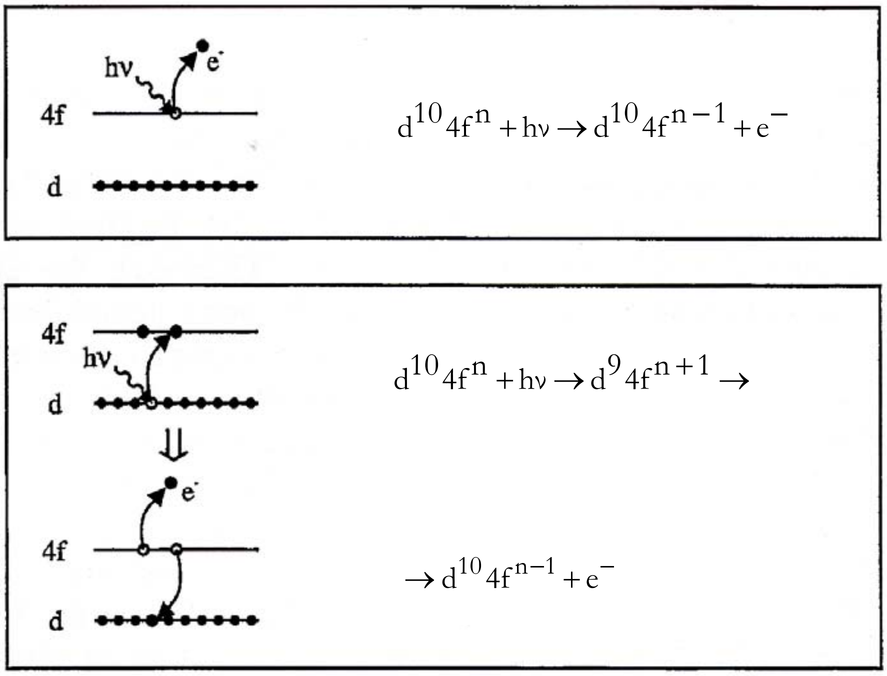

Figure 3.10: schematic diagram of the resonant $d \rightarrow 4f$ process for a rare earth atom, where $h\nu$ is the incident photon energy and e^{-} the emitted electron. Top panel: standard 4f photoemission process. Bottom panel: threshold excitation ($d \rightarrow 4f$ absorption) creating f^{n+1} the intermediate state which decays via a super Coster-Krönig Auger process [17].

Nowadays, the improved experimental resolution, that sharpens the 4f contribution with respect to the broad non-f emissions, and a deeper understanding of the non-f resonant behaviour allow a better quantification of the Ce 5d contribution to the spectra recorded at the $4d \rightarrow 4f$ threshold. The situation has been investigated for La compounds, a periodic table neighbour of Ce that gives no 4f emission in the photoemission spectra, and the results have been compared with iso-structural Ce compounds: it has been established that at the $4d \rightarrow 4f$ resonance a fraction as large as 30% of the total intensity can be ascribed to the Ce 5d emission [33]. Nevertheless, assuming that the 4f spectral shape and the Ce 5d partial density of states do not vary across the $4d \rightarrow 4f$ threshold, after a correct normalisation and subtraction of the off-resonance spectrum from the on-resonance one, the 4f spectral line shape can be obtained. While the $4d \rightarrow 4f$ resonance may be exploited to obtain surface sensitive 4f line shapes, the Ce $3d \rightarrow 4f$ resonance at $h\nu \cong 880\,\text{eV}$ gives more bulk sensitive 4f spectral functions due to the considerably larger kinetic energy of the outgoing photoelectrons. In actual fact, the resonance process that takes place at the 3d threshold should be indicated as a $3d_{5/2} \rightarrow 4f$ transition, since the Ce 3d spin-orbit splitting is large ($\cong 18\,eV$) and the two spin-orbit split channels are well separated. This is not the case for the Ce 4d orbitals in which the small spin-orbit splitting makes the two spin-split channels unresolved in a resonant process. With respect to the $4d \rightarrow 4f$ resonance a couple of important observations should however be made. Firstly, as the photoionisation cross-sections decrease with increasing photon energy [18], the photoemission intensity will be low if compared to the intensity obtained at the $4d \rightarrow 4f$ threshold, requiring the construction of bright photon sources and a longer data acquisition time. Added to this, the resolution of the photon sources at the Ce $3d \rightarrow 4f$ edge and the transmission of the electron analysers for the required high retarding voltages have been, until not so long ago, much lower than the respective quantities at the $4d \rightarrow 4f$ threshold. Hence, a clear separation of the 4f–related features in the photoemission spectra has been difficult. Only recently, with the advances of both synchrotron radiation facilites and electron analyser instrumentations, have soft X-ray high energy resolution photoemission experiments seen the light, making it possible to exploit the full potential of bulk sensitive resonant photoemission spectroscopy. In order to extract the 4f contribution from the measured photoemission signal a subtraction procedure identical to the one described above for the surface sensitive threshold can be generally used. As far as the Ce 5d resonance across the 3d threshold is concerned it is known [34] that the La valence band shape, that mainly reflects the 5d partial density of states, does not show appreciable variations withing this energy range and it has been estimated that the Ce 5d contribution to the total photoemission signal at the maximum intensity of the 3d resonance is 15%, half the size of the contribution found at the $4d \rightarrow 4f$ edge [33]. This makes the on-resonance minus off-resonance procedure less necessary for the determination of the real 4f contribution. In actual fact, considering the strong enhancement of the 4f signal at resonant conditions and the difficulty in acquiring off-resonance spectra with good statistics mainly because of the low photon flux, some authors, among them ourselves, avoid the subtraction altogether.

In order to obtain a correct enhancement of the Ce 4f signal, valence band photemission spectra have been recorded by varying the photon energy across the Ce M_5 absorption edge. The procedure is described below for the $CeNi_2Ge_2$ compound and has been repeated for both $CeCu_2Ge_2$ and $CeCo_2Ge_2$. Figure 3.11 shows the X-ray absorption spectrum at the Ce M_5 edge corresponding to the $3d_{5/2} \rightarrow 4f$ transition. The measurement is taken at $T = 20K$, in the total electron yield mode and normalised to the I_0 current from the focusing mirror or equivalently from a Au grid postioned before the sample.

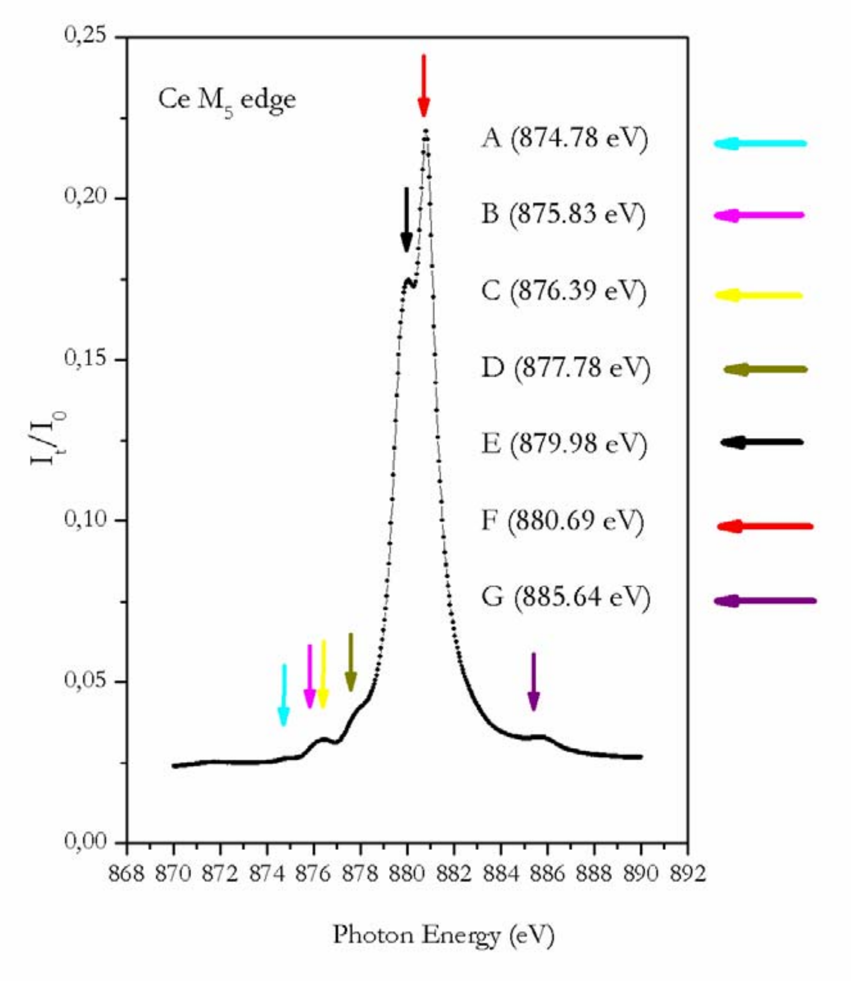

Figure 3.11: X-ray absorption spectroscopy (XAS) spectrum taken at the Ce $3d \rightarrow 4f$ edge and T=20K for $CeNi_2Ge_2$. The coloured arrows indicate the position of the two main peaks and the multiplet structures. The corresponding energies are shown in brackets.

Two main peaks positioned at $h\nu \cong 879.9$ eV and 880.8 eV, together with some multiplet structure at lower energies, are observed. These features are ascribed to the $3d^9 4f^2$ final state representing the $4f^1$ character of the ground state. Furthermore, an additional feature is visible at $h\nu \cong 886$ eV. Such a satellite is ascribed to the $3d^9 4f^1$ final state reflecting the $4f^0$ character of the ground state [7, 8]. The coloured arrows in Figure 3.11 indicate the different structures and the valence band measurements shown below in Figures 3.13 and 3.14 are taken by tuning $h\nu$ to the energy of these features. Added to this, an off resonance valence band measurement is taken at $h\nu_{\text{off res}} = 840\,\text{eV}$, an energy that is positioned below the Ni L_3 edge as can be seen in Figure 3.12.

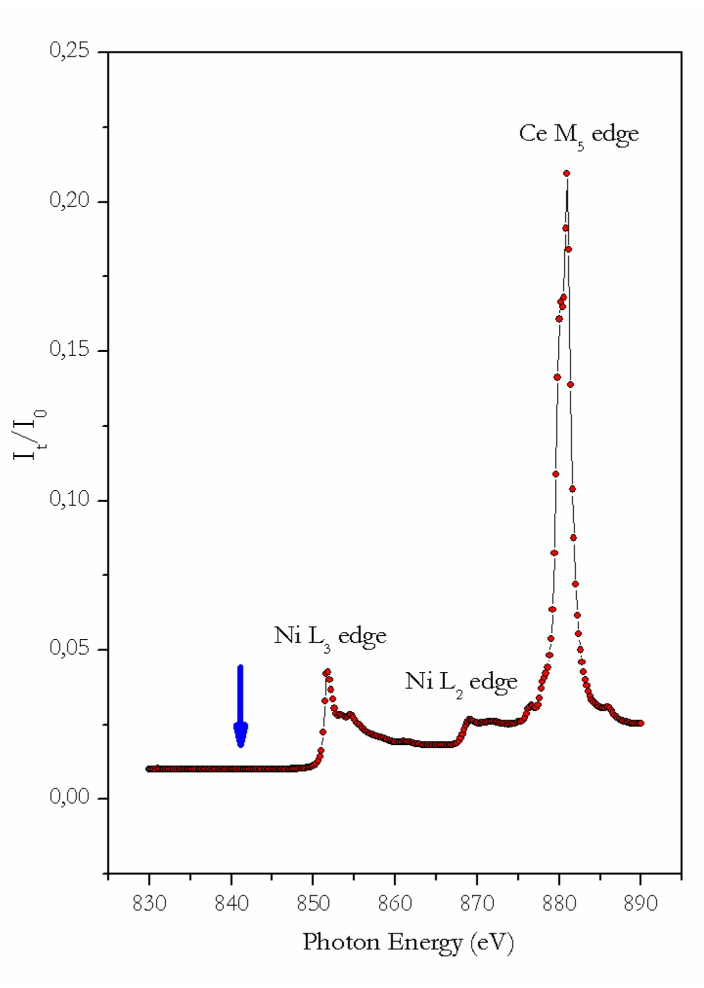

Figure 3.12: XAS spectrum of $CeNi_2Ge_2$ showing both the Ni L_2 , L_3 edges and the Ce M_5 edge. T=20K. The blue arrow shows the energy at which the off resonance valence band spectrum is taken (see blue plot in Figure 14).

Figure 3.13 shows the valence band spectra obtained by tuning the photon energy to the energy of the less intense structures in the absorption spectrum. The spectra are very similar to each other and to the off resonance measurement shown in blue in the same plot. In agreement with [1, 25, 35, 36] the most intense feature observed in Figure 3.13 originates from the Ni 3d states, whose density of states according to the calculations presented in [25], is peaked between 1 and 2.5 eV approximately. In each spectrum the Ce $4f^1$ final state is clearly visible close to the Fermi level. However, due to the experimental resolution with which these measurements are taken, the fine structure of the latter feature is not resolved in these spectra. The structures observed between 2 eV and 5 eV originate from the tail of the Ni 3d contribution, together with both the Ce $4f^0$ final state [1, 2, 35, 36] and the Ge 4p states [25].

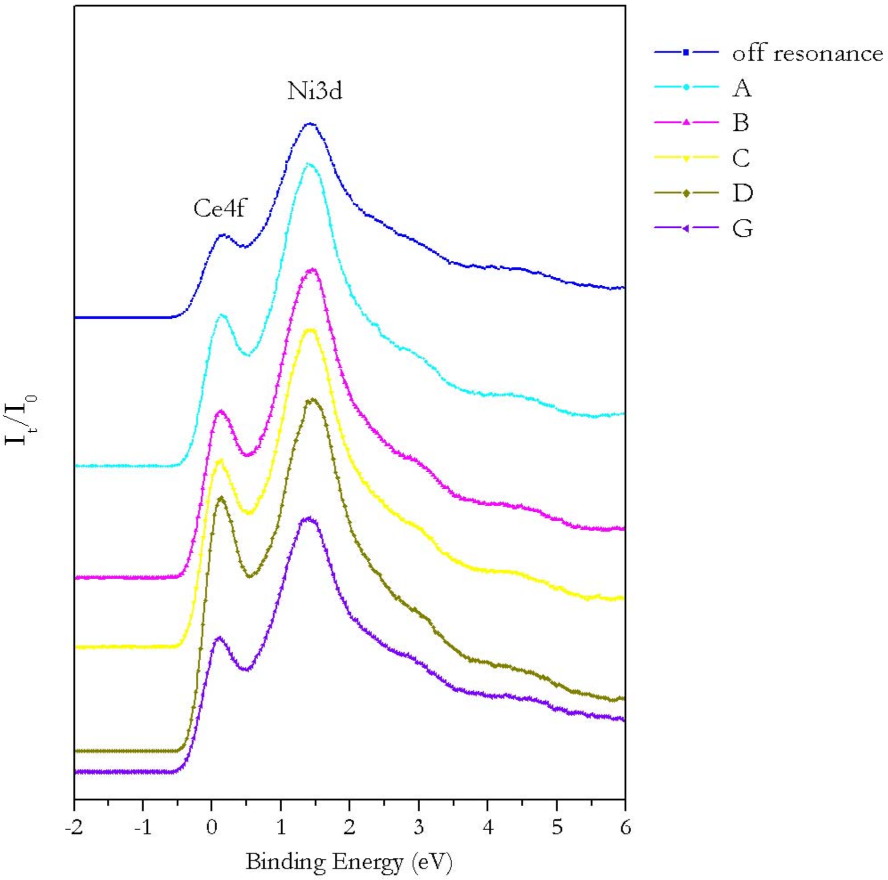

Figure 3.13: valence band spectra of $CeNi_2Ge_2$ taken at the different energies of the multiplet structures that appear in the XAS spectrum shown above. The colour scheme is consistent with the arrows shown in Figure 3.11 and indicates the incoming photon energy. The blue spectrum (top) is measured off resonance with $h\nu = 840eV$. The measuring temperature is T=20K and the data are normalised to the I_0 current and shifted vertically for a better comparison. E_F=0eV.

The spectra plotted in Figure 3.14 are measured with $h\nu$ tuned to the energy of the two main absorption peaks. The two spectra, although very similar to each other, show strong differences if compared to the results displayed in Figure 3.13. In particular, a strong enhancement of the Ce 4f signal is clearly visible and most intense for the coherent $4f^1$ feature close to E_F. The Ni 3d contribution can be seen as a wide shoulder positioned between 1 eV and 2.5 eV, but the signal is strongly suppressed with respect to the Kondo resonance. The enhancement of the 4f signal is maximum when the incoming photon energy is tuned to the energy of the main peak in the absorption spectrum. For this reason, all the resonant photoemission results presented in the following are obtained by tuning the incoming photon energy to the energy of the main peak of the X-ray absoprtion spectra at the Ce M_5 edge.

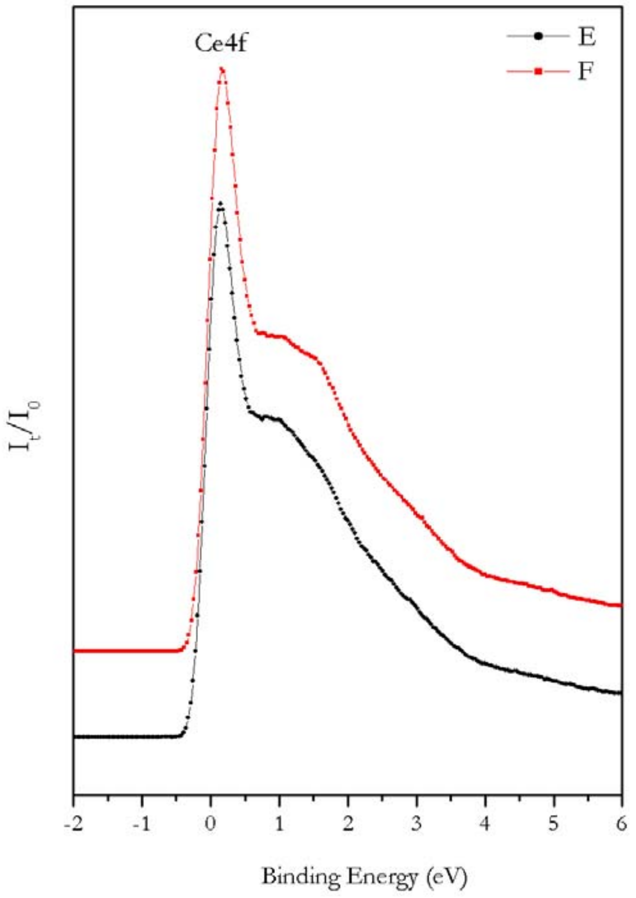

Figure 3.14: on resonance valence band spectra of $CeNi_2Ge_2$ taken by tuning hν to the energy of the two main peaks in the XAS spectrum. T=20K. The data are normalised to the I_0 current and shifted vertically. E_F=0eV.

Figure 3.15 shows the off resonance (blue) and on resonance (red) valence bands of $CeNi_2Ge_2$. As the previous measurements, these spectra are taken at $T = 20K$ and the energy resolution is $\Delta E \leq 220meV$. In the off resonance spectra the contribution of the transition metal is clearly visible. The enhancement of the Ce 4f contribution in the on resonance measurements is of approximately one order of magnitude.

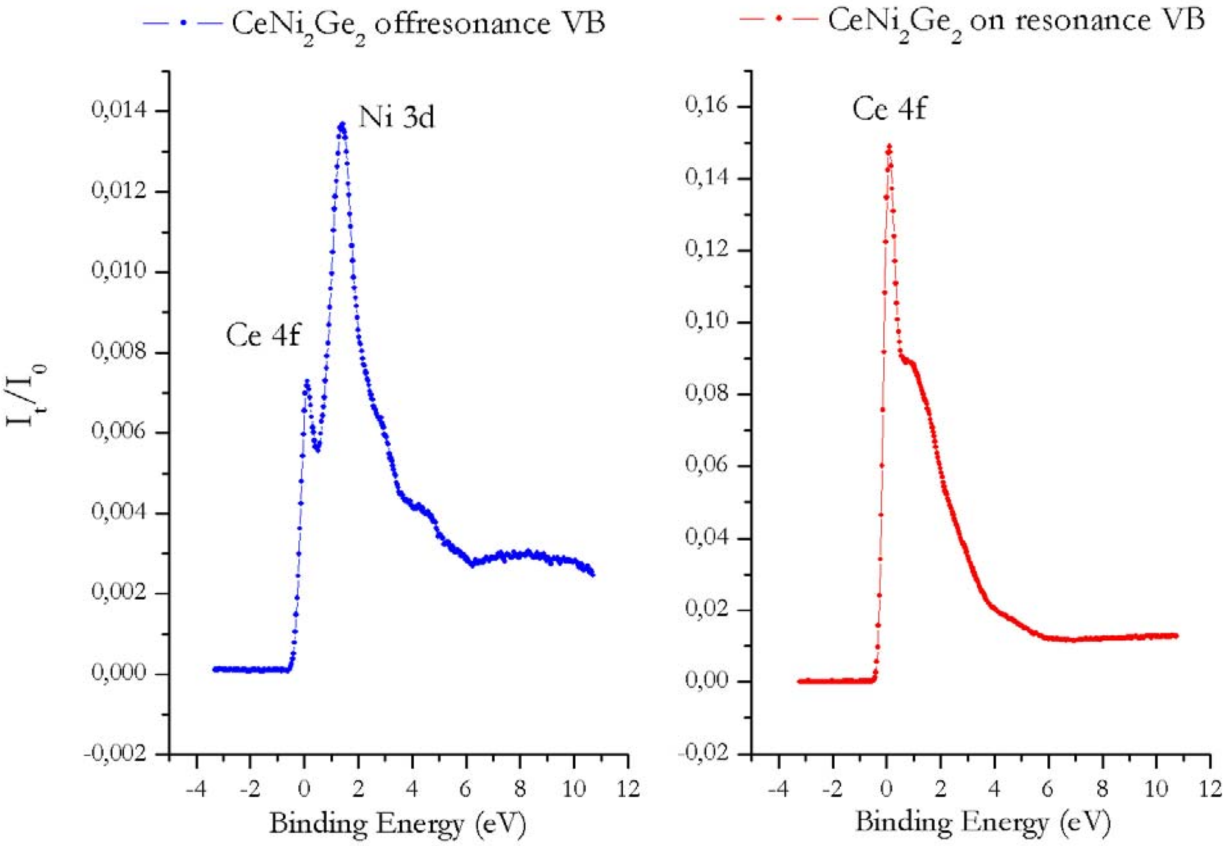

Figure 3.15 : off (blue) and on (red) resonance valence band spetra shown for $CeNi_2Ge_2$. T=20K. E_F=0eV.

3.4.2 A temperature dependent study.

The direct spectroscopic observation of the Kondo energy scale is demanding and requires high resolution measurements. The first spectroscopic investigation of the low energy excitations in a Kondo system is a high resolution, ultra-violet photoemission spectroscopy study performed on $CeSi_2$ [37]. The experimentally observed temperature dependence of the near-E_F peak, which is reproduced by the calculations, has been interpreted as the evidence of the collapse of the Kondo resonance predicted by the single impurity Anderson model [15, 16]. A similar temperature dependence is also observed in other high resolution ultra-violet studies [38, 39, 40]. The intensity of the photoemission peak pinned at E_F clearly scales with T_K in [38, 39] and a variety of different Ce compounds are studied. Similar bulk sensitive results are to be found in [23, 41, 42, 43]. However, in the light of the resonant photoemission spectroscopy results published in [44], the high-resolution data obtained on $CeSi_2$ [37] have been critically re-interpreted. The authors of [44] observe that the measured width of the near-E_F feature, which the single impurity model associates to the tail of the Kondo resonance, is significantly larger than the relevant characteristic energy scale, $\delta = k_B T_K$, and conclude that this discrepancy is large enough to have to reconsider the interpretation of the experimental spectra in terms of the Kondo scenario. They also point out that the observed temperature dependence is not sufficient to invoke Kondo effects, since the experimental data can be reproduced by considering the combined effect of a temperature-dependent phonon broadening and of the Fermi function. Added to this, additional data, taken at $h\nu = 120$ eV for various Ce compounds characterised by different thermodynamic properties and estimated values of T_K, are presented. Surprisingly, all spectra exhibit two near-E_F features that do not appear to be T_K-dependent. Similar resonant low energy results are also discussed in [45]. These findings have raised questions regarding the validity of the impurity Anderson model. The authors of [44, 45] conclude that, although the model correctly describes the thermodynamic properties of the systems under investigation, it is not needed for the interpretation of the photoemission results. This conclusion, however, is far from being unanimously accepted. The surprising lack of correlation between the spectral weight at E_F and T_K is not understood and the difficulty in extracting the 4f spectrum from the experimental data might play a role [2]. Furthermore, in an ideal experiment, in order to demonstrate the existence of the predicted scaling behaviour with T_K, it is necessary to compare near-E_F intensities of compounds with different values of T_K but equal non-4f density of states. This is done in the ultra-violet photoemission study performed on $CeSi_x$, with x ranging from 1.6 to 2, and published in [46]. Here, the value of T_K changes with the Si concentration and the progressive evolution of the 4f spectral function as a function of x is qualitatively consistent with the single impurity Anderson model's predictions. The discrepancy between the line shape of the Kondo resonance and the theoretical predictions of the model discussed by the authors of [44, 45] is more easily understood. As a general rule, when comparing theory and experiment, it must not be forgotten that a given model provides only an approximate description of a complicated physical situation, not an exact solution. In this context, the single impurity Anderson Hamiltonian retains only the elements that are necessary to capture the essential nature of the Kondo problem. It is therefore not surprising that such a simplified approach can be unable to quantitatively reproduce the experimental results. It should be mentioned that the temperature-independent results discussed above have been obtained from cleaved single crystalline samples, while the remaining experiments, that are in agreement with the single impurity model, have been performed on scraped polycrystalline ones [37-40, 46]. It has therefore been suggested [44, 45] that surface effects dominate and distort the experimental photoemission results presented in [37-40, 46]. The surface sensitivity of the conflicting low energy studies discussed above has to be taken into consideration. As already discussed in Section 3.4.1, the most powerful technique for the extraction of the bulk 4f states comes with the exploitation of synchrotron radiation at the Ce $3d \rightarrow 4f$ absorption edge. For this reason the importance of the high energy photoemission results published in [23, 41, 42, 43] should not be underestimated. It is also important to mention that, exception made for [43], these results have been obtained on single crystalline samples.

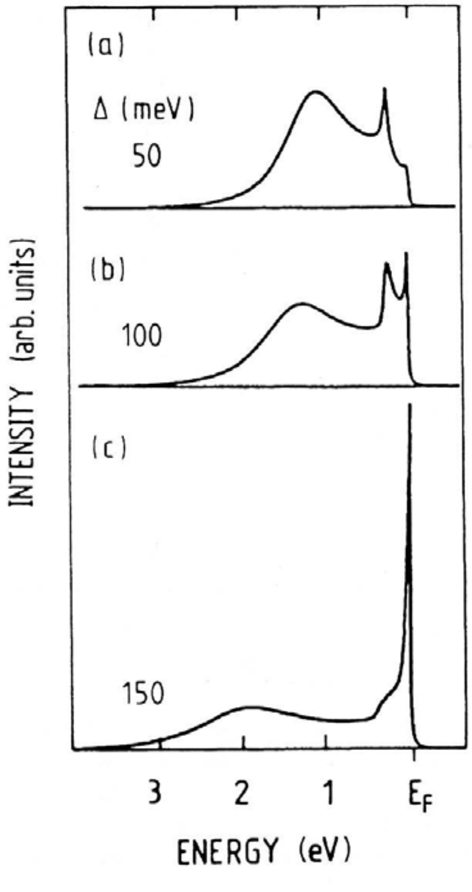

Figure 3.16: influence of the hybridisation, Δ, on the 4f spectral function calculated within the GS model [38].

Within the impurity model the magnitude of the Kondo resonance is proportional to the hybridisation or, equivalently, to the degree with which Ce deviates from trivalency; indeed, it is proportional to the thermodynamic quantity T_K, and is therefore a bulk property of the material. Figure 3.16 shows the influence of the hybridisation strength, Δ, on the calculated 4f spectral function [38]. For the largest hybridisation (curve (c)), a strong intensity can be seen at the Fermi level, the Kondo resonance, whereas the spin-orbit partner and the final states with f^0 character are not very pronounced. When the value of Δ becomes smaller, the relative intensity of the Kondo peak decreases for the benefit of the more atomic-like excitations at higher binding energies (curve (b)). For very weak hybridisation the spin-orbit component survives at the expenses of the Kondo peak (curve (a)). In the purely atomic limit ($\Delta=0$) the low energy excitation would disappear completely leaving only the f^0 peak at ε_f. The intensity of the structure at E_F strongly decreases with Δ and therefore with T_K. On the other hand, the spin–orbit partner shows a much weaker hybridisation dependence and is clearly observed even in the case of weak hybridisation.

In order to test the scaling behaviour of the Kondo resonance with T_K, we have measured the valence band of each compound at $T = 20K$. Figure 3.17 shows the bulk sensitive, resonant photoemission spectra of the three investigated compounds near the Fermi level. The combined beamline and electron analyser energy resolution is better than the nominal value of $\Delta E = 180\,\mathrm{meV}$. Such an energy resolution allows us to observe not only of the tail of the Kondo resonance ($4f^1_{5/2}$ final state) close to the Fermi level, but also the deeper spin orbit partner ($4f^1_{7/2}$ final state). The spectral weight near E_F represents the deviation from the pure atomic limit and the impurity model predicts this intensity to scale approximately with T_K. The results shown below make a case in favour of the existence of a correlation between the 4f spectral weight near the Fermi level and the value of the Kondo temperature. Within the model the T_K-dependence of the spin orbit partner is weak and we have therefore scaled our data to the intensity of this peak as already done in [38, 39]. Despite the different values of T_K, the photoemission signals of $CeNi_2Ge_2$ ($T_K = 30\,K$) and $CeCo_2Ge_2$ ($T_K \cong 120\,K$) are similar, as the experimental temperature of $T = 20K$ places both systems in the temperature range where the Kondo effect takes places. However, the intensity at the Fermi level is stronger in the case of the most hybridised compound, namely $CeCo_2Ge_2$, in qualitative agreement with the model. On the contrary, in the case of the less hybridised compound, $CeCu_2Ge_2$ with $T_K = 4K$, the Kondo resonance is greatly suppressed with respect to the spin-orbit partner, reflecting both the weaker hybridisation and the fact that the measuring temperature is this time higher than the value of T_K. The fact that the spin-orbit feature survives at the expenses of the Kondo resonance probably reflects a mixing of the $4f^1_{7/2}$ level with the $4f^0$ final state configuration that is significantly larger than for the lower-lying $4f^1_{5/2}$ state [2]. These results are in agreement with the low energy data discussed in [38, 39, 46] and with the more bulk sensitive results presented in [23, 41, 42].

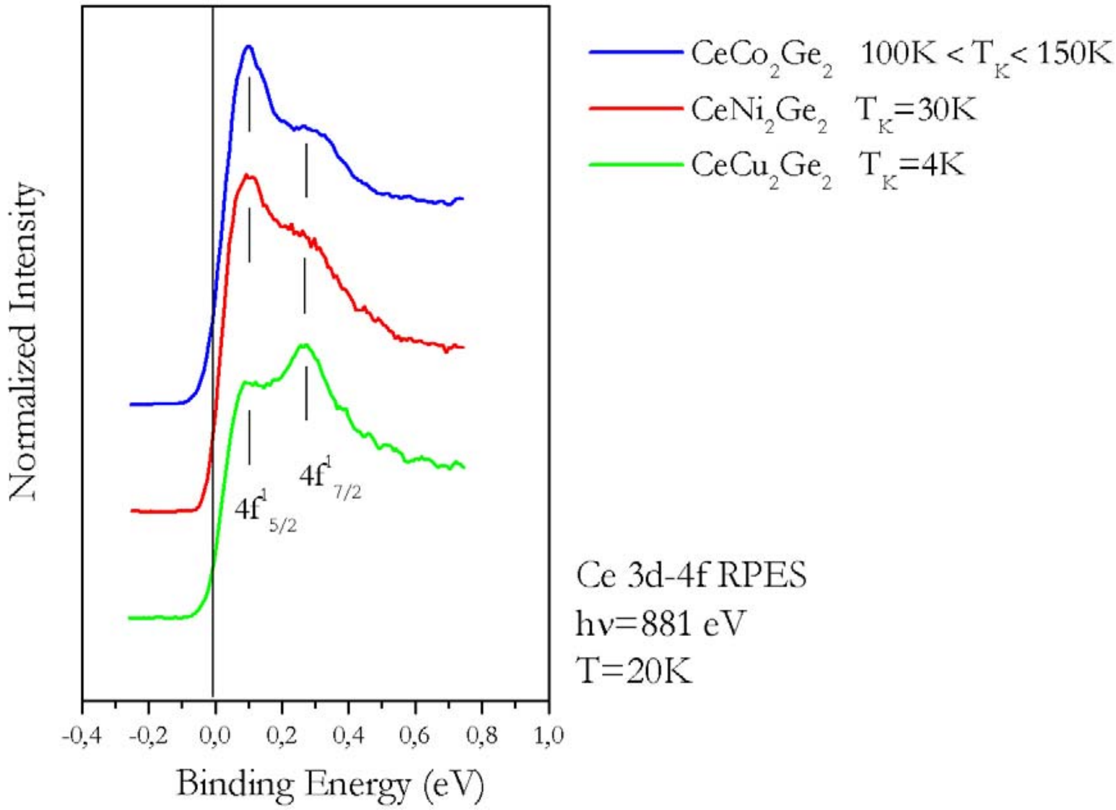

Figure 3.17: on resonance valence band spectra taken at T=20K for the three different compounds. The $4f^1_{5/2}$ peak (Kondo resonance) and the $4f^1_{7/2}$ peak (spin-orbit partner) are visible. The data are normalised to the intensity of the spin-orbit partner and shifted vertically for clarity. E_F=0eV.

Below, X-ray absorption spectra measured at the Ce M_5 edge corresponding to the $3d_{5/2} \rightarrow 4f$ transition are shown for each sample. The high energy satellite can be understood as being the effect of hybridisation between the Ce 4f electrons and the conduction electrons as described by the impurity Anderson model [7, 8]. In passing from $CeCu_2Ge_2$ to $CeCo_2Ge_2$ the intensity of the high energy satellite increases, indicating that the $4f^1$ occupation number of the ground state, n_f, decreases. Equivalently, the intensity increase reflects a hybridisation increase. The single impurity model relates the hybridisation strength, Δ, to the value of T_K. As can be seen from Table 2 (page 112), the intensity increase of the $3d^9 4f^1$ final state satellite is consistent with the increase of the values of T_K. Therefore, in as much as the values of T_K follow the intensity increase of the high energy satellite, these X-ray absorption results also lead us to suggest a qualitative agreement with the single impurity Anderson model. Similar phenomena have already been observed in [41, 42, 47, 48].

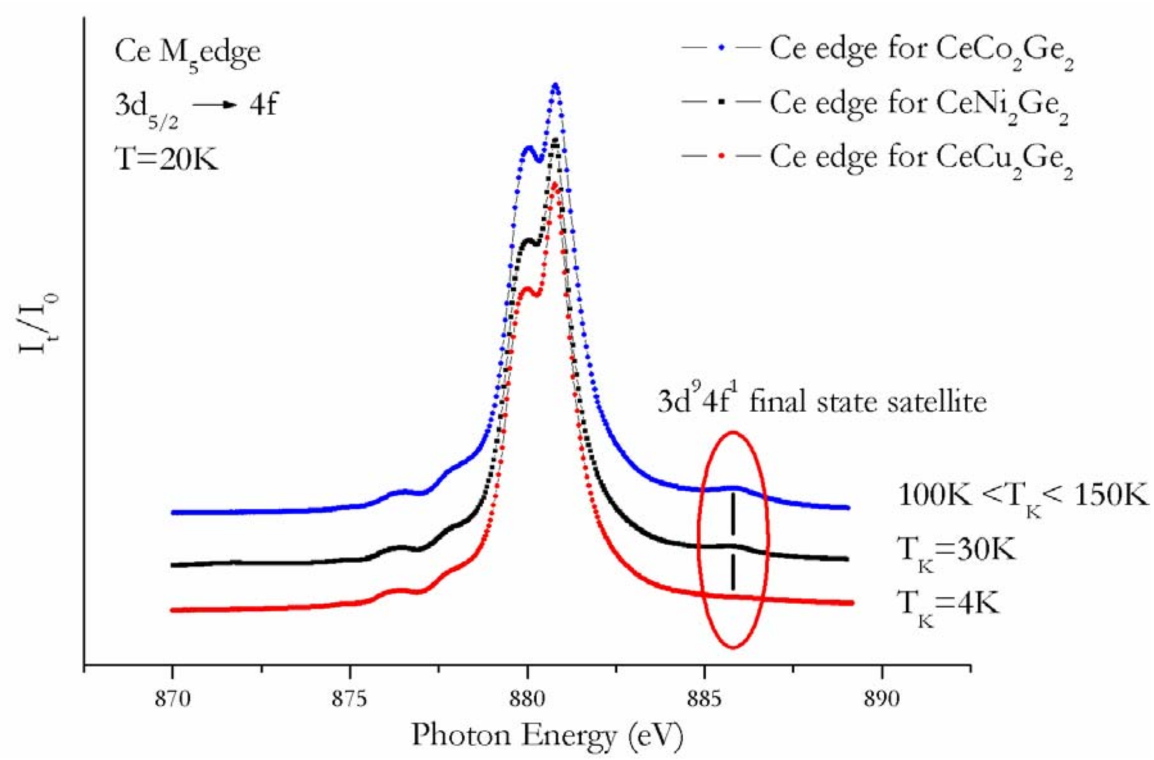

Figure 3.18: XAS spectra taken at the Ce M_5 edge for $CeCu_2Ge_2$, $CeNi_2Ge_2$ and $CeCo_2Ge_2$. The data are normalised to I_0 and shifted vertically. The high energy satellite circled in red is a measure of the hybridisation of each system. The data are taken at T=20K

Within the Kondo framework, as the temperature rises above T_K, the non-magnetic singlet ground state is gradually depopulated by thermally activated spin fluctuations. From a spectroscopic point of view the cross-over from the low to the high temperature regime is associated with a decrease of the Kondo resonance's intensity. Therefore, the temperature dependence of the Kondo resonance is a fundamental test of the validity of the predictions of the single impurity model. As previously discussed, high resolution, bulk sensitive, resonant, photoemission measurements of the valence band of Ce compounds are very demanding. This is especially so in the case of a temperature dependent investigation, where the deterioration of the sample quality with time and temperature has to be taken into account. To the best of our knowledge, the only bulk sensitive and temperature dependent study of the Ce 4f spectral function is to be found in [43]. Temperature dependent measurements performed on two of the investigated samples, namely $CeCo_2Ge_2$ and $CeCu_2Ge_2$, are shown in Figures 3.19 and 3.20 respectively .

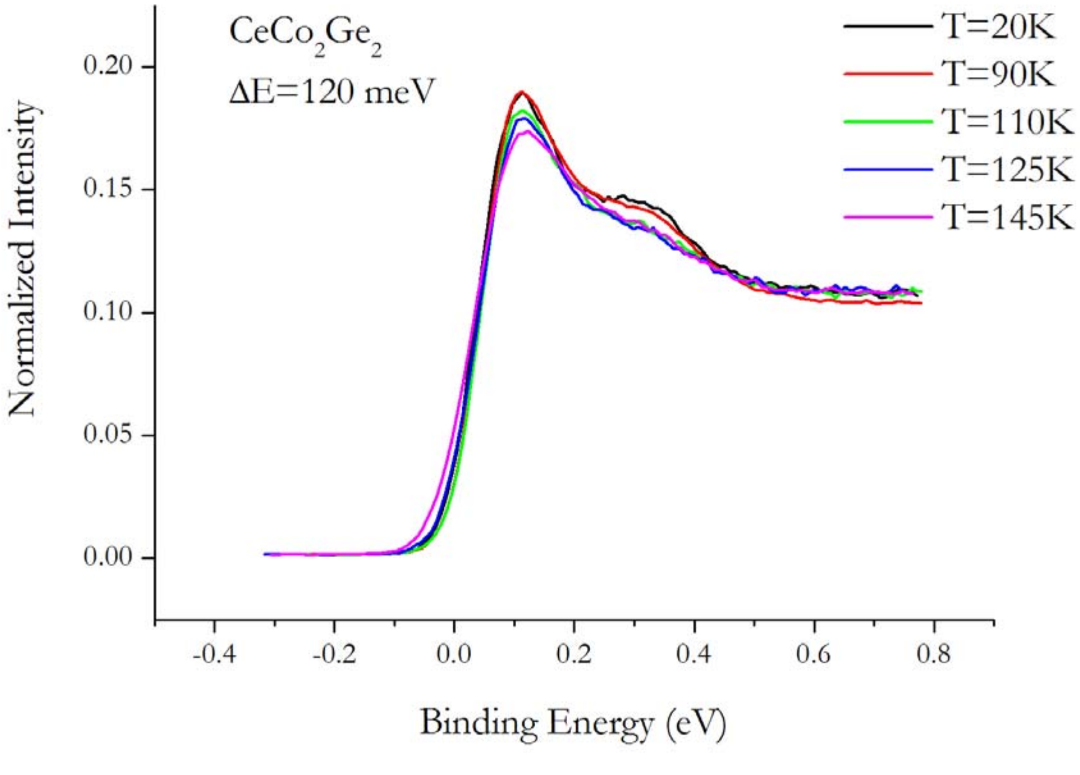

Figure 3.19: temperature dependent resonant photoemission valence band spectra of $CeCo_2Ge_2$. $T_K \cong 120K$ [30]. The data are normalised to the area of the Ge 3p spectral feature. E_F=0eV.

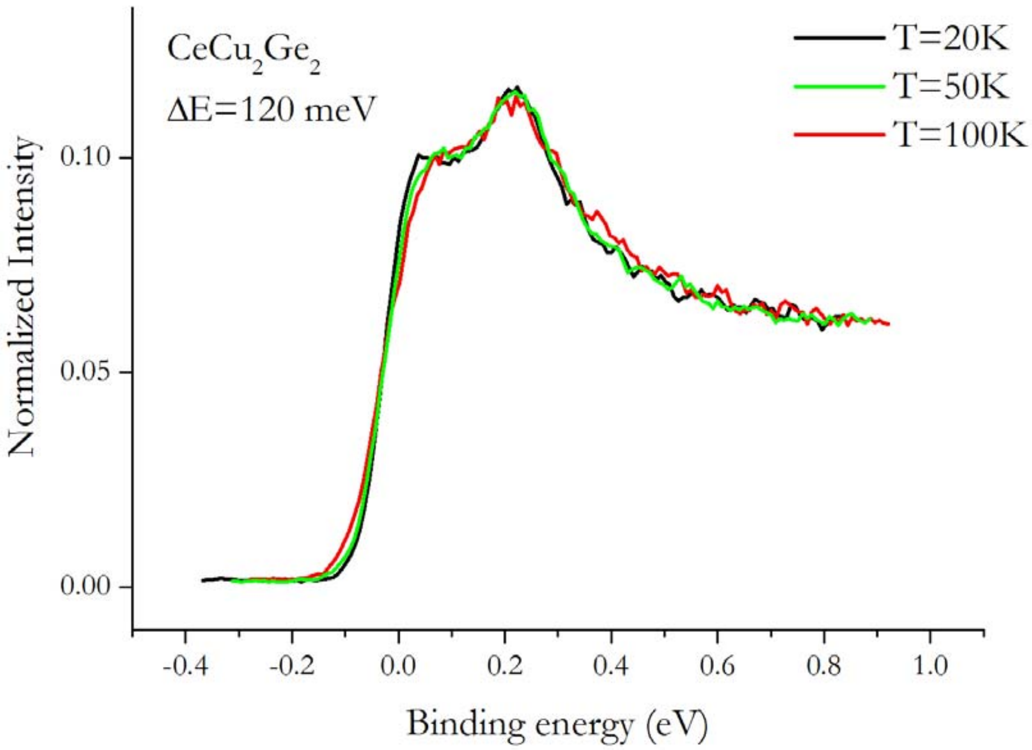

Figure 3.20: temperature dependent resonant photoemission valence band spectra of $\mathrm{CeCu_2Ge_2}$. $T_K \cong 4K$ [29]. The data are normalised to the area of the Ge 3p spectral feature. E_F=0eV.

For each temperature change, the position of the sample with respect to the photon beam and electron analyser has been carefully adjusted to compensate for the thermal expansion or contraction of the sample manipulator. The samples have been cleaved at $T = 20K$ and the spectra are recorded starting from $20K$, subsequently increasing to higher temperatures. In order to exclude possible effects such as diffusion of impurities from the bulk of the samples with increasing temperature, the samples have been cooled a second time and the low temperature measurement has been repeated. The two low temperature measurements are consistent. To further exclude other artificial effects the measurements have been repeated using several different samples of the same compound. In order to ensure a correct data normalisation, for each sample the raw data are normalised to the area of the temperature independent signal photoemitted by the Ge 3p core level and like in the previous measurements the overall energy resolution is approximately $\Delta E = 120\,\mathrm{meV}$. The choice of $\mathrm{CeCu_2Ge_2}$ and $\mathrm{CeCo_2Ge_2}$ is justified by their values of T_K. The lowest temperature that can be reached with our experimental set up is $T = 20K$. Therefore, in the case of $\mathrm{CeCo_2Ge_2}$, whose T_K is expected to be of the order of 120K [30], a detailed temperature dependent study is possible and spectra have been recorded for several temperatures ranging from 20K to 145K. As can be seen in Figure 3.19, the Kondo resonance is clearly observed for all the investigated temperatures. The spectra taken at 20K and 90K are practically identical but as the temperature is increased above 90K the decrease of the intensity of the Kondo resonance, together with the smearing out of its spin orbit partner, is clearly observed. This result is in agreement with a value of T_K that is higher than 90K. In agreement with the predictions of the single impurity model, we observe a progressive temperature dependent transition that reflects the decrease of the narrow and intense low energy excitations when the temperature is raised to values that are of the order of or higher than the estimated value of T_K. It should not be overlooked that a very similar temperature dependence has already been observed in [43], where the Kondo resonance is well visible for temperatures that are at least twice the value of the estimated T_K. On the other hand, the fact that the intensity at the Fermi level is still observable for relatively high temperatures could lead to suggest that the intensity change of the Kondo resonance with increasing temperature is actually slower than predicted by the impurity model. The $CeCu_2Ge_2$ compound is chosen as an archetype low T_K system. As already seen in Figure 3.17, because of the low hybridisation of this compound, the Kondo resonance is highly suppressed. On the contrary, the spin-orbit partner survives thanks to a weaker hybridisation dependence. The measuring temperature of 20K is approximately five times higher than $T_K = 4K$. Therefore the absence of an unconventional temperature dependence as T rises is not surprising.

Core level X-ray photoemission spectroscopy can also be exploited to gain a better understanding of the electronic structure of Ce and its compounds [1, 2, 8, 9, 20, 49, 50]. In as much as the Ce 3d X-ray photoemission spectrum reflects the removal of a 3d core electron, its rather complex nature has been interpreted in terms of the presence of two different screening channels. In particular, the “well screened” and “poorly screened” final states that are referred to in [49], describe the 3d core hole being screened either by a strongly localised 4f orbital or by a delocalised state, respectively. In terms of the single impurity Anderson model [7, 8, 9] from the analysis of a Ce 3d core level spectrum it is possible to estimate the weight of the different ground state contibutions, namely $4f^0, 4f^1, 4f^2$. However, with respect to the ground state, the relative energies of these configurations can be modified due to the additional attractive core hole potential generated during the photoemission process. We have measured the core level photoemission spectrum of $CeCo_2Ge_2$ for two different temperatures, T=20K and T=145K, and the results are shown in Figure 3.21. The spectral assignments based on the $4f^0, 4f^1, 4f^2$ configurations are given by the vertical bars [1, 2]. The data are in agreement with the impurity model, as the spectral intensity of the magnetic $4f^1$ state increases with temperature, marking a decrease of the hybridisation. A further confirmation of this effect comes from the decrease of the $4f^0$ and $4f^2$ contributions circled in blue.

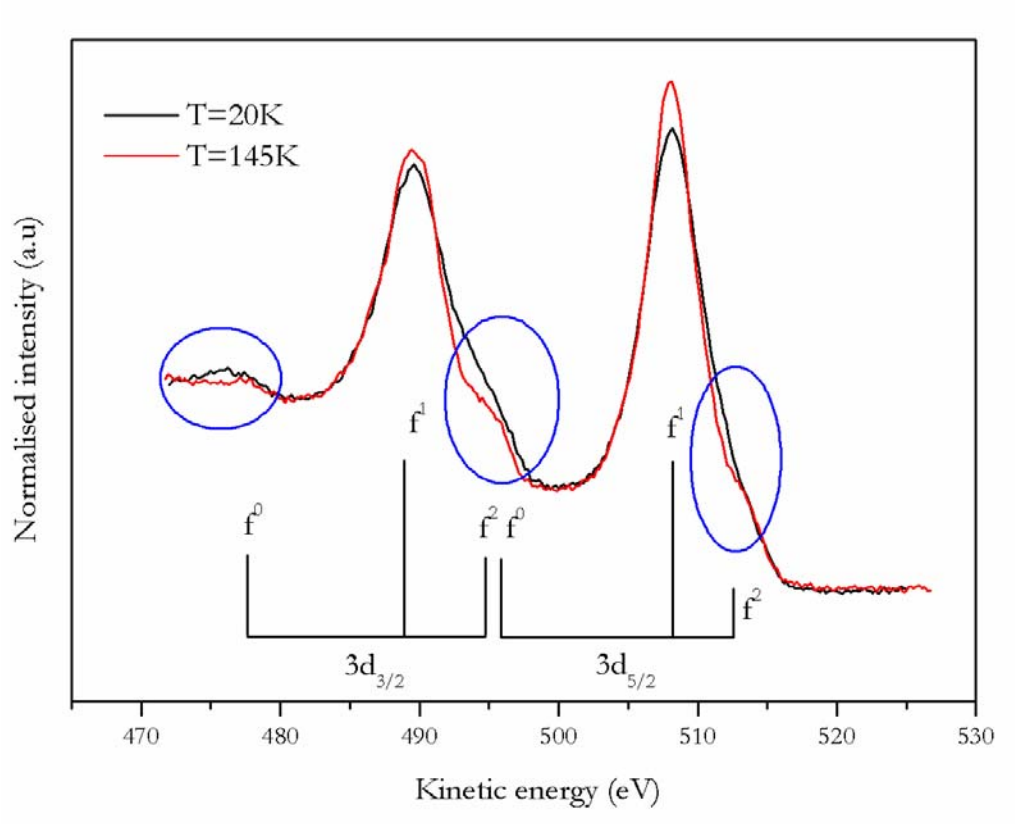

Figure 3.21: Ce 3d core level X-ray photoemission spectra of $CeCo_2Ge_2$ measured for T=20K and T=145K.

The photoemission results discussed so far are further confirmed by a temperature dependent X-ray absorption study of $CeCo_2Ge_2$. The spectra shown in Figure 3.22 are measured at the Ce $M_{4,5}$ edge for different values of T ranging from 30K to 240K. The high energy satellite that corresponds to the $3d^9_{5/2}4f^1$ final state configuration is circled in red. As already discussed, this feature represents the $4f^0$ character of the ground state and is a measure of the system's hybridisation. Therefore, the stronger the intensity of this satellite, the lower the occupation number of the $4f^1$ ground state, n_f. Figure 3.23 shows the temperature dependence of this feature in detail. The clear intensity reduction of the peak with increasing temperature implies an increase of n_f with T, just as predicted by the Kondo scenario and the non-crossing approximation calculations [8, 16]. Similar results are found in [43] for $CeSi_2$ and in [51, 52] for Yb compounds. The area of this peak is obtained after subtraction of a linear background and one minus the integrated signal, a quantity that is proportional to n_f, is plotted as a function of the temperature in Figure 3.24. Figure 3.25 shows the temperature dependence of n_f for different zero-temperature occupation numbers, i.e. for different hybrid ground states, as calculated from the non-crossing approximation [16]. The qualitative agreement of our data with the impurity model calculations is clear and by assuming $T_K \cong 120K$ [30], the midpoint of the transition is found at $\frac{T}{T_K} = 1$.

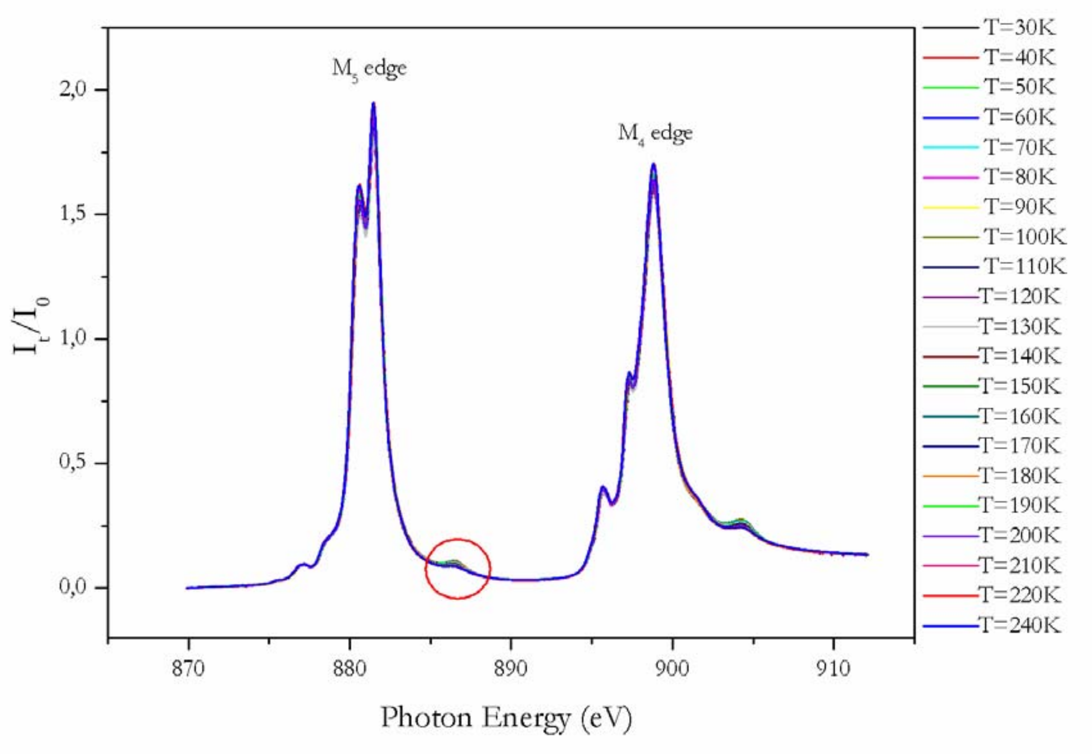

Figure 3.22: temperature dependent XAS spectra of $CeCo_2Ge_2$. The M_5 and M_4 edges are visible. The satellite that represents the $3d^9 4f^0$ ground state is circled in red.

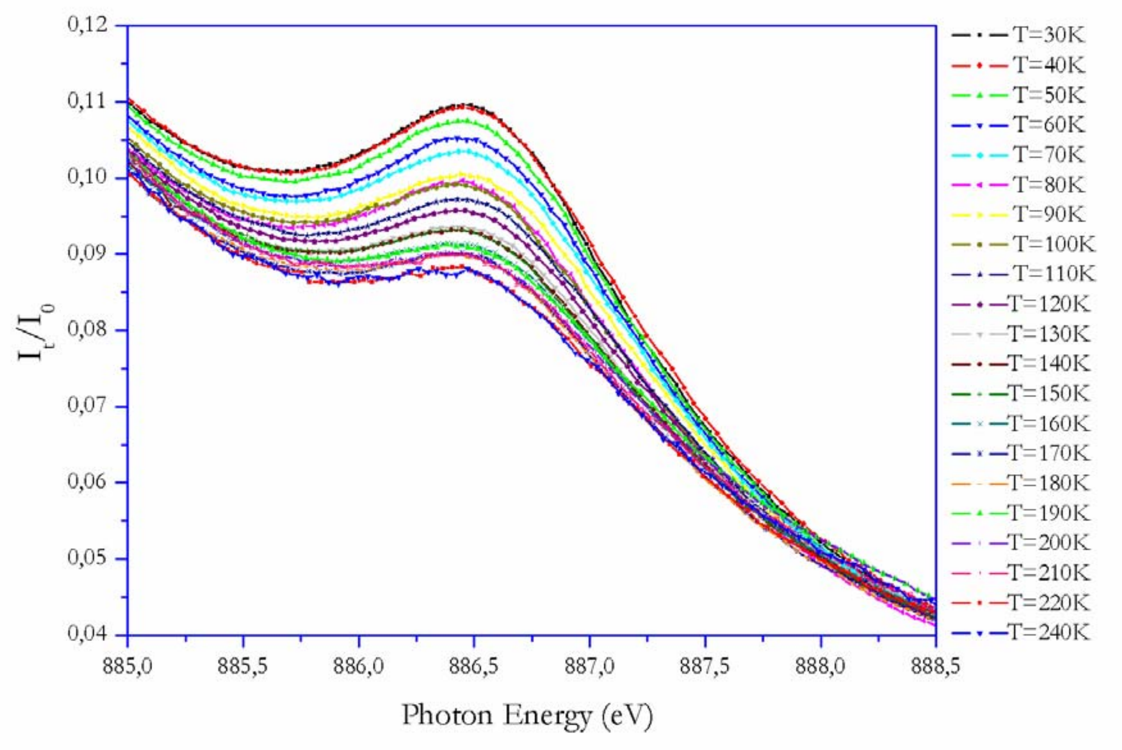

Figure 3.23: temperature dependence of the XAS M_5 edge satellite.

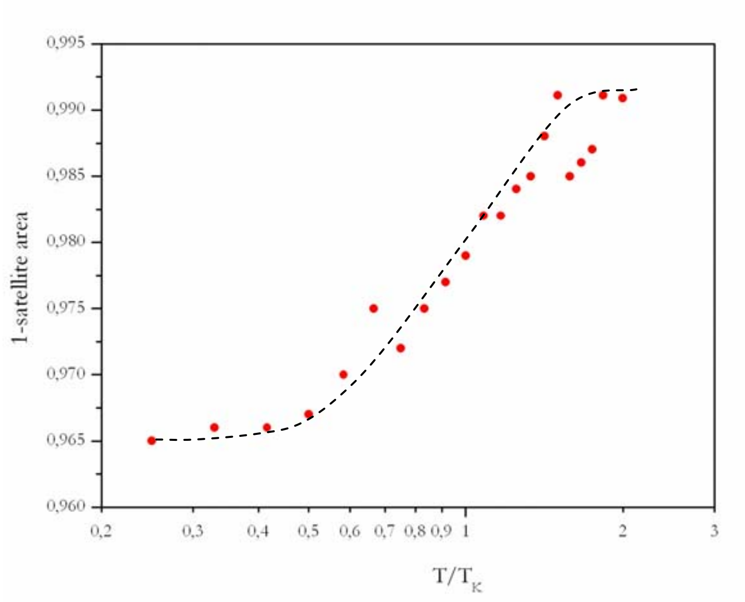

Figure 3.24: 1 minus the integrated intensity of the high energy XAS satellite as a function of $\frac{T}{T_K}$.

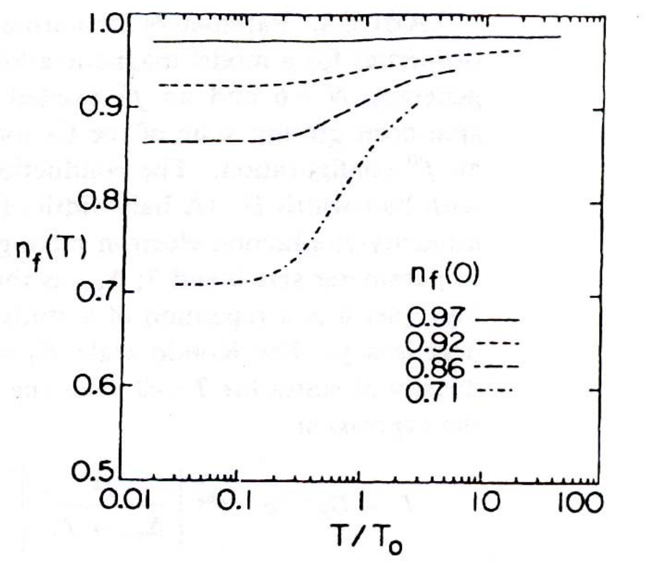

Figure 3.25: temperature dependence of the $4f^1$ ground state occupation number, $n_f(T)$, for different zero-temperature values [16].

3.4.3 The observation of momentum-dependent effects.

At the heart of the single impurity Anderson model is the postulate that the 4f electrons in heavy Fermion Ce compounds are essentially localised, isolated, impurities and that it is only the small hybridisation with the conduction electrons that gives rise to the 4f spectral weight near the Fermi level. Within the single impurity model, the Kondo resonance has no $\underline{k}$-momentum dependence by construction, since calculating the spectral weight requires integration over all the conduction electrons in $\underline{k}$-space. However, momentum-dependent intensity variations of the $4f_{5/2}$ peak in Ce compounds have been first reported in [53] for $CePt_{2+x}$ (where $0 < x < 1$ and $T_K < 20\,K$). Actual dispersion of the peak is not clearly observed but is considered to be very probably the underlying cause of the amplitude variations. These $\underline{k}$-dependent variations are observed at a temperature that exceeds T_K by a factor of more than ten, calling into question the applicability of the single impurity Anderson model for which at $T > T_K$ the 4f electrons are considered to be localised impurities. The first spectroscopic evidence of dispersion of the 4f features is found in $CeBe_{13}$ [54] ($T_K = 400\,K$), demonstrating that $\underline{k}$-dependent effects are observed in both low and high T_K materials. Again, in [54] as in [53], the $4f_{5/2}$ peak does not display a constant amplitude across the Brillouin zone as predicted by the single impurity model but, on the contrary, it exhibits periodic intensity modulations that are consistent with itinerant states. Actual dispersion of the Kondo resonance is not observed but is obtained by fitting the experimental data, resulting in a 50 meV shift of the $4f_{5/2}$ peak. Most interestingly, the spin-orbit partner of the Kondo resonance shows a dispersion that can be observed without help from the fits, between 75 and 95 meV and with a momentum dependence that is out of phase with respect to the momentum dependence obtained by fitting the $4f_{5/2}$ spectral feature. In [54] the temperature dependence of the $4f_{5/2}$ peak is also examined, the conclusion being that any dependence is completely accounted for by the conventional effects of Fermi statistics and phonon broadening, as already stated in [44, 45]. Both in [53] and [54] the data are taken at the $4d \rightarrow 4f$ resonance ($h\nu \cong 120\,eV$) and from single crystalline samples. In this regard, in [53] data from polycrystalline $CePt_3$ and single crystalline $CePt_{2+x}$ are compared and the latter clearly show an intensity at the Fermi level that is too strong to be explained within the single impurity model, especially if one considers the low T_K value of the compound ($T_K < 20\,K$). In [53], as in [44, 45], it is suggested that the agreement of the photoemission results presented in [37-40, 46] with the single impurity Anderson model may come from the polycrystalline nature of the samples. Particularly if scraped, polycrystalline samples are good candidates for having disordered surfaces and are known to give a weak intensity at the Fermi level. This could be due to the requirement of long range order at the surface in order to obtain the full intensity at E_F. Evidence of narrow 4f dispersing bands has been obtained from low energy

($h\nu = 45\,\mathrm{eV}$) photoemission measurements performed at $T \cong 20\,\mathrm{K}$ on $CeSb_2$ [45, 55, 56], a system that has an estimated T_K of $\cong 3\,\mathrm{K}$. The observed dispersion is of about 25 meV and is measured at a temperature that is nearly an order of magnitude larger than T_K. The existence of dispersion at $T > T_K$ is considered to be a direct spectroscopic evidence of the fact that the Ce 4f levels cannot be treated as isolated impurities. A similar dispersive behaviour has also been observed for the 5f electrons in U compounds [45, 55, 56, 57, 58].

Angle-resolved photoemission spectroscopy has revealed its usefulness in studying the electronic structures of correlated materials. The high resolution in energy and momentum have been mostly achieved at low photon energies. However, it is a well known fact that caution is required to discriminate possible surface effects which strongly influence the photoemission spectra because of the short mean free path of low energy photoelectrons [18]. The quality of the investigated sample surface is very important for reliable angle-resolved experiments: contamination, surface roughness and disorder can strongly influence the experimental results. Although *in situ* cleaved single crystals are know to give well ordered and contamination free surfaces, there are not many measurements performed on *in situ* cleaved single crystalline Ce compounds [25, 53-58, 59, 60], mainly because of the restricted availability of such crystals and the technical problems given by the *in situ* cleaving procedure. In the particular case of $CeNi_2Ge_2$, apart from [25], the only published angle-resolved photoemission measurements have been performed on *in situ* epitaxially grown films [61, 62, 63, 64] and mostly limited to the use of VUV He lamps as photon sources, except for [62] where the measurements are performed at the $4d \rightarrow 4f$ resonance. A breakthrough in this field has been given by the advent of high energy angle-resolved photoemission spectroscopy. To the best of our knowledge, no angle-resolved photoemission measurement has been performed so far on the remaining compounds under investigation in this study, namely $CeCu_2Ge_2$ and $CeCo_2Ge_2$. In order to shed a new light on the momentum-dependent behaviour of heavy Fermion Ce compounds, we have performed bulk sensitive, angle-resolved photoemission spectroscopy measurements of the valence band of $CeCo_2Ge_2$. Again, this particular compound is chosen because of its value of T_K, that allows us to perform a temperature dependent study with spectra recorded both above and below T_K. In the following, data obtained from two samples of the same compound will be discussed. Particular attention has been devoted to faithfully reproduce the experimental conditions during the different experimental runs. However, because of the effects of the cleaving procedure on the samples, a one-to-one direct comparison between results coming from different cleaves has to be done carefully. In particular, it is observed that from cleave to cleave the general features are reproduced but the details of the spectra vary. In both cases, as described at the beginning of this section, the samples are cleaved at T=20K. The single crystallinity of the cleaved samples is checked with the use of low energy electron diffraction (LEED), a technique that is also used to choose the high symmetry direction to be measured in $\underline{k}$-space. During the first experiment both non-resonant and resonant valence band measurements have been performed, with $h\nu = 570\text{eV}$ and $h\nu = 882\text{eV}$ respectively. In both measurements the temperature is kept at T=20K and the combined energy resolution is better than the nominal value of $\Delta E = 220\,\text{meV}$. From the value of the lattice constants given in Table 1, the zone boundaries along both directions are found at ${}^{2\pi}\!/_{a} = 1.54\,\text{Å}^{-1}$ and ${}^{2\pi}\!/_{c} = 0.62\,\text{Å}^{-1}$ respectively. Therefore, if $V_0 = 13.18\text{eV}$ is used as a value for the inner potential [25], in agreement with equation (2.9) $h\nu \cong 570\text{eV}$ corresponds to the Γ high symmetry point along the $\underline{k}_z$ direction that is the direction perpendicular to the sample's surface. For the resonant measurement the incoming photon energy is determined by following the procedure described in section 3.4.1 and $h\nu \cong 882\text{eV}$ corresponds to a point that is approximately half way between Γ and the next high symmetry point along the same direction that is Z. A sketch of the first Brillouin zone of a body centred tetragonal lattice is shown in Figure 3.26. Because of the chosen orientation of the sample (see LEED pattern in Figure 3.9) the electron analyser collects photoelectrons that are emitted in the $\Gamma - N - Z$ plane, within an emission angle ϑ of approximately $\pm 7.25^{\circ}$ with respect to the $\underline{k}_z$ axis.

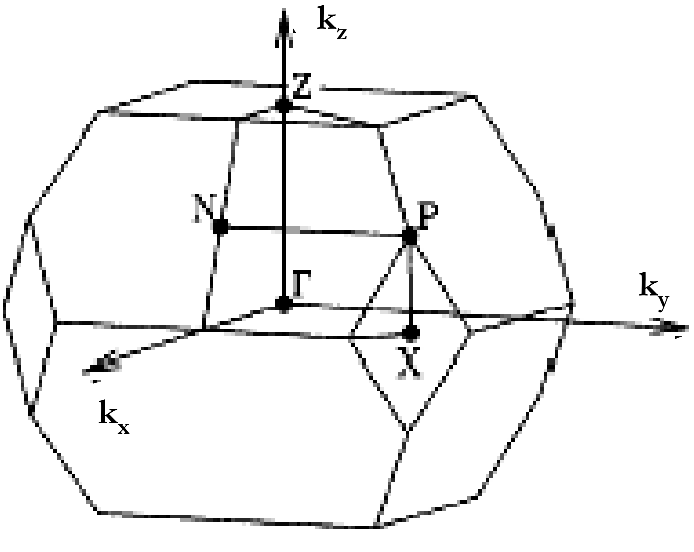

Figure 3.26: Brillouin zone of the centred tetragonal structure with high symmetry points. The photoemission data are taken at $\underline{k}$ points in the Γ-N-Z plane. $\underline{k}_z$ is parallel to the surface normal.

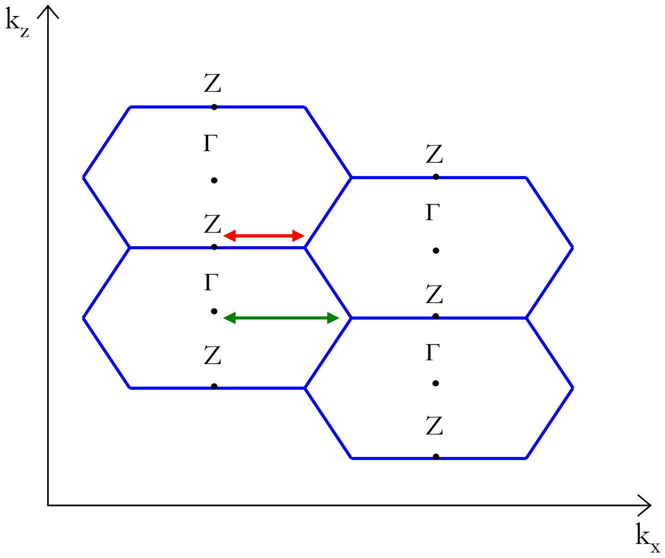

Figure 3.27: cut through four neighbouring Brillouin zones in the in the $\underline{k}_z$ - $\underline{k}_x$ plane. The red and green arrows indicate the distances between the high symmetry points and the zone boundary.

In the direction perpendicular to $\underline{k}_z$ the distance between the centre of the Brillouin zone and the zone boundary varies by changing the incoming photon energy. From simple geometrical considerations the distance between the Z point and the zone boundary along a direction that is parallel to $\underline{k}_x$ can be calculated and is approximately 1.2 Å^{-1}. According to equation (2.5) the zone boundary is reached and crossed for both the measurements taken with $h\nu \cong 570\text{eV}$ and $h\nu \cong 882\text{eV}$ respectively. For $k_{par} = 0\,\text{Å}^{-1}$ the electrons leave the sample in normal emission conditions, i. e. along the $\underline{k}_z$ direction, and with respect to $k_{par} = 0\,\text{Å}^{-1}$ the images are symmetric. However, in Figures 3.28 and 3.29, due to a slight misalignment of the tilt angle, β, the spectra are not centred in the image. Added to this, the binding energy window differs from one measurement to the other. In particular, because of our desire to investigate the Kondo behaviour of the system, in the resonant measurement we focus our attention on the near-E_F region. In Figure 3.28 the results obtained with $h\nu \cong 570\text{eV}$ are shown: a feature, whose intensity is strongest close to the zone centre ($k_{par} = 0\,\text{Å}^{-1}$), is observed dispersing between approximately 0.7 eV and 1.1 eV binding energy. From the known values of the photoionisation cross-sections at $h\nu \cong 570\text{eV}$ [18], we assign this feature mainly to the Co 3d conduction electrons. However, because of the absence of such a well defined peak in a reference valence band spectrum measured at the Co resonance and not shown here, this structure is believed to arise from the hybridisation between the Co 3d and the Ce 4f electrons.

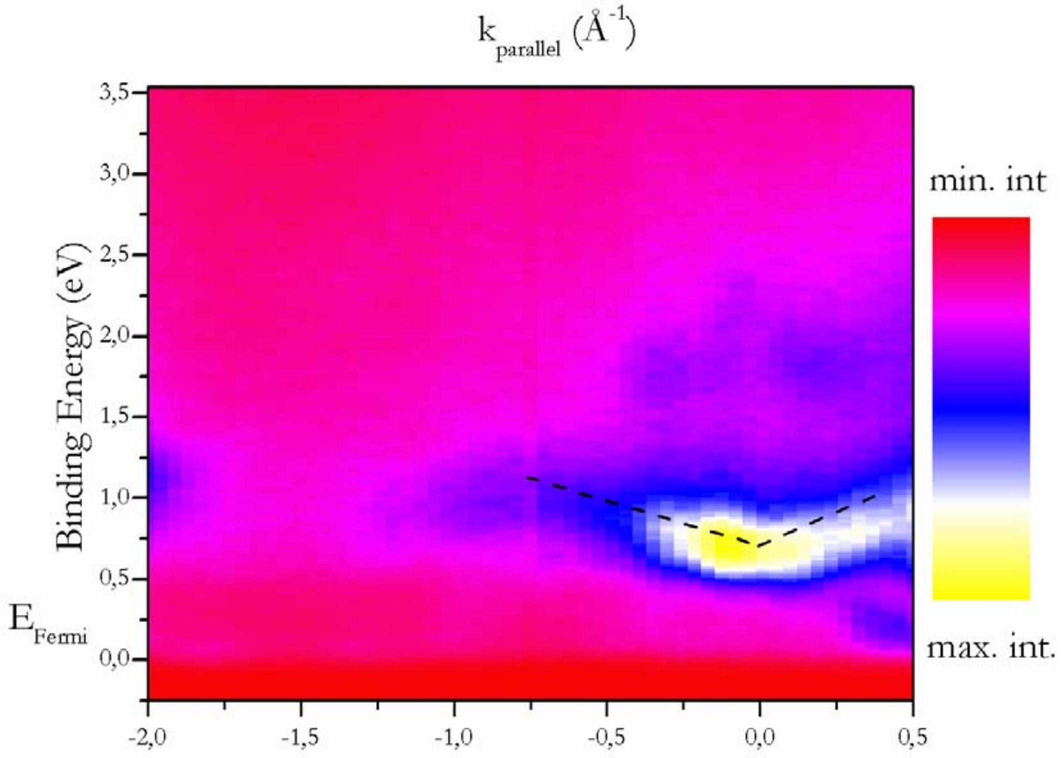

Figure 3.28: off-resonance angle-resolved photoemission data of $CeCo_2Ge_2$ taken at T=20K and $h\nu \cong 570eV$. The colour map indicates the intensity.

Figure 3.29 shows the near-E_F region measured under resonant conditions at the Ce M_5 absorption edge. Due to the strong enhancement of the Ce 4f signal, the observed spectral features have a definite 4f character. Because of the spherical geometry of the electron analyser, the entrance slit is imaged onto a slightly curved line at the detector, therefore introducing an uncertainty in determining the exact position of the Fermi edge. Since an angle-resolved energy reference spectrum has not been measured, we place the zero of energy at the midpoint of the 4f intensity edge jump. In agreement with [54], for $T < T_K$ we observe intensity modulations of the Kondo resonance, whose spectral weight is concentrated close to the centre of the Brillouin zone at approximately 150 meV binding energy. For the same values of k_{par} a dispersion of the spin-orbit partner is observed and shown by the dashed line, with a minimum binding energy of approximately 370 meV at $k_{par} = 0\,Å^{-1}$. It should be noticed that the magnitude and the location in $\underline{k}$-space of the dispersing feature observed in Figure 3.28 are very similar to the dispersion seen here. As we move away from the centre of the zone the 4f intensity vanishes altogether. These $T = 20K$ results are in disagreement with the single impurity Anderson model that describes a $\underline{k}$-independent Kondo resonance for $T < T_K$. On the contrary, our data seem to suggest that at low temperatures the nature of this spectral feature varies throughout the Brillouin zone.

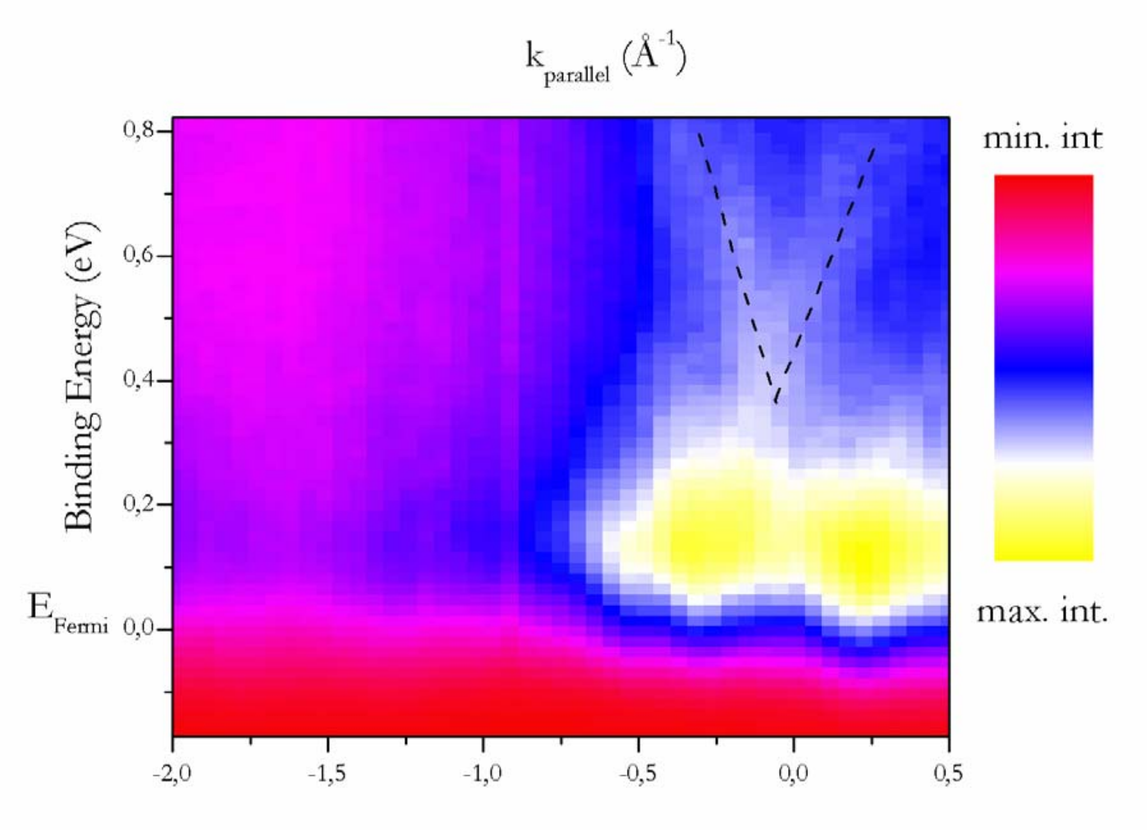

Figure 3.29: on-resonance angle-resolved photoemission data of $CeCo_2Ge_2$ taken at T=20K and $h\nu \cong 882eV$. The colour map indicates the intensity.

Motivated by the previous results, we have performed a second set of angle-resolved measurements with the aim to investigate the $\underline{k}$-dependence of the near-E_F 4f intensity as a function of the temperature. The results shown below in Figures 3.30, 3.33 and 3.34 are obtained for T=30K, 120K and 180K, i.e below, at and above T_K respectively. Due to a better alignment of the sample, the analyser collects photoelectrons that are emitted within an equal angular interval with respect to the normal to the sample's surface giving images that are centred with respect to $k_{par} = 0\,Å^{-1}$. In order to perform a direct comparison between the temperature dependent measurements, the data are normalised to the non-f background below the Fermi level. In Figure 3.30, like in the previous low temperature measurements (see Figure 3.29), the majority of the 4f intensity is concentrated within $\pm 0.6\,Å^{-1}$ around the zone centre and decreases as we move away from it. This can be seen in Figure 3.31, where the energy distribution curves are plotted for different values of k_{par} in the top graph. These plots are qualitatively equivalent to the angle integrated results discussed in Section 3.4.2 . However, they are given only by the photoelectrons that are collected within a narrow angular range centred around the value of k_{par}, whereas the angle integrated results are obtained by integrating the intensity over the entire angular range accepted by the electron analyser. It is clearly observed that for T=30K the spectral intenstiy of the Kondo resonance varies as a function of k_{par} and is maximum for $k_{par} = 0.4\,\text{Å}^{-1}$. The same effect can be seen in the bottom graph, where the intensity of the Kondo resonance is plotted as a function of k_{par}. The observed $\underline{k}$-dependent effects are not as marked as in Figure 3.29 and although the intensity coming from the spin-orbit partner of the Kondo resonance is visible, it is not clearly defined as a separate feature and dispersion is not observed. This is probably due to a different quality cleave, to a not as good energy resolution, or both. As the temperature is increased to T=120K, the $\underline{k}$-dependent intensity modulation of the Kondo resonance is still visible but less pronounced, whereas for T=180K the 4f intensity is close to being a constant function of k_{par}. As for the low temperature measurement, the momentum dependence is clearly observed in Figures 3.32 and 3.35, for T=120K and T=180K respectively.

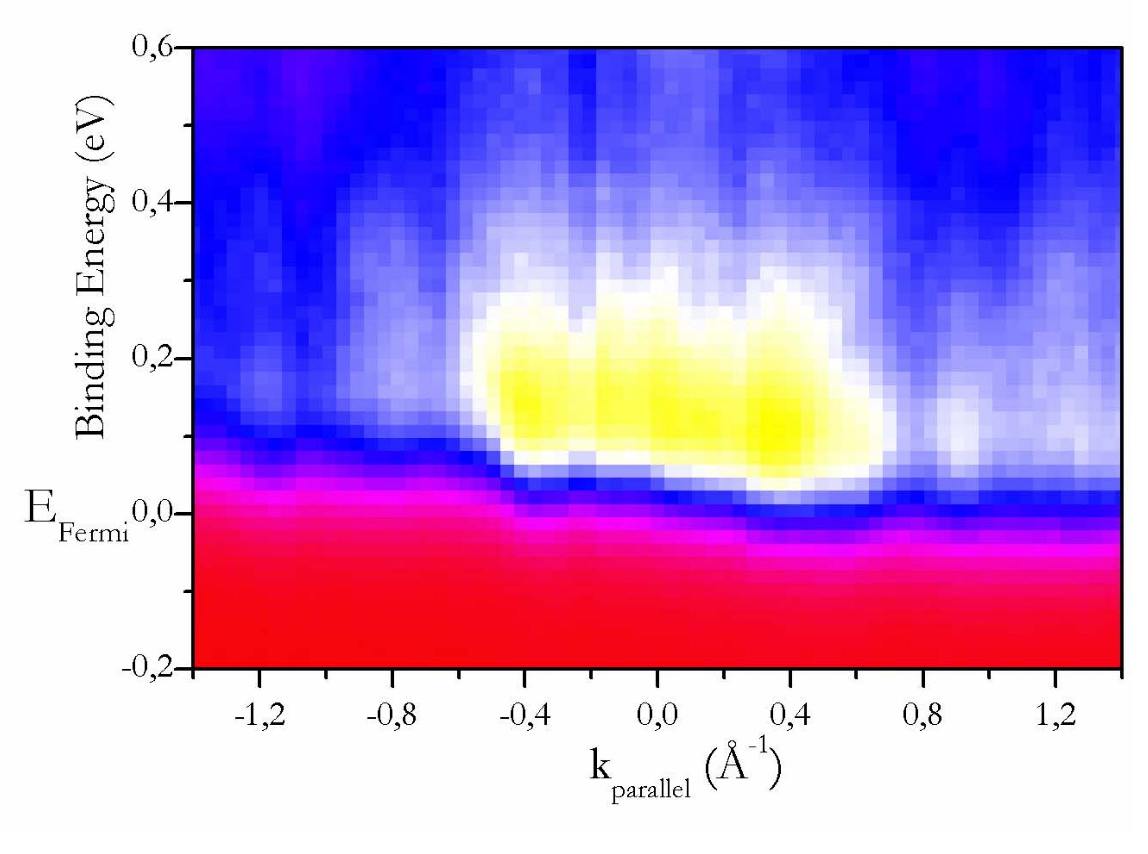

Figure 3.30: on-resonance angle-resolved photoemission data of $CeCo_2Ge_2$ taken at T=30K and $h\nu \cong 882eV$. The colour map is as for Figures 3.28 and 3.29.

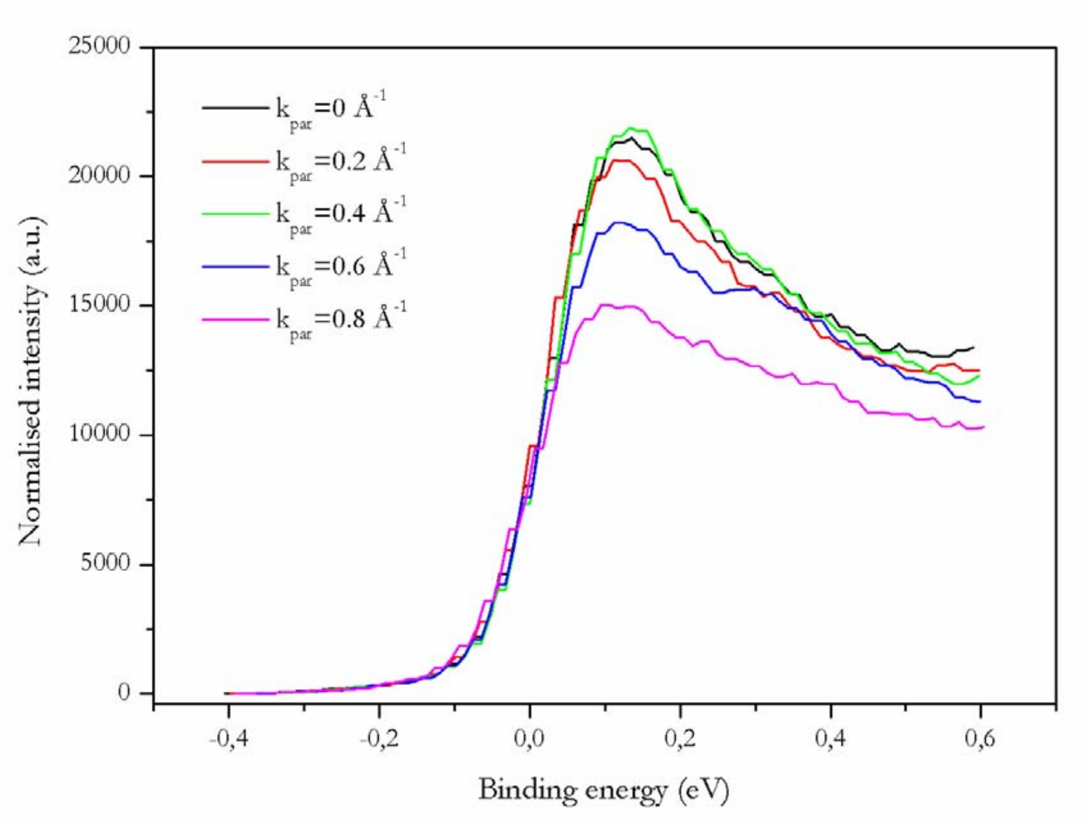

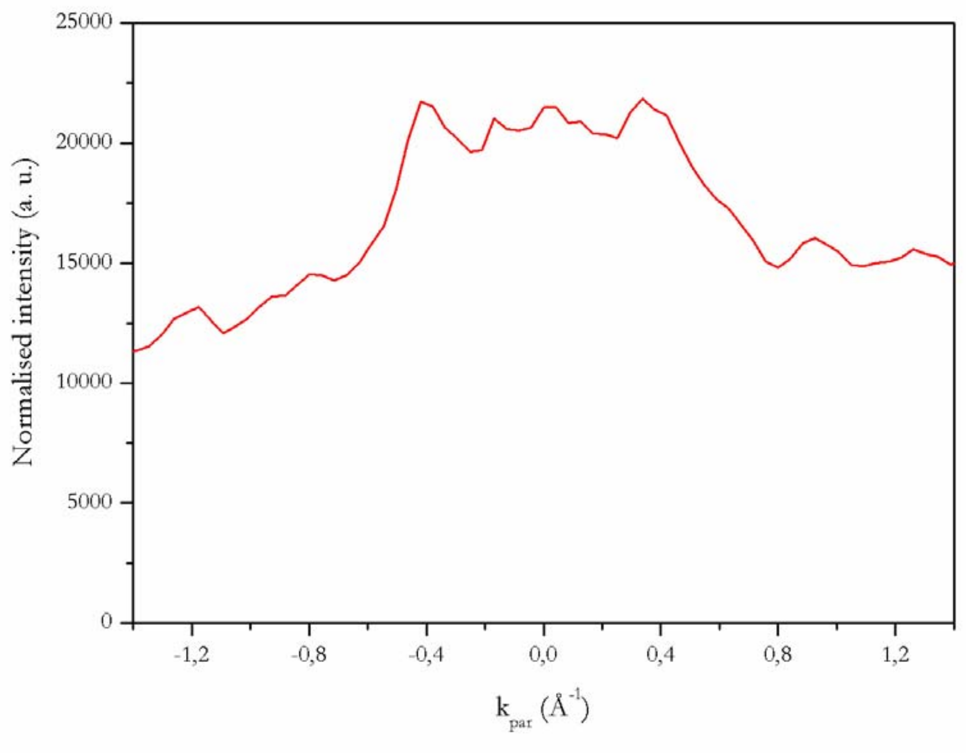

Figure 3.31. Top: $CeCo_2Ge_2$ energy distribution curves measured for different values of k_{par}. E_F=0eV. Bottom: plot of the normalised intensity as a function of k_{par} and relative to the binding energy of the Kondo resonance. T=30K and $h\nu \cong 882eV$.

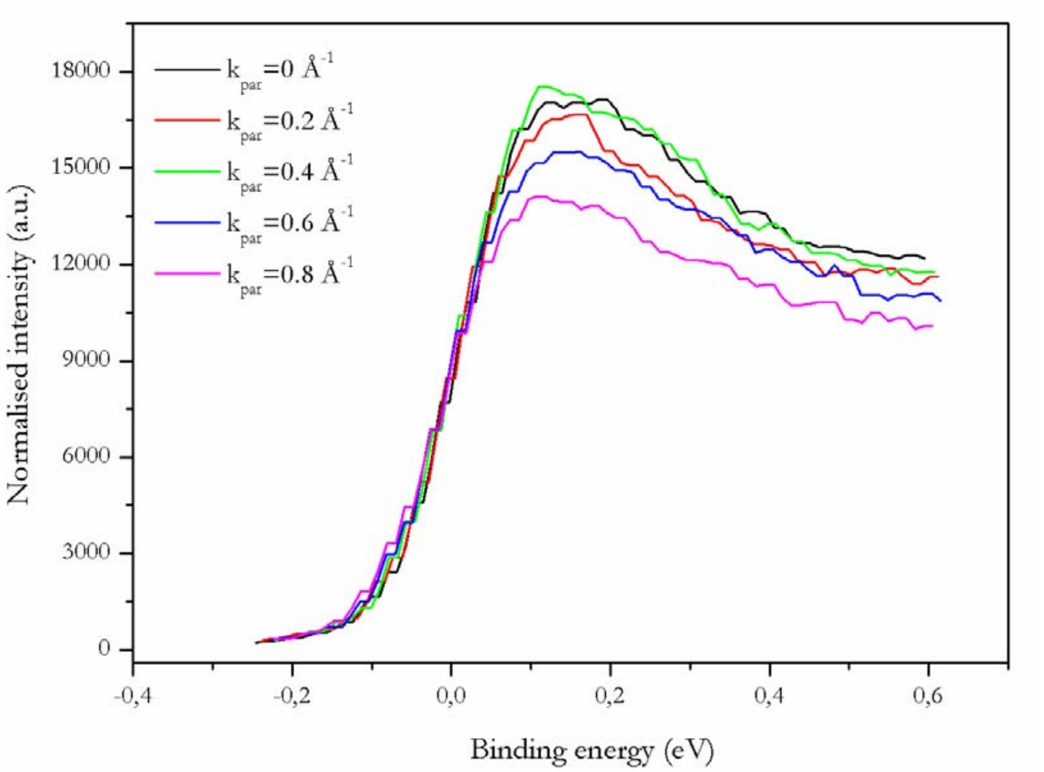

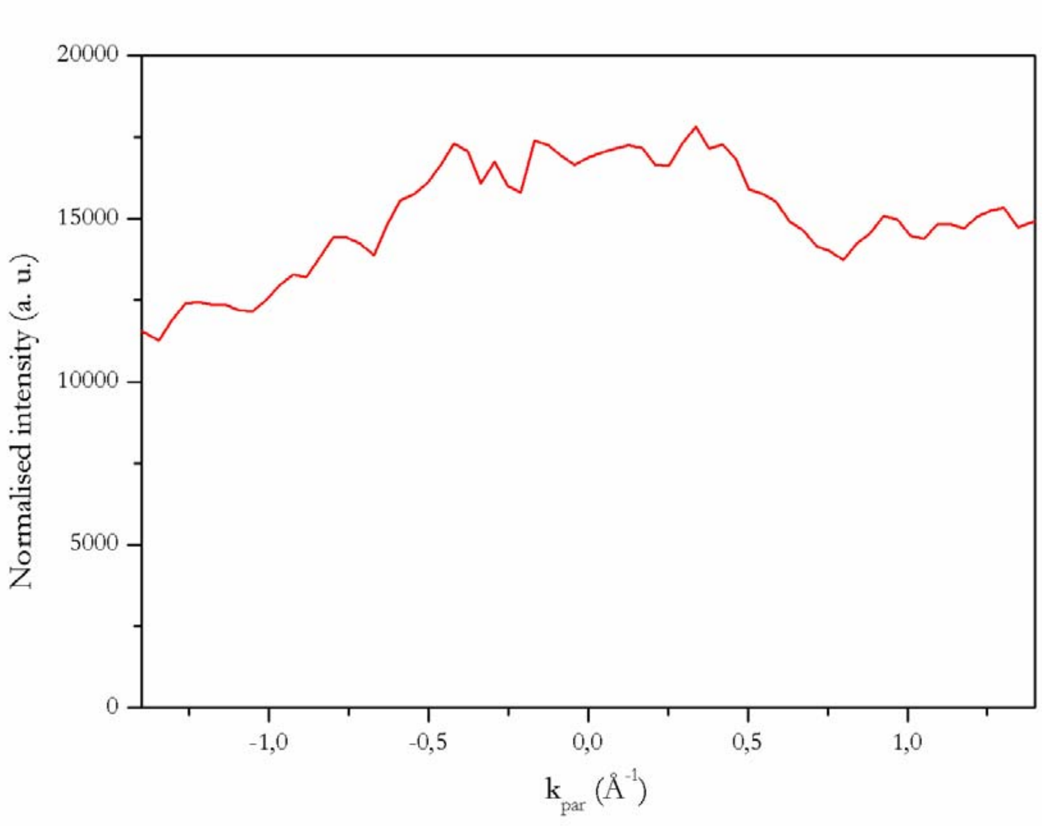

Figure 3.32. Top: $CeCo_2Ge_2$ energy distribution curves measured for different values of k_{par}. $E_F=0$eV. Bottom: plot of the normalised intensity as a function of k_{par} and relative to the binding energy of the Kondo resonance. T=120K and $h\nu \cong 882$eV .

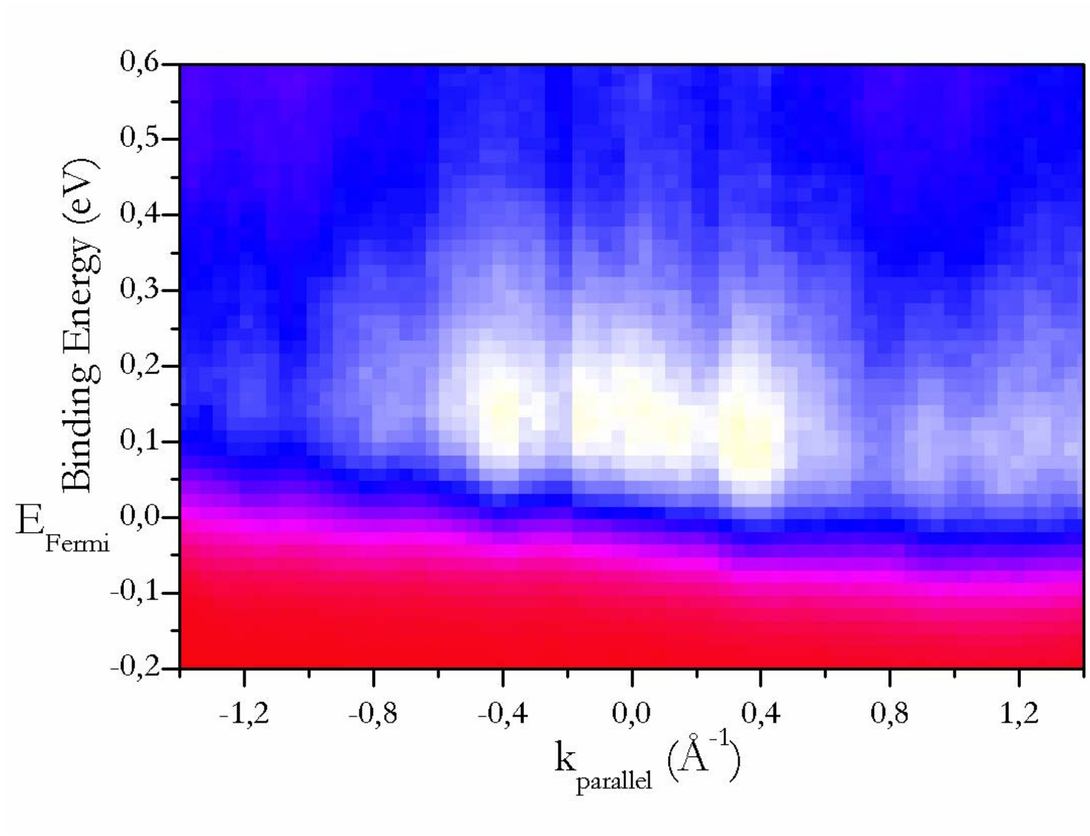

Figure 3.33: on-resonance angle-resolved photoemission data of $CeCo_2Ge_2$ taken at T=120K and $h\nu \cong 882eV$.

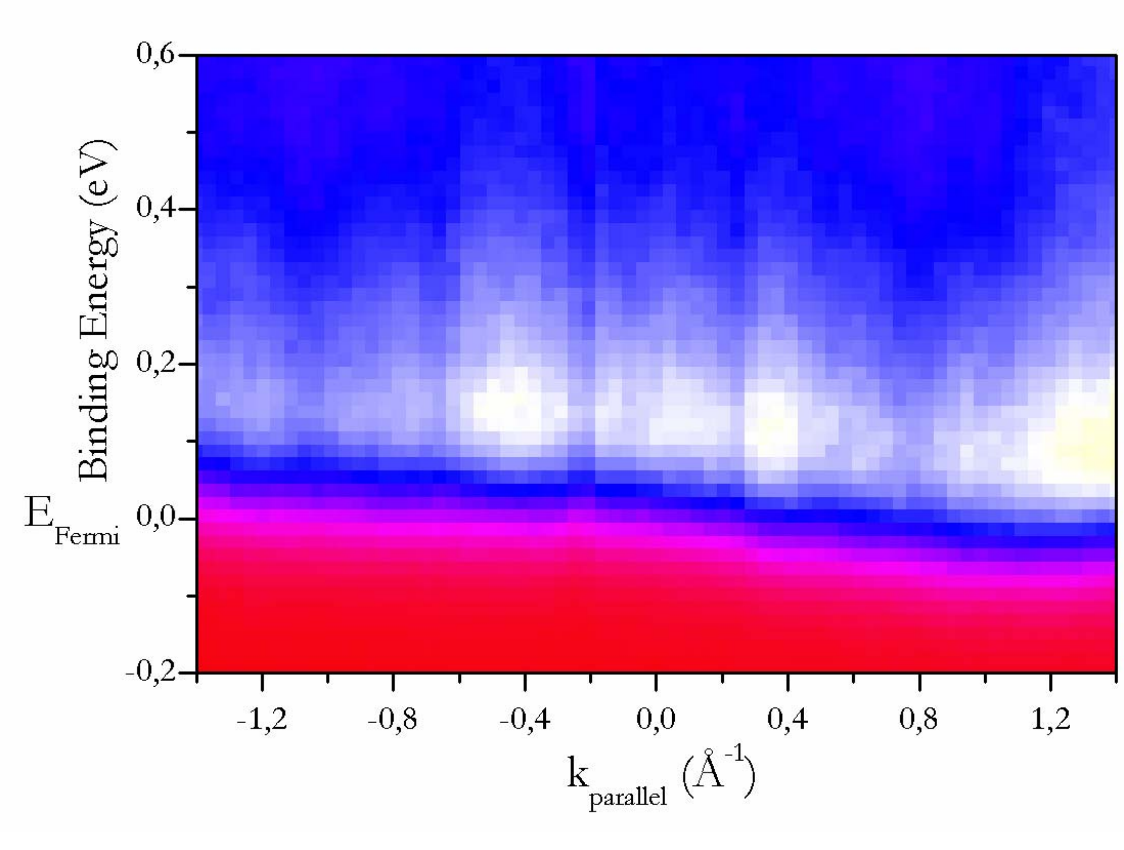

Figure 3.34: on-resonance angle-resolved photoemission data of $CeCo_2Ge_2$ taken at T=180K and $h\nu \cong 882eV$.

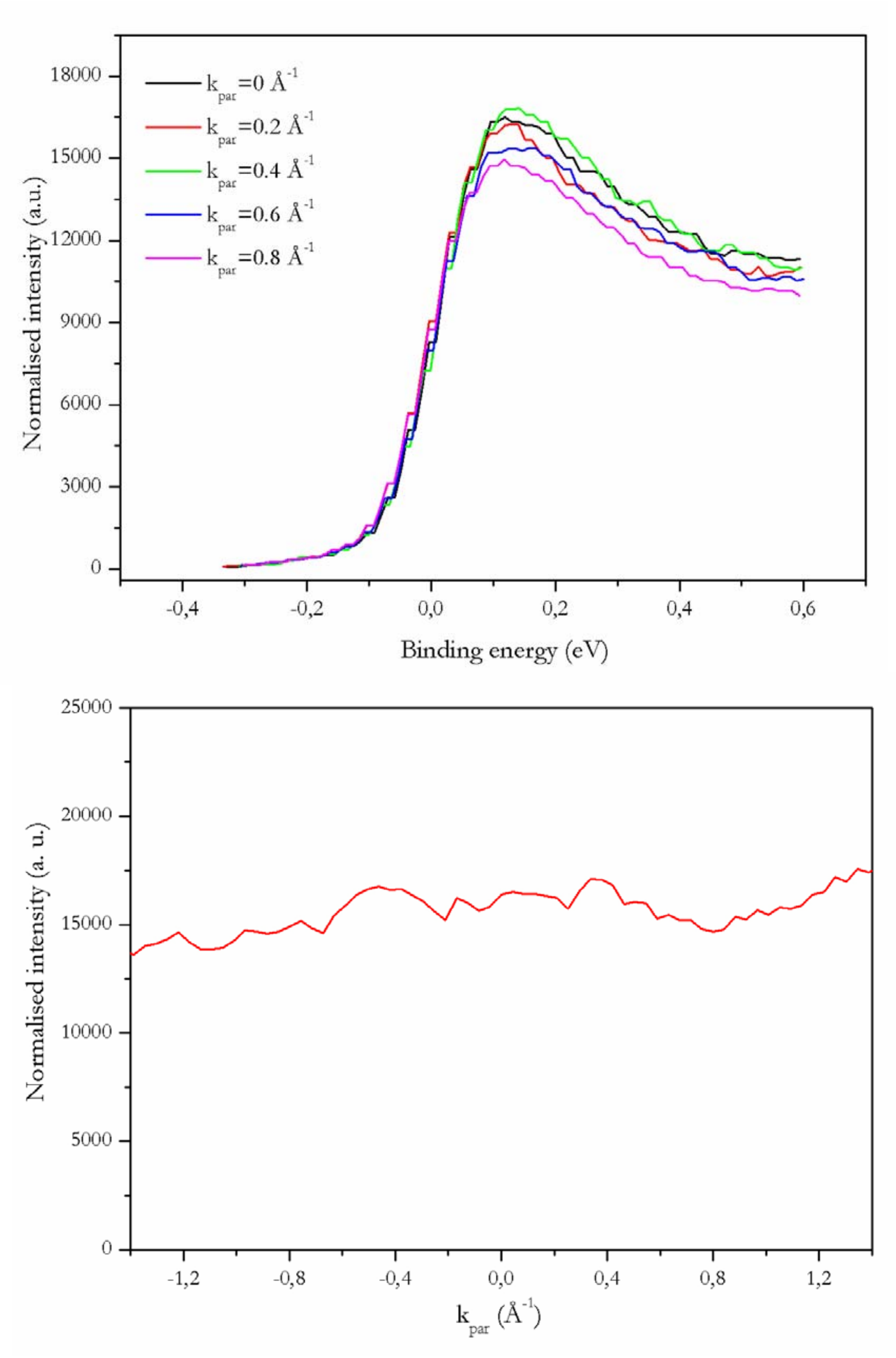

Figure 3.35. Top: $CeCo_2Ge_2$ energy distribution curves measured for different values of k_{par}. E_F=0eV. Bottom: plot of the normalised intensity as a function of k_{par} and relative to the binding energy of the Kondo resonance. T=180K and $h\nu \cong 882eV$.

Therefore, we observe a definite temperature dependence of the angle-resolved 4f intensity close to the Fermi level. In disagreement with the single impurity model momentum dependent effects are indeed observed for low temperatures. As the temperature increases from below to above T_K $\underline{k}$-dependent effects become less important suggesting that the system evolves from a situation that can be described by a more band-like approach to a single impurity framework where the 4f electrons are considered as isolated impurities. Figure 3.36 shows the energy distribution curves obtained in normal emission, i.e. at $k_{par} = 0\,\text{Å}^{-1}$, for the three investigated temperatures. The trend already observed in the statistically more accurate temperature dependent angle integrated results is reproduced. In particular, the intensity of the Kondo peak decreases markedly between 30K and 120K, witnessing the gradual destruction of the hybrid ground state on behalf of the thermally activated spin fluctuations. As in the case of the angle integrated measurements, in order to rule out effects due to diffusion of impurities from the bulk to the surface, after having heated the sample to T=180K the low temperature measurement at T=30K has been repeated. The obtained results (not shown here) are in agreement with Figure 3.30, as the intensity peaks again close to the zone centre.

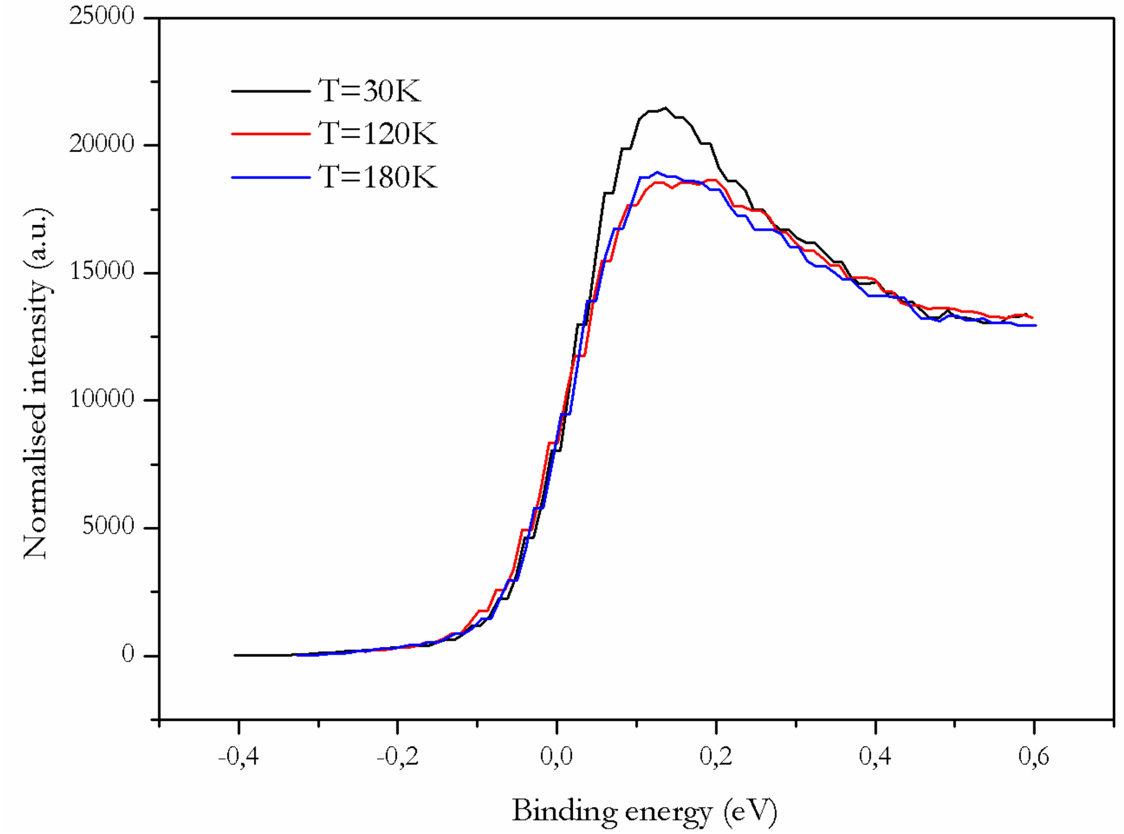

Figure 3.36: temperature dependence of the normal emission energy distribution curves. E_F=0eV.

3.5 Discussion and conclusions.

The majority of the spectroscopic data accumulated during the last two decades consistently indicates a qualitative agreement with the predictions of the single impurity Anderson model. On the basis of these results the Kondo scenario has become a widely accepted paradigm for the electronic structure of Ce-based compounds. In valence band photoemission spectroscopy, the cross-over from the low temperature regime ($T < T_K$) to the high temperature ($T > T_K$) regime is associated with a decrease of the Kondo resonance's intensity together with an increase of its line width and a smearing out of the spin-orbit partner. The physics of a single spin impurity antiferromagnetically coupled to the conduction electrons is now well understood and described by this model. Heavy Fermion materials may be considered as Kondo lattices formed by a periodic array of magnetic impurities. In general, the compensation of the f-moments by means of the Kondo effect leads to the formation of a non-magnetic ground state. However, due to the presence of the lattice, magnetic interactions between the f-moments are provided via the conduction electrons by the Rudermann-Kittel-Kasuya-Yoshida (RKKY) interaction. Therefore, the low temperature ground state of a system is a direct consequence of the competition between the Kondo effect and the RKKY interaction. From a microscopic point of view, one of the main problems lies in the failure of the single impurity Anderson model to account for the observed periodic nature of the 4f electrons. While several theoretical approaches claim to be able to account for this dispersive behaviour [65, 66, 67], at issue is which of the models captures most correctly the physics of heavy Fermion phenomena. Any successful theory must simultaneously predict the unusual low temperature thermodynamic and transport properties as well as the microscopic properties, the major question being whether or not lattice effects alter the physics described by the single impurity model. A low temperature deviation from the single impurity Kondo behaviour can be seen most easily from the temperature dependence of the electrical resistivity as shown in Figure 3.37 [68]. While impurity systems show a logarithmic increase of the resistivity towards lower temperatures, the lattice systems are characterised by a pronounced maximum for a certain characteristic temperature, T_0, and by a strong decrease of $\varrho(T)$ below this temperature.

The periodic Anderson model (PAM) [69, 70, 71] retains the physics of the single impurity problem but is further complicated by the interactions between the impurity moments within the lattice. Added to this, and most importantly for us, it is able to account for the periodic nature of the f electrons.

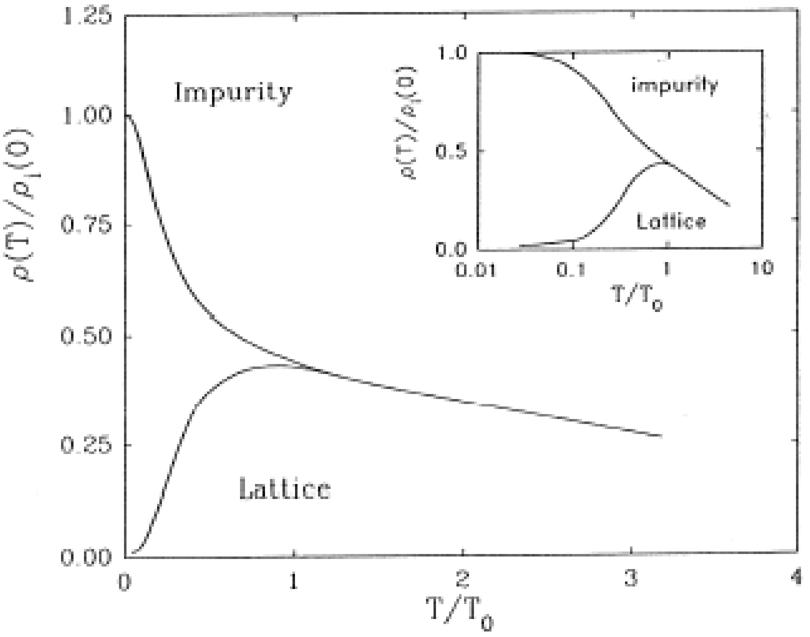

Figure 3.37: temperature dependence of the electrical resistivity of single impurity and lattice systems [68].

The formation of narrow f-bands within the periodic Anderson model is based on the Nozières exhaustion principle [72]. Nozières argued that since the screening cloud of a local magnetic moment involves conduction electrons within $k_B T_K$ from the Fermi level, only a fraction of the moments, typically $n_{eff} = \varrho_d(E_F)k_B T_K$, where $\varrho_d(E_F)$ is the density of states of the conduction electrons at the Fermi level, can be screened by the conventional Kondo effect. It is then proposed that the screened and the unscreened sites can be mapped onto holes and particles of an effective single-band Hubbard model. The screening clouds hop from site to site and effectively screen all the remaining moments in a dynamical fashion. The results of the periodic model strongly depend on the number of d electrons, n_d, and are consistent with a simple band-formation picture. With no hybridisation the available electronic states are a d band and two doubly degenerate f levels separated by U. When the hybridisation is turned on the Kondo resonance forms near the Fermi surface. The original d band mixes with the local f levels and the resonant level, giving rise to a renormalized band which has f-character near the renormalized f level energies and has d-character far from them. Therefore, the f-like portion of the renormalised band exists only in a part of the zone. Where exactly this is, depends on the system and ultimately on the filling of the conduction band. In particular, the Kondo states below the Fermi level are only present for $\underline{k}$ near the zone centre when $n_d < 1$ and $\underline{k}$ near the zone corner when $n_d > 1$. Much of this can be seen in Figure 3.38 where the model calculations are shown for the metallic state with $n_d < 0.8$ (where $n_d = 1$ when the conduction band is half filled).

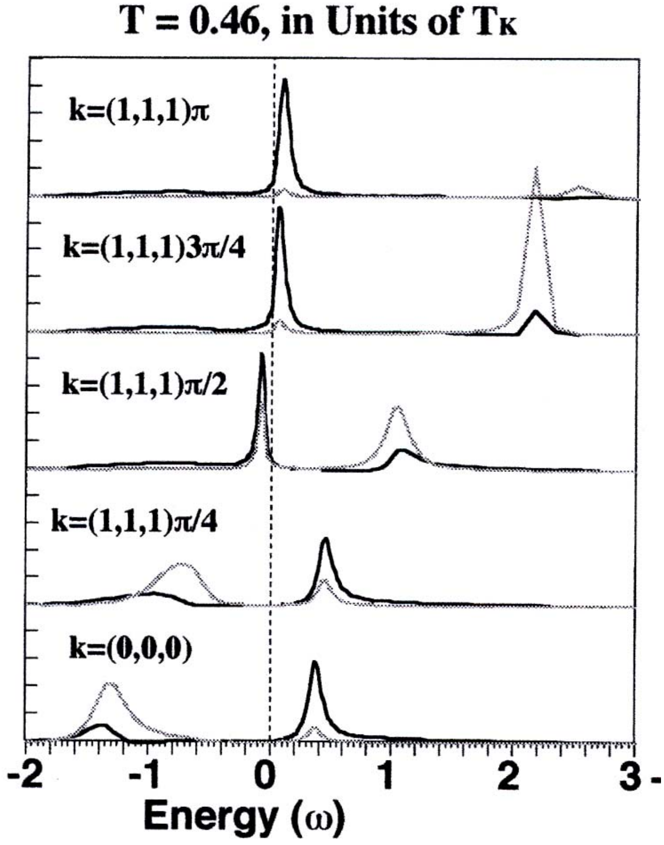

Figure 3.38: periodic Anderson model f (dark line) and d (light line) spectral functions calculated for various vectors along the diagonal of a simple cubic zone. Both the f and d features are sharp at the Fermi level but as the band moves below E_F (dashed line) it becomes mostly d-like [70].

The f-d renormalised band is shown for various momenta in a simple cubic Brillouin zone. There is no f-intensity at E_F for $\underline{k} = (0,0,0)$, i.e. at the zone corner, where the Kondo states are essentially unoccupied and the main contribution to the occupied states has a d-character. The Kondo states below the Fermi level develop only as the centre of the zone, reached by $\underline{k} = (1,1,1)\pi/2$, is approached. The localisation of the 4f intensity close to the centre of the zone, as observed from our angle-resolved measurements, is therefore well described by the periodic model and a single impurity approach is not sufficient. In particular, the decrease of the 4f intensity away from the zone centre is understood as a dispersion of the Kondo resonance above the Fermi level and a loss of f-admixture in the band below E_F.

Our angle integrated photoemission spectroscopy data, together with the X-ray absorption results, are in qualitative agreement with the single impurity Anderson model. In particular, the scaling of the $4f^1$ final state intensity with T_K and the decrease of this intensity as the temperature is increased towards and above the Kondo temperature have been verified. These experimental results are consistent with the idea that a many body ground state is generated by the hybridisation between the localised 4f electrons and the itinerant conduction electrons and that T_K is a measure of such a hybridisation. However, the angle-resolved measurements performed on $CeCo_2Ge_2$ require an extension of such an interpretation, as $\underline{k}$-dependent intensity modulations are observed for the Kondo resonance. Within the single impurity model the Kondo peak is considered to be a momentum-independent feature. The more complicated impurity screening mechanism suggested by the periodic Anderson model is able to explain the observed directional character of the near-E_F 4f intensity. This model retains the underlying physics of the single impurity approach, such as the intensity scaling with T_K, the temperature dependence and indeed the disappearance of the singlet ground state state upon heating above T_K. The periodic model is also consistent with the idea that, for a measured value of T_K and because of the itinerant character of the screening clouds, the hybridisation between the f and the conduction electrons is actually stronger than assumed within the single impurity model. Therefore, the local moment description is valid for temperatures that are higher than the values predicted by the single impurity model. The periodic model would therefore be able to explain the experimental observation of $\underline{k}$-dependent 4f features both below and above T_K. From our data we cannot say that at T=180K, i.e. at $T > T_K$, momentum dependent effects are observed. On the contrary for this temperature we suggest a local moment description. However, at T=120K the cross over from the many body ground state to a single impurity framework is not complete, as the 4f intensity still peaks slightly close to the zone centre (see bottom plot in Figure 3.32), reflecting the renormalised band character described by the periodic model. This leads us to suggest that, because of the introduction of the lattice, the screening of the 4f impurities takes place on a wider temperature scale and that the different magnetic ions on the regular lattice sites are decoupled from each other for temperatures that are higher than the temperature originally suggested by the single impurity model.

[1] J. W. Allen, S. J. Oh, O. Gunnarsson, K. Schönhammer, M. B. Maple, M. S. Torikachvili, I. Landau, Adv. Phys. **35**, 275 (1986).

[2] D. Malterre, M. Grioni, Y. Baer, Adv. Phys. **45**, 299 (1996).

[3] J. W. Allen, Physica B **206** & **207**, 65-70 (1995).

[4] J. W. Allen, G. H. Gweon, H. T. Schek, L. Z. Liu, L. H. Tjeng, J. H. Park, W. P. Ellis, C. T. Chen, O. Gunnarsson, O. Jepsen, O. K. Andersen, Y. Dalichaouch, M. B. Maple, J. Applied Physics **87**, 6088 (2000).

[5] A. S. Edelstein, J. Magn. Magn. Mat **256**, 430-448 (2003).

[6] O. Gunnarsson, K. Schönhammer, Phys. Rev. Lett. **50**, 604 (1983).

[7] J. C. Fuggle, F. U. Hillebrecht, Z. Zolnierek, R. Lässer, Ch. Freiburg, O. Gunnarsson, K. Schönhammer, Phys. Rev. B **27**, 7330 (1983).

[8] O. Gunnarsson, K. Schönhammer, Phys. Rev. B **28**, 4315 (1983).

[9] O. Gunnarsson, K. Schönhammer, C. Fuggle, F. U. Hillebrecht, J. M. Esteva, R. C. Karnatak, B. Hillebrand, Phys. Rev. B **28**, 7330 (1983).

[10] J. C. Fuggle, F. U. Hillebrecht, J. M. Esteva, R. C. Karnatak, O. Gunnarsson, K. Schönhammer, Phys. Rev. B **27**, 4637 (1983).

[11] A. W. Lawson, T. Y. Yang, Phys. Rev. **76**, 301 (1949).

[12] L. Pauling, J. Chem. Phys. **18**, 145 (1950).

[13] J. W. Allen, R. M. Martin, Phys. Rev. Lett. **49**, 1106 (1982).

[14] M. Lavagna, C. Lacroix, M. Cyrot, J. Phys. F **13**, 1007 (1982).

[15] N. E. Bickers, D. L. Cox, J. W. Wilkins, Phys. Rev. Lett. **54**, 230 (1985).

[16] N. E. Bickers, D. L. Cox, J. W. Wilkins, Phys. Rev. B **36**, 2036 (1987).

[17] L. Duò, Surf. Sci. Reports **32**, 233-289 (1998).

[18] J. J. Yeh, I. Lindau, *At. Data Nucl. Data Tables* **32**, 1 (1985).

[19] C. Laubschat, E. Weschke, C. Holtz, M. Domke, O. Strebel, G. Kaindl, Phys. Rev. Lett. **65**, 1639 (1990).

[20] L. Braicovich, N. B. Brookes, C. Dallera, M. Salvietti, G. L. Olcese, Phys. Rev. B **56**, 15047 (1997).

[21] E. Weschke, C. Laubschat, T. Simmons, M. Domke, O. Strebel, G. Kaindl, Phys. Rev. B **44**, 8304 (1991).

[22] L. Duò, S. De Rossi, P. Vavassori, F. Ciccacci, G. L. Olcese, G. Chiaia, I. Lindau, Phys. Rev. B **54**, R17363 (1996).

[23] A. Sekiyama, T. Iwasaki, K. Matsuda, Y. Saitoh, Y. Onuki, S. Suga, Nature **403**, 396 (2000).

[24] S.-H. Yang, S. J. Oh, H.-D. Kim, A. Sekiyama, T. Iwasaki, S. Suga, Y. Saitoh, E. J. Cho, J. G. Park, Phys. Rev. B **61**, R13329 (2000).

[25] D. Ehm, F. Reinert, G. Nicolay, S. Schmidt, S. Hüfner, R. Claessen, V. Eyert, C. Geibel, Phys. Rev. B. **64**, 235104 (2001).

[26] P. Villars, L. D. Calvert, *Pearson's Handbook of Crystallographic data for Intermetallic Phases*, second edition, Vol 2, ASM International (1991).

[27] F. Steglich, J. Aarts, C. D. Bredl, W. Lieke, D. Meschede, W. Franz, H. Schäfer, Phys. Rev. Lett. **43**, 1892 (1979).

[28] F. R. de Boer, J. C. P. Klaasse, P. A. Veenhuizen, A. Böhm, C. D. Bredl, U. Gottwick, H. M Mayer, L. Pawlak, U. Rauchschwalbe, H. Spille, J. Magn. Magn. Mat. **63-64**, 91-94 (1987).

[29] G. Knopp, A. Loidl, R. Caspary, U. Gottwick, C. D. Bredl, H. Spille, F. Steglich, A. P. Murani, J. Magn. Magn. Mat. **74**, 341-346 (1988).

[30] H. Fujii, E. Ueda, Y. Uwatoko, T. Shigeoka, J. Magn. Magn. Mat. **76-77**, 179-181 (1988).

[31] G. Knopp, H. Spille, A. Loidl, K. Knorr, U. Rauchschwalbe, R. Felten, G. Weber, F. Steglich, A. P. Murani, J. Magn. Magn. Mat. **63-64**, 88-90 (1987).

[32] U. Fano, Phys. Rev. **124,** 1866 (1961).

[33] J. M. Lawerence, A. J. Arko, J. J. Joyce, R. I. R. Blyth, R. J. Bartlett, P. C. Canfield, Z. Fisk, P. S. Riseborough, Phys. Rev. B **47**, 15460 (1993).

[34] L. Duò, G. Chiaia, S. De Rossi, P. Vavassori, F. Ciccacci, I. Lindau, unpublished.

[35] T. Kashiwakura, S. Suzuki, T. Okane, S. Sato, T. Kinoshita, T. Ishii, Y. Isikawa, H. Yamagami, A. Hasegawa, Phys. Rev. B **47**, 6885 (1993).

[36] D. Purdie, M. Garnier, M. Hengsberger, Y. Baer, G. Panaccione, G. Indlekofer, C. Grupp, Solid Sate Comm. **106**, 799-803 (1998).

[37] F. Patthey, W. D. Schneider, Y. Baer, B. Delley, Phys. Rev. Lett. **58**, 2810 (1987).

[38] F. Patthey, J. M. Imer, W. D. Schneider, H. Beck, Y. Baer, B. Delley, Phys. Rev. B **42**, 8864 (1990).

[39] M. Garnier, K. Breuer, D. Purdie, M. Hengsberger, Y. Baer, D. Delley, Phys. Rev. Lett. **78**, 4127 (1997).

[40] F. Reinert, D. Ehm, S. Schmidt, G. Nicolay, S. Hüfner, J. Kroha, O. Trovarelli, C. Geibel, Phys. Rev. Lett. **87**, 106401 (2001).

[41] S. Suga, A. Sekiyama, J. Electron Spectrosc. Relat. Phenom. **124**, 81-97 (2002).

[42] A. Sekiyama, S. Suga, Physica B **312-313**, 634-639 (2002).

[43] B.-H. Choi, R.-J. Jung, S.-J. Oh, E.-J. Cho, T. Iwasaki, A. Sekiyama, S. Imada, S. Suga, T. Muro, Y. S. Kwon, J. Electron Spectrosc. Relat. Phenom. **136**, 15-20 (2004).

[44] J. J. Joyce, A. J. Arko, J. Lawrence, P. C. Canfield, Z. Fisk, R. J. Bartlett, J. D. Thompson, Phys. Rev. Lett. **68**, 236 (1992).

[45] A. J. Arko, J. J. Joyce, D. P. Moore, J. L. Sarrao, L. Morales, T. Durakiewicz, Z. Fisk, D. D Koelling, C. G. Olson, J. Electron Spectrosc. Relat. Phenom. **117-118**, 323-345 (2001).

[46] D. Malterre, M. Grioni, P. Weibel, B. Dardel, Y. Baer, Phys. Rev. B **48**, 10599 (1993).

[47] P. Vavassori, L. Duò, G. Chiaia, M. Qvarford, I. Lindau, Phys. Rev. B **52**, 16503 (1995).

[48] R.-J. Jung, B.-H. Choi, S.-J. Oh, H.-D. Kim, E.-J. Cho, T. Iwasaki, A. Sekiyama, S. Imada, S. Suga, J.-G. Park, Phys. Rev. Lett. **91**, 157601 (2003).

[49] J. C. Fuggle, M. Campagna, Z. Zolnierek, R. Lässer, A. Platau, Phys. Rev. Lett. **45**, 1597 (1980).

[50] L. Braicovich, L. Duò, P. Vavassori, G. L. Olcese, Surf. Sci. **331**-**333**, 782-786 (1995).

[51] L. H. Tjeng, S.-J. Oh, E.-J. Cho, H.-J. Lin, C. T. Chen G.-H. Gweon, J.-H. Park, J. W. Allen, T. Suzuki, M. S. Makivić, D. L. Cox, Phys. Rev. Lett. **71**, 1419 (1993).

[52] J. M. Lawerence, G. H. Kwei, P. C. Canfield, J. G. DeWitt, A. C. Lawson, Phys. Rev. B **49**, 1627 (1994).

[53] A. B. Andrews, J. J. Joyce, A. J. Arko, J. D. Thompson, J. Tang, J. M. Lawrence, J. C. Hemminger, Phys. Rev. B **51**, 3277 (1995).

[54] A. B. Andrews, J. J. Joyce, A. J. Arko, Z. Fisk, P. S. Riseborough, Phys. Rev. B **53**, 3317 (1996).

[55] A. J. Arko, J. J. Joyce, A. B. Andrews, J. D. Thompson, J. L. Smith, D. Mandrus, M. F. Hundley, A. L. Cornelius, E. Moshopoulou, Z. Fisk, P. C. Canfield, A. Menovsky, Phys. Rev. B **56**, R7041 (1997).

[56] A. J. Arko, J. J. Joyce, L. E. Cox, L. Morales, J. Sarrao, J. L. Smith, Z. Fisk, A. Menovsky, A. Tahvildar-Zadeh, M. Jarrell, Journal of Alloys and Compounds **271-273**, 826-830 (1998).

[57] J. D. Denlinger, G. H. Gweon, J. W. Allen, C. G. Olson, M. B. Maple, J. L. Sarrao, P. E. Armstrong, Z. Fisk, H. Yamagami, J. Electron Spectrosc. Relat. Phenom. **117**-**118**, 347-369 (2001).

[58] T. Takahashi, J. Electron Spectrosc. Relat. Phenom. **117**-**118**, 311-321 (2001).

[59] H Kumigashira, S. H. Yang, T. Yokoya, A. Chainani, T. Takahashi, A. Uesawa, T. Suzuki, O. Sakai, Phys. Rev. B **54**, 9341 (1996).

[60] S. Souma, Y. Iida, T. Sato, T. Tagahashi, S. Kunii, Physica B **351**, 283-285 (2004).

[61] B. Schmied, M. Wilhelm, U. Kübler, M. Getzlaff, G. H. Fecher, G. Schönhense, Surface Science **377**-**379**, 251-255 (1997).

[62] M. Getzlaff, B. Schmied, M. Wilhelm, U. Kübler, G. H. Fecher, J. Bansmann, L. Lu, G. Schönhense, Phys. Rev. B **58**, 9670 (1998).

[63] G. H. Fecher, B. Schmied, G. Schönhense, J. Electron Spectrosc. Relat. Phenom. **101-103**, 771-776 (1999).

[64] G. H. Fecher, B. Schmied, A. Oelsner, G. Schönhense, J. Electron Spectrosc. Relat. Phenom. **114-116**, 747-752 (2001).

[65] P. Strange, D. M. Newns, J. Phys. F **16**, 335 (1986).

[66] Q. G. Sheng, B. R. Cooper, Phil. Mag. Lett. **72**, 123 (1995).

[67] S. H. Liu in: K. A. Gschneidner, L. Eyring, *Handbook on the Physics and Chemistry of Rare Earths*, Vol. **17**, pp. 87-148, North-Holland, Amsterdam (1993).

[68] E. Bauer, R. Hauser, Lecture given at the Vienna University of Technology, summer semester, 2003.

[69] A. N. Tahvildar-Zadeh, M. Jarrel, J. K. Freericks, Phys. Rev. B **55**, R3332 (1997)

[70] A. N. Tahvildar-Zadeh, M. Jarrel, J. K. Freericks, Phys. Rev. Lett. **80**, 5168 (1998).

[71] A. J. Arko et al in: K. A. Gschneidner, L. Eyring, *Handbook on the Physics and Chemistry of Rare Earths*, Vol. **26**, pp. 265-382, North-Holland, Amsterdam, (1999).

[72] P. Nozières, Eur. Phys. J. B. **6**, 447 (1998).

Conclusions

The main aim of this thesis has been to shed light on the potentialities, the experimental requirements and the limitations of soft X-ray angle-resolved photoemission spectroscopy.

The investigation performed on the (001) surface of Ag described in Chapter 2, adresses several questions regarding the application of the technique in this energy range, such as the role of the photon momentum, the applicability of the free-electron-like final state approximation and the feasability of performing accurate band mapping. For all the investigations described in this thesis an experimental geometry where the photoelectron emission plane is orthogonal to the plane defined by the incoming photon beam and the normal to the sample's surface has been chosen. Refering to Figure 2.7 that shows the experimental geometry used in this thesis, if the chosen azimuthal angle is $\varphi = 0^{\circ}$, the photon momentum has no component along the [100] crystallographic direction. In order to take into account the momentum transferred along the [001] direction, the free-electron-like final state approximation is modified by simply adding a factor $k_{h\nu}\cos\psi$ to the expression that is generally used in the low energy range, where ψ is the angle of incidence of the light with respect to the sample's normal. By doing so, equation (2.18) that describes the variation of $\underline{K}_{perp}$ with photon energy along the direction that is normal to the sample's surface, accurately follows the experimental determination of the high symmetry points along this direction. For a given value of $h\nu$ the effect of the photon momentum along the [010] direction is to "kick" the photoelectron in a direction that is perpendicular to the probed high symmetry direction. This effect is corrected for during the initial alignment procedure discussed in the beginning of Section 2.3 and shown in Figure 2.8. Nervertheless, in order to perform accurate band mapping, the magnitude of the photon momentum along the [010] direction should be minimised by choosing a small angle of incidence of the light with respect to the normal to the sample's surface. By choosing $\psi = 35^{\circ}$, a precise determination of the electronic structure along four high symmetry directions is obtained by probing two different azimuthal angles, $\varphi = 0^{\circ}$ and $\varphi = 45^{\circ}$, for both $h\nu = 551\text{eV}$ and $h\nu = 698\text{eV}$ with T=20K. If along with band mapping one is also interested in the exploitation of the polarisation of the incoming photon beam, a more careful choice of the angle of incidence, ψ, is required. For example, a normal incidence geometry would allow for the most accurate investigation of the high symmetry directions belonging to the crystallographic plane of the sample but, given the absence of a component of the polarisation vector along the direction normal to the sample's surface, a full polarisation dependent study would not be possible. Therefore, an appropriate compromise must be found. The angle of incidence chosen for the experimental set up described in this thesis not only allows to determine the electronic structure of the investigated crystal, but is also large enough to show a clear distinction between the two orthogonal polarisations of the light, hence the symmetry of the probed initial states can be determined. In the particular case of circular dichroism in the angular distribution of the emitted photoelectrons (CDAD), the basic ingredient for its observation is the non-coplanar arrangement of the photon momentum, the normal to the sample's surface and the wave vector of the outgoing photoelctron. Therefore, an experimental geometry like the one used here, where the emission plane is orthogonal to the plane defined by the photon beam and the [001] direction, is essential. Finally, bearing in mind that one of the main motivations behind the choice of such a well known sample comes from the desire to compare our experimental results with recent calculations of angle-resolved photoemission spectra obtained for these relatively high incoming photon energies [1], it should not be overlooked that the spectra shown in Figure 2.34 are the very first results of this kind. In as much, the qualitative agreement with the experimental results is all the more promising.

Despite the accuracy of the experimental results obtained at low temperature (T=20K) for $h\nu = 551\text{eV}$ and $h\nu = 698\text{eV}$, the temperature and photon energy dependent study also discussed in Chapter 2 clearly shows the onset, in the high T and $h\nu$ range, of the non-direct transtions caused by the breakdown of the $\underline{k}$-conservation laws. In equation (2.16) the effects of temperature and photon energy on the direct transition intensity are treated through the Debye-Waller factor, the important parameters being the mean square displacement of the atoms within the crystal, $U^2(T)$, and the reciprocal lattice vector involved in the direct transition, $\underline{G}$. The magnitude of $U^2(T)$ increases with temperature giving rise to a finite probability of electron scattering due to the phonons. Hence the appearance of transitions in which the electron momentum is not conserved and the subsequent decrease of the direct transition intensity. The increase of the incoming photon energy, and therefore of $\underline{G}$, effects the direct transition intensity in a similar way. In particular, for a finite value of T, the increase of $h\nu$ gives rise to an overall modification of the photoemission spectrum and apparent energy shifts of the direct transition peaks are observed. The higher $h\nu$, the steeper the free-electron-like final state expressed by equation (2.6), the more important this effect will be. Our results show that the contribution of the non-direct transitions is indeed controlled by a delicate balance between $h\nu$ and T. The results displayed in Figures 2.17-2.21 show that the direct transitions are dominant for both T=20K and T=100K when $h\nu = 428\text{eV}$ and $h\nu = 703\text{eV}$. When probing the system with $h\nu = 1042\text{eV}$ the contribution of the direct transitions is distinguishable only for T=20K. Refering to the values of the Debye-Waller factor, W, listed in Table 2b of Chapter 2, our data suggest that the effects of increasing photon energy and temperature are somewhat underestimated by the model. A possible explanation can be found in [2, 3] where it is shown that even the so-called direct transitions always contain a significant non-direct contribution. The results discussed in Chapter 2 show that precise soft X-ray band mapping is possible if restricted to a rather small range of temperatures and photon energies. In particular, for a given value of the Debye temperature, ϑ_D, the higher the incoming photon energy, the lower the temperature required for an accurate determination of the band structure.

Given the location of the Cerium $3d \rightarrow 4f$ absorption edge ($h\nu = 880\text{eV}$) within the soft X-ray range and the different surface and bulk electronic properties [4], Cerium and its compounds can be viewed as ideal systems on which to exploit the higher bulk sensitivity of resonant soft X-ray photoemission spectroscopy. The conclusions regarding whether or not the single impurity Anderson model is capable of describing the low temperature behaviour of the iso-structural Ce compounds, $\mathrm{CeCu_2Ge_2}$, $\mathrm{CeNi_2Ge_2}$, $\mathrm{CeCo_2Ge_2}$, have already been discussed in Section 3.5 of Chapter 3. With regards to the validity of resonant angle-resolved photoemission spectroscopy as an appropriate tool for studying the electronic structure of solids, here it is important to remember that a wave vector dependent intensity variation of the Kondo resonance is observed, together with a clear dispersion of the spin-orbit partner as shown in Figure 3.29. Therefore, in agreement with [5], we conclude that despite the interference that takes place during the resonance process, the wave vector information is not lost. If compared to the use of the Ce $4d \rightarrow 4f$ absorption edge found at approximately $h\nu = 120\mathrm{eV}$, where the inelastic mean free path of the outgoing photoelectrons is close to its minimum, the exploitation of the higher energy $3d \rightarrow 4f$ edge gives rise to more bulk sensitive results. Added to this, the observed enhancement of the 4f signal (slightly more than one order of magnitude, see Figure 3.15) has made the classical on-resonance/off-resonance spectrum subtraction unnecessary for isolating the 4f contribution to the photoemitted intensity. As already commented on many times before, the photoionisation cross sections decrease with increasing photon energy [6]. This is especially so in the case of the Ce 4f electrons, whose cross section decreases more than two orders of magnitude between $h\nu = 120\mathrm{eV}$ and $h\nu = 880\mathrm{eV}$. Therefore, especially for angle-resolved measurements, a high photon flux is required. This is all the more difficult to achieve as high energy resolution is also a must. For example, in the case of the temperature dependent angle-resolved study presented in Figures 3.30, 3.33 and 3.34, in order to measure the same cleaved sample for the three investigated temperatures, a compromise between photon flux and energy resolution has been made. In particular, to avoid contamination caused by a too long acquisition time, the choice of a relative high photon flux has prevailed over the energy resolution requirement, giving rise to spectra with a nominal energy resolution of $\Delta E \cong 220\mathrm{meV}$, where a clear distinction between the Kondo resonance and its spin-orbit partner is not possible. Such a distinction is instead observed in the angle-integrated spectra, for which, thanks to the integration of the photoemitted intensity over the angular acceptance of the electron analyser, a lower incoming photon flux has been chosen in favour of a better energy resolution (better than the nominal value of $\Delta E \cong 180\mathrm{meV}$). In order to perform the mentioned temperature dependent angle-resolved investigation with an energy resolution that is comparable to the value used for the angle-integrated measurements, the photon flux at the sample decreases by approximately a factor of four. Gaining in energy resolution, without having to compromise on the incoming flux, would essentially require improving the beamline, for example by having a better vertical focusing of the beam onto the entrance slit of the monochromator, a higher reflectivity of the optics and a better efficiency of the gratings. Obviously, an additional undulator coupled to a higher ring current would also greatly contribute.

One of the main lessons that has been learnt from the studies presented in this thesis regards the necessity of good quality single crystalline samples and the particular attention that must be devoted to their preparation. Additional soft X-ray angle-resolved investigations of low dimensional systems (not shown here) have failed to show well defined band-like signatures. In our opinion, such a failure is probably due to the much higher sensitivity of soft X-ray angle-resolved photoemission spectroscopy, if compared to the low energy application of the same technique, to angular distortions caused by the sample mounting and cleaving procedures. As a rule of thumb, we suggest that thick three dimensional samples, like the Ce compounds studied here or the $\mathrm{Nd_{1.85}Ce_{0.15}CuO_4}$ single crystal whose Fermi surface is investigated in [7], can indeed be glued and post-cleaved without running the risk of inducing a mosaic spread but that this is probably not the case for lower dimensional systems where great care must be taken in sample preparation and alternative solutions should be looked for.

Given the used experimental geometry, five of the six available degrees of freedom (see Figure 1.20) of the sample manipulator are needed for a correct alignment of the sample. The tilt angle, β, has in fact only been used to centre the photoemission image on the detector. Added to this, if a temperature dependent study is to be performed on a cleaved sample whose measurable surface is generally small, an accurate monitoring system of the manipulator's contraction/expansion should be used in order to ensure that the same part of the sample is being illuminated by the beam. Although a direct investigation of the role of the photon beam spot size has not been addressed in this thesis, its importance is refered to in [8] where the effect of the momentum resolution is discussed showing that the smaller the spot size, the better the resolution. The Scienta SES 2002 electron analyser has an angular resolution that is better than 0.3° (FWHM) for all the peaks within an angle of $\pm 3.5^\circ$ from normal emission and better than 0.5° for all the peaks within an angle of $\pm 5^\circ$. According to equation (2.5), for $h\nu = 880\mathrm{eV}$ the momentum resolution is better than $0.1\,\text{Å}^{-1}$. For the kind of experiments performed in this thesis, where Brillouin zones of the order of 3Å^{-1} have been investigated, the momentum resolution has proven to be more than acceptable. However, for studies whose attention is focused on the nature of the Fermi surface for example, where an accurate determination of the Fermi level crossings is essential, an improvement of the momentum resolution would no doubt be appreciated. It is also true that a smaller illuminated area of the sample would reduce problems related to intrinsic or cleaving-induced non-homogeneities. Finally, a smaller spot size would also allow a better matching to the electron optics of the analyser.

To conclude, soft X-ray angle-resolved photoemission spectroscopy is a demanding and challenging technique whose advantages, with respect to the low energy application of the same technique, are not free of charge. However, provided particular attention is devoted to issues such as energy and momentum resolution, photon flux and sample quality, the higher bulk sensitivity pays for the additional experimental efforts. This is particularly so for highly corrrelated systems such as the Ce compounds investigated here, or for high-T_c cuprate superconductors where the Cu-O planes in which the superconductivity originates are located at several Å below the surface. Finally, it is worth noting that very recent work at low photon energies ($h\nu = 7\text{eV}$) offers the possibility of bulk sensitive measurements with sub-meV energy resolution and excellent $\underline{k}$-resolution [9]. However, the possibility of exploiting resonances, measuring far below the Fermi level and combining core-level and absorption measurements is unique to the soft X-ray range. Therefore, depending on the problem, one should probably envisage performing both types of measurements.

---

[1] J. Minár, S. Chadov, H. Ebert, L. Chioncel, A. Lichtenstein, C. de Nadaï, N. B. Brookes, Nucl. Instrum. Meth. Phys. Res. A, accepted for publication (2005).

[2] Ch. Søndergaard, Ph. Hofmann, Ch. Schultz, M. S. Moreno, J. E. Gayone, M. A. Vicente Alvarez, G. Zampieri, S. Lizzit, A. Baraldi, Phys. Rev. B **63**, 233102 (2001).

[3] Ph. Hofmann, Ch. Søndergaard, S. Agergaard, S. V. Hoffmann, J. E. Gayone, G. Zampieri, S. Lizzit, A. Baraldi, Phys. Rev. B **66**, 245422 (2002).

[4] L. Duò, Surf. Sci. Reports **32**, 233-289 (1998).

[5] C. G. Olson, P. J. Benning, M. Schmidt, D. W. Lynch, P. C. Canfield, D. M. Wieliczka, Phys. Rev. Lett. **76**, 4265 (1996).

[6] J. J. Yeh, I. Lindau, *At. Data Nucl. Data Tables* **32**, 1 (1985).

[7] T. Claesson, M. Månsson, C. Dallera, F. Venturini, C. de Nadaï, N. B. Brookes, O. Tjenberg, Phys. Rev. Lett. **93** 136402 (2004).

[8] A. Sekiyama, S. Suga, J. Electron Spectrosc. Relat. Phenom. **137**-**140**, 681-685 (2004).

[9] T. Kiss, F. Kanetaka, T. Yokoya, T. Shimojima, K. Kanai, S. Shin, Y. Onuki, T. Togashi, C. Zhang, C. T. Chen, S. Watanabe, Phys. Rev. Lett. **94**, 057001 (2005).